Searches for Supersymmetry With Multiple b-jets With the ATLAS Detector

Jack Joseph Hall

Supervisor: Prof. Daniel R. Tovey

Department of Physics and Astronomy

The University of Sheffield

This thesis is submitted for the degree of

Doctor of Philosophy

20th February 2023

Dedicated to the memory of John James Hall

Searches for Supersymmetry With Multiple b-jets With the ATLAS Detector

Author: Jack Joseph Hall, University of Sheffield

Supervisor: Prof. Daniel R. Tovey, University of Sheffield

Internal Examiner: Dr. Matthew Malek, University of Sheffield

External Examiner: Prof. Tina Potter, University of Cambridge

Abstract

This thesis presents two searches for supersymmetry using proton-proton collision data collected with the ATLAS detector from 2015 to 2018 corresponding to the Run 2 dataset with a total integrated luminosity of 139fb^{-1} at $\sqrt{s} = 13$ TeV. The calibration of the DL1r algorithm responsible for the identification of jets originating from b-hadrons (b-jets) for jets reconstructed using the ParticleFlow algorithm and the Run 2 dataset, is also presented.

The first search targets the supersymmetric signature of pair-produced gluinos decaying to top-anti-top or bottom-anti-bottom pairs and the lightest neutralino. The resulting detector signature is expected to contain multiple b-jets and large amounts of missing transverse energy. The second search presents a model-independent strategy that utilises a Gaussian function to search for excesses above the Standard Model (SM) in a observable sensitive to beyond the SM (BSM) events. No significant excesses above the SM prediction were observed from either search. Subsequently, 95% confidence limits (CL) were set in the gluino-neutralino mass plane and for the cross section of a signal distributed according to Gaussian function, respectively. Additionally, model-independent limits on the number of BSM events at 95% CL have also been set.

Contents

List of Figures

List of Tables

Part I

Opening

Chapter 1

Introduction

Over the past century, there has been a substantial development in the physical understanding of what constitutes the fundamental building blocks of the Universe. Ranging from the particles that form observable matter, to the mathematics of how they interact and obtain their mass; all can be understood from the Standard Model (SM) of particle physics. Measurements of the properties of the SM from high-energy particle physics experiments indicate the theory to be successful to a high level of precision. However, from astrophysical and cosmological measurements of dark matter, the baryonic matter we understand so well only contributes to a small fraction to the composition of the Universe. Because of this and other unexplained phenomena, there are strong indications that the SM of particle physics is incomplete.

One particularly concerning aspect of the SM is the sensitivity of the Higgs mass to quantum corrections at large energy scales. For the Higgs mass to be consistent with that observed from the Large Hadron Collider (LHC), large cancellations of these terms would be required at high energy scales, which is not currently expected in the SM. Supersymmetry (SUSY) provides a solution to this problem by introducing supersymmetric particles that cancel the large corrections. The lightest supersymmetric particle (LSP) also has the characteristics that correspond to a weakly interacting massive particle (WIMP). Therefore, SUSY provides an elegant extension to the SM for large energy scales and provides a solution to a key challenge in modern particle physics; dark matter.

The LHC is a proton-proton circular collider with collision energies in the TeV scale. The collider is capable of producing all SM particles as well as heavier beyond the SM (BSM) particles, should they exist. This energy scale also determines the subsequent two primary objectives of the LHC programme following the discovery of the Higgs boson in 2012. These are; measuring the properties of all SM particles and probing the existence of new physics. The aim of this thesis is to contribute towards the latter, using data recorded from 2015 to 2018 at the ATLAS experiment corresponding to the Run 2 dataset with a total integrated luminosity of 139fb^{-1} at $\sqrt{s} = 13$ TeV.

The hadronisation of quarks and gluons in a detector are reconstructed as jets. Jets originating from b-quarks (b-jets) are common detector signatures at hadron colliders because of their

production in QCD interactions, the coupling of the Higgs boson to massive particles, top quark decays and their production in BSM processes. Therefore, the ability to correctly identify and classify a b-jet is an important challenge at the ATLAS experiment. To do this, b-jet identification algorithms are used, in a process known as b-tagging. The algorithm has a different efficiency for correctly b-tagging jets for data and simulation. Therefore, a measurement must be performed for simulated events to correctly calibrate for the efficiency observed in the data. This provides a collection of calibrated b-jets for use in the ATLAS physics programme.

This thesis presents the search for SUSY with events originating from the decays of the supersymmetric partner of the gluon (gluino), because of the high production cross section at hadron-hadron colliders. Gluinos are expected to predominantly decay to the supersymmetric partners of quarks (squarks), with the third generation expected to dominate from being the lightest. Therefore, the detector signature is expected to contain multiple b-jets and large quantities of missing transverse momentum. Two searches for SUSY are performed in this thesis that target this process. The first is an evolution of the searches performed in Refs. [1, 2] and uses the ATLAS Run 2 dataset. The previous searches (2015 to 2016 data corresponding to a total integrated luminosity of 36.1fb^{-1} [1] and 2015 to 2017 data corresponding to a total integrated luminosity of 79.8fb^{-1} [2]) found no statistically significant excesses above the SM, consistent with other searches for SUSY at the ATLAS and CMS experiments using the Run 2 dataset.

The second search focuses on a novel method to improve the existing ATLAS SUSY search strategy, which depends highly on the signal processes sought. This method makes use of a generic mathematical function to search for deviations in the data with respect to the SM expectation for a given observable. The example illustrated in this thesis uses a Gaussian function and the observable is the logarithm of a quantity that sums the transverse momentum of the hadrons and leptons and the missing transverse momentum in the event. The benefits of this method are three-fold. Firstly, the statistical inference technique exploits the shape of the observable to enhance sensitivity to signal processes with a small mass difference between the produced SUSY particle and the LSP. Secondly, the use of an arbitrary mathematical function extends the sensitivity of the search, beyond a targeted signal process, to a greater number of BSM processes. Finally, there is a simplification of the process to interpret the results of the search in context of different BSM processes. This is because the 95% confidence limits are presented as a function of the mathematical shape parameter(s), not parameters of specific signal processes.

The opening component of the thesis begins by summarising the theoretical basis. It starts in Chapter 2 with a discussion of the framework that provides the current best theoretical predictions of particle physics; the SM. The chapter is concluded with a description of the various limitations of the SM; SUSY provides an elegant solution to several of these. Therefore, Chapter 3 discusses the mathematics of supersymmetry and the resulting phenomenological consequences, which allow a detector signature to be sought at the LHC.

The subsequent component is dedicated to the experimental foundations and methodology of the thesis. Chapter 4 introduces the phenomenological principles of proton-proton collisions.

This motivates the discussion, in Chapter 5, of the methods for detection and reconstruction of the particles produced in pp collisions detected by the ATLAS experiment. The final chapter comprising the methodology section is Chapter 6, which discusses the statistical inference techniques used by the subsequent analysis chapters.

The final component contains the various analyses and measurements performed with significant contributions from the author. Chapter 7 presents the measurement of the b-tagging efficiency for the DL1r b-tagging algorithm for simulated events with jets reconstructed with the ParticleFlow algorithm. This is followed by Chapter 8, where the Run 2 search for pair-produced gluinos decaying to multiple b-jets and large quantities of missing transverse momentum is presented. Chapter 9 presents the search for SUSY using a Gaussian function and the results are reinterpreted for signal events, where pair-produced gluinos decay to multiple b-jets and large quantities of missing transverse momentum.

Part II

Theory

Chapter 2

The Standard Model

Over a century of development in the quantum understanding of the observable matter of the Universe has resulted in the Standard Model (SM) of particle physics. The framework includes all the properties of the currently detected particles and the particles responsible for the interactions between them. The predictions of the SM are being studied in high-energy particle physics (HEP) experiments and so far, have been found to be consistent with experimental observations for various measurements. Consequently, the SM currently comprises the greatest understanding of particle physics. This chapter will begin by introducing the mathematical basis of the theory, which results in the physical processes observed in HEP experiments. The SM, however, is known to be an incomplete theory and therefore, the chapter is concluded with a discussion in relation to these limitations.

2.1   The Standard Model

2.1.1   Symmetries

The SM of particle physics is a combination of two quantum field theories (QFTs); Electroweak Theory (EWT) and Quantum ChromoDynamics (QCD). EWT is the unification of Quantum ElectroDynamics (QED) and the weak interaction for energy scales above the order of ($\mathcal{O}(246 \text{ GeV})$) due to electroweak symmetry breaking (EWSB). QCD is the framework describing the strong interaction. Therefore, the SM describes all known fundamental interactions excluding gravity. For each QFT, the field is required to be invariant under specific transformations known as gauge symmetries. The combined conserved symmetry of the SM is given by

$$G_{SM} = SU(3)_c \times SU(2)_L \times U(1)_Y, \tag{2.1}$$

where $(S)U(N)$ is a (special) unitary group of N dimensions and so, $SU(3)_c$, $SU(2)_L$ and $U(1)_Y$ are the unbroken gauge symmetries corresponding to the strong, weak and electromagnetic

interactions respectively. The conserved quantities of the unbroken symmetries of QCD, weak and QED interactions are colour charge (c), weak isospin (I_3) and weak hypercharge (Y) respectively.

The generators of the $SU(2)_L$ group correspond to three massive gauge bosons of the weak interaction, where their non-zero mass would break the gauge symmetry of the electroweak (EW) interaction. However, the masses of the bosons associated with the $SU(2)_L$ group can be non-zero if the symmetry is broken from EWSB or, equivalently, the Brout-Englert-Higgs (BEH) mechanism. The non-zero vacuum expectation value of the Higgs field spontaneously breaks EW symmetry, resulting in three massive and one massless bosons. QCD remains unbroken and therefore also has a massless gauge mediator. The SM was confirmed to be a spontaneously broken gauge theory by the discovery of the Higgs boson resonance with a mass ~ 125 GeV [3, 4].

2.1.2 Particles

The SM of particle physics is a framework that also allows all known fundamental particles to be classified into groups based upon their properties. It can be most simply separated into fermions and bosons. Fermions constitute the observable matter of the Universe and are characterised by their half-integer spin. Whereas, bosons are the mediators of the fundamental interactions of the Universe, characterised by their integer spin. A schematic presenting these can be seen in Figure 2.1.

Figure 2.1: The elementary particles of the Standard Model. Taken from Ref. [5].

Fermions can be split into two further elementary particles; quarks and leptons. Exactly three generations of fermions exist, where each subsequent generation has a larger mass than that proceeding it. In the lepton sector, each generation also has a unique lepton flavour. Each SM fermion also has an equivalent antimatter particle, where they have equal mass but all other quantum numbers are the negative of the matter particle. The only exception related to this is the neutrino sector, where right-handed (RH) neutrinos and left-handed (LH) anti-neutrinos have never been observed.

Within Figure 2.1 is a visualisation of the permitted interaction mechanisms for the SM fermions. The weak interaction couples to all massless LH fermions and RH anti-fermions. Quarks are the only elementary particles that interact via the strong force because of their colour charge. Charged leptons possess electric charge and consequently can interact electromagnetically or via the weak interaction. The interaction rate for neutrinos is known to be very small because they are electrically and colour neutral and hence, only interact via the weak force.

Figure 2.1 also presents the respective mediator(s) for each interaction. Both the photon and gluon are massless, whereas the gauge bosons have relatively large masses obtained from the BEH mechanism. The spin-0 Higgs boson is distinct from all other SM bosons because its interaction is completely unique, where the coupling to fermions and bosons is based upon their mass. The Higgs boson is responsible for the origin of mass for all fermions and bosons via the BEH mechanism and therefore, has an essential purpose in the SM.

2.1.3   Electroweak Symmetry Breaking and the Higgs

The previous section described the essential inclusion of the EWSB mechanism in the SM. This section will discuss the mechanism in greater detail to motivate a broader discussion of the Higgs potential. The EWSB mechanism posits a self-interacting complex scalar SU(2) doublet field (ϕ), with four degrees of freedom, given by [6];

$$\phi = \frac{1}{\sqrt{2}} \begin{pmatrix} \phi_1 + i\phi_2 \\ \phi_3 + i\phi_4 \end{pmatrix} = \begin{pmatrix} \phi^+ \\ \phi^0 \end{pmatrix}. \tag{2.2}$$

The scalar field couples to the EW gauge fields through the covariant derivative (D^μ) in the kinetic terms of the Higgs Lagrangian ($\mathcal{L}_{\text{Higgs}}$) [7];

$$\mathcal{L}_{\text{Higgs}} = (D_\mu \phi)^\dagger (D^\mu \phi) - V(\phi) \ \text{ where } \ D_\mu \phi = \left(\partial_\mu + i\frac{g_w}{2}\sigma_a W_\mu^a + i\frac{g'}{2}Y B_\mu\right)\phi, \tag{2.3}$$

g_w and g' are coupling constants of the SU(2)$_L$ and U(1)$_Y$ symmetries, σ_a are the generators of the SU(2)$_L$ group, $Y = 2(Q - I_W^{(3)})$ is the weak hypercharge and W_μ^a for $a = 1, 2, 3$ and B_μ are the four unbroken bosons of the EW symmetry. Also within Equation 2.3 is the scalar potential ($V(\phi)$) given by

$$V(\phi) = \mu^2 \phi^\dagger \phi + \lambda (\phi^\dagger \phi)^2, \tag{2.4}$$

where λ is the quartic self-coupling parameter and must be positive for the potential to have a finite minimum. The vacuum state of the potential corresponds to the minimum energy state of the scalar field in Equation 2.4 [6]. If $\mu^2 > 0$, which is depicted in Figure 2.2(a), the minimum of the potential occurs at $\phi = 0$ and the masses of the scalar and EW gauge fields would be zero, which is not experimentally observed. If $\mu^2 < 0$, which is depicted in Figure 2.2(b), the neutral component of the scalar doublet acquires a non-zero real vacuum expectation value (VEV) given by; $\langle \phi \rangle = v/\sqrt{2}$.

(a)   (b)
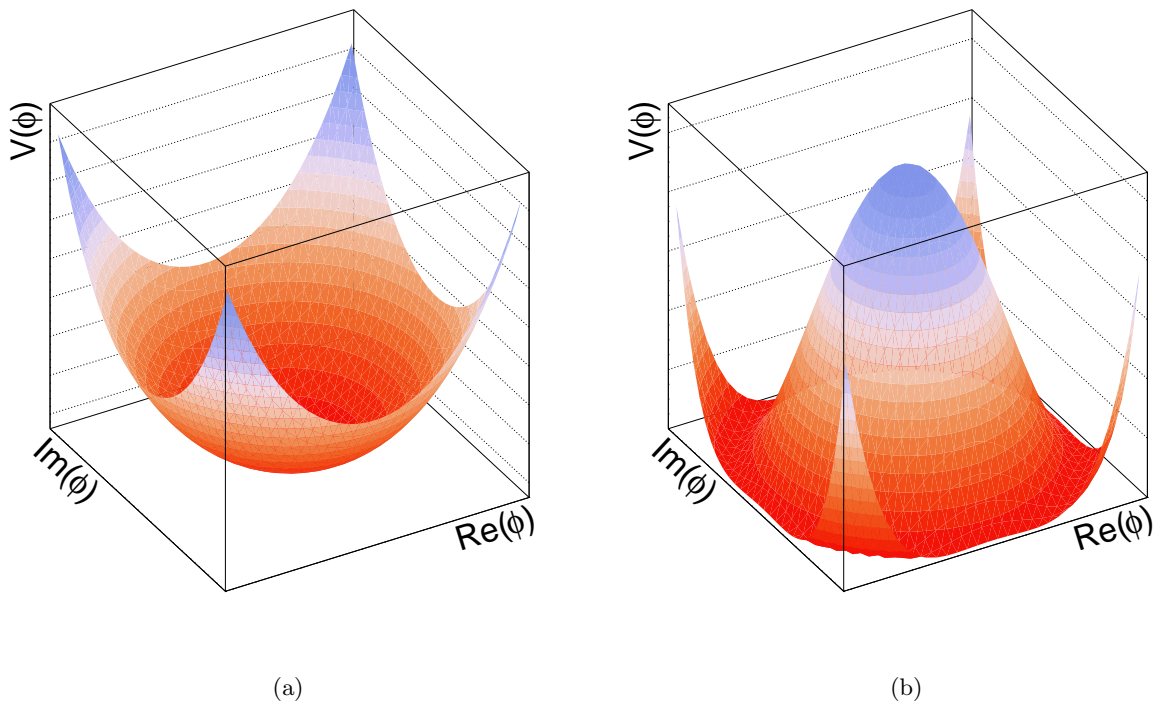
Figure 2.2: The Higgs potential ($V(\phi)$) when $\lambda > 0$ and (a) $\mu^2 > 0$ or (b) $\mu^2 < 0$. Taken from Ref. [8].

Since there is an infinite set of potential vacuum state minima, the choice spontaneously breaks the $\mathrm{SU(2)}_L \times \mathrm{U(1)}_Y$ symmetry and the value of the VEV determines the scale of the symmetry breaking [7]. By expanding the scalar field about the VEV, one can rewrite the neutral component of the scalar field as [8];

$$\phi = \frac{1}{\sqrt{2}} \exp \left\{ i \vec{\sigma} \cdot \vec{\theta}(x)/v \right\} (v + \eta(x)), \tag{2.5}$$

where $\vec{\theta}(x)$ are three (massless) Goldstone[1] bosons associated with three of the four spontaneously

---

[1] Goldstone's Theorem states that for every spontaneously broken continuous symmetry, the theory must contain a massless particle called a Goldstone boson [9].

broken generators of the electroweak group and $\eta(x)$ is a massive scalar field.

Using the unitary gauge[2] on the Lagrangian eliminates the Goldstone bosons and causes the gauge bosons to gain longitudinal polarisation states, that is, acquire mass [6]. The charged (neutral) W_μ^1 (W_μ^3) and W_μ^2 (B_μ) interaction eigenstates combine to form the physical $W^\pm$ (Z, γ) mass eigenstates. In the unitary gauge, the massive scalar field becomes the physical Higgs boson (H), where the mass is determined from $m_H = \sqrt{2\lambda}v$ [6, 7].

The resulting Lagrangian is known as Salam–Weinberg model [6], where the mass terms and couplings of the EW bosons can be identified. The mass term for the W boson is a function of fixed parameters (g_w and v or equivalently, e and the Weinberg angle θ_W) and is given by [6];

$$m_W = \frac{g_w v}{2} = \frac{ev}{2\sin\theta_W} \quad \text{where} \quad \sin\theta_W = \frac{g'}{\sqrt{g_w^2 + g'^2}}. \tag{2.6}$$

Using the experimentally measured values for the W boson mass and coupling, the obtained VEV is $v \sim 246$ GeV and therefore $\langle\phi\rangle \sim 174$ GeV. The equations for the remaining EW bosons are also obtained from the Salam-Weinberg model, where the observed masses for the two bosons are consistent with the theorised prediction.

The Higgs boson is theorised to couple to fermions through Yukawa interactions via the Lagrangian,

$$\mathcal{L}_{\text{Yukawa}} = -\hat{y}_{d_{ij}}\bar{q}_{L_i}\phi d_{R_j} - \hat{y}_{u_{ij}}\bar{q}_{L_i}\tilde{\phi}u_{R_j} - \hat{y}_{l_{ij}}\bar{l}_{L_i}\phi e_{R_j} + \text{h.c.}, \tag{2.7}$$

where q_L (l_L) and u_R, d_R (e_R) are the quark (lepton) SU(2)$_L$ doublets and singlets[3], respectively, and $\hat{y}_{f_{ij}}$ for $f = u, d, l$ are the Yukawa matrices for the up-quark, down-quark and charged lepton sectors respectively [7]. Once the Higgs field acquires a VEV, for the ith fermion family ($i = u, d, l$), a fermion acquires mass calculated by $m_{f_i} = y_{f_i}v/\sqrt{2}$ [7] and so, all SM fermions acquire mass through the Higgs boson due to EWSB. Since all gauge and fermions masses as well as the gauge couplings are fixed by the scale of the VEV, the entire mass scale and interactions of the SM are determined by the Higgs potential.

The observation of atmospheric neutrino oscillations [11] is only possible if there is a mass hierarchy between the three generations of neutrinos, which would mean the masses would be inherently non-zero. Cosmological observations have constrained the sum of the neutrino masses, such that; $\sum_{i=e,\nu,\tau} m_{\nu_i} \leq 0.3$ eV. This is contrary to the SM prediction, which constructs them to be massless. If neutrinos are SM Dirac fermions, this would imply an unnaturally small Yukawa coupling to the Higgs field ($\leq 10^{-12}$) [6] and thus, it is probable that they obtain mass by a different mechanism [6]. The SM can construct neutrinos to have mass if the mass term is Majorana. However, the classification of neutrinos being Majorana particles from the observation

---

[2]The unitary gauge is the gauge where the complex scalar field $\phi(x)$ is entirely real i.e $\vec{\theta}(x) = 0$ [6, 10].

[3]Right-handed fermions are not SU(2)$_L$ doublets because the fermion mass Lagrangian term is forbidden by SU(2)$_L \times$ U(1)$_Y$ gauge invariance.

of neutrinoless double beta decay is yet to occur.

The Higgs coupling to fundamental fermions is linearly proportional to the fermion masses, whereas the couplings to bosons are proportional to the square of the boson masses, therefore it does not directly couple to the gluon or photon [7]. The dominant mechanisms for Higgs boson production and decay involve vector bosons (W, Z) and/or third-generation charged fermions. The predicted fermion and gauge boson masses originating from each SM Yukawa coupling are consistent with the experimental observations, which can be seen in Figure 2.3.
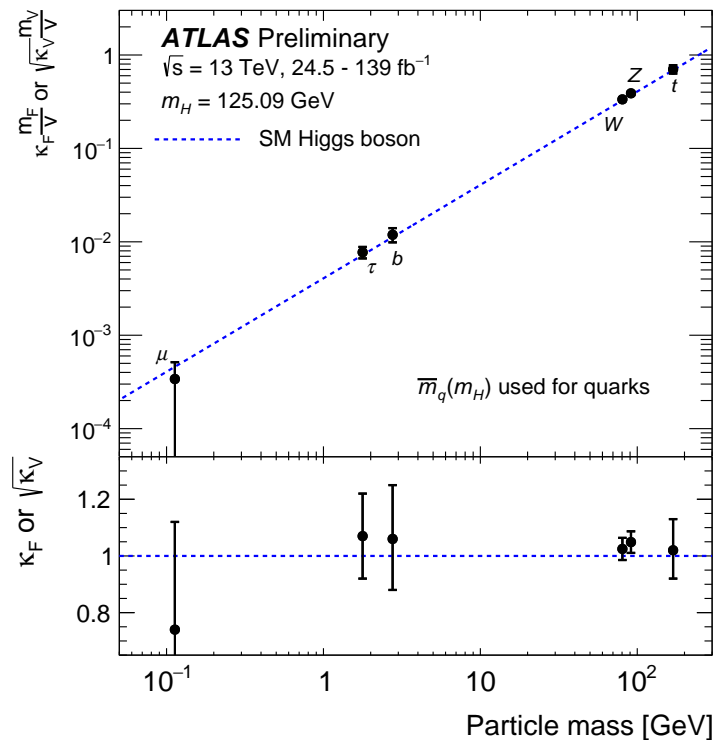
Figure 2.3: The measured charged fermion and boson masses in accordance to the prediction from the experimentally observed Higgs boson mass. Taken from Ref. [12].

The SM has 19 parameters; four from the electroweak sector $(g_w, g', \mu^2$ and $\lambda)$, the combined nine quark and charged lepton masses (or more precisely the nine fermion Yukawa couplings to the Higgs field [6]), three mixing angles and one Charge-parity (CP)[4] phase from the Cabibbo-Kobayashi-Maskawa (CKM) matrix [13, 14] and from QCD, the QCD coupling and phase[5]. The only unpredicted parameter is $\mu^2 = m_H$, which upon measuring determines all gauge couplings and masses of all SM particles. Using the current average of the Higgs boson mass measurements $(m_H = 125.25 \pm 0.17$ GeV [7]), implies $\lambda \sim 0.13$ and $|\mu| \sim 88.4$ GeV. From constraints from precision electroweak and flavour measurements, the Higgs boson seems a fundamental scalar and weakly coupled up to the Planck scale; $M_P = (8\pi G_N)^{-0.5} = 2.4 \times 10^{18}$ GeV [15].

---

[4]CP symmetry is the combined symmetry of charge-conjuation (C) and parity (P) symmetries.

[5]The QCD phase is experimentally known to be very small and so, is often assumed to be zero [6]).

2.2 Limitations of the Standard Model

The experimental predictions of the Standard Model are consistent with the large majority of observations in HEP experiments. However, experimental evidence from other fields, such as astrophysics and cosmology, indicate that our understanding of particle physics is incomplete. Also within this section, the aesthetic shortcomings of the SM will be discussed. Aesthetic shortcomings could be those considered as those that do not result in the SM being mathematically or physically incomplete but instead those that are desired to not be present.

2.2.1 Unexplained Phenomena

Dark matter (DM) and dark energy - One of the most significant pieces of experimental evidence for additional matter not predicted by the Standard Model is the cosmological evidence for a invisible and weakly-interacting (*dark*) matter in the Universe. The greatest direct evidence for this originates from the analysis of galactic rotation curves, which are velocity distributions of stars as they orbit the galactic centre [16]. By relating the classical centripetal acceleration to the gravitational acceleration, one would expect the mass to be distributed $\propto r^{-\frac{1}{2}}$, whereas it is observed to be $\propto r$, which suggests an additional component of non-luminous matter unaccounted for.

Additional key evidence for dark matter originates from the cosmological and astrophysical measurements of the large-scale structure of the Universe by measuring the cosmic microwave background (CMB) radiation [17, 18]. These and other observations have provided a strong experimental basis for the ΛCDM cosmological model, which is the Standard Model of cosmology [6]. In the ΛCDM model of the Universe, the total energy density (Ω) in the Universe is consistent with the flat geometry of space-time predicted by inflationary models; $\Omega = 1$ [6]. The current predictions from cosmological and astrophysical observations suggest that the normal baryonic matter is $\Omega_B = 0.02237h^{-2} = 0.0493$ [19–21], photons and neutrinos contribute $\Omega_\gamma = 2.473 \times 10^{-5}h^{-2} = 5.38 \times 10^{-5}$ and $\Omega_\nu = < 0.003$ [19] respectively. Cold (i.e non-relativistic) dark matter is $\Omega_C = 0.1200h^{-2} = 0.265$ [19–21] and the remaining component originates from dark energy ($\Omega_\Lambda = 0.685$) [19, 20], where dark energy is the energy responsible for the accelerated expansion of the Universe. This means that approximately only 5% of the energy density of the Universe can be explained with the SM of particle physics.

A particle suggested as the solution to dark matter is the stable weakly-interacting massive particle (WIMP), whose mass[6] and interaction rate is governed by the new physics associated with the TeV-scale. The properties of the WIMP result in a particle compatible with the observed density of dark matter [7]. Figure 2.4 presents the current experimental limits on the WIMP mass limit as a function of the nucleon cross section.

---

[6]Because of the specified relic density at freeze-out, the so-called "WIMP miracle" suggests $m_\chi \leq 5$ TeV.
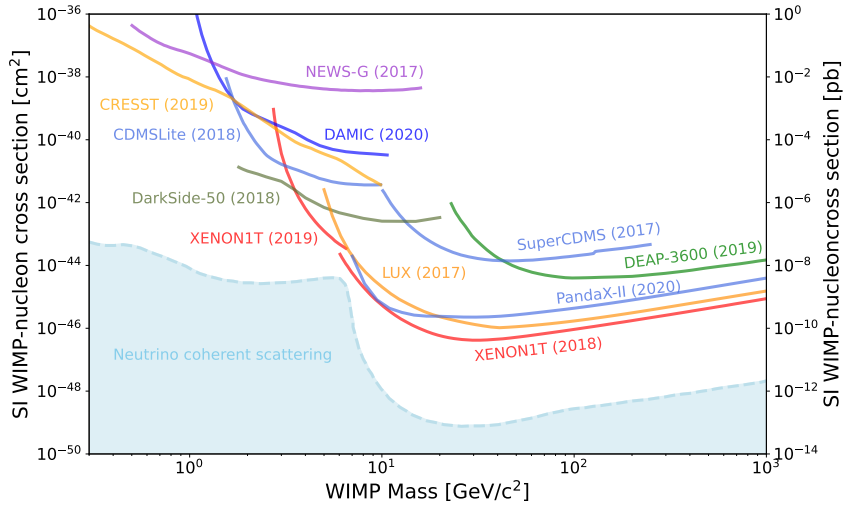
Figure 2.4: WIMP mass $[\text{GeV}/c^2]$ as a function of the nucleon cross section. Taken from Ref. [7].

Gravity is the only fundamental interaction not described by the SM. Theorists have struggled to quantise gravity through a spin-2 mediator as it results in a non-renormalisable theory and thus, a combined solution into the SM has yet to be achieved [8]. The interaction strength of gravity is much smaller compared to the three SM interactions at the EW scale and so, it has no measurable effect on the subatomic scale and thus, is commonly excluded from HEP predictions [22]. However, the strength of gravitational interaction is expected to be similar to that of other interactions at the Plank scale [22].

2.2.2 Aesthestic Shortcomings

Fermion mass hierarchy - The masses of all SM fermions, or experimentally known bounds for those that have not been directly measured, can be seen in Figure 2.5.
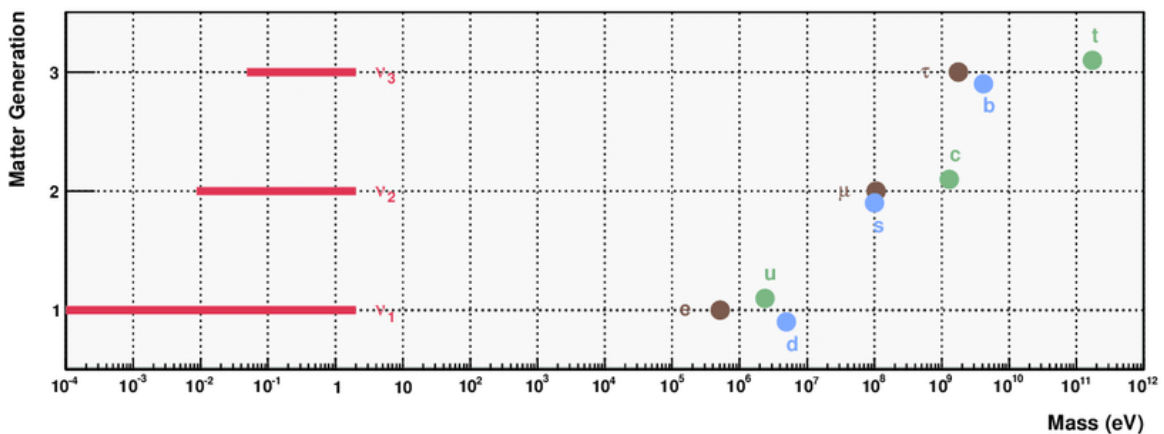
Figure 2.5: The SM fermion masses as a function of their generation. Taken from Ref. [23].

The SM fermions span approximately six orders of magnitude with no clear indication as to why. The masses of fermions of the same generation are approximately of the same order - excluding the top quark, which is nearly two orders of magnitude higher than the next heaviest fermion; the

b-quark. Also, there are no particles between the energy range of the SM charged fermion sector and the less-understood neutrino sector ($10-10^5$ eV). This indicates a well-established hierarchy between the two scales and may be a hint to neutrinos obtaining mass via other mechanisms.

Unification of coupling constants - The SM coupling constants have different interaction strengths at the weak scale, but extrapolating them to higher energies shows near unification shortly before the Planck scale. This may be interpreted as an indicator of the underlying grand unification of the fundemental interactions, given the simplicity of the SM. However, considering only the SM particles, this unification does not occur, as can be seen by the dashed lines in Figure 2.6.
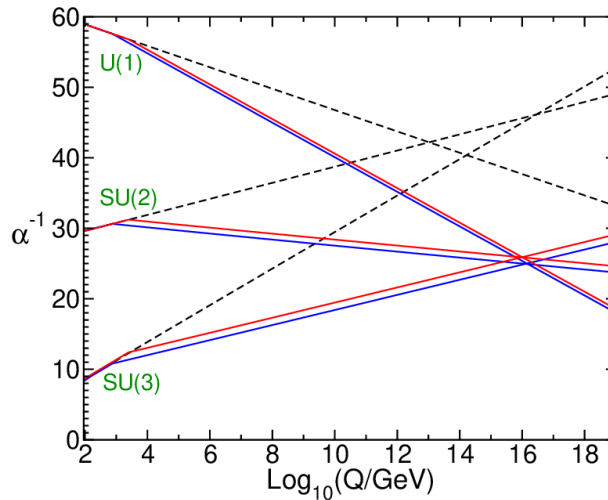
Figure 2.6: The interaction strength of the gauge couplings in the Minimal supersymmetric Standard Model (MSSM, coloured) and the Standard Model (SM, dashed) as a function of the energy scale Q. It is extrapolated from the weak scale to the Planck scale assuming the SM particle content and SM-plus-MSSM, where the MSSM particles enter above the weak scale but below the few-TeV scale, particle content, respectively. Taken from Ref. [24].

Hierarchy problem - As discussed in Section 2.1.3, the SM seems to be a correct effective field theory (EFT) for $\lambda = 0.126$ and $\mu^2 = -(88.4 \text{ GeV})^2$ [24]. Charged fermions and the electroweak gauge bosons of the SM all obtain masses from $\langle H \rangle$, so that the entire mass spectrum of the Standard Model is directly or indirectly sensitive the scale at which the SM is no longer appliable, termed the ultraviolet cut-off (Λ_{UV}). The ultraviolet cut-off can also be interpreted as the energy scale at which new physics enters to alter high-energy behaviour, but should be considered as real because of the significance of the gravitational interaction strength at this scale [24].

The problem is that μ^2, or will henceforth be known as m_H^2, receives quantum corrections from the virtual effects of every particle that couples directly or indirectly to the Higgs field. If the Higgs field couples to a fermion f (with mass m_f) with coupling strength λ_f, the field receives a quantum correction from the fermion [24] calculated by

$$\Delta m_H^2 = -\frac{|\lambda_f^2|}{8\pi^2}\Lambda_{\text{UV}}^2 + \mathcal{O}(\ln \Lambda_{\text{UV}}) + \dots. \tag{2.8}$$

The correction of Equation 2.8 is depicted in the LHS of Figure 2.7.
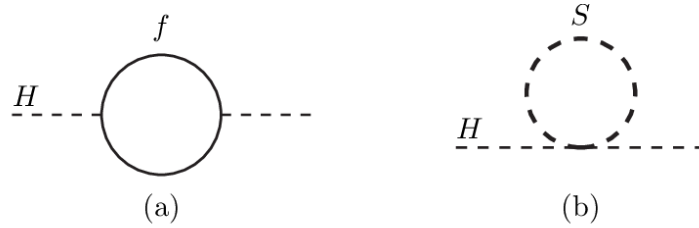
Figure 2.7: Correction to the Higgs field via a (a) fermion (b) scalar particle. Taken from Ref. [24].

Each correction is proportional to the Yukawa coupling of the fermion and additionally for quarks, the corrections are multiplied by three because of the number of colours, therefore the largest contribution comes from the top quark; $\lambda_t \sim 0.94$. If Λ_{UV} is $\mathcal{O}(M_P)$, the problem occurs that the quantum correction to m_H^2 is ~ 30 orders of magnitude larger than the obserbed value. Therefore, the stability of the Higgs field from radiative corrections is highly sensitive to the energy scale and hence why it has been deemed to be the hierarchy problem. Consequently, the SM is referred to as unnatural and hence, fine-tuned [25, 26] because the SM ought be in-sensitive to the scaling of the ultraviolet cut-off (natural). The hierarchy problem is therefore not an issue of the SM itself but instead a sensitivity of the Higgs potential to new physics in almost any extension to the SM [24].

One could consider this as suggesting new physics existing in the 16 orders of magnitude difference between the presently explored electroweak scale, $M_W \sim 100$ GeV, and the Planck scale. If the Higgs boson is a fundamental particle, and there really is physics far above the electroweak scale, a possible solution is a cancellation between the various contributions to Δm_H^2 via a symmetry. Consider a heavy complex scalar particle S, with mass m_S, that couples to the Higgs field, then the correction is calculated by [24];

$$\Delta m_H^2 = \frac{|\lambda_S|}{16\pi^2}[\Lambda_{\mathrm{UV}}^2 - 2m_S^2 \ln(\Lambda_{\mathrm{UV}}/m_S) + \ldots]. \tag{2.9}$$

This correction is schematically depicted on the right-hand side (RHS) of Figure 2.7 [24]. Comparing Equations 2.8 and 2.9 suggests that the new symmetry ought to relate fermions and bosons, which is known as supersymmetry (SUSY) [24]. If each of the fermions of the SM is related to two complex scalars with $\lambda_S = |\lambda_f^2|$, the existence of SUSY cancels the quadratic divergence and the remaining logarithmic terms can be cancelled in the renormalization proceedure. SUSY is therefore a natural framework for elementary scalar fields. SUSY will be discussed in greater detail in the next chapter due to being the BSM theory that is searched for in this thesis.

2.3 Conclusion

In this chapter, the gauge symmetries of the Standard Model of particle physics are discussed, which ultimately determines the predictions for the interactions between each fundamental particle. Although the SM has been successful at predicting the experimental observed matter of the Universe, many challenges and issues remain for a complete understanding of particle physics. This chapter concluded with a description of those challenges, in particular the hierarchy problem, that is, the extreme sensitivity of the Higgs mass to radiative corrections at large energy scales. A natural solution to this could be supersymmetry, which cancels the large corrections by the addition of supersymmetric particles.

Chapter 3

Supersymmetry

The previous chapter concluded with a discussion on the incomplete nature of the Standard Model (SM) of particle physics. A potential solution to the large logarithmic corrections to the Higgs mass at large energy scales is a symmetry relating fermions and bosons known as supersymmetry (SUSY). In this chapter, the mathematical algebra of the symmetry and the phenomenological consequences of the R-parity conserving (RPC) minimal supersymmetric Standard Model will be discussed. The chapter concludes with a discussion of the dark matter candidate predicted by RPC SUSY, and how it could be observed in direct detection searches at the Large Hadron Collider (LHC).

3.1   Transformation and Supermultiplets

SUSY is a space-time symmetry that transforms a bosonic state into a fermionic state, and vice versa. The symmetry can be described by the operator Q, such that;

$$Q \left| \text{Boson} \right\rangle = \left| \text{Fermion} \right\rangle \quad \text{and} \quad Q \left| \text{Fermion} \right\rangle = \left| \text{Boson} \right\rangle. \tag{3.1}$$

The fermion and boson states of the same particle fall into irreducible representations of SUSY algebra, called supermultiplets [24]. Within a specified supermultiplet, the supersymmetric partner of the recognised SM particle is known as the superpartner. The commutation relations of symmetry cause the particles in a supermultiplet to have equal mass. Additionally, the SUSY generators commute with the generators of gauge transformations, therefore the particles in the same supermultiplet must also have the same electric charge, weak isospin and colour degrees of freedom [24].

The simplest possibility for a supermultiplet consistent with an equal number of bosonic and fermionic degrees of freedom is a two-component Weyl fermion (ψ) and complex scalar field (ϕ), called a chiral supermultiplet [24]. The next simplest possibility for a supermultiplet contains a spin-1 vector boson and therefore its superpartner is a massless spin-1/2 Weyl fermion, known as

a gauge supermultiplet [24].

3.2 Minimal Supersymmetric Standard Model

In the minimal phenomenologically-viable extension of the SM, named the minimal supersymmetric Standard Model (MSSM), each known fundamental particle is in either a chiral or gauge supermultiplet [24]. Because all SM fermions are in chiral supermultiplets, their superpartners are spin-0. The names for these superpartners are the fermion names prefixed by an "s" for "scalar" and therefore are generically referred to as sleptons or squarks and symbolically assigned a tilde $\sim$. The LH and RH quarks and leptons are in separate two-component Weyl fermions so each has its own complex scalar partner. A summary of the predicted particles corresponding to the chiral supermultiplets in the MSSM can be seen in Table 3.1.

Description	Spin-$\frac{1}{2}$	Spin-0
Left-handed Quarks	$Q_i = \begin{pmatrix} u \\ d \end{pmatrix}, \begin{pmatrix} c \\ s \end{pmatrix}, \begin{pmatrix} t \\ b \end{pmatrix}$	$\tilde{Q}_i = \begin{pmatrix} \tilde{u} \\ \tilde{d} \end{pmatrix}, \begin{pmatrix} \tilde{c} \\ \tilde{s} \end{pmatrix}, \begin{pmatrix} \tilde{t} \\ \tilde{b} \end{pmatrix}$
Right-handed Quarks	$u_i = u, c, t$ $d_i = d, s, b$	$\tilde{u}_i = \tilde{u}, \tilde{c}, \tilde{t}$ $\tilde{d}_i = \tilde{d}, \tilde{s}, \tilde{b}$
Left-handed Leptons	$L_i = \begin{pmatrix} \nu_e \\ e \end{pmatrix}, \begin{pmatrix} \nu_\mu \\ \mu \end{pmatrix}, \begin{pmatrix} \nu_\tau \\ \tau \end{pmatrix}$	$\tilde{L}_i = \begin{pmatrix} \tilde{\nu}_e \\ \tilde{e} \end{pmatrix}, \begin{pmatrix} \tilde{\nu}_\mu \\ \tilde{\mu} \end{pmatrix}, \begin{pmatrix} \tilde{\nu}_\tau \\ \tilde{\tau} \end{pmatrix}$
Right-handed Leptons	$e_i = e, \mu, \tau$	$\tilde{e}_i = \tilde{e}, \tilde{\mu}, \tilde{\tau}$
Up-type Higgs	$\tilde{H}_u = (\tilde{H}_u^+ \ \tilde{H}_u^0)$	$H_u = (H_u^+ \ H_u^0)$
Down-type Higgs	$\tilde{H}_d = (\tilde{H}_d^0 \ \tilde{H}_d^-)$	$H_d = (H_d^0 \ H_d^-)$

Table 3.1: List of chiral fermions from the minimal supersymmetric Standard Model. Taken from Ref. [24, 27].

The scalar Higgs boson is spin-0, and so it is in a chiral supermultiplet [24]. However, one supermultiplet is not sufficient. Two supermultiplets are required to avoid the EW gauge symmetry suffering a gauge anomaly and they are named H_u and H_d for weak hypercharge $Y = \frac{1}{2}$ and $Y = -\frac{1}{2}$ respectively [24]. The third components of the weak isospin for H_u (H_d) are $T_3 = 1/2 \ (-1/2)$ and has electric charges $1, 0 \ (0, -1)$ and are denoted $(H_u^+ \ H_u^0) \ ((H_d^0 \ H_d^-))$ [24]. A neutral scalar, that most probably corresponds to the SM Higgs boson, is a linear combination of H_u^0 and H_d^0 [24]. The names for these superpartners are the boson names suffixed by an "ino" therefore, the fermionic partners of Higgs scalars are called Higgsinos, also denoted by a tilde $\sim$.

As presented in Section 2.1.3, the unbroken EW gauge symmetry $SU(2)_L \times U(1)_Y$ is associated with the spin-1 gauge bosons $W^\pm, W^0$ and B^0. In the MSSM, the spin-$\frac{1}{2}$ superpartners of the EW gauge bosons ($\tilde{W}^\pm, \tilde{W}^0$ and $\tilde{B}^0$), are called winos and the bino, respectively, or more generally referred to as gauginos. The spin-$\frac{1}{2}$ partner of the $SU(3)_c$ symmetry is called the gluino. A summary of the gauge supermultiplets can be seen in Table 3.2.

Spin-$\frac{1}{2}$	Spin-1
$\tilde{g}$	g
(gluino)	(gluon)
$\tilde{W}^1, \tilde{W}^2, \tilde{W}^3$	W^1, W^2, W^3
(wino)	(W-boson)
$\tilde{B}^0$	B^0
(bino)	(B-boson)

Table 3.2: Gauge supermultiplets of the Minimal supersymmetric Standard Model. Taken from Ref. [24, 27].

3.3 Soft Supersymmetry Breaking

If supersymmetry were an exact symmetry of nature, then SM particles and their superpartners would be mass degenerate and since these superpartners have not yet been observed, a realistic phenomenological supersymmetry model must be spontaneously broken. If the SUSY breaking is *soft*[1], that is, only broken at low energy scales, the stability of the gauge hierarchy can be maintained. The most general soft SUSY-breaking Lagrangian, compatible with gauge invariance and R-parity conservation[2] in the MSSM, introduces 105 soft new parameters that have no counterparts in the SM [24]. The total number of independent physical parameters that define the MSSM is largely because of these additional parameters.

After EW and SUSY symmetry breaking, there can be mixing between higgsinos and electroweak gauginos [24]. Neutral higgsinos combine with neutral gauginos to form neutralinos ($\tilde{\chi}_i^0$ for $i = 1, 2, 3, 4$) and charged higgsinos combine with charged winos to form charginos ($\tilde{\chi}_i^\pm$ for $i = 1, 2$), where the higher the index indicates a higher mass with respect to the previous neutralino or chargino. Mixing can also occur for various sets of squarks and sleptons and in principle, any scalars with the same electric charge, R-parity, and colour quantum numbers can mix with eachother [24]. Mixing is very small for most sfermions except for the third generation, which has large Yukawa and soft couplings [24]. The MSSM predicts that the $\tilde{t}_1/\tilde{b}_1$ will be the lightest squarks because of these mixing effects [24]. The only exception to this mixing is the gluino, which does not have the permissible quantum numbers to mix with any other particle [24]. The corresponding gauge and mass eigenstates for the MSSM can be seen in Table 3.3.

3.4 R-Parity and the Neutralino

An additional experimental constraint that is desirable to include in the MSSM originates from proton decay not been observed. Because the baryon (B) and lepton (L) quantum numbers are not conserved in the superpotential (Equation A.2 of Appendix A.1) of the SUSY lagrangian [24], the lifetime of the proton would be extremely short (10^{-2}s) and therefore, not consistent

---

[1] In general particle physics, *soft* is considered the opposite of *hard*, where the term hard originates from "hard scattering" and therefore, is associated to high-energy processes.

[2] Defined in Section 3.4.

Particles	Spin	P_R	Gauge eigenstates	Mass eigenstates
Higgs Bosons	0	+1	$\tilde{H}_u^0 \ \tilde{H}_d^0 \ \tilde{H}_u^+ \ \tilde{H}_d^-$	$h^0 \ H^0 \ A^0 \ H^\pm$
			$\tilde{u}_L \ \tilde{u}_R \ \tilde{d}_L \ \tilde{d}_R$	(same)
Squarks	0	−1	$\tilde{s}_L \ \tilde{s}_R \ \tilde{c}_L \ \tilde{c}_R$	(same)
			$\tilde{t}_L \ \tilde{t}_R \ \tilde{b}_L \ \tilde{b}_R$	$\tilde{t}_1 \ \tilde{t}_2 \ \tilde{b}_1 \ \tilde{b}_2$
			$\tilde{e}_L \ \tilde{e}_R \ \tilde{\nu}_e$	(same)
Sleptons	0	−1	$\tilde{\mu}_L \ \tilde{\mu}_R \ \tilde{\nu}_\mu$	(same)
			$\tilde{\tau}_L \ \tilde{\tau}_R \ \tilde{\nu}_\tau$	$\tilde{\tau}_1 \ \tilde{\tau}_2 \ \tilde{\nu}_\tau$
Neutralinos	$\frac{1}{2}$	−1	$\tilde{B}^0 \ \tilde{W}^0 \ \tilde{H}_u^0 \ \tilde{H}_d^0$	$\tilde{\chi}_1^0 \ \tilde{\chi}_2^0 \ \tilde{\chi}_3^0 \ \tilde{\chi}_4^0$
Charginos	$\frac{1}{2}$	−1	$\tilde{W}^\pm \ \tilde{H}_u^+ \ \tilde{H}_d^-$	$\tilde{\chi}_1^\pm \ \tilde{\chi}_2^\pm$
Gluinos	$\frac{1}{2}$	−1	$\tilde{g}$	(same)
Gravitino	$\frac{3}{2}$	−1	$\tilde{G}$	(same)

Table 3.3: Gauge and mass eigenstates of the particles introduced from the MSSM, along with their spin and R-parity values. Taken from Ref. [24].

with the lower limit provided by the Super-Kamiokande Collaboration[3]. By the addition of a new symmetry, termed R-parity, these violating terms can be eliminated and when the MSSM is defined to conserve this quantity, it is referred to as R-parity conserving (RPC) SUSY. R-parity is calculated by;

$$P_R = (-1)^{3(B-L)+2s}. \tag{3.2}$$

The R-parity values for the MSSM particles can be seen in Table 3.3. R-parity could be an exact and fundamental symmetry, whereas baryon and lepton numbers cannot because they are known to be violated by non-perturbative electroweak effects [29].

Because all SM particles have even R-parity ($P_R = +1$) and SUSY particles have odd R-parity ($P_R = -1$), there are a number of important phenomenological consequences that arise. In collider experiments, sparticles can only be produced in even numbers, i.e, typically pair-produced. Next, the lightest sparticle is called the lightest supersymmetric particle (LSP) and must be a stable particle. With the LSP being the only stable SUSY particle, every other sparticle must eventually decay into a state that contains an odd number of LSPs. Because RPC SUSY cascade decays result in final states with the lightest neutralino, it is often assumed to be the LSP. If the LSP is electrically neutral, like the lightest neutralino, and therefore only interacts weakly with baryonic matter, it provides a strong basis as a candidate for being a cold dark matter (CDM) particle.

---

[3]Lower limits on the proton lifetime are set at $\tau/B(p \rightarrow e^+\pi^0) > 1.6 \times 10^{34}$ years and $\tau/B(p \rightarrow \mu^+\pi^0) > 7.7 \times 10^{33}$ years at 90% confidence level [28].

3.5   Grand Unified Theory

In Chapter 2, it was stated that the three SM couplings, assuming the SM particle content, fails to unify at energies near the Planck scale. If the gauge couplings were to unify, it would be an indication that the SM gauge couplings originate from a single coupling. Additionally unification automatically defines an ultraviolet scale and may additionally provide a framework for gauge-gravity unification [30]. Grand-unified theories (GUT) extend coupling unification to include all matter and gauge fields in the mathematical representation of the GUT group [30].

In the context of SUSY, by including the MSSM particle content between weak scale and a TeV scale, the SM couplings unify at a scale $M_U \sim 3 \times 10^{16}$ GeV with value $g_U = 0.7$ or $\alpha_U = 0.04$ defining the unification scale [30]. This scenario is depicted in the coloured lines of Figure 2.6. The RPC MSSM is a framework of grand-unification because of the additional predictions of the unification of the SM Yukawa couplings at the GUT scale, the existence of DM and the retention of a long proton lifetime and EWSB at a scale far below the unification scale [31].

3.6   Phenomenological MSSM

With the MSSM possessing 124 independent real degrees of freedom, it is not a phenomenologically viable theory over much of its parameter space because of the absence of conservation of the lepton flavours, unsuppressed flavour-changing neutral currents (FCNCs) and new sources of CP violation that are inconsistent with the experimental bounds [7]. To address these issues, several constraints are included which result in the phenomenological MSSM (pMSSM).

To suppress FCNC processes, all off-diagonal elements in the sfmerion masses and trilinear couplings are set to zero and the first and second generation soft terms are set to be equal [32]. Experimental limits from electron and neutron dipole moments and results from K-meson system experiments constrain the possible sources of CP violation [32]. Additionally, the trilinear coupling for the electron and muon is set to be equal to be consistent with the experimental observation of the anomalous magnetic moment of the muon [32, 33]. The trilinear couplings for the first and second generation of quarks are set to zero due to being proportional to the SM Yukawa coupling, which are considered to be negligible [32]. The remaining quantities that define the parameters of the pMSSM are presented in Table 3.4.

The pMSSM can be constrained even further to 10 parameters by assuming one common squark mass parameter for the first two generations, a second common squark mass parameter for the third generation, a common (charged) slepton mass parameter and a common A-parameter for the third generation [7]. This thesis uses simplified models derived in pMSSM-19 phase-space.

Parameter	Description
M_1, M_2, M_3	Gaugino mass parameters
$\tan \beta$	Ratio of VEVs of the two Higgs doublets
m_A	Pseudoscalar Higgs boson mass parameter
μ	Higgsino mass parameter
A_t, A_b, A_τ	Third generation trilinear coupling
$m_{qL}, m_{uR}, m_{dR}, m_{lL}, m_{eR}$	First and second generation sfermion masses
$m_{q3L}, m_{tR}, m_{bR}, m_{\tilde{L}}, m_{\tilde{\tau}_R}$	Third generation sfermion masses

Table 3.4: A list of the 19 parameters of the pMSSM. Taken from Ref [8].

3.7   A Natural SUSY Particle Spectrum

In the decoupling limit (i.e the pseudo-scalar mass $m_A \gg m_Z$), the mean of the stop soft masses m_{q3} and m_{u3} determines the dominant one-loop correction to the Higgs mass, calculated by

$$
\begin{aligned}
m_H^2 &= M_Z^2 \cos^2 2\beta + \delta_t^2 \\
&\sim M_Z^2 \cos^2 2\beta + \frac{3m_t^4}{16\pi^2 v^2} \left[\ln \frac{m_{\tilde{t}}^2}{m_t^2} + \frac{X_t^2}{m_{\tilde{t}}^2} \left(1 - \frac{X_t^2}{12m_{\tilde{t}}^2} \right) \right],
\end{aligned}
\tag{3.3}
$$

where $X_t = A_t - \mu \cot \beta$ and is termed the stop mixing parameter and β is the ratio of vacuum expectation values presented in Table 3.4 [34]. As X_t evolves, so does the stop mass and therefore, the correction to the Higgs mass depends upon these soft terms. For SUSY to be a solution to the hierarchy problem, which is one of the key motivating factors for weak-scale SUSY, the scale of the soft terms cannot be too large and this is called the naturalness constraint. A mass scale that solves the hierarchy problem is referred to as a natural SUSY. It is found that at large stop mixing ($A_t = \sqrt{6m(\tilde{t}_1)m(\tilde{t}_2)}$), stop masses are achieved in the sub-TeV range, subject to the observed Higgs mass constraint [35]. The third-generation LH squark and RH stop masses suffer from their own naturalness problem, originating from one-loop mass corrections in QCD that restricts the gluino mass [36]. The upper limit, would be $\mathcal{O}(\leq 3 \text{ TeV})$ [36]. This scenario is depicted in Figure 3.1.

3.8   Supersymmetry at Hadron Colliders

This section will present a broader contextualisation to how supersymmetry is probed in direct detection searches at hadron colliders, such as those presented in Chapters 8-9.
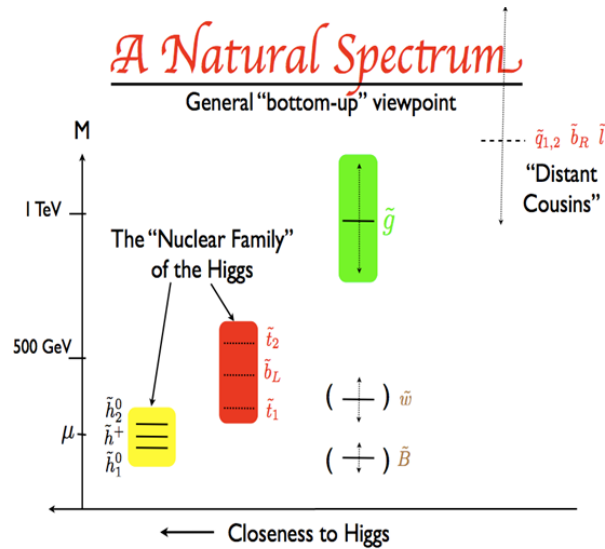
Figure 3.1: The mass spectrum of the MSSM with the naturalness constraint imposed. Taken from Ref. [37].

3.8.1   Simplified Models

As discussed in Section 3.2, the MSSM still has a large number of free parameters which experimentally cannot be searched for. One method to perform an experimental search for a BSM theory, such as the MSSM, is to use simplified models. Simplified models can be considered limits of general BSM scenarios where all particles except those involved in a specific process can be discarded [38]. The physical justification is that the removed SUSY particles are assumed to be too heavy to produce because of, for example, the naturalness constraint. The simplified model masses and cross section (minimally) parameterise the BSM process. Therefore, it should not be considered a model that encompasses the entire theoretical parameter space but instead a natural starting point for quantifying if the presence of a signal with a similar final state is observed in the search. However, experimental limits set on the observation of such a signal, are only relevant to the simplified model-space and do not represent the inclusive parameter-space of the theory.

3.8.2   Multiple b-jets$+E_\text{T}^\text{miss}$ From Gluino Decays

At the hadron-hadron colliders, such as the LHC (Section 5.1.1), the production of gluinos and squarks proceeds through the dominant gluon-gluon and gluon-quark fusion processes [24]. Consequently, Feynman diagrams presenting the production mechanisms of pair-produced gluinos (and squarks) for RPC SUSY are shown in Figure 3.2.

The pair production of gluinos usually involves both the s-channel and t-channel parton-parton interactions can be seen in Figure 3.2. The calculation of the cross section of gluinos pair-produced at next-to-next-to-leading order and next-to-next-to-leading logarithmic (NNLO+NNLL) accuracy for $\sqrt{s} = 13$ TeV can be seen in Figure 3.3, along with squark and stop/sbottom pair production.
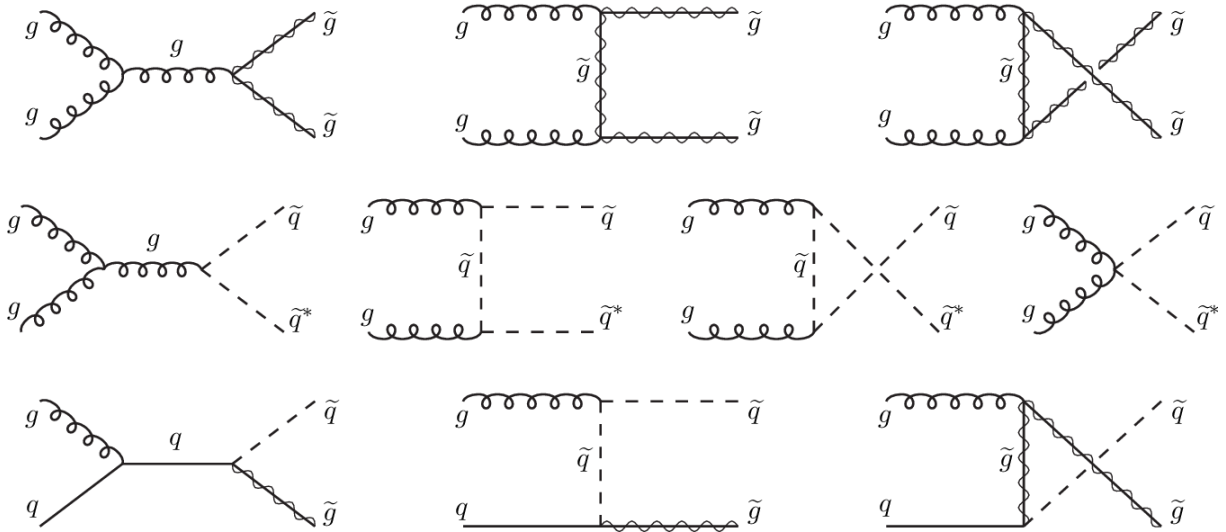
Figure 3.2: Feynman diagrams for the dominant production mechanisms for pair-produced gluinos at hadron-hadron colliders. Taken from Ref. [24].
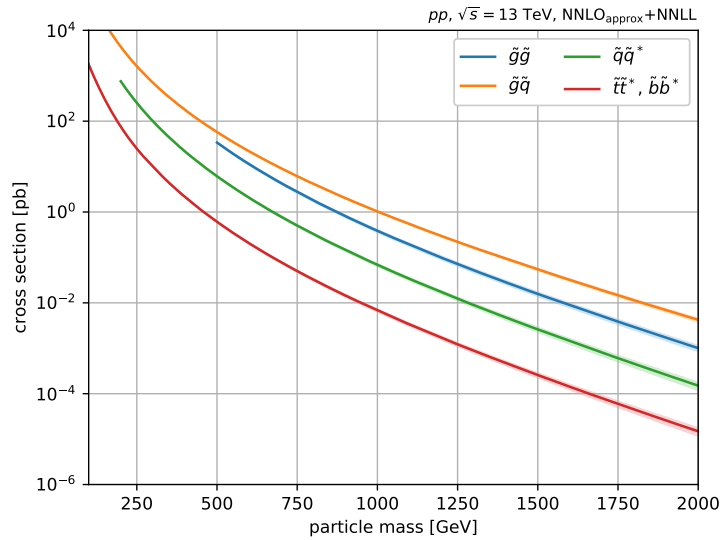
Figure 3.3: Next-to-next-to-leading order and next-to-next-to-leading logarithmic gluino, squark and stop/sbottom pair production cross section [pb] as a function of the mass at $\sqrt{s} = 13$ TeV. Taken from Ref. [7].

The decay of the gluino can only proceed through a squark, either on-shell or virtual [24]. Of course, if all squarks are heavier than the gluino, the gluino can only decay off-shell to a squark. Because of the relevant gluino-quark-squark coupling, if the two-body $\tilde{g} \to \tilde{q}q$ is an available channel, this process will dominate [24]. Because the top and bottom squarks are predicted to be much lighter than the other squarks, it is expected that the $\tilde{q}q$ pair is either a $\tilde{t}t$ or $\tilde{b}b$. Feynman diagrams for the dominant Gluino decay processes can be seen in Figure 3.4.
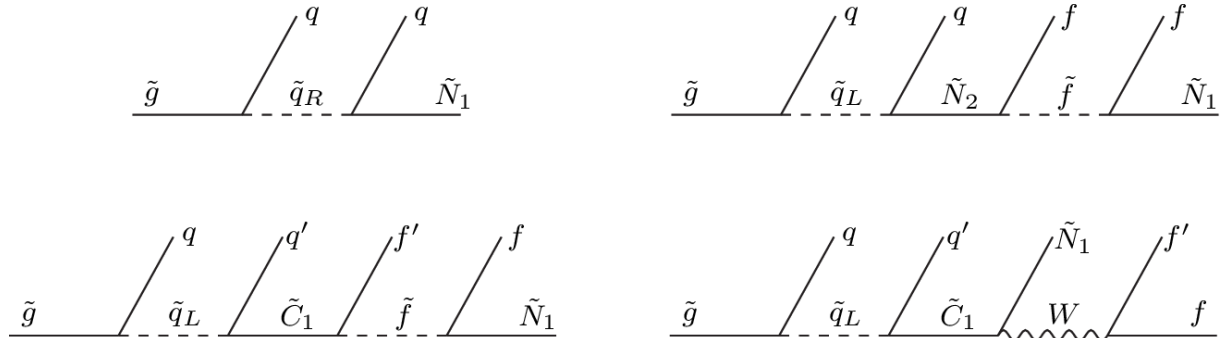
Figure 3.4: Feynman diagrams of R-parity conserving supersymmetry gluino decays. For decays to $\tilde{g} \to \tilde{t}t$ or $\tilde{g} \to \tilde{b}b$, the top left will dominate. However, if a three-body decay occurs via the lightest chargino, the bottom left also yields a significant contribution. Taken from Ref. [24].

In the direct production of RPC SUSY, the undetected LSPs result in missing energy of at least twice the LSP mass, but only the momentum component transverse (Section 5.2.4) to the colliding beam is physically observable[4] [24]. Therefore, a typical direct search for RPC SUSY follows a channel of m leptons plus n jets and missing transverse energy[5] where $m, n \geq 0$. The SM background processes that can replicate a BSM detector signature are generally referred to as *background*(-processes) i.e not the *signal* searched for, but contribute events to the experimental observables. Specific background processes relevant to the analysis chapters (7-9) will be described explicitly in the relevant chapter, but in general, the only *real* contributor to replicate this channel is from W- and Z-bosons in association with jets and the decays of pair-produced top quarks, that can produce neutrinos and therefore real missing energy.

3.8.3 Pure Higgsino Dark Matter

Assuming SUSY does exist, in the early Universe, sparticles would have existed in thermal equilibrium with SM particles [24]. As the Universe expanded and cooled, the heavier sparticles would no longer be kinematically produced and so they would have annihilated or decayed into LSPs as a consequence of R-parity conservation [24]. As the Universe continued to expand, the annihilation rate became small compared to the cosmological expansion and the LSP experienced *freeze-out*, where the density of this object in the Universe today is equal to the density at the time of freeze-out. As mentioned in Section 2.2.1, the observed cold dark matter density (CDM)

---

[4]Information is lost with final-state particles travelling down the beampipe.

[5]More specific detail about the explicit defintions of these objects can be found in Sections 5.2.5-5.1.6, 5.2.2 and 5.2.4, respectively.

of the Universe is currently estimated to be $\Omega_C = 0.12h^{-2} = 0.265$ [19–21]. In general, the LSP has roughly the correct electroweak interaction strength and mass to produce this, however, this cosmological constraint can be used to further restrict the mass range of a specified LSP DM candidate.

Depending on the mixing between the higgsinos and electroweak gauginos, the LSP can be a mixture of bino, wino and higgsino. When $|M_1|$ and m_Z are small compared to $|M_2|$ and $|\mu|$, the lightest neutralino would be pure bino [7]. When $|M_2|$ and m_Z are small compared to $|M_1|$ and $|\mu|$, the lightest chargino pair and neutralino would be a triplet of roughly mass-degenerate pure winos ($\tilde{W}^\pm$ and $\tilde{W}_3^0$) [7]. If $|\mu|$ and m_Z are small compared to $|M_1|$ and $|M_2|$, the lightest chargino pair and neutralino would be nearly pure higgsino states and still be consistent with the CDM density constraint [7]. A bino LSP predicts the observed DM relic density if $m_{\tilde{l}_R}^4/m_{\tilde{\chi}_1^0} \simeq (200\text{GeV})^2$, where $\tilde{l}_R$ is the SU(2) singlet for sleptons [39]. The sparticle masses from this constraint are consistent with naturalness arguments [39]. A MSSM model with a pure higgsino or wino LSP typically results in a LSP that is too efficient to match the observed CDM density unless the LSP is very heavy (≥ 1 TeV) [7]. However, a very heavy LSP mass is considered contrary to the principle that SUSY is the solution to the hierarchy problem albeit still permissible by experimental lower limits on sparticle masses [24].

Assuming a particular SUSY parameter-space, one can test the free parameters of the Lagrangian and observe whether a particular set is consistent with the CDM density constraint and discover the resulting LSP mass and composition by using a combination of the SUSY-HIT [40] and MicrOMEGAs [41] software. Using a MSSM configuration, with parameters motivated by naturalness constraints and the simplified model of Section 3.8.2, provides an almost purely higgsino LSP with $m(\tilde{\chi}_1^0) = 1.09$ TeV and a relic density of $\Omega_C h^{-2} = 0.119$, therefore for this LSP mass and composition, it is consistent within the CDM density constraint. Another appealing feature of a significant higgsino (or wino) LSP mixture is that if $|\mu|$ is not too large, the correct relic abundance can be achieved even for very heavy squarks and sleptons [42], which addresses the current limits on excluded simplified models for squarks lighter than 1 TeV (see Section 3.8.4) [24].

3.8.4   Limits on Simplified SUSY Model-space

Many direct searches for SUSY have been performed at the LHC using the two general-purpose experiments; ATLAS and CMS. No statistically significant excesses were observed at any search, so this section will present the currently excluded simplified model phase-space at a 95% confidence limit (CL). The exclusion contour from previous ATLAS supersymmetry searches as a function of the model parameters of various pair-produced gluino simplified models can be seen in Figure 3.5(a). Additionally from ATLAS, the 95% CL on pair-produced squarks, stops and sbottoms can also be seen in Figures 3.5(b), 3.5(c) and 3.5(d) respectively. Limits obtained from the equivalent direct searches at CMS for the final states; $\tilde{g} \to t\bar{t}\tilde{\chi}_1^0$ and $\tilde{g} \to b\bar{b}\tilde{\chi}_1^0$ can be seen in Figures 3.6(a)-3.6(b). Additional results obtained for the $\tilde{g} \to q\bar{q}\tilde{\chi}_1^0$ simplified models and squark pair production can be seen in Figures 3.6(c) and 3.6(d) respectively.
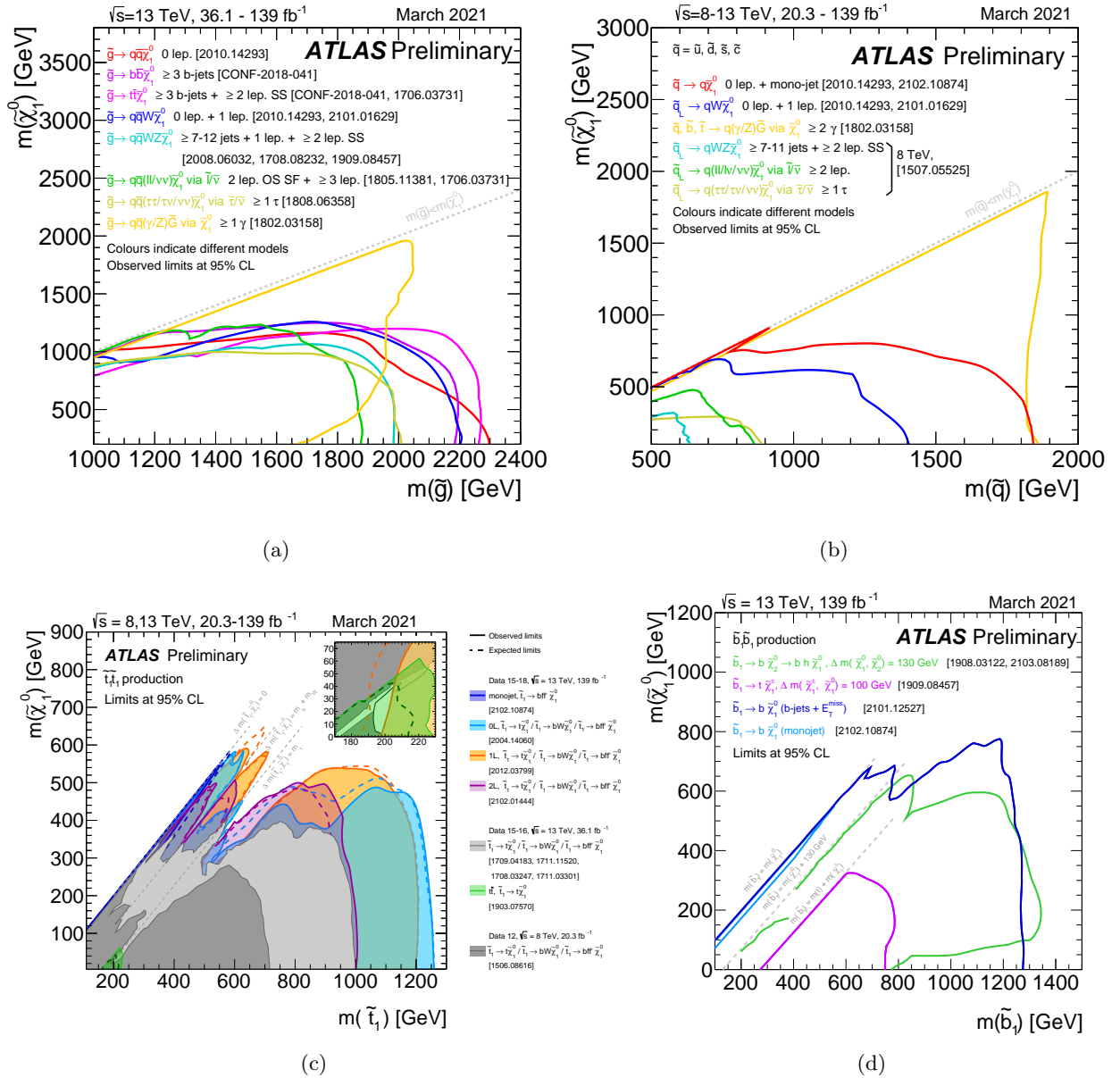
Figure 3.5: The greatest 95% confidence limits as a function of simplified model parameters from various ATLAS SUSY searches (ArXiv reference for each paper is labelled) for (a) gluino, (b) squark, (c) stop and (d) sbottom pair production. Taken from Ref. [43].
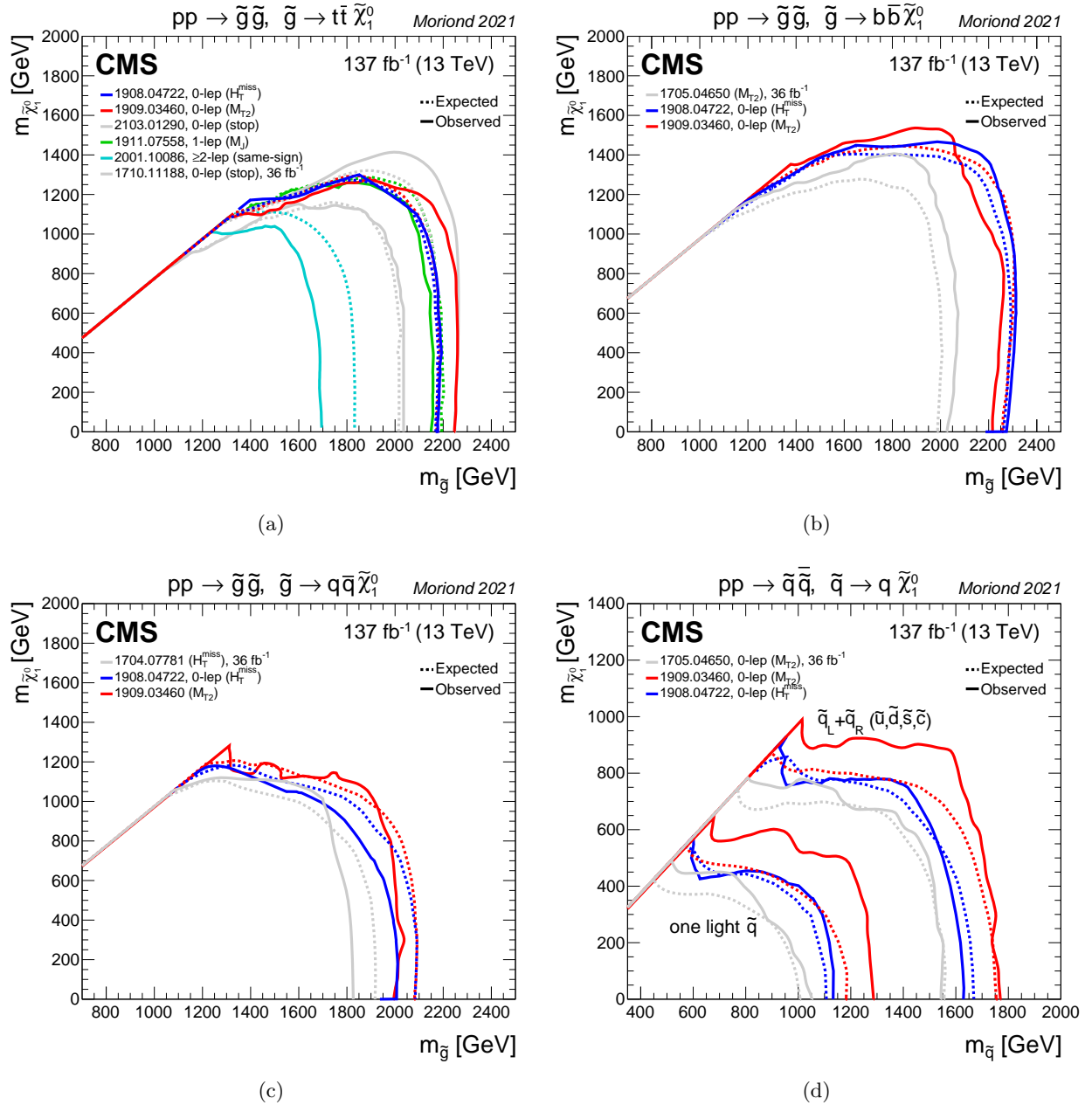
Figure 3.6: The current 95% CL exclusion limits as a function of simplified model parameters from various CMS SUSY searches (ArXiv reference for each paper is labelled) for (a) $\tilde{g} \to t\bar{t}\tilde{\chi}_1^0$, (b) $\tilde{g} \to b\bar{b}\tilde{\chi}_1^0$, (c) $\tilde{g} \to q\bar{q}\tilde{\chi}_1^0$ and (d) squark pair production. Taken from Ref. [44].

ATLAS excluded the $\tilde{g} \to t\bar{t}\tilde{\chi}_1^0$ simplified model up to a gluino mass of ~ 2.27 TeV for a 800 GeV LSP. As the gluino mass is lowered to ~ 2.1 TeV, the corresponding LSP mass is excluded up to ~ 1.2 TeV. CMS excluded the same simplified model up to a gluino mass of ~ 2.25 TeV for a 800 GeV LSP. As the gluino mass is lowered to ~ 1.85 TeV, the corresponding LSP mass is excluded up to ~ 1.3 TeV. However, the ATLAS search used data corresponding to an integrated luminosity of 79fb^{-1} whereas the CMS search used the LHC Run 2 dataset corresponding to $\sim 139\text{fb}^{-1}$. A similar pattern is observed with the gluino decaying to a bottom-anti-bottom pair final state. ATLAS excluded the simplified model, $\tilde{g} \to b\bar{b}\tilde{\chi}_1^0$, up to a gluino mass of ~ 2.2 TeV for a 600 GeV LSP. As the gluino mass is lowered to ~ 1.8 TeV, the corresponding LSP mass is excluded up to ~ 1.25 TeV. CMS excluded the same simplified model up to a gluino mass of ~ 2.3 TeV for a 800 GeV LSP. As the gluino mass is lowered to ~ 2.0 TeV, the corresponding LSP mass is excluded up to ~ 1.55 TeV.

Limits from ATLAS for SUSY searches that are sensitive to or specifically search for a pure-Higgsino LSP that have not already been presented can be found in Figure 3.7.

It can be observed that only gluino pair production is sensitive to a LSP mass beyond > 1.0 TeV. Therefore, one could argue the current best approach to be sensitive to a pure higgsino LSP, motivated by the dark matter relic density constraint, favours gluino production. A summary of the 95% model limits across a wider range of SUSY production mechanisms and final states for ATLAS at $\sqrt{s} = 13$ TeV with the Run 2 dataset can be seen in Figure 3.8. An equivalent plot for CMS can be seen in Figure 3.9, however, this has not been updated since 2014 and thus is highly probable to be outdated.

(a)

(b)

(c)

(d)
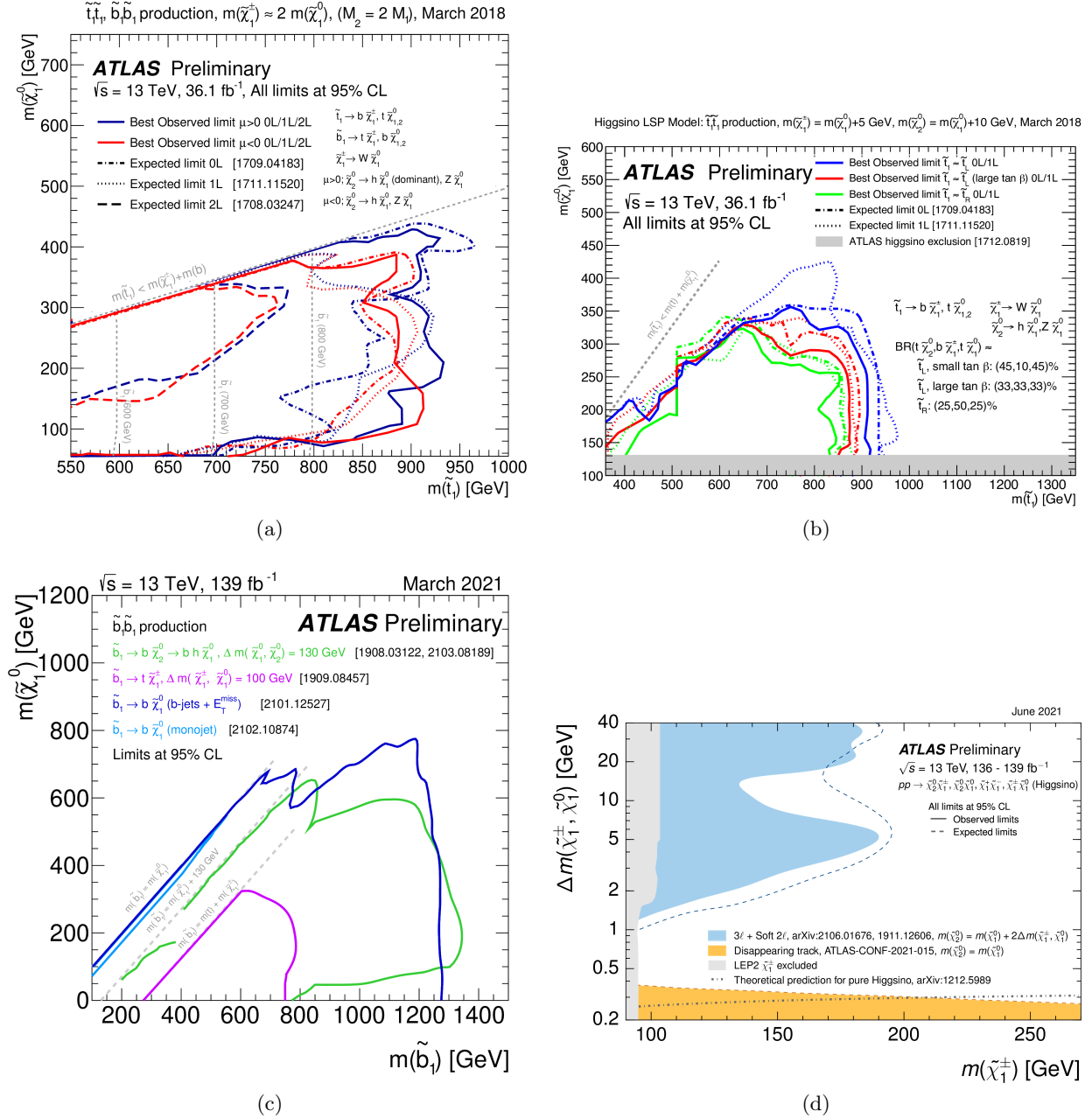
Figure 3.7: The greatest 95% confidence limits on various simplified models that are sensitive to or specifically search for a pure higgsino LSP from ATLAS SUSY searches (ArXiv reference for each paper is labelled) as of June 2021. The subfigures are as follows; (a) is stop and sbottom pair production, where the chargino is twice the mass of the neutralino (b) is stop pair production (c) is sbottom pair production and (d) specifically targets a pure higgsino LSP. Taken from Ref. [43].

ATLAS SUSY Searches* - 95% CL Lower Limits

June 2021

ATLAS Preliminary

$\sqrt{s}$ = 13 TeV

Model	Signature	$\int \mathcal{L}\, dt$ [fb^{-1}]	Mass limit		Reference

Inclusive Searches

$\tilde{q}\tilde{q}, \tilde{q}\to q\tilde{\chi}_1^0$	$0\ e,\mu$	2-6 jets E_T^{miss}	139	$\tilde{q}$ [1×, 8× Degen.] 1.0 1.85	m($\tilde{\chi}_1^0$)<400 GeV	2010.14293
	mono-jet	1-3 jets E_T^{miss}	36.1	$\tilde{q}$ [8× Degen.] 0.9	m($\tilde{q}$)-m($\tilde{\chi}_1^0$)=5 GeV	2102.10874
$\tilde{g}\tilde{g}, \tilde{g}\to q\bar{q}\tilde{\chi}_1^0$	$0\ e,\mu$	2-6 jets E_T^{miss}	139	$\tilde{g}$ 2.3	m($\tilde{\chi}_1^0$)=0 GeV	2010.14293
				$\tilde{g}$ Forbidden 1.15-1.95	m($\tilde{\chi}_1^0$)=1000 GeV	2010.14293
$\tilde{g}\tilde{g}, \tilde{g}\to q\bar{q}W\tilde{\chi}_1^0$	$1\ e,\mu$	2-6 jets E_T^{miss}	139	$\tilde{g}$ 2.2	m($\tilde{\chi}_1^0$)<600 GeV	2101.01629
$\tilde{g}\tilde{g}, \tilde{g}\to q\bar{q}(\ell\ell)\tilde{\chi}_1^0$	$ee,\mu\mu$	2 jets E_T^{miss}	36.1	$\tilde{g}$ 1.2	m($\tilde{g}$)-m($\tilde{\chi}_1^0$)=50 GeV	1805.11381
$\tilde{g}\tilde{g}, \tilde{g}\to q\bar{q}WZ\tilde{\chi}_1^0$	$0\ e,\mu$	7-11 jets E_T^{miss}	139	$\tilde{g}$ 1.97	m($\tilde{\chi}_1^0$)<600 GeV	2008.06032
	SS e,μ	6 jets	139	$\tilde{g}$ 1.15	m($\tilde{g}$)-m($\tilde{\chi}_1^0$)=200 GeV	1909.08457
$\tilde{g}\tilde{g}, \tilde{g}\to t\bar{t}\tilde{\chi}_1^0$	0-1 e,μ	3 b E_T^{miss}	79.8	$\tilde{g}$ 2.25	m($\tilde{\chi}_1^0$)<200 GeV	ATLAS-CONF-2018-041
	SS e,μ	6 jets	139	$\tilde{g}$ 1.25	m($\tilde{g}$)-m($\tilde{\chi}_1^0$)=300 GeV	1909.08457

3rd gen. squarks direct production

$\tilde{b}_1\tilde{b}_1$	$0\ e,\mu$	2 b E_T^{miss}	139	$\tilde{b}_1$ 1.255	m($\tilde{\chi}_1^0$)<400 GeV	2101.12527
				$\tilde{b}_1$ 0.68	10 GeV<$\Delta m(\tilde{b}_1,\tilde{\chi}_1^0)$<20 GeV	2101.12527
$\tilde{b}_1\tilde{b}_1, \tilde{b}_1\to b\tilde{\chi}_2^0 \to bh\tilde{\chi}_1^0$	$0\ e,\mu$	6 b E_T^{miss}	139	$\tilde{b}_1$ Forbidden 0.23-1.35	$\Delta m(\tilde{\chi}_2^0,\tilde{\chi}_1^0)$=130 GeV, m($\tilde{\chi}_1^0$)=100 GeV	1908.03122
	$2\ \tau$	2 b E_T^{miss}	139	$\tilde{b}_1$ 0.13-0.85	$\Delta m(\tilde{\chi}_2^0,\tilde{\chi}_1^0)$=130 GeV, m($\tilde{\chi}_1^0$)=0 GeV	ATLAS-CONF-2020-031
$\tilde{t}_1\tilde{t}_1, \tilde{t}_1\to t\tilde{\chi}_1^0$	0-1 e,μ	≥ 1 jet E_T^{miss}	139	$\tilde{t}_1$ 1.25	m($\tilde{\chi}_1^0$)=1 GeV	2004.14060,2012.03799
$\tilde{t}_1\tilde{t}_1, \tilde{t}_1\to Wb\tilde{\chi}_1^0$	$1\ e,\mu$	3 jets/1 b E_T^{miss}	139	$\tilde{t}_1$ Forbidden 0.65	m($\tilde{\chi}_1^0$)=500 GeV	2012.03799
$\tilde{t}_1\tilde{t}_1, \tilde{t}_1\to \tilde{\tau}_1 bv, \tilde{\tau}_1\to\tau\tilde{G}$	1-2 τ	2 jets/1 b E_T^{miss}	139	$\tilde{t}_1$ Forbidden 1.4	m($\tilde{\tau}_1$)=800 GeV	ATLAS-CONF-2021-008
$\tilde{t}_1\tilde{t}_1, \tilde{t}_1\to c\tilde{\chi}_1^0 / \tilde{c}\tilde{c}, \tilde{c}\to c\tilde{\chi}_1^0$	$0\ e,\mu$	2 c E_T^{miss}	36.1	$\tilde{c}$ 0.85	m($\tilde{\chi}_1^0$)=0 GeV	1805.01649
	$0\ e,\mu$	mono-jet E_T^{miss}	139	$\tilde{t}_1$ 0.55	m($\tilde{t}_1,\tilde{c}$)-m($\tilde{\chi}_1^0$)=5 GeV	2102.10874
$\tilde{t}_1\tilde{t}_1, \tilde{t}_1\to t\tilde{\chi}_2^0, \tilde{\chi}_2^0\to Z/h\tilde{\chi}_1^0$	1-2 e,μ	1-4 b E_T^{miss}	139	$\tilde{t}_1$ 0.067-1.18	m($\tilde{\chi}_2^0$)=500 GeV	2006.05880
$\tilde{t}_2\tilde{t}_2, \tilde{t}_2\to \tilde{t}_1 + Z$	3 e,μ	1 b E_T^{miss}	139	$\tilde{t}_2$ Forbidden 0.86	m($\tilde{\chi}_1^0$)=360 GeV, m($\tilde{t}_1$)-m($\tilde{\chi}_1^0$)= 40 GeV	2006.05880

EW direct

$\tilde{\chi}_1^\pm\tilde{\chi}_2^0$ via WZ	Multiple ℓ/jets	E_T^{miss}	139	$\tilde{\chi}_1^\pm/\tilde{\chi}_2^0$ 0.96	m($\tilde{\chi}_1^0$)=0, wino-bino	2106.01676, ATLAS-CONF-2021-022
	$ee,\mu\mu$	≥ 1 jet E_T^{miss}	139	$\tilde{\chi}_1^\pm/\tilde{\chi}_2^0$ 0.205	m($\tilde{\chi}_1^\pm$)-m($\tilde{\chi}_1^0$)=5 GeV, wino-bino	1911.12606
$\tilde{\chi}_1^+\tilde{\chi}_1^-$ via WW	2 e,μ	E_T^{miss}	139	$\tilde{\chi}_1^\pm$ 0.42	m($\tilde{\chi}_1^0$)=0, wino-bino	1908.08215
$\tilde{\chi}_1^\pm\tilde{\chi}_2^0$ via Wh	Multiple ℓ/jets	E_T^{miss}	139	$\tilde{\chi}_1^\pm/\tilde{\chi}_2^0$ Forbidden 1.06	m($\tilde{\chi}_1^0$)=70 GeV, wino-bino	2004.10894, ATLAS-CONF-2021-022
$\tilde{\chi}_1^\pm\tilde{\chi}_1^\mp$ via $\tilde{\ell}_L/\tilde{\nu}$	2 e,μ	E_T^{miss}	139	$\tilde{\chi}_1^\pm$ 1.0	m($\tilde{\ell},\tilde{\nu}$)=0.5(m($\tilde{\chi}_1^\pm$)+m($\tilde{\chi}_1^0$))	1908.08215
$\tilde{\tau}\tilde{\tau}, \tilde{\tau}\to\tau\tilde{\chi}_1^0$	$2\ \tau$	E_T^{miss}	139	$\tilde{\tau}$ [$\tilde{\tau}_L, \tilde{\tau}_{R,L}$] 0.16-0.3 0.12-0.39	m($\tilde{\chi}_1^0$)=0	1911.06660
$\tilde{\ell}_{L,R}\tilde{\ell}_{L,R}, \tilde{\ell}\to\ell\tilde{\chi}_1^0$	2 e,μ	E_T^{miss}	139	$\tilde{\ell}$ 0.7	m($\tilde{\chi}_1^0$)=0	1908.08215
	$ee,\mu\mu$	≥ 1 jet E_T^{miss}	139	$\tilde{\ell}$ 0.256	m($\tilde{\ell}$)-m($\tilde{\chi}_1^0$)=10 GeV	1911.12606
$\tilde{H}\tilde{H}, \tilde{H}\to h\tilde{G}/Z\tilde{G}$	$0\ e,\mu$	≥ 3 b E_T^{miss}	36.1	$\tilde{H}$ 0.13-0.23 0.29-0.88	BR($\tilde{\chi}_1^0 \to h\tilde{G}$)=1	1806.04030
	4 e,μ	0 jets E_T^{miss}	139	$\tilde{H}$ 0.55	BR($\tilde{\chi}_1^0 \to Z\tilde{G}/h\tilde{G}$)=1	2103.11684
	$0\ e,\mu$	≥ 2 large jets E_T^{miss}	139	$\tilde{H}$ 0.45-0.93	BR($\tilde{\chi}_1^0 \to Z\tilde{G}$)=1	ATLAS-CONF-2021-022

Long-lived particles

Direct $\tilde{\chi}_1^+\tilde{\chi}_1^-$ prod., long-lived $\tilde{\chi}_1^\pm$	Disapp. trk	1 jet E_T^{miss}	139	$\tilde{\chi}_1^\pm$ 0.66	Pure Wino	ATLAS-CONF-2021-015
				$\tilde{\chi}_1^\pm$ 0.21	Pure higgsino	ATLAS-CONF-2021-015
Stable $\tilde{g}$ R-hadron		Multiple	36.1	$\tilde{g}$ 2.0		1902.01636,1808.04095
Metastable $\tilde{g}$ R-hadron, $\tilde{g}\to qq\tilde{\chi}_1^0$		Multiple	36.1	$\tilde{g}$ [$\tau(\tilde{g})$=10 ns, 0.2 ns] 2.05 2.4	m($\tilde{\chi}_1^0$)=100 GeV	1710.04901,1808.04095
$\tilde{\ell}\tilde{\ell}, \tilde{\ell}\to\ell\tilde{G}$	Displ. lep		139	$\tilde{e},\tilde{\mu}$ 0.7	$\tau(\tilde{\ell})$ = 0.1 ns	2011.07812
				$\tilde{\tau}$ 0.34	$\tau(\tilde{\ell})$ = 0.1 ns	2011.07812

RPV

$\tilde{\chi}_1^+\tilde{\chi}_1^-/\tilde{\chi}_1^0, \tilde{\chi}_1^\pm\to Z\ell\to\ell\ell\ell$	3 e,μ		139	$\tilde{\chi}_1^\pm/\tilde{\chi}_1^0$ [BR($Z\tau$)=1, BR(Ze)=1] 0.625 1.05	Pure Wino	2011.10543
$\tilde{\chi}_1^+\tilde{\chi}_1^-/\tilde{\chi}_2^0 \to WW/Z\ell\ell\ell\ell\nu\nu$	4 e,μ	0 jets E_T^{miss}	139	$\tilde{\chi}_1^\pm/\tilde{\chi}_2^0$ [$\lambda_{i33} \neq 0, \lambda_{12k} \neq 0$] 0.95 1.55	m($\tilde{\chi}_1^0$)=200 GeV	2103.11684
$\tilde{g}\tilde{g}, \tilde{g}\to qq\tilde{\chi}_1^0, \tilde{\chi}_1^0\to qqq$		4-5 large jets	36.1	$\tilde{g}$ [m($\tilde{\chi}_1^0$)=200 GeV, 1100 GeV] 1.3 1.9	Large λ''_{112}	1804.03568
$\tilde{t}\tilde{t}, \tilde{t}\to t\tilde{\chi}_1^0, \tilde{\chi}_1^0 \to tbs$		Multiple	36.1	$\tilde{t}$ [λ''_{323}=2e-4, 1e-2] 0.55 1.05	m($\tilde{\chi}_1^0$)=200 GeV, bino-like	ATLAS-CONF-2018-003
$\tilde{t}\tilde{t}, \tilde{t}\to b\tilde{\chi}_1^\pm, \tilde{\chi}_1^\pm \to bbs$		$\geq 4b$	139	$\tilde{t}$ Forbidden 0.95	m($\tilde{\chi}_1^\pm$)=500 GeV	2010.01015
$\tilde{t}_1\tilde{t}_1, \tilde{t}_1\to bs$		2 jets + 2 b	36.7	$\tilde{t}_1$ [qq, bs] 0.42 0.61		1710.07171
$\tilde{t}_1\tilde{t}_1, \tilde{t}_1\to q\ell$	2 e,μ	2 b	36.1	$\tilde{t}_1$ 0.4-1.45	BR($\tilde{t}_1 \to be/b\mu$)>20%	1710.05544
	$1\ \mu$	DV	136	$\tilde{t}_1$ [1e-10< λ'_{23k} <1e-8, 3e-10< λ'_{23k} <3e-9] 1.0 1.6	BR($\tilde{t}_1 \to q\mu$)=100%, cosθ_t=1	2003.11956
$\tilde{\chi}_1^\pm/\tilde{\chi}_2^0/\tilde{\chi}_1^0, \tilde{\chi}_{1,2}^0, \tilde{\chi}_1^\pm\to bbs$	1-2 e,μ	≥ 6 jets	139	$\tilde{\chi}_1^0$ 0.2-0.32	Pure higgsino	ATLAS-CONF-2021-007

10^{-1} 1   **Mass scale [TeV]**

Only a selection of the available mass limits on new states or phenomena is shown. Many of the limits are based on simplified models, c.f. refs. for the assumptions made.

Figure 3.8: The greatest 95% confidence limits on various simplified models from ATLAS SUSY searches (ArXiv reference for each paper is labelled) as of June 2021. Taken from Ref. [43].
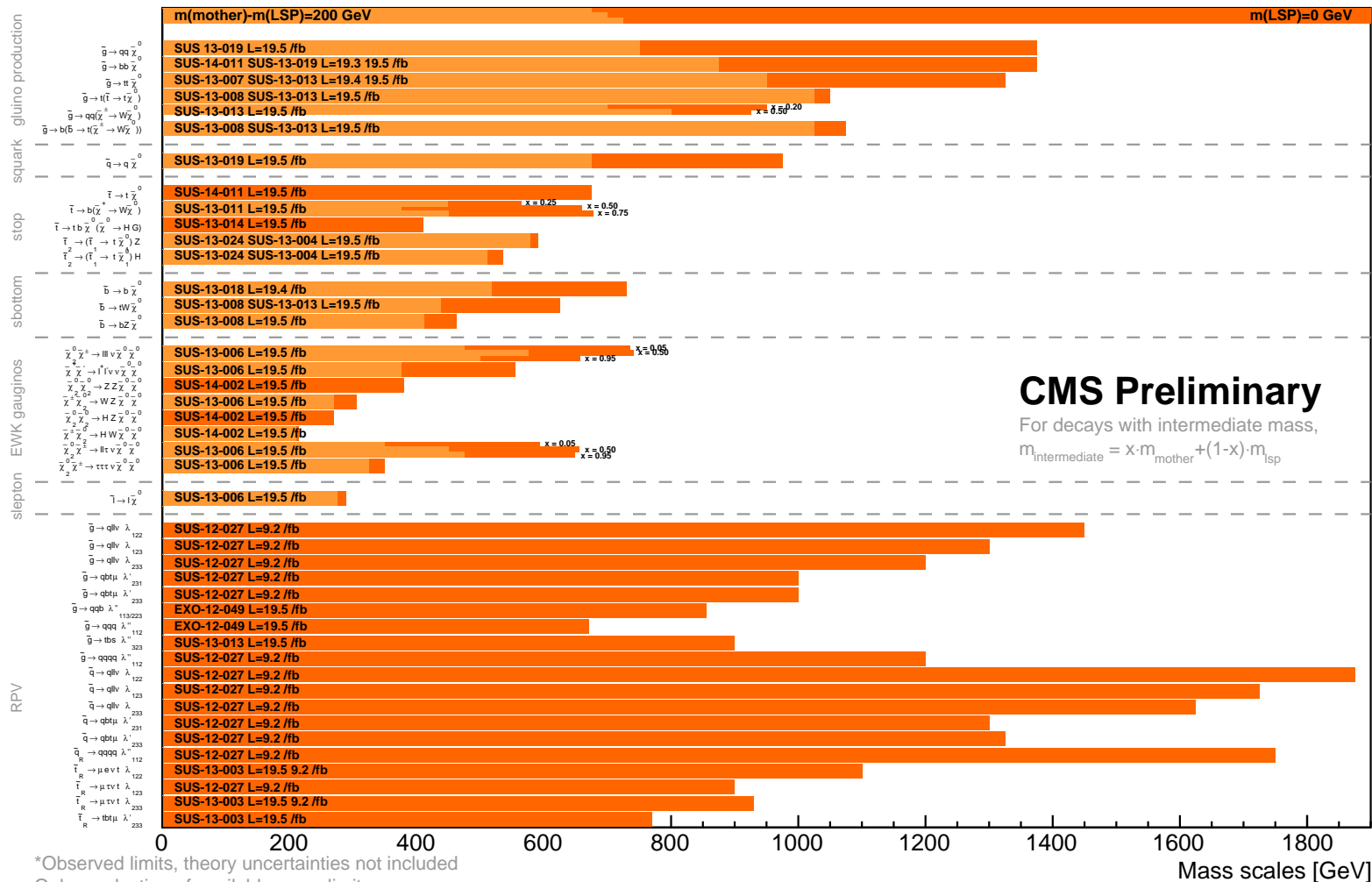
Figure 3.9: The 95% confidence limits on various simplified models from CMS SUSY searches (ArXiv reference for each paper is labelled). Note, this plot has not been updated since 2014 and thus many of these results will have updated limits. Taken from Ref. [44].

At present, no significant evidence for weak-scale SUSY has been discovered from the data collected at the LHC. ATLAS and CMS have excluded significant chunks of simplified-SUSY parameter space based on gluino and squark pair production with masses well above 2 and 1 TeV, respectively. Because of the impressive nature of these limits, the principle of a natural SUSY spectrum is being challenged.

3.9 Conclusion

Supersymmetry can provide a solution to the hierarchy problem whilst also providing a candidate for one of the largest challenges in particle physics, that is, dark matter. DM is approximately five times more abundant than baryonic matter, however, our understanding of the exact properties of such particle(s) is limited. SUSY predicts additional fermionic particles for every boson and bosonic particles for every fermion and EWSB, supersymmetry breaking and naturalness ensure these particles would have a mass at a scale much higher than their Standard Model partner. Within these constraints, gluinos are expected to have a mass $\mathcal{O}(\leq 3 \text{ TeV})$ and thus could be within the reaches of the collision energy and luminosity of the Large Hadron Collider. This chapter concludes by presenting the current statistical limits on simplified SUSY processes and it is found that simplified gluino (squark) models have already been excluded for masses in the $\lesssim 2(1)$ TeV range.

Part III

Experimental Method

Chapter 4

Phenomenology of Proton-proton Interactions

With the theoretical and phenomenological motivations for supersymmetry (SUSY) established in Part II, the next chapter will discuss the phenomenology of proton-proton (pp) collisions to understand the physical processes occurring in direct searches for SUSY at the Large Hadron Collider (LHC).

This chapter starts by discussing important collider-physics quantities that are related to the production of pp collisions. This is followed by a discussion of the physical processes that occur in pp collisions. This chapter concludes with a description of the Monte Carlo generators used to simulate the physical processes occuring from Standard Model and beyond the Standard Model events.

4.1   Proton-proton Interactions

4.1.1   Collider Quantities

A particle collider has two main quantities that characterise the proton-proton (pp) collisions and how they interact. The first is the cross section (σ), which describes the particle interaction in the scattering process. It has the units m^2, but is more commonly presented in barns (b) where $1\text{b} = 10^{-28}\text{m}^2$. It can therefore be considered an effective area or physically interpreted as the probability of the scattering process occurring. The total cross section of a process is independent of the intensity and focus of a particle collider beam and depends upon the scattering amplitude or matrix element (ME, $\mathcal{M}$) of the process [45], calculated by

$$\sigma_{\text{tot}} = \int \frac{d\sigma}{d\omega}d\omega = \int \frac{1}{F}|\mathcal{M}|^2 dQ, \qquad (4.1)$$

where F is the particle flux in the interaction process and dQ is an element of the kinematic

phase space, which can be integrated to sum all possible momentum states of the particles [45]. The second quantity that characterises pp collisions describes the beam physics of the particle collider. This quantity is the instantaneous luminosity (L), which can be defined by

$$L = f_c n_b \frac{N^2}{\Sigma} R, \tag{4.2}$$

for n_b bunches, each containing N particles, colliding with revolution frequency f_c, for the area of the colliding surface Σ and where R is a correction factor to account for dependencies on the bunch length and the beam crossing angle [45]. The units of this quantity are $\mathrm{m}^{-2}\mathrm{s}^{-1}$ or more commonly used is $\mathrm{b}^{-1}\mathrm{s}^{-1}$, which is the unit of inverse cross section per unit time. Equation 4.3 relates the total event rate (N) to the total or integrated luminosity ($\mathcal{L}$) that is, the instantaneous luminosity integrated over the collision operation time of a (circular) particle collider and the cross section for the process;

$$N = \sigma \cdot \mathcal{L} = \sigma \cdot \int L dt. \tag{4.3}$$

4.1.2 QCD Coupling

In the event of assuming the QCD phase is zero, the one free parameter of QCD is the strong coupling constant (α_s), which evolves as a function of the energy scale (Q). The quantity is calculated by

$$\alpha_s(Q^2) = \frac{12\pi}{(11N_c - 2N_f) \log \frac{Q^2}{\Lambda_{\mathrm{QCD}}^2}}, \tag{4.4}$$

where the number of colours $N_c = 3$, number of quark flavours $N_f \leq 6$ and Λ_{QCD} is the infrared cut-off scale [6]. The denominator is greater than the numerator, so as Q^2 increases (i.e tending to smaller distances), the coupling constant decreases. The QCD coupling constant has been measured from several deep inelastic scattering (DIS) experiments and this is presented in Figure 4.1 as a function of the energy scale.

As can be seen in Figure 4.1, for momentum transfers in the $\mathcal{O}(100)$ GeV, $\alpha_s \sim 0.1$, whereas the theory is strongly interacting for scales $\lesssim 1$ GeV. This has some important phenomenological consequences at the two scales. For processes involving large momentum transfer, "hard processes" (small distances), the coupling strength becomes sufficiently weak for perturbation theory techniques to be applicable; named perturbative QCD (pQCD). In this scenario, quarks and gluons behave as free particles in a process known as asymptotic freedom. At larger distances, pQCD cannot be used because of colour confinement and QCD-inspired phenomenological models must be used. Colour confinement is thought to originate from gluon-gluon self-interactions, where coloured objects are confined to colourless states because of the interaction potential requiring an infinite amount of energy to separate them. By inputting sufficient energy, more
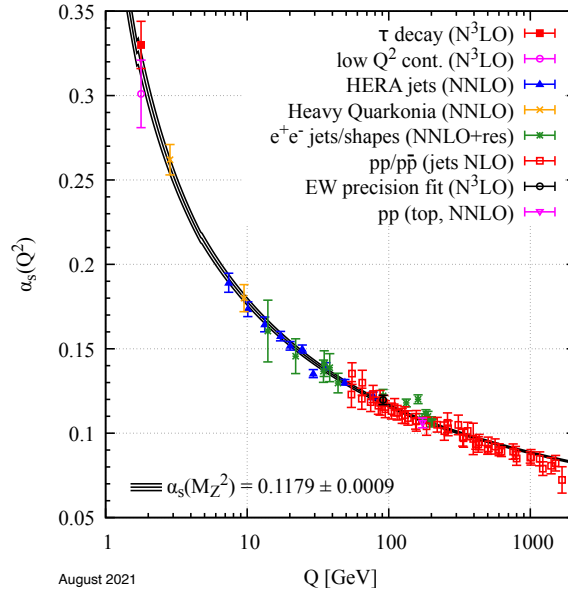
Figure 4.1: The strong coupling constant (α_s) as a function of the energy scale (Q) measured from several deep inelastic scattering experiments. Taken from Ref. [7].

quarks and gluons are produced from self-interactions and the object remains in a colourless state, in a process known as hadronisation.

4.1.3   Parton Distribution Functions

Protons are formed from quarks and gluons (known as partons) and are typically thought to compose of two up and one down quarks, however, quantum fluctuations also cause strange and charm quarks as well as quark-anti-quark pairs ($q\bar{q}$) to be present [27]. The probability distribution of the momentum fraction of a parton or parton distribution function (PDF), is defined as the probability that a gluon or specific quark type takes part in the hard scattering collision at the energy scale Q [46]. Partons cannot be observed as free particles because of the colour confinement condition imposed in QCD, therefore PDFs cannot be predicted theoretically with perturbative QCD. PDFs are known at scale Q are determined from the equations derived by Dokshitzer [47], Gribov and Lipatov [48] and Altarelli and Parisi [49] (DGLAP equations) [8]. The parameterisations of PDFs are well known over a wide range of momentum fractions and scales due from precise measurements of DIS experiments such as CTEQ [50], MSTW [51] (can be seen in Figure 4.2 for $Q = 10, 10^4 \text{GeV}^2$), and NNPDF [52] collaborations.

4.2   Event Generation

A general-purpose Monte Carlo (GPMC) generator describes the physics of the pp collision from very short distance scales, up to the typical scale of hadron formation and decay [7]. The first process of interest is the colliding partons involving large momentum transfer, named hard-scattering (HS) collision. The resulting hadrons (charged particles) radiate breamstrahlung

MSTW 2008 NLO PDFs (68% C.L.)
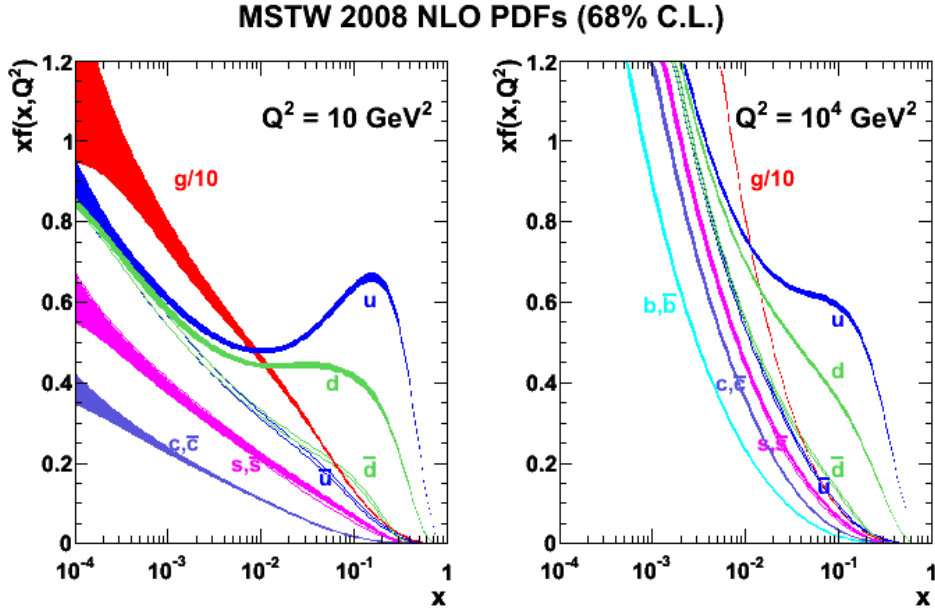
Figure 4.2: Next-to-leading-order parton distribution functions at $Q = 10$ GeV^2 (left) and $Q = 10^4$ GeV^2 (right) from the MSTW Collaboration. Taken from Ref. [51].

quarks and gluons (photons) to form showers, named parton showers (PS) and this process is calculated using perturbation theory. As the showers evolve to larger distance scales, perturbation theory becomes no longer applicable and the parton will stop radiating and form a stable hadron in a process known as hadronisation [7]. Two problems arise from here; the description of hadron formation and the transition from short to long distance scales. Both can be solved by Monte Carlo (MC) methods to a good approximation [53]. The incoming partons may also undergo (collinear) radiation before (after) the HS process known as initial (final) state radiation (ISR, FSR) [7]. The final component, named the underlying event (UE), is when the remaining partons, not involved in the large momentum transfer, collide. At these larger distances, all soft hadronic phenomena, such as hadronisation and the formation of the underlying event rely upon QCD-inspired models [7]. An example of a simulated event where these parts are demonstrated, can be seen in Figure 4.3. The proceeding sections will discuss each of these in greater depth.

4.2.1   Hard Scattering

The hard scattering process can be defined as the colliding partons that involve a large momentum transfer compared with the proton mass [46], where the term *hardness* refers to the momentum component of the parton that is transverse to the beam[1] (p_{T}) being large. The hard scattering processes probes distance scales far below the radius of the proton and hence can be best understood as collisions between the constituent partons of the proton [46]. Therefore, the scattering occurs where α_s is small, meaning the partonic cross sections can be computed in perturbation theory. The calculation of a cross section for process $pp \rightarrow X$ is calculated by

---

[1]Explicitly defined in Equation 5.1.
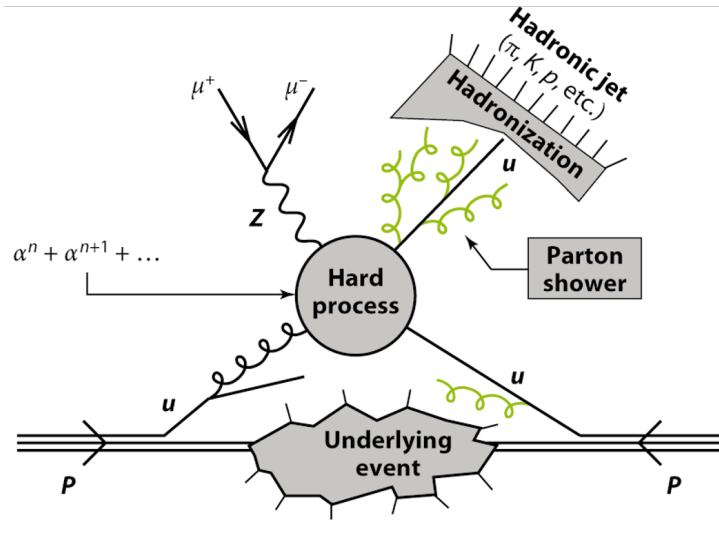
Figure 4.3: Schematic presenting the key aspects of simulating a proton-proton collision involving a Z boson and a jet in the final state. Taken from Ref. [46].

$$\sigma(pp \to X) = \sum_{i,j} \int dx_1 dx_2 f_{i,p}(x_1, \mu_F^2) f_{j,p}(x_2, \mu_F^2) \hat{\sigma}_{ij \to X}(x_1 x_2 s, \mu_R^2, \mu_F^2), \qquad (4.5)$$

where the sum runs over all possible initial-state partons, with longitudinal momentum fractions $x_{1,2}$, that can produce the final state X for a specific renormalisation (factorisation) scale (μ_R^2 (μ_F^2), Q^2) [46]. The equation relates a quantity that describes the partonic scatter ($\hat{\sigma}_{ij \to X}$) with the incoming flux of partons, fixed by the PDFs ($f_{i,p}$), at centre-of-mass energy (s), which itself is calculated by

$$s = \left(\sum_{i=1}^{2} E_i \right)^2 - \left(\sum_{i=1}^{2} \mathbf{p}_i \right)^2, \qquad (4.6)$$

where E and p are the total energy and momentum of the ith initial-state particle and has units of eV^2. The calculation of hard scatter process or matrix element is performed at either leading order (LO), next-to-leading order (NLO), next-to-next-to-leading order NNLO or NXLO for the specific order X for X ≥ 3.

The rate of particles produced in pp collisions depends on the centre-of-mass energy and the probability of the particle constituents interacting, which is determined by the PDF [27]. A schematic presenting the production cross section for each SM particle X for Runs 1 and 2 of the ATLAS experiment can be seen in Figure 4.4.

---

[2]Use natural units i.e $c = 1, \hbar = 1$, from here onwards.
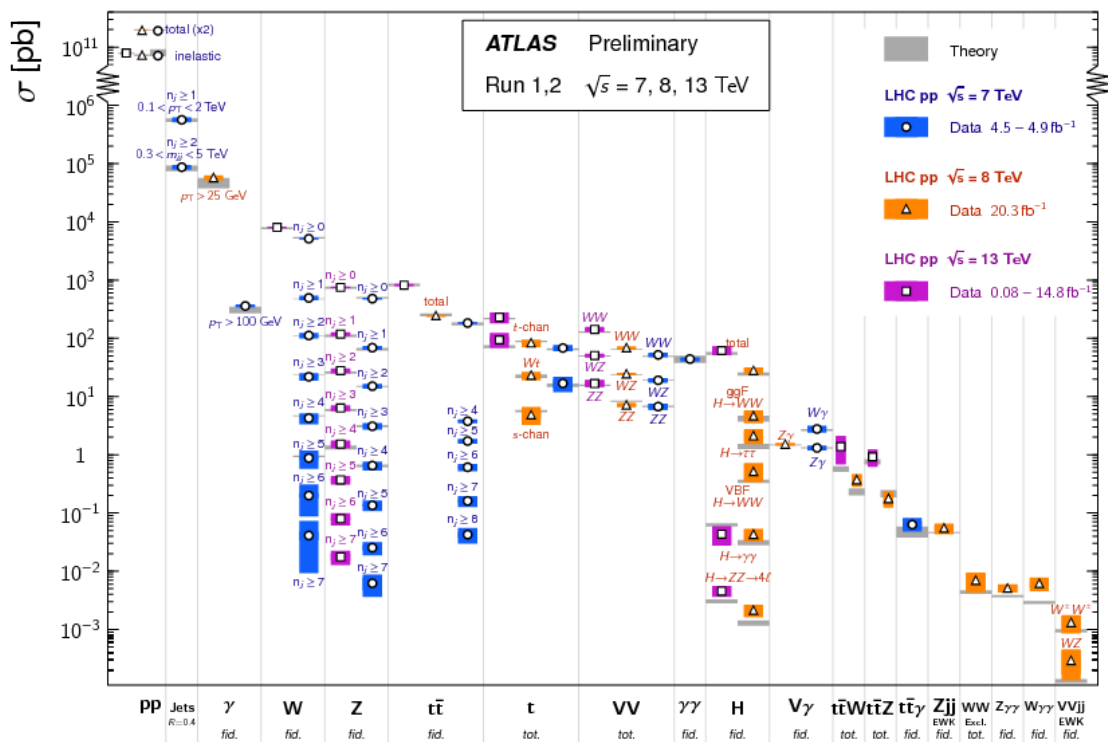
Figure 4.4: A schematic presenting the production cross section [pb] for each $pp \to X$ final state for Runs 1 and 2 of the ATLAS experiment. Taken from Ref. [54].

4.2.2 Parton Shower

Shortly after being produced, partons involved in the hard scattering process repeatedly induce cascades of QCD and QED radiation. The QCD radiation is computable in perturbation theory for time scales $\ll 1/\Lambda_{\text{had}}$ where Λ_{had} is a typical hadronic scale $\mathcal{O}(300 \text{ MeV})$ [7]. Therefore, PS algorithms are used to compute the cross section for generic hard processes, including all dominant (collinear) radiation kinematics of the basic process [7].

Hadronic and electromagnetic showers have different detector signatures because of their properties in QFT. Hadronic showers originate from colour-charged particles emitting further gluons or $q\bar{q}$ pairs leading to a directional shower of hadronic activity [46]. The electromagnetic showers originate from scattered electric charges radiating photons that can produce lepton-antilepton pairs [45]. The structure of the two shower shapes is highly different because of the self-interaction properties of gluons and the generation of many soft partons leading to an extended and more unpredictable shower shape compared to EM showers.

4.2.3 Hadronisation

The non-abelian nature of QCD leads to colour confinement at long distances, resulting in the breakdown in perturbation theory and instead QCD-inspired phenomenological models are required to describe the formation of colourless bound states [53]. The hadronisation process describes the non-perturbative transition from partons to hadrons. The two commonly used methods to describe this phenomenon are the cluster-hadronisation [55] and the Lund string [56] models.

The Lund string model uses a linear confinement potential, $V(R) = \kappa \cdot r$, where the string tension ($\kappa \sim 1 \text{GeV/fm}$) between two coloured particles increases linearly with their separation for distances $\lesssim 1 \text{fm}$ [7]. This effectively implements a computational threshold for colour confinement to occur. This potential can be physically interpreted as a string being stretched between the $q\bar{q}$ pair and as the distance increases so does the potential until it becomes sufficiently large that the non-perturbative creation of $q\bar{q}$ pairs can break the string. This is repeated for all strings until each has a mass of the order of a typical hadron [53].

The cluster-hadronisation model is based upon the preconfinement property of QCD [55]. This means that at each point, the PS forms colour-singlet combinations of partons, called clusters, dependent on the PS cut-off scale or, equivalently, the hadronisation scale [53]. Once primary clusters are formed, those with mass below 4 GeV are transformed into hadrons through a two-body decay [55].

4.2.4 Matching With Matrix Elements

PS algorithms are based upon a combination of approximations for collinear (small-angle) and soft radiation and are therefore typically inaccurate for hard, wide-angle emissions [7]. Improvements

to the PS description of hard collisions usually occur in the form of matrix element and parton shower matching (ME+PS) or the matching of NLO calculations and parton showers (NLO+PS) [7].

The ME+PS starts by generating a tree-level ME for the production process plus a certain number of other partons [7]. Truncated showers are then required to maintain colour coherence when interfacing to angular-ordered parton showers and α_s is carefully chosen for real (ME-driven) and virtual (PS-driven) corrections [7, 57]. The generated configurations are tree-level accurate at large angles and at small angles match the PS [7]. ME+PS matching is important because of the dominance of QCD processes in searches for new physics at hadron colliders, where the jets[3] are required to be well-separated (large-angle) and have large p_{T}, which is where PS algorithms are known to be unreliable [7].

NLO+PS promotes the increased generation accuracy of the HS process from LO to NLO, thereby including an extra parton with tree-level accuracy and NLO virtual corrections [7]. Generators that use this method are the MC@NLO [58] programme, the aMC@NLO [59] development and the Powheg-Box[60] framework. Sherpa also implements a variant of the MC@NLO method [7].

For processes that require an accurate description of more than one hard, large-angle jet associated with the primary process, ME+PS schemes are superior to NLO+PS ones [7].

4.2.5 Underlying Event and Pile-up

At hadron colliders, multiple scattering and rescattering effects arise which lead to the remaining key features of a pp collision; the underlying event (UE) and pile-up (PU). The UE can be defined as any additional activity beyond the hard scatter process and its associated ISR and FSR activity [7]. The dominant contribution to the UE is believed to originate from additional colour exchanges between the colliding hadronic states [7]. These additional exchanges can be modelled either as additional perturbative (mainly t-channel gluon) exchanges, called multiple parton-parton interactions (MPIs) or non-perturbatively using cut pomerons [7].

A possible consequence of MPIs is observing several hard parton-parton interactions in the same pp collision, called in-time pile-up (PU). The other source of PU originates from consecutive bunch crossings colliding before the first bunch has been fully detected, named out-of-time PU. In-time PU interactions are primarily soft, which typically result in the exchange of colour and small quantities of momentum without producing observable jets [7]. Experimentally, PU results in many additional vertices and hadronic activities that must be identified and reconstructed in an environment that is harder to discriminate within.

An important aspect of simulating events is to replicate the effect of PU observed in data due to the collider experiment. Pile-up conditions are replicated in simulated events by generating pp collisions with $\langle \mu \rangle = 1$[4], named minimum-bias, and superimposing them and the overlaid events

---

[3]Jets are explicitly defined in Section 5.2.2.

[4]This is the mean number of interactions per brunch crossing and is discussed in more detail in Section 5.1.1.

are varied and reweighted to match the actual bunch crossing in data, in a process known as pile-up reweighting [45].

4.3   Monte Carlo Generators

4.3.1   Theoretical Uncertainties

The estimation of Standard Model processes is performed using MC simulation. Simulation can also be used to assess the theoretical impact of parameters used to generate the process. All GPMC provide automatic evaluation of perturbative shower uncertainties via vectors of alternate event weights for renormalisation and factorisation scale ($\mu_{\mathrm{R}}, \mu_{\mathrm{F}}$) variations [7]. Although, note that the variations are not necessarily exhaustive [7]. Similarly, can be performed for different PDF sets [27]. Additionally, variations on generator parameters, such as h_{damp}, which control the amount of radiation, can also be evaluated [27]. Uncertainties related to the non-perturbative regime must be evaluated by varying salient model parameters by hand [7]. An uncertainty to describe the UE can be evaluated using Perugia [61] tunes with PYTHIA 6.

4.3.2   Specific Generators

Several programmes have been created to enact the event simulation process of Section 4.2 and so a brief description of their properties and purposes is presented.

- PYTHIA [62, 63] is a general-purpose generator that uses LO (NLO) MEs for $2 \rightarrow n(n \leq 3)$ processes [64]. It is capable of simulating both hard and soft interactions, however, it is commonly used as a PS generator and interfaced with a different ME generator. The generator uses a p_{T} ordered PS and the Lund string hadronisation model [64].

- SHERPA [65] is a general-purpose event generator for multi-leg MEs at LO (up to 4 extra partons) and at NLO (up to two extra partons) [64]. The matching procedure follows CKKW prescription and the cluster model is used for hadronisation [64].

- POWHEG-BOX[60] is a NLO ME generator using a five flavour scheme and POWHEG method for matching [8].

- MADGRAPH5_aMC@NLO [59] is a ME generator at LO for any lagrangian or NLO for selected processes [8]. The generator implements MC@NLO and is then interfaced to a PS using MLM prescription at LO [8].

4.4   Conclusion

This chapter discusses the important phenomenological aspects of proton-proton collisions, that being, the hard-scatter process, parton shower, hadronisation, matching and merging, the

underlying event and pile-up. Also within this chapter is the discussion of how this is recreated in simulated events and the designed purposes of several specific Monte Carlo generators.

Chapter 5

The ATLAS Experiment

The dataset and simulated events used in the analysis chapters (7-9) of this thesis were collected and generated by the A Toroidal Large ApparatuS (ATLAS) experiment. Therefore, this chapter discusses the experimental hardware of the ATLAS experiment used to detect particles produced in the pp collisions of the LHC. The final component of this chapter discusses the computational objects reconstructed from the detector signals, which allow for analysers to target specific detector signatures.

5.1   Hardware

5.1.1   LHC Facility and Luminosity

The ATLAS Experiment is one of the two general-purpose detectors situated along the Large Hadron Collider (LHC) at the Conseil Européen pour la Recherche Nucléaire (CERN) in Geneva, Switzerland. The LHC beam pipe is situated in the existing 26.7km tunnel, which was constructed between 1984 and 1989 for the CERN Large Electron-Positron (LEP) collider [66]. The beam pipe is superconducting and contains two proton accelerator rings. An overview of the present-day CERN facility, which presents the beam structure and the experiments, can be seen in Figure 5.1.

The primary design goal of the LHC is to explore physics above the electroweak symmetry–breaking (EWSB) scale ($\mathcal{O}(\gtrsim 100)$ GeV) [46]. Consequently, the Higgs boson was discovered in 2012 by the ATLAS [3] and Compact Muon Solenoid (CMS) [4] experiments. A further objective was to search for physics beyond the Standard Model (BSM) by probing pp collisions above the TeV scale. The collider is designed to accelerate protons up to $\sqrt{s} = 14$ TeV, however, Run 1 (2010-2014) achieved $\sqrt{s} = 7-8$ TeV and Run 2 (2015-2018) operated at $\sqrt{s} = 13$ TeV. The results presented in this thesis use data collected from Run 2.

The source of protons for the LHC beams begins with a hydrogen gas source in Linac2 [67]. Negative hydrogen ions are accelerated to 50 MeV using radiofrequency (RF) cavities and
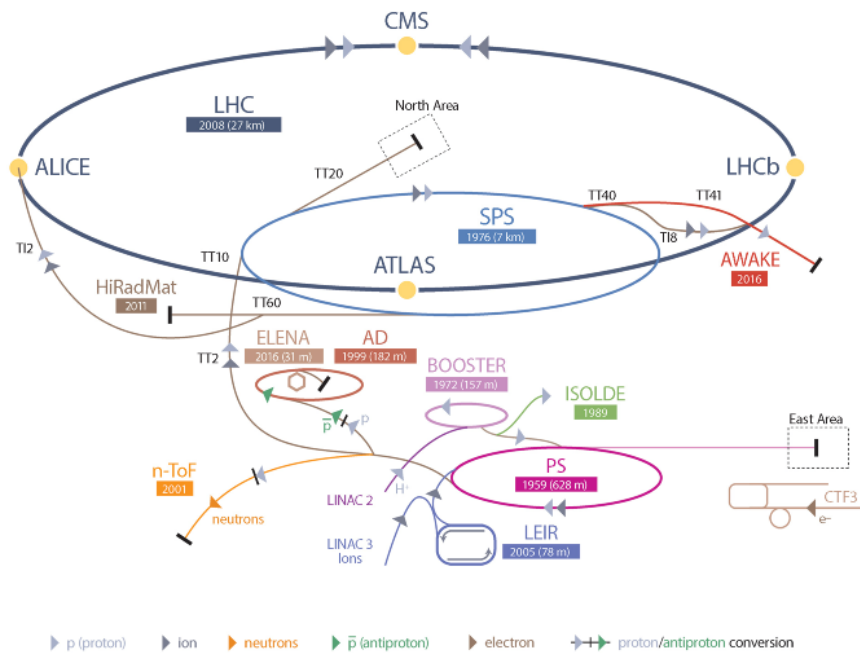
Figure 5.1: Schematic overview of the present-day CERN facility presenting the beam trajectories and experiments. Taken from Ref. [54].

quadrupole magnets in the linear accelerator [67]. Following Linac2, the negative hydrogen ions enter the Proton Synchrotron Booster (PSB), which is composed of four synchrotron rings, where the ions are stripped of their two electrons, leaving only protons [68] that achieve an energy of 2 GeV. Next, the protons enter the Proton Synchrotron (PS), which is a synchrotron with a circumference of 628m and achieves a proton energy up to 26 GeV [69]. Following this, the protons enter the Super Proton Synchrotron (SPS), which is a synchrotron with a circumference of 7km and achieves a proton energy up to 450 GeV and yielding a bunch length of 1.6ns [66, 70]. Finally, the protons enter the LHC beam pipes where they can reach up to 7 TeV using a 400MHz superconducting-cavity system allowing magnetic fields above 8T [66].

The ATLAS detector is situated at interaction point 1 (IP1) along the LHC. Bunches of 10^{11} protons collide 40 million times a second or equivalently, there is 25ns between bunch collisions [71]. The designed instantaneous luminosity is $10^{34}\mathrm{m}^{-2}\mathrm{s}^{-1}$ and thus, the number of events produced for each physical process can be calculated from the Equations defined in Section 4.1.1. The integrated luminosity for Run 2 can be seen in Figure 5.2(a).

The data used in this thesis originates from the "Good for Physics" luminosity, i.e that is suitable for analysis. Ideally all data that is recorded would be used for analysis, but because of the imperfect nature of the detector subsystems, the spontaneous and difficult nature of the LHC collisions and technological and resource limitations of the experiment, this is not possible. The uncertainty in the measured luminosity of the ATLAS Run 2 dataset is 1.7% [73]. It is derived, following a methodology similar to that detailed in Ref. [73], from calibrations of the luminosity
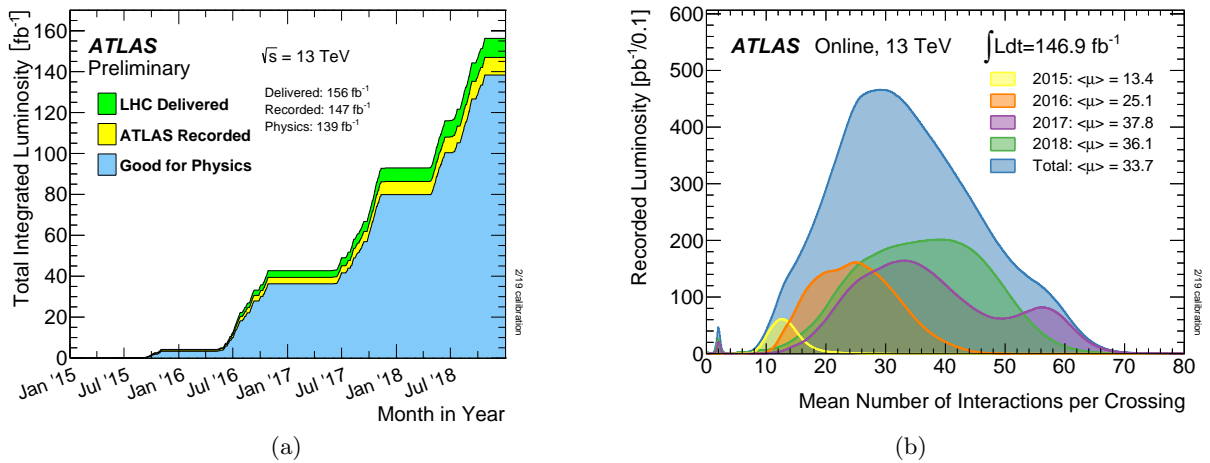
Figure 5.2: Plots of the integrated luminosity and the mean number of interactions per bunch crossing for the Run 2 data recording period taken at the ATLAS detector. Taken from Ref. [72].

scale using x-y beam-separation scans performed in August 2015, May 2016, July 2017 and July 2018.

Also within Figure 5.2, is the mean number of interactions per bunch crossing ($\langle\mu\rangle$) for the total dataset and the individual data taking periods, which provides a measure of the pile-up for the dataset. The mean number of interactions per bunch crossing for data taking periods 2015, 2016, 2017, 2018 and Run 2 is; $\langle\mu\rangle = 13.4, 25.1, 37.8, 36.1$ and 33.7 respectively.

5.1.2 ATLAS Coordinate System

Firstly, a coordinate system is required to quantify the structure of the detector geometry. A combination of Cartesian and spherical polar coordinates are used [74], where the interaction point defines the origin of the coordinates [71]. For the Cartesian, the positive z direction is defined along the collider beampipe, the positive x-axis is directed towards the centre of the LHC ring and the positive y is defined upwards (outward of the Earth as it would be) [71]. In spherical polar coordinates, the azimuthal angle ϕ is measured around the beam axis, where usually zero is defined in the direction of the positive x axis and the polar angle θ is defined from the beam axis such that it is zero in the positive z axis [71]. A diagram presenting the two coordinates can be seen in Figure 5.3 [75].

The z-axis is defined along the beam direction so it is often useful to define quantities in the $x-y$ plane that is, transverse to the beam direction. Most simply would be to define the transverse momentum (p_T) of an object;

$$\vec{p}_\mathrm{T} = \begin{pmatrix} p_x \\ p_y \end{pmatrix} \quad \text{and} \quad p_\mathrm{T} = \sqrt{p_x^2 + p_y^2}. \tag{5.1}$$
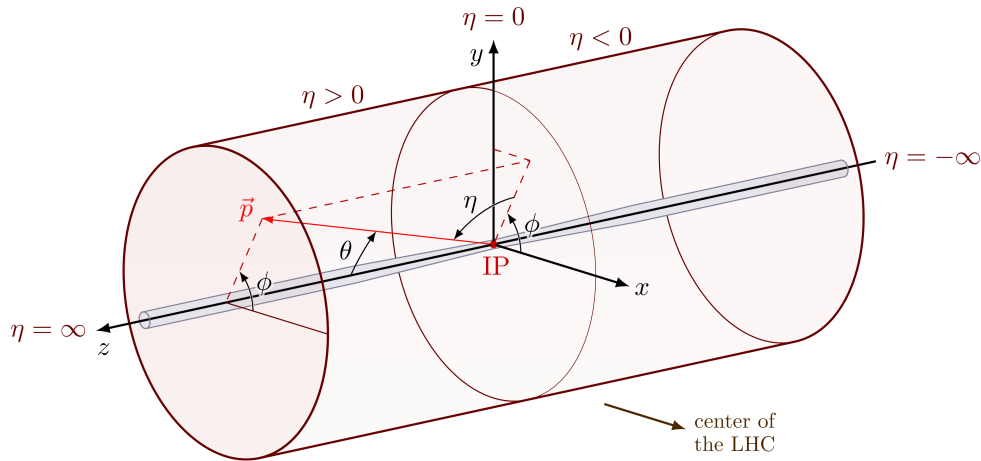
Figure 5.3: The definitions of the Cartesian and spherical polar coordinate systems used by the ATLAS experiment [75].

Instead of the polar angle θ, typically the rapidity (y) or pseudorapitity (η) is used. For massive objects, such as jets, the rapidity is used, whereas for massless (relativistic) particles, the pseudorapidity is used. The definition can be achieved using the approximation $p_z = E\cos\theta$ in the equation for the rapidity [6];

$$y = \frac{1}{2}\ln\left(\frac{E + p_z}{E - p_z}\right) \;\; \text{and} \;\; \eta \equiv -\ln\left(\tan\frac{\theta}{2}\right). \tag{5.2}$$

It is also useful to define the angular separation between objects in η-ϕ space, labelled ΔR and this is calculated by

$$\Delta R^2 = \Delta\phi^2 + \Delta\eta^2. \tag{5.3}$$

This quantity is invariant under longitudinal (z-axis) boosts as is $\Delta\phi$ and $\Delta\eta$ [6]. The angular separation commonly used in particle isolation algorithms and physics analyses to measure the particle activity or association surrounding a particle within a specified radius. An example of this is the combination of calorimeter energy deposits within a specified cone radius (R_C) in jet reconstruction algorithms (Section. 5.2.2).

5.1.3 ATLAS Detector Overview

ATLAS is one of the two general-purpose detectors along the LHC, the other being CMS. The purpose of having two independent experiments along the same particle collider is to cross-validate each other [76]. The ATLAS detector and the main detector subsystems can be seen in Figure 5.4.

ATLAS has a cylindrical forward-backwards symmetric design with respect to the interaction point and an onion-like series of layers of detectors around the interaction point [27]. The inner most detector is a tracking-based system for pattern recognition, momentum and vertex measurements
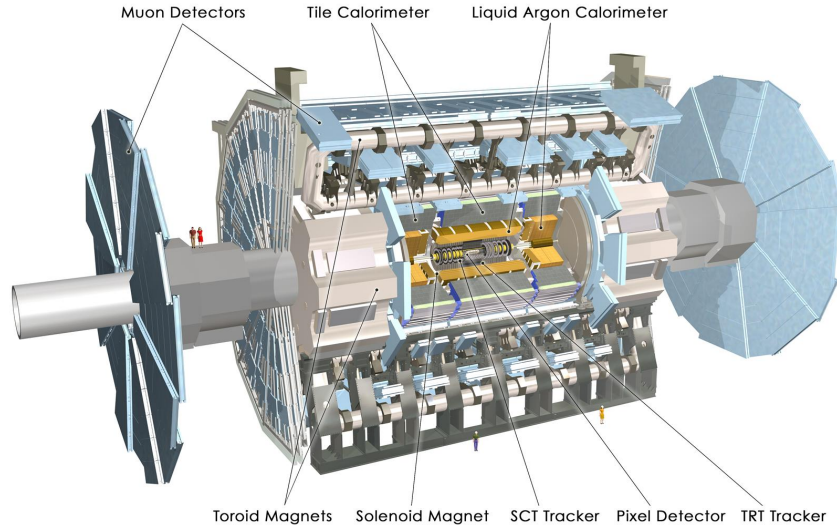
Figure 5.4: Cut-away view of the ATLAS detector and the main detecting subsystems. Taken from Ref. [77].

and electron identification, which is surrounded by a thin 2T superconducting solenoid magnet [71]. The next series of layers are the electromagnetic (EMcal) and hadronic (Hcal) calorimeters followed by the muon spectrometers (MS), each needed for measuring the energy of each respective targeted particles. The MS are arranged within three large superconducting toroidal magnets [71]. A summary of the respective resolution of each of these systems can be found in Table 5.1.

Detector Component	Specified Resolution	$|\eta|$ coverage	
		Measurement	Trigger
Tracking	$\sigma(p_\mathrm{T})/p_\mathrm{T} = 0.05\% \oplus 1\%$	± 2.5	
EM Calorimetry	$\sigma(E)/E = 10\% \oplus 0.7\%$	± 3.2	± 2.5
Hadronic Calorimetry Barrel (Bulk+Endcap)	$\sigma(E)/E = 50\% \oplus 3\%$	± 3.2	± 3.2
Forward	$\sigma(E)/E = 100\% \oplus 10\%$	$\in [3.1, 4.9]$	$\in [3.1, 4.9]$
Muon Spectrometer	$\sigma(p_\mathrm{T})/p_\mathrm{T} = 10\%$ at $p_\mathrm{T} = 1$ TeV	± 2.7	± 2.4

Table 5.1: Energy (momentum) resolutions of the main detector subsystems. Taken from Ref. [71].

5.1.4 Inner Detector

As discussed in Section 5.1.1, the LHC is designed for high-luminosity collisions. The mean number of pp interactions for the total Run 2 period is $\langle\mu\rangle = 33.7$ where $\mathcal{O}(100)$ particles per pp interaction are produced with approximately 50 precise localisation measurements, termed *hits*, recorded in the tracking system per charged particle. Therefore, the tracking system provides precise information close to the interaction point for charged particles, all whilst operating in a highly challenging environment [53].

Precise measurements of charged particles are obtained by having a series of high-granular

detectors as close as possible to the collision vertex. The detection techniques are composed of a combination of semiconductor and drift tube technologies. The final component of the tracking system is the magnetic field created by the ATLAS superconducting magnet system. All ID trackers utilise the magnetic system, and they are; Pixels and the Insertable B-Layer (IBL), the SemiConductor Tracker (SCT) and the Transition Radiation Tracker (TRT). Each of these is presented in Figure 5.5 along with their distance from the centre of the beam pipe.
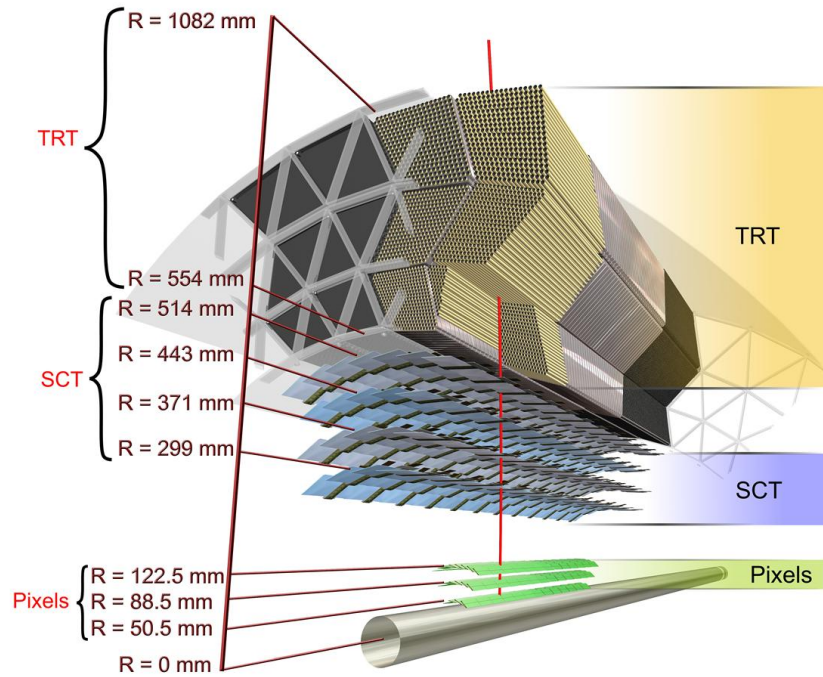
Figure 5.5: Cut-away view of the ATLAS Inner Detector subsystems along with its radial distance from the centre of the beam pipe. Taken from Ref. [78].

Semiconductor tracking detectors use pixel technologies or silicon microstrip detectors. The ionisation of the detection medium (typically silicon) caused by a traversing charged particle produces an ionisation charge, which can be collected in the presence of an electric field. In the presence of a magnetic field, the ionisation charge is further deflected by the Lorentz angle θ_L. IBL, Pixels and SCT use these technologies. The design of semiconductor tracking detectors follows a pattern of cylinders and discs, resulting in an overlap of modules in ϕ to guarantee precision measurements over the full angular coverage [79]. The highest granularity is in the innermost pixel layers and is designed to be as close to the beam pipe as possible. The primary purpose of this sub-detector is to determine the impact parameter (IP, see Section 5.2.2) resolution and identify short-lived particles such as B-hadrons and τ leptons [79]. The silicon pixel detectors provide four position measurements per track, where the first hit usually occurs in the IBL [80]. The SCT provides eight precision measurements per track, contributing to the measurement of the momentum, IP and vertex position as well as having good pattern recognition [79, 80].

Drift tubes are gas-filled tubes with a central wire. Similar to semiconductors, the charged particle causes an ionisation charge in the gas and drifts towards the central wire, which is the anode. The measurement comes in the form of a drift time, which can be converted to a drift radius when reconstructing a track from several drift times. This technology is used for the TRT. Having a large number of tracking points per track (36), the TRT provides continuous track-following and a significant contribution to each momentum measurement [79]. The capability of electron identification was added by including xenon gas to detect transition-radiation photons created in the radiator between the straws [79].

A combination of IBL, pixels, SCT and TRT results in highly robust pattern recognition and high precision ϕ and z coordinates. Additionally, this layout provides full tracking coverage for $\eta < 2.5$.

5.1.5 Calorimetry

Calorimeters are designed to stop and fully contain a target set of particles i.e, hadronic or electromagnetic showers. The absorption of the energy deposition by a shower enables one to measure the energy of that shower and its spatial location within the calorimeter [81]. This can be extended by linking the energy deposits in the calorimeter to hits in the tracking detector for showers originating from charged particles and can therefore identify the trajectory of the original particle.

When a particle interacts with a calorimeter medium, its entire kinetic energy is used to excite the atoms or molecules of the medium. These atoms emit this excitation energy in the form of visible light when returning to the ground state and this scintillation light is the basis of a calorimeter signal. In the instance of a charged particle, ionisation of the calorimeter medium also contributes to the calorimeter signal.

ATLAS uses the EMcal and Hcal calorimeters to detect and reconstruct electromagnetic and hadronic showers, respectively. They are also essential in the calculation of the missing transverse energy (discussed in Section 5.2.4). Figure 5.6 presents a visual overview of the ATLAS calorimetry system.

The EM calorimeter is a series of sampling calorimeters with an accordion geometry and is divided into a barrel section ($|\eta| < 1.475$) and two end-caps ($1.375 < |\eta| < 3.2$). The accordion geometry provides complete ϕ symmetry without azimuthal cracks in the detector [79]. The calorimeter medium is chosen to be lead and liquid-argon (LAr) because of the requirement to withstand high radiation from being relatively close to the interaction vertex and the end-cap occupying a high pseudorapidity range. The lead thickness in the absorber plates was optimised to maximise the energy resolution as a function of η [79].

The hadronic calorimeters cover a wide range in pseudorapidity ($|\eta| < 4.9$), where different calorimetry techniques are utilised based on the physics requirements [79]. The hadronic barrel calorimeter is a cylinder divided into three sections: the central barrel and two identical extended barrels, which are all tile sampling calorimeters [79]. Tile calorimeter technology is based on a
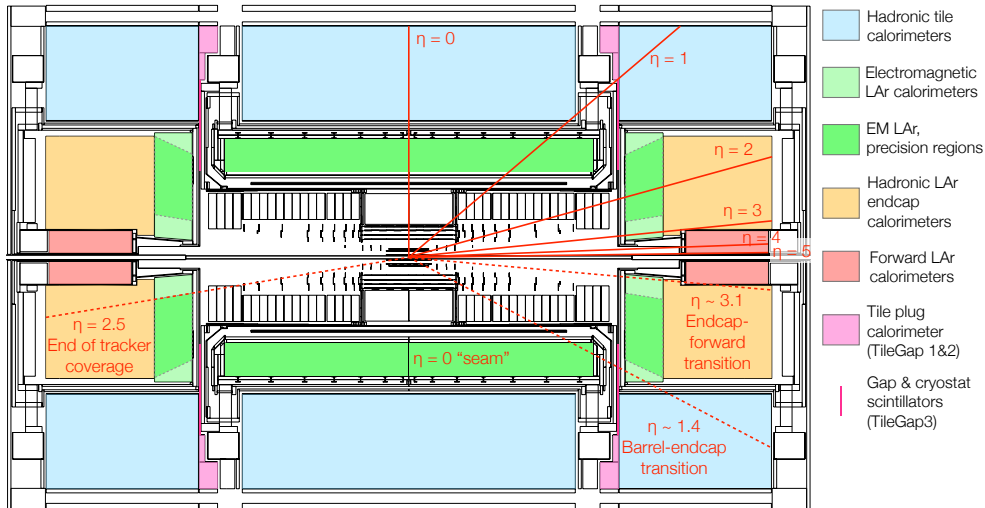
Figure 5.6: Cut-away view of the ATLAS calorimetry system with relevant pseudorapidity directions overlayed. Taken from Ref. [82].

sampling technique with plastic scintillator plates (tiles) embedded in an iron absorber. The barrel cylinder covers the region $|\eta| < 1.0$ and the extended barrel covers the region $0.8 < |\eta| < 1.7$. The hadronic end-cap calorimeter (HEC) and the high-density forward calorimeter (FCAL) occupy the remainder of the η range, which extend to $|\eta| < 3.2$ and $3.1 < |\eta| < 4.9$ respectively. Both calorimeters are LAr sampling calorimeters because of the higher radiation resistance required in this pseudorapidity range [79]. The thickness of the Hcal is 11 interaction lengths (λ) at $\eta = 0$, which has been observed to sufficiently contain hadronic showers and reduce the *punch-through* of hadronic showers into the muon system well below the irreducible level of prompt or decay muons [79].

5.1.6 Muon Spectrometer

The remaining particles exiting the inner detector and subsequent calorimeters, will largely compromise of muons and thus, surrounding these systems is a combination of large superconducting air-core toroidal magnets and muon detectors. The magnetic field is between $2-6$T across most of the muon detector. The magnets deflect the muon tracks to separate trigger and high-precision tracking chambers, both can be seen in Figure 5.7 [71].

Designed to measure the deflection in the $r-z$ plane of muons exiting the barrel and end-cap calorimeters, the muon spectrometers cover the pseudorapidity range $|\eta| < 2.7$ and trigger over the range $|\eta| < 2.4$ [71, 80]. At the extremities of the particle momenta, the muon system is capable of measuring muon momenta down (up) to a few GeV (~ 3 TeV) with adequate momentum resolution and excellent charge identification [71].

The muon chambers use four separate detecting media where they are arranged such that particles from the IP traverse at least three and are positioned for essentially full coverage in the
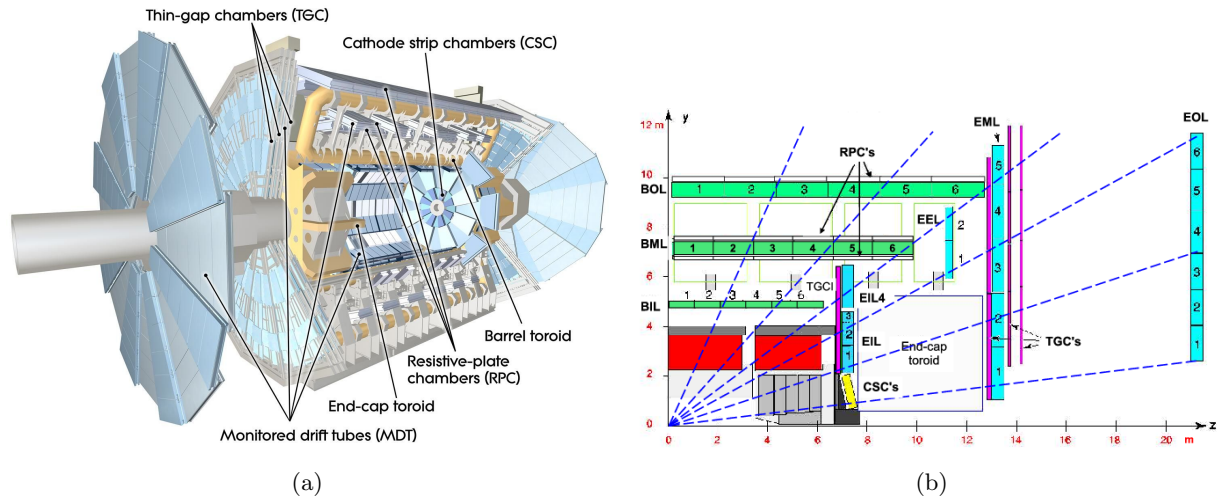
Figure 5.7: Schematics presenting cut-away views of the individual muon detecting subsystems. Taken from Ref [71].

pseudorapidity range [71]. The first is Monitored Drift Tubes (MDTs) that provide precision measurements of the track coordinates over most of the η-range and have a resolution of $30\mu m$ [71]. Each MDT chamber provides between six and eight η measurements along a muon track [80]. At larger pseudorapidities ($2 < |\eta| < 2.7$) and close to the IP, Cathode Strip Chambers (CSCs) with higher granularity are used to withstand the demanding rate and background conditions [71]. The CSCs are multiwire proportional chambers capable of precision coordinate measurements and have good spatial resolution [71]. The CSCs provide four simultaneous measurements of η and ϕ [80].

In terms of the muon trigger system, it is present over the pseudorapidity range $|\eta| \leq 2.4$ and Resistive Plate Chambers (RPCs) are used in the barrel and Thin Gap Chambers (TGCs) in the end-cap regions [71]. RPCs are gaseous detectors that use ionisation to produce an electronic signal. Whereas, TGCs are similar to the multiwire proportional chambers. RPCs and TGCs, provide tracking information complementary to precision chambers by improving the determination of the track coordinate in the non-bending direction [80]. The spatial resolution for the position measurements of the two trigger components are $5-10$mm in the bending (non-bending) plane (direction) [80].

5.1.7 Magnet System

An overview of the magnet system, which aids in charged particle detection and measurements, can be seen in Figure 5.8.

There are two main components of the magnet system. Firstly, is the central solenoid (CS), which provides the ATLAS inner detector (ID) with a nominal magnetic field of 2T [79]. Secondly, are the two end-cap toroids (ECT) and barrel toroid (BT). The toroid magnet system is a series of three large air-core toroids which generate the magnetic field for the muon spectrometer, with a peak magnetic field of 3.9 and 4.1T respectively [79]. The barrel toroid provides a magnetic
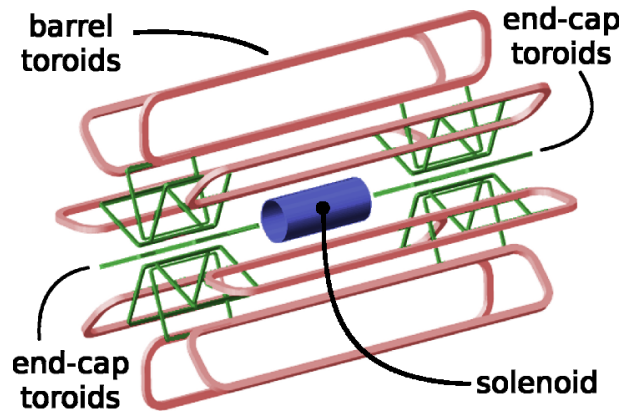
Figure 5.8: Schematic presenting the ATLAS magnet system. Taken from Ref. [83].

field of $1.5-5.5$ Tm in the pseudorapidity range $0 < |\eta| < 1.4$. The end-cap toroids provide a magnetic field of approximately $1-7.5$ Tm for the range $1.6 < |\eta| < 2.7$ [71].

5.1.8 Trigger and Data Acquisition

As discussed in Section 5.1.1, it would be preferable to analyse all pp event collisions to maximise the integrated luminosity, however, in practise, this is difficult to achieve. It is therefore important that a trigger system exists which decides which events to record during data collection dependent on "interesting" features or whether all subsystems are operating correctly. Figure 5.9 presents the workflow for the ATLAS trigger and data acquisition (DAQ) system.
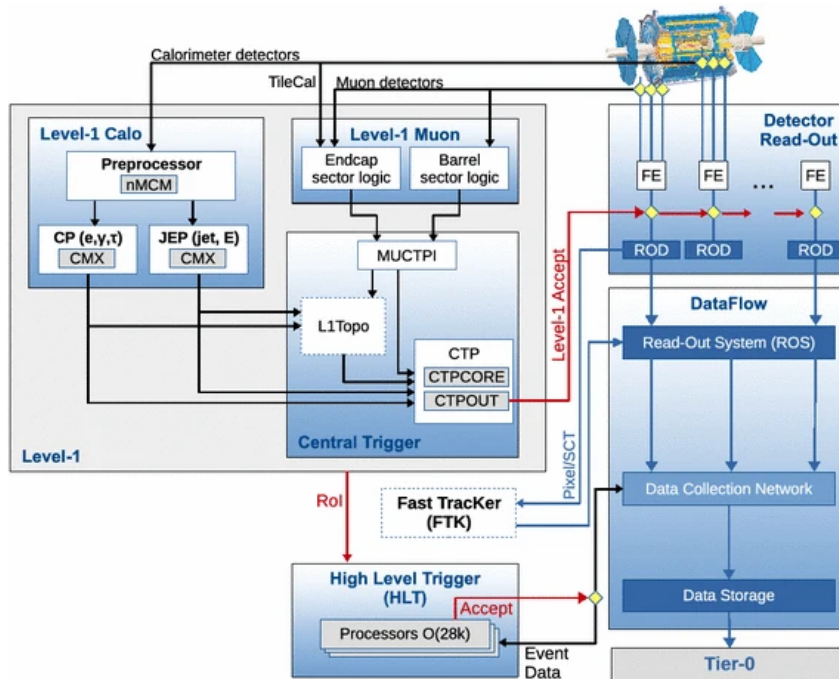
Figure 5.9: The ATLAS trigger and data acquisition system. Taken from Ref. [84].

The trigger system is composed of three distinct levels; Level-1 (L1), Level-2 (L2), and the event filter (EF). Each trigger level refines the decisions made at the previous stage and, where

necessary, applies additional selection criteria [71]. The L1 trigger searches for high p_T muons, electrons, photons, jets, τ-leptons decaying into hadrons, and large missing and total transverse energy (defined in Section 5.2.4) [71], where the selection is based on information from the detectors depicted in Figure 5.9. The decision is required in less than $2.5\mu s$ reducing the event recording rate to ~ 75kHz [71]. A trigger *menu* is created, which is a combination of trigger selections from the L1 muon and calorimeter triggers [71]. The L1 trigger also defines one or more Regions-of-Interest (RoIs) that are geographical coordinates in η-ϕ-space of the detector where its selection process has identified interesting features [71]. Events passing the L1 trigger selection are transferred to the L2 trigger. Event acceptance by the L2 trigger is determined from the seeding of RoI information, such as the type of feature identified and the criteria passed from the RoI [71]. The L2 trigger is designed to reduce the trigger rate to approximately ~ 3.5kHz [71]. The final EF stage reduces the event rate to roughly ~ 200Hz where its selections are implemented for specific physics analyses.

After the L1 trigger accepts an event, the data from the workflow are transferred from the detector to the detector-specific electronic readout drivers (ROD) [71]. These digitised signals are then formatted as a standard raw data format before being transferred to the DAQ system [71]. The data is temporarily stored and the L2 trigger checks for the event data associated with the RoIs [71]. Those events selected by the L2 trigger are then transferred to the event-building system and subsequently to the event filter for final selection [71].

5.1.9   Simulating ATLAS

All ATLAS SM measurements and searches use a simulated dataset to create a testable prediction from the SM. In this section, the processes detailing how this simulated dataset is created are introduced.

The final output from the hadronisation MC generators is the four-vectors of all stable particles in the final state [8]. This *generator-level* information, or sometimes referred to as *truth* information, is essential for experimental calibration because it is inaccessible in real data. The generator-level information needs to be processed through the ATLAS simulation chain [85] to emulate the interaction with the detector. A schematic presenting the workflow of the ATLAS simulation chain can be seen in Figure 5.10.

The detector is fully simulated using GEANT 4 [86], which includes all the material in the detector and surrounding environment [27, 76]. It can also model detector-related effects in a wide energy range from $\mathcal{O}(100)$ eV to the TeV scale for electromagnetic and hadronic processes [45].

The complete simulation of the ATLAS detector is extremely time-consuming, requires a large quantity of CPU time, IO and disk space [27]. Consequently, ATLAS also uses a simulation of the detector that is less computationally intensive, called fast simulation. It uses all simulation steps for the inner detector and muon spectrometer with a simplified approach for the calorimeter system based on a parameterisation of its response to different particles [45]. Because of these approximations, this method results in a loss in simulation accuracy and therefore it is

Figure 5.10: A schematic presenting the workflow of the ATLAS simulation chain. Taken from Ref. [85].

typically used for sub-dominant backgrounds, signal processes and the calculation of theoretical uncertainties related to the ME and PS [27].

5.2 Event Reconstruction and Physics Objects

The goal of event reconstruction is to have a computational representation of each particle observed in a pp collision. Each representation would contain the four-vectors of the particles and any other information required by SM measurements or beyond the SM searches. In this section, each object used in the analysis chapters (Chapters 7, 8, 9) is defined.

5.2.1 Tracks

A track could be defined as the representation of the trajectory of a charged particle through a tracking detector by combining a series of measurements in each detector layer. An important component in the reconstruction of tracks is the (reconstructed) primary vertex (PV) or equivalently, hard-scatter (HS) vertex. The PV can be physically interpreted as the interaction point in a pp collision and experimentally it is reconstructed as the vertex with the highest sum of p_T tracks associated with it[1] [87]. Being the vertex from which all hard objects originated, its importance is evident for all reconstructed objects used in physics analyses. Tracks are generally used as input to higher-level reconstruction objects, such as Particle Flow objects (see Section 5.2.2), for use in SM measurements and BSM searches.

5.2.2 Jets

Partons scattering off one another is the most common hard process at hadron-hadron colliders because of the high density of the gluons in the proton and the fact that the QCD coupling

---

[1] Also requires greater than one associated to it.

is significantly larger than the electroweak couplings [46]. Successively softer gluons may be radiated, at an angle based upon the p_T of the original parton and therefore, the shape of the shower in the calorimeter is strongly-p_T dependent. The result is a collimated shower of hadrons in the detector whose collective energy and momentum reflect those of the initially scattered parton. The experimental object that characterises a hadronic shower is known as a jet. Jets are an important component in the final state of many physics analyses because of their high production cross section at the LHC [81]. A jet can be defined more explicitly as a collection of particles contained in a well-defined region of the $\eta-\phi$ space, with cone radius R_C around the jet axis, where the jet axis is defined as the axis that connects the interaction vertex with the centre of gravity of the energy deposit of the jet in the calorimeter [81].

The nominal reconstruction method for jets, used in both Runs 1 and 2 of the ATLAS physics programme, is the sequential recombination jet algorithm named anti-k_t [88]. The anti-k_t algorithm is infrared and collinear (IRC) safe and therefore, the shape of the outputted jets is not influenced by soft radiation [88]. The algorithm effectively performs as an idealised cone algorithm where soft particles do not modify the shape of the jet, only hard particles. This results in the boundary of the jet being resilient with respect to soft radiation, but flexible with respect to hard radiation. Particles that belong to the jet may be excluded when the energy of the jet is determined and similarly for particles travelling within the acceptance of the cone may be included incorrectly [81]. The workflow of the algorithm is as follows:

1. Identify proto-jets from a series of jet inputs (tracks, calorimeter cells or other) and order them based on their transverse momentum $p_T^{-2}(i)$.

2. Calculate the distance (d_{ij}) between each proto-jet i and j,

$$d_{ij} = \min\{p_T^{-2}(i), p_T^{-2}(j)\}\frac{\Delta R_{ij}^2}{R_C}, \tag{5.4}$$

   where $\Delta R_{ij}^2 = \Delta y_{ij}^2 + \Delta \phi_{ij}^2$ and R_C is the cone radius. Typically, the cone radius has a value of $R_C = 0.4$ for most ATLAS physics analyses [27, 88]. The distance (d_{iB}) between proto-jet i and the beam B is also calculated using

$$d_{iB} = p_T^{-2}(i). \tag{5.5}$$

3. Find the smallest distance ($d_{\min}$) by determining

   (a) If $d_{\min} = d_{ij}$, combine jet inputs i and j and d_{ij} is calculated for the next jet input in the list.

   (b) If $d_{\min} = d_{iB}$, the jet input i is considered a jet and removed from the list.

4. The distances are recalculated and the procedure repeated until no entities are left.

An example of the algorithm in use for a parton-level event along with random soft particles can be seen in Figure 5.11.
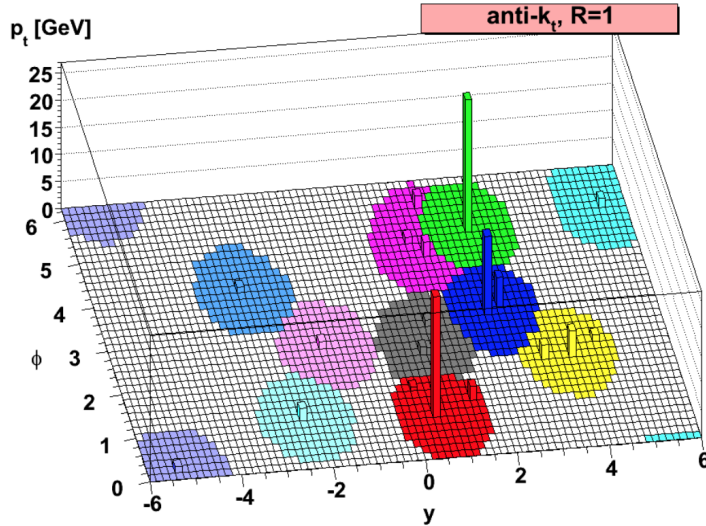
Figure 5.11: Example of the anti-k_t sequential recombination jet algorithm using $R_C = 1.0$ for a parton-level event with ~ 104 random soft particles. Taken from Ref. [88].

Within the workflow, the inputs to the proto-jets can be tracks, referred to as track-jets, however, this jet type is not used in this thesis. Until recently, another dominant jet type was used in ATLAS SUSY searches (such as those of Chapter 8-9), which used measurements of energy deposits in the calorimeters, referred to as calorimeter-jets. Finally, is the combination of both tracking and calorimeter information, which ATLAS and CMS refer to as Particle Flow jets [89, 90]. Calorimeter-jets were used for the majority of Run 1 and 2 physics analyses in ATLAS. In ATLAS, calorimeter-jets are specifically known as *EMTopo*-jets which are named after the topological clustered calorimeter cell signals calibrated at the electromagnetic scale from which they are built [91]. The topological clustering algorithm collects calorimeter signal cells following a spatial signal-significance pattern calculated by

$$\zeta_{\text{cell}}^{\text{EM}} = \frac{E_{\text{cell}}^{\text{EM}}}{\sigma_{\text{noise,cell}}^{\text{EM}}}. \tag{5.6}$$

The seeding, growth and boundary features of the growing-volume algorithm, are controlled by

$$
\begin{aligned}
&|E_{\text{cell}}^{\text{EM}}| > S\sigma_{\text{noise,cell}}^{\text{EM}} \rightarrow |\zeta_{\text{cell}}^{\text{EM}}| > S \text{ Primary seed threshold, default } S = 4, \\
&|E_{\text{cell}}^{\text{EM}}| > N\sigma_{\text{noise,cell}}^{\text{EM}} \rightarrow |\zeta_{\text{cell}}^{\text{EM}}| > N \text{ Growth control threshold, default } N = 2 \text{ and} \\
&|E_{\text{cell}}^{\text{EM}}| > P\sigma_{\text{noise,cell}}^{\text{EM}} \rightarrow |\zeta_{\text{cell}}^{\text{EM}}| > P \text{ Principal cell filter } P = 0,
\end{aligned}
\tag{5.7}
$$

which ensures strong cell signal retention whilst suppressing noise from insignificant signals [91].

Pile-up can result in negative signal cell contributions because of the modulus in Equation 5.7. However, cells where $E_{\text{cell}}^{\text{EM}} < 0$ can be used as a tool to quantify the amount of noise in a calorimeter and thus the number of negative seeds is an estimator for out-of-time pile-up [91].

The clustering algorithm remains unaffected by these because the negative contributions from the neighbouring cells will cancel the positive fluctuations originating from out-of-time pile-up [91].

The topological clustering algorithm is used for both electromagnetic interacting particles in the EMcal and hadronic activity in the Hcal. All ATLAS calorimeters are non-compensating, which means that the signal obtained for hadrons is smaller than that for EM particles of a specified energy [91]. Therefore, a local clustering weight (LCW) is applied to the cell signal to correctly calibrate particles for the non-compensating calorimeter response, the loss in efficiency due to clustering or topoclusters and the energy loss in inactive detector material [91].

The recommended jet reconstruction algorithm that has superseded EMTopo-jets in ATLAS, is the Particle Flow (PFlow) reconstruction algorithm [89], which utilises both calorimeter and tracking measurements. The designed ATLAS calorimeter energy resolution and tracking inverse momentum resolution for a charged pion in the centre of the detector is given by

$$
\frac{\sigma}{E} = \frac{50\%}{\sqrt{E}} \oplus 3.4\% \oplus \frac{1\%}{E} \text{ and}
$$
$$
\sigma\left(\frac{1}{p_\mathrm{T}}\right) \cdot p_\mathrm{T} = 0.036\% \cdot p_\mathrm{T} \oplus 1.3\%
$$
(5.8)

respectively [89]. This results in a significantly better momentum resolution for the tracker (calorimeter) for (high) low-energy charged particles. This is what the PFlow reconstruction algorithm aims to achieve when reconstructing jets - information for a specific particle is obtained from the optimal sub-detector depending on the energy of the particle. Demonstrating the improved momentum resolution, Figure 5.12 compares the p_T and $|\eta|$ resolution distributions for PFlow and calorimeter jets calibrated with local clustering weights plus a jet energy scale correction [91], both reclustered with the anti-k_t algorithm with $R = 0.4$.

The largest benefit to physics analyses is from the improvement in the momentum resolution at low p_T (< 100 GeV), resulting in increased sensitivity to soft particles. Additionally, there is an increase in the resolution of the measurement of the pseudorapidity observable for the range $|\eta| < 1.4$ when using PFlow. Similarly, improvements are observed for the angular resolution (η, ϕ) of a single particle [89]. PFlow reconstruction of hadronic jets is also observed to be robust against pile-up compared to locally calibrated calorimeter-jets because of the association of the track reconstruction with the HS vertex and consequently, in-time determination of a track association to pile-up vertex is performed [89].

Jet Calibration

Whether a jet is reconstructed from hits in the tracking system, or with cells in the calorimeter, or a combination of both, each jet object must be calibrated to match the particle (or generator) level properties. This does not occur in practise because of the imperfect calibration of calorimeters
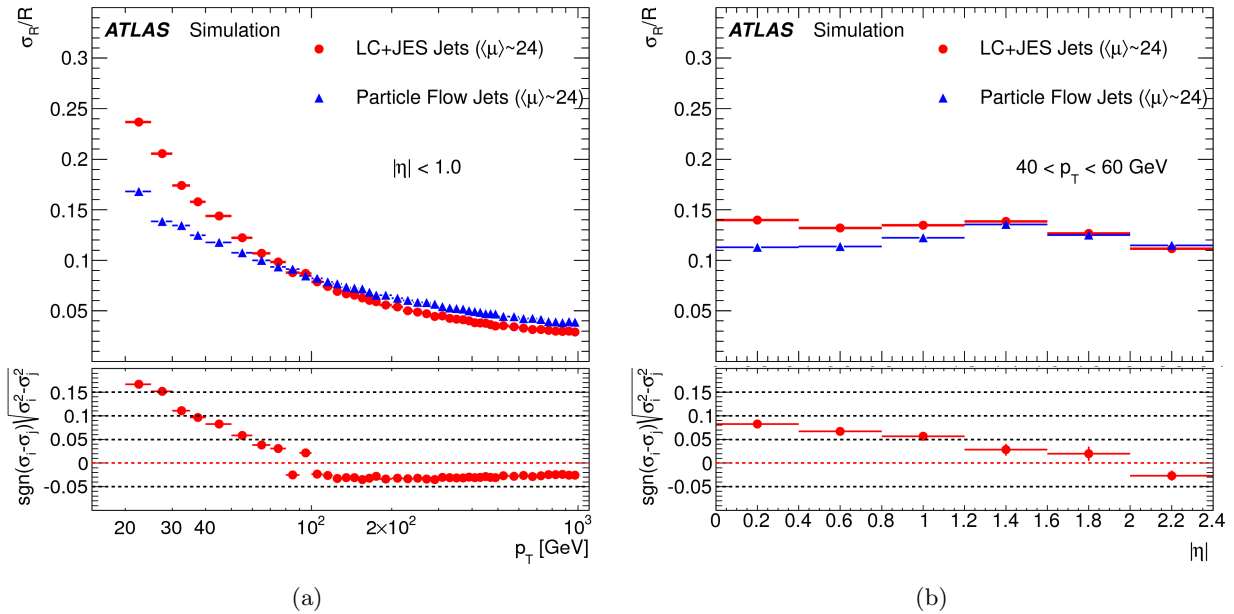
Figure 5.12: Comparison between Particle Flow jets and calorimeter jets calibrated with local clustering weights plus jet energy scale correction for simulation in the distributions of (a) p_T and (b) $|\eta|$ resolution. The figures assume a pile-up condition of $\langle\mu\rangle \sim 24$. Taken from Ref. [89].

(or biases in track momentum reconstruction), calorimeter gaps/cracks (or tracking inefficiencies), detector noise or pile-up. Therefore, a series of simulation-based corrections are applied, in addition to the usage of a series of in situ techniques to correct for differences between data and simulation [82].

Initially, pile-up corrections are performed by removing excess energy caused by the same or nearby bunch-crossings which are applied as a function of the event pile-up p_T density and jet area [82]. Further pile-up corrections are performed to remove the residual pile-up dependency on $\langle\mu\rangle$ and the number of PVs (N_{PV}) [82]. The next stage is the simulation-based calibration to correct the four-momentum between the reconstructed and truth jets [82]. Following this, the dependence of the reconstructed jet response on observables constructed from the tracking, calorimeter and muon detectors is removed to improve the jet p_T resolution and the associated uncertainties. This stage also reduces the jet flavour dependence and energy leakage from the detector response [82]. The final in situ correction is applied to only to data to correct for the remaining differences between data and simulation [82]. These corrections are derived using well-measured objects (photons, Z bosons and calibrated jets) [82].

The jet energy scale (JES) calibration results in 125 individual terms derived from in situ, pile-up, flavour dependence and estimates of additional effects for a complete systematic configuration [82]. Because of physically meaningful correlations between the terms, they cannot be simply added in quadrature and instead two reduction schemes are employed, that is, to reduce the total number of terms in the eigenvector decomposition. The first of the two schemes is the global reduction that combines all p_T-dependent in situ uncertainty components for a total of 23 [82]. The second is the category reduction, which combines all p_T-dependent in situ uncertainty components into separate groups based on their origin; detector, statistical, modelling or mixed

which results in 15 reduced components for a total of 30 [82]. Figures of the total JES and JER uncertainty as well as a function of the calibration corrections can be seen for p_{T} and η distributions for EMTopo and PFlow jets in Figures 5.13.

5.2.3   Impact Parameter and Secondary Vertices

Because of the dominant nature of the strong interaction in pp collisions at the LHC, b-quarks are produced at high production rates and are a component of multiple detector signatures of SM measurements and BSM searches. The b-quark hadronises to form a b-hadron, which has a long lifetime of 1.5ps ($c\tau = 470\mu$m) [92] resulting in a significant mean flight length compared to the rest of the Standard Model quarks, before subsequently decaying in the detector. The long lifetime can be exploited for the classification (or *tagging*) of the hadronic jet as originating from a b-quark, named b-jet, in a process referred to as b-tagging. This can be achieved by reconstructing the displaced or, what is more commonly referred to as, secondary vertex (SV) caused by the significant lifetime or alternately by examining the impact parameter (IP) of the daughters [79]. A diagram presenting both these quantities for a b-hadron decay can be seen in Figure 5.14.

A SV vertex is typically located outside the beam profile in a collider experiment [94] and hence, can be discussed in the context of short- and long-lived particle decays. Long-lived particles are those that decay in the tracker volume, such as K-short mesons and λ baryons [94]. Short-lived particles can be defined as those that decay before they enter the first layer of the innermost tracking device, typically travelling less than a few millimetres [94]. This includes B- and D-hadrons and τ-leptons and therefore SVs will only be discussed in the context of short-lived particles for this thesis.

As discussed in Section 5.2.1, the PV reconstruction is essential for the total event reconstruction. The PV is used as the reference point to which the IP is measured and hence can be defined, for the transverse (d_0) and longitudinal (z_0) components, as the point of closest approach of the trajectory of a track to the primary vertex in the r-ϕ and z-axis respectively [27]. Two further quantities related to the IP are also typically defined. Firstly is the IP normalised by its associated uncertainty, known as the IP significance, calculated by

$$s_{d_0} = \frac{d_0}{\sigma_{d_0}} \quad \text{and} \quad s_{z_0} = \frac{z_0}{\sigma_{z_0}}. \tag{5.9}$$

The motivation for this quantity is that the uncertainty in d_0 (z_0) depends on the angle and momentum of the track and thus one can better quantify the significance of the IP of a track. The second quantity is used in the low-level b-tagging algorithms (Section 7.1) and in electron and photon reconstruction (Section 5.2.5), is known as the *signed* transverse and longitudinal IPs, which are defined by

$$\mathrm{IP}_{d_0} = sign \times |d_0| \quad \text{and} \quad \mathrm{IP}_{z_0} = sign \times |z_0 \sin\theta|, \tag{5.10}$$
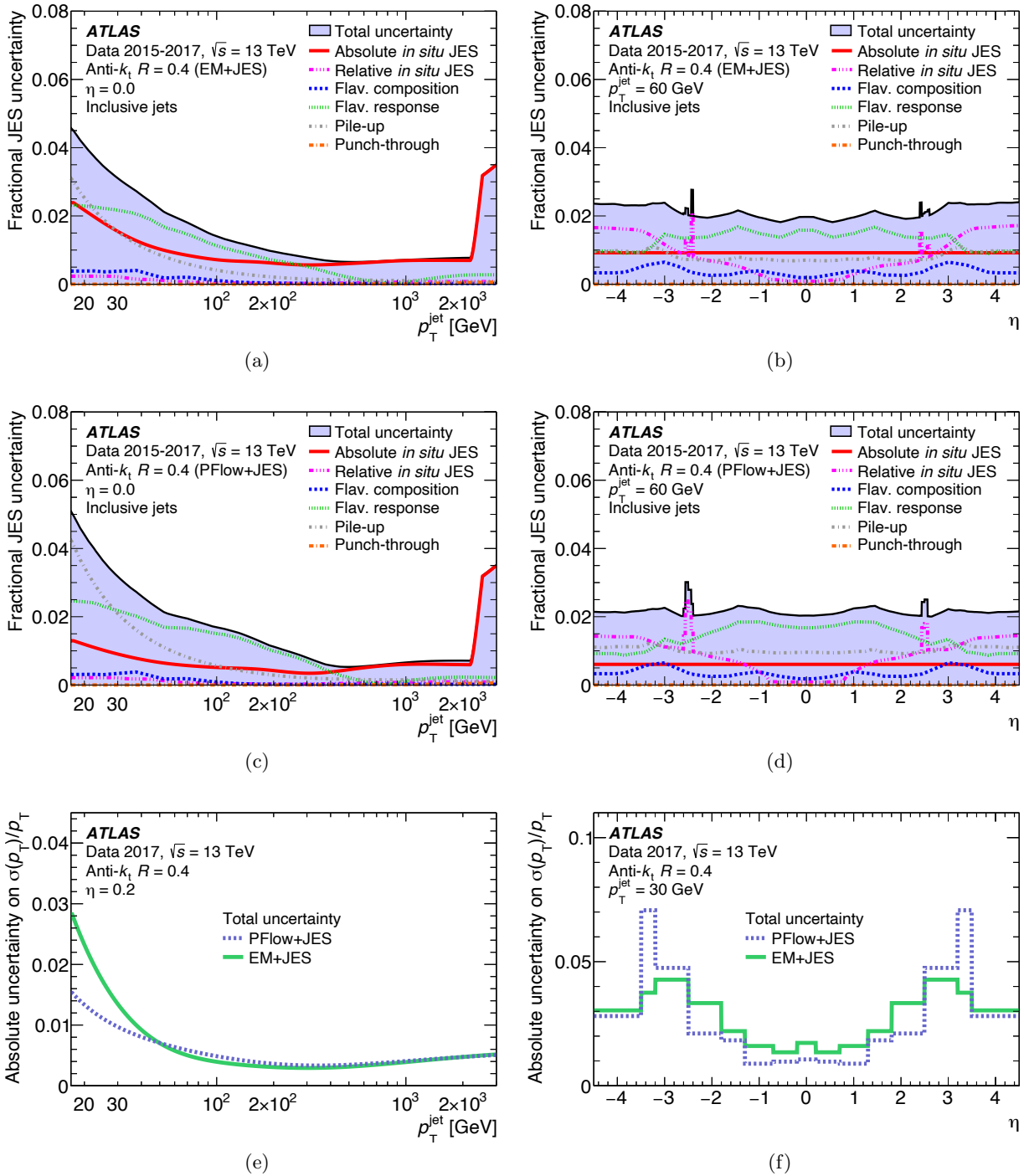
Figure 5.13: Plots of the jet energy scale ((a)-(d)) and jet energy resolution ((e)-(f)) uncertainty as a function of p_T and η for jets reconstructed with topological clustering at the electromagnetic scale and Particle Flow. Taken from Ref. [82].
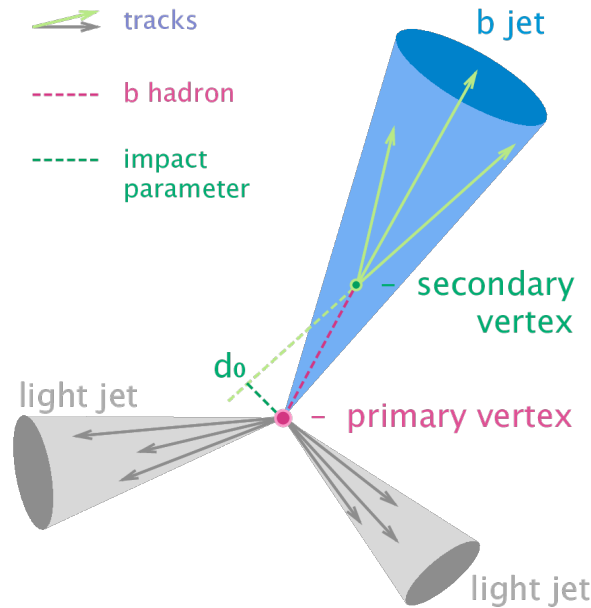
Figure 5.14: Schematic demonstrating the transverse impact parameter (d_0) and the detectable displaced or secondary vertex caused by the significant lifetime of the b-hadron compared with other decaying hadrons with short lifetimes. Taken from Ref. [93].

where *sign* is defined as positive if the track intersects the trajectory of the decaying hadron and negative otherwise [94]. Only these tracks are considered for secondary tracks [94]. Events with large positive values typically correspond to those with displaced charged-particle tracks [92]. In particular, b-jets generally have large positive values because of their genuine lifetime, whereas the lifetimes for light-flavour quark- and gluon-jets are short because of originating from interactions with detector material, daughters of V^{02} and heavy quarks formed in fragmentation (gluon-jets only). Additionally, Equations 5.9 and 5.10 can be combined to create the signed transverse (longitudinal) IP significance, calculated by

$$S_{d_0} = \frac{\mathrm{IP}_{d_0}}{\sigma_{d_0}} \ \text{ and } \ S_{z_0} = \frac{\mathrm{IP}_{z_0}}{\sigma_{z_0}}. \tag{5.11}$$

5.2.4   Missing Transverse Energy

If a weakly-interacting particle traverses the detectors and hence goes undetected, such as SM neutrinos and weakly-interacting BSM particles, the total transverse momentum of the system will be at an imbalance. The net momentum is zero in the transverse plane before the collision and therefore, will be *missing* transverse momentum after the collision, according to the principle of momentum conservation. The only SM particles that have a real contribution to this quantity are neutrinos, but for RPC SUSY models, such as those introduced in Chapter 3, large quantities of missing transverse momentum are expected from the LSP. The total missing transverse momentum (energy) is the negative sum of the transverse momenta of all fully calibrated and corrected physics objects for muons, electrons, τ-leptons, photons and jets [95]; calculated by

---

[2]V^0 refers to neutral particles such as Kaons and Sigma baryons.

$$E_{x,y}^{\text{miss}} = \sum_{\text{invisible}} \mathbf{p}_{\text{T}} = -\sum_{\text{visible}} \mathbf{p}_{\text{T}}$$

$$= \underbrace{-\sum_{\mu} \mathbf{p}_{\text{T}}^{\mu} - \sum_{e} \mathbf{p}_{\text{T}}^{e} - \sum_{\tau} \mathbf{p}_{\text{T}}^{\tau} - \sum_{\gamma} \mathbf{p}_{\text{T}}^{\gamma} - \sum_{j} \mathbf{p}_{\text{T}}^{\text{jet}}}_{\text{Hard term}} - \mathbf{p}_{\text{T}}^{\text{miss,soft}}, \qquad (5.12)$$

where the components of $E_{x,y}^{\text{miss}}$ are the same as those defined in Equation 5.1. Using these in Equation 5.12, quantities are defined for the magnitude of the $E_{\text{T}}^{\text{miss}}$ and its direction in the transverse plane i.e, the azimuthal angle (ϕ^{miss}) [95], calculated by

$$E_{\text{T}}^{\text{miss}} = \sqrt{(E_x^{\text{miss}})^2 + (E_y^{\text{miss}})^2} \ \text{ and } \ \phi^{\text{miss}} = \arctan\left(\frac{E_y^{\text{miss}}}{E_x^{\text{miss}}}\right). \qquad (5.13)$$

The contribution from the fully calibrated objects is referred to as the hard term, whereas the soft term, originates from energy contributions that are not assigned to any hard objects [95]. The preferred method to calculate the soft term is to use tracks exclusively reconstructed from the ID originating from the hard-scatter vertex and are not associated with any electron, τ-lepton, muon, or jet. This is referred to as the track-based soft term (TST) [96–98]. This improves the $E_{\text{T}}^{\text{miss}}$ scale[3] and resolution, particularly for final states with low hard-object multiplicity and is robust to pile-up [95].

Fluctuations in the measurement of the $E_{\text{T}}^{\text{miss}}$ originate from the limitations in the detector acceptance not allowing the reconstruction of the complete p_{T} flow from the hard interaction, the irreducible intrinsic signal fluctuations in the detector response, and from pile-up [95]. A systematic uncertainty related to the $E_{\text{T}}^{\text{miss}}$ scale and resolution can be determined from data-to-MC comparisons.

5.2.5 Leptons and Photons

The reconstruction of stable particles that primarily interact via the electromagnetic interaction such as electrons[4], muons and photons will be discussed in this section. It will begin with a discussion with regard to electrons and photons because of their highly-correlated nature before moving onto the reconstruction of muons. Leptons are used in Chapter 7 to provide a clean signature for a high-purity b-jet background for calibrating b-tagging algorithms. Photons are not an explicit final state object targeted in this thesis, but they can emulate electrons in the calorimeter and thus why their inclusion is in this section. Prompt leptons can be defined as those originating from the direct production of electrons, muons, or photons from the hard-scatter vertex or from the decays of heavy resonances such as the Higgs or vector bosons [99]. The aim is to reconstruct these, identify them with high efficiency, isolate them from misidentified hadrons,

---

[3]Also known as the $E_{\text{T}}^{\text{miss}}$ response, which is determined by the deviation of the observed $E_{\text{T}}^{\text{miss}}$ from the expectation value for a specific final state [95].

[4]The term electron usually indicates both electrons and positrons.

electrons from photon conversions and non-isolated electrons originating from heavy-flavour decays [99] and then, in the instance of electrons, suppress incorrect electron-charge identification.

Electrons and Photons

An electron can lose a significant amount of its energy to bremsstrahlung radiation when interacting with the detector medium, resulting in a strongly collimated shower of electrons and photons. This would result in a series of energy deposits in the EMcal called a cluster, which can be matched to multiple tracks originating from the primary electron [99]. This process uses Topoclusters and track reconstruction described in Sections 5.2.2 and 5.2.1 respectively. The results of the reconstruction procedure are classified as either an unambiguous electron candidate or an ambiguous photon conversion or electron. A schematic presenting an electron traversing the ID and EMcal can be seen in Figure 5.15.
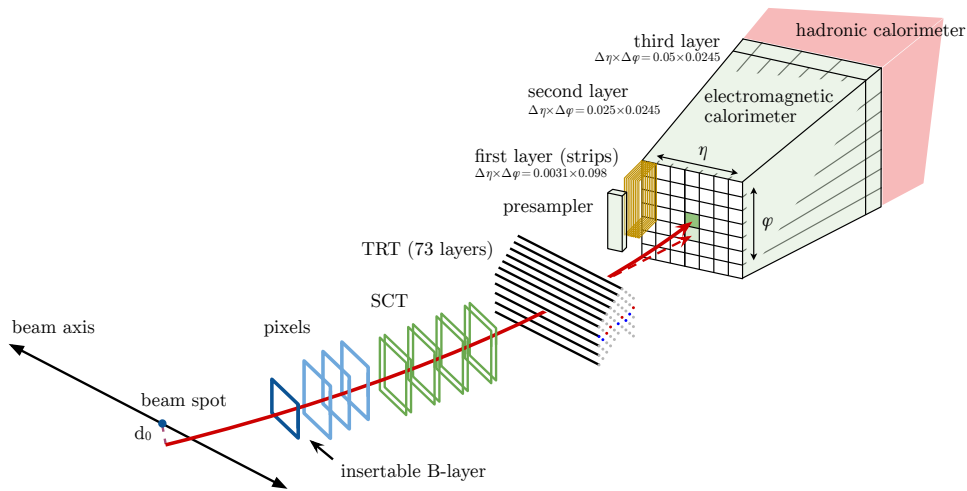
Figure 5.15: Schematic presenting an electron traversing the inner detector and decaying in the electromagnetic calorimeter. Taken from Ref. [99].

The identification procedure uses a likelihood-based discriminant to define five operating points (OP) to provide a prompt-electron selection efficiency (and corresponding background rejection) to be used by ATLAS physics analyses [99]. For example, the efficiency for identifying a prompt electron with $E_{\mathrm{T}} = 40$ GeV is $93\%, 88\%, 80\%$ for the Loose, Medium and Tight OPs respectively [99]. For background studies, a VeryLoose OP is also defined. Additionally, a LooseAndBLayer OP is also defined, that uses the same likelihood discriminant threshold as the Loose OP but adds a requirement of a hit in the IBL [99].

To isolate prompt electron and photon decays, the characteristic signature of little activity in EMcal and ID is used [99]. By using the ΔR variable (Equation 5.3) one can quantify the amount of activity in the vicinity of a candidate object. In combination with the use of topoclusters to measure the energy deposited by the electron core, surrounding cone radius (R_C), leakage and pile-up provides a simple and stable energy subtraction [99]. From this, three OPs are defined depending on the specific isolation criteria required by the physics analysis; Loose, Gradient and Fixed cut [99].

Photon reconstruction is analogous to that of electron reconstruction, using both the information from the tracking detectors and calorimeter [76].

Muons

Muons are reconstructed using a combination of information from several sub-detectors to reach almost 100% reconstruction efficiency and identification efficiency over an entire range of p_{T} with background contamination at the per-mille level [80]. The main signature exploited for muon identification in ATLAS is the minimum ionising particle (MIP) which is revealed in the detector as the presence of a track in the MS or characteristic energy in the calorimeters [80]. Therefore, information is primarily used from tracking in the ID and MS because energy can be lost in calorimeters, but this is also used as it can be adjusted for [80]. This results in five strategies and therefore, five representations of muons; combined (CB), inside-out combined (IO), MS extrapolated (ME), segment-tagged (ST) and calorimeter-tagged (CT) [80].

CB muons are reconstructed by matching MS tracks to ID tracks and performing a combined track fit based on hits in both detectors as well as the energy lost in the calorimeters [80]. IO muons are reconstructed using an inside-out algorithm where ID tracks are extrapolated into the MS and MS hits are searched for [80]. Since this type does not rely on an independent MS track, IO is typically more efficient in selection than CB [80]. ME muons are reconstructed if a MS track is not matched to an ID track, the MS track parameters are extrapolated to the beamline and a ME is defined [80]. The benefit of ME muon strategy is that they can be used to extend the acceptance outside of the ID pseudorapidity range ($|\eta| < 2.5$) and thus exploit the full MS coverage up to $|\eta| \leq 2.7$ [80]. ST muons are reconstructed from the extrapolation of an ID track into the MS with an angular matching requirement of at least one MS segment [80]. Finally, CT muons are reconstructed by extrapolating ID tracks through the calorimeters to search for energy deposits consistent with the MIP hypothesis [80].

After reconstruction, high-quality muon candidates used for physics analyses are selected from a series of requirements on the number of hits in the different tracking sub-detectors, on the track fit properties, and on variables that test the compatibility of the individual measurements in the two detector systems [80]. Similar to the electron identification, a series of operating points are defined, which determine the selection criteria and results in a specific muon identification efficiency and purity as well as the incorrect identification rate for the background. The rejected background is light hadrons, which in general result in lower-quality muon tracks because of the change in trajectory stemming from the in-flight decay within the detector [80]. Three standard OPs are defined in the order of increasing purity and decreasing efficiency; Loose, Medium and Tight [80]. Where Loose was optimised for reconstructing Higgs decays in a four-muon final state and Tight benefit analyses that are limited by background from non-prompt muons [80]. Two further operating points for unique scenarios are also defined; High-pT and Low-pT [80].

The method for defining muon isolation criteria is analogous to electron isolation. Most non-prompt muons are removed because of the lack of track association with muon tracks [80]. Since information is available from the tracking and calorimeter sub-detectors; isolation criteria are

defined for track-only, two Loose, two Tight and two criteria based upon a Boosted Decision Tree (BDT) selection [80].

5.2.6   Taus

The τ lepton, which has a lifetime of 290.3×10^{-15}s [7], is identified by its decay products. The largest contributing decay modes are; $\tau^- \rightarrow e^- \bar{\nu}_e \nu_\tau$ (17.8%), $\tau^- \rightarrow \mu^- \bar{\nu}_\mu \nu_\tau$ (17.4%), $\tau^- \rightarrow \pi^- (n\pi^0)\nu_\tau$ (48%) and $\tau^- \rightarrow \pi^- \pi^+ \pi^- (n\pi^0)\nu_\tau$ (15%) where $n = 0, 1, 2$ where the π^0 decays to a pair of photons ($\pi^0 \rightarrow \gamma\gamma$) [6, 7]. Hadronic decays of the τ lepton can therefore be identified as a jet originating from a τ, referred to as τ-jets, or one can treat them as unlabelled jets, which is the strategy in this thesis. Leptonic decays of the τ lepton are observed as electrons or muons plus missing energy, originating from the neutrino. [6, 27].

5.3   Conclusion

This chapter summarised both hardware and software components of the reconstruction of Standard Model particles in the ATLAS experiment. The chapter began by outlining the design and purpose of each sub-detector component and finished by discussing the computationally-reconstructed objects obtained from these detector signals. These *physics* objects form the basis for which a Standard Model measurement or search can be performed .This chapter focused in particular on the reconstruction and calibration of jets as well as jets originating from the decays of *b*-quarks because of their inclusion in the detector signature of the two final analysis chapters (8-9).

Chapter 6

Statistical Methods

In experimental particle physics, statistical inference is used to interpret data. The generic statistical goals of the ATLAS experiment are to measure properties of SM processes, search for new physics and, if required, set statistical limits on the probability of the model parameters of the new physics existing. Therefore, this chapter discusses the statistical methods used in the Chapters 7-9.

The statistical methods used in this thesis are frequentist statistical tests of compatibility between a dataset and a model predicted by Monte Carlo. One method is to quantify the level of agreement with a hypothesis and the observed data with a Pearson's χ^2 statistic. The other is by minimising the (profile) likelihood ratio for a null hypothesis (H_0) and alternate hypothesis (H_1) with a test statistic that depends on the statistics goal. This chapter will present the reader the mathematics that is used in each of these statistical methods.

6.1 Pearson's χ^2 Statistical Test

Often one wants to measure the compatibility between a null hypothesis with observed data without an explicit reference to an alternate hypothesis, in a statistical test called a *goodness-of-fit* test. This is done by defining a test statistic whose value reflects the level of agreement between the data and the hypothesis. One common goodness-of-fit test is the Pearson's χ^2 test [100]. For a series of N Poisson measurements, the sum of the squared deviations is calculated by

$$\chi^2 = \sum_{i=1}^{N} \frac{(n_i - \mu_i)^2}{\mu_i},$$

(6.1)

where n_i (μ_i) is the observed (expected) number of events in bin i distributed according to the null hypothesis [101]. Equation 6.1 represents the level of agreement between the two, therefore can be used for assessing goodness-of-fit and defines the Pearson's χ^2 test. If the expected values from hypothesis $\vec{\mu}$ are sufficiently large or equivalently can be considered as following a Gaussian

distribution, then the χ^2 statistic will follow a χ^2 probability density function with number of degrees of freedom (N_{dof}) [7];

$$f_{\chi^2}(\chi^2; N_{\text{dof}}) = \frac{1}{2^{N_{\text{dof}}}\Gamma(N_{\text{dof}}/2)}(\chi^2)^{\frac{N_{\text{dof}}}{2}-1}\exp\left[-\frac{\chi^2}{2}\right], \tag{6.2}$$

where the function $\Gamma(N_{\text{dof}}/2)$ is calculated from

$$\Gamma(x)\int_0^{+\infty}e^{-t}t^{x-1}dt. \tag{6.3}$$

The number of degrees of freedom can be defined as the number of measurements minus the number of fitted parameters [101]. The χ^2 distribution, for N_{dof}, has mean $E[\chi^2] = N_{\text{dof}}$ and variance $V[\chi^2] = 2N_{\text{dof}}$ [101]. The probability, under the null hypothesis, for a set of measurements giving a value of χ^2 or larger is then calculated by

$$p = \int_z^{+\infty} f_{\chi^2}(z, N_{\text{dof}})dz. \tag{6.4}$$

Because the $E[\chi^2] = N_{\text{dof}}$, one would expect the obtained values from an experiment to be $\chi^2 \sim N_{\text{dof}}$ and hence χ^2/N_{dof} is typically reported [7]. Both p-value and χ^2/N_{dof} values are used to assess the agreement between the observed data and null hypothesis and thus, either can be quoted. However, the χ^2 test only assesses the agreement in the shape, not the normalisation [100] and, in general, the p-value provides more information.

6.2   The Likelihood Equation

The other statistical method used for assessing the compatibility between data and two hypotheses is by performing a likelihood fit, that is, maximising the likelihood equation ($L(H)$). A likelihood function is obtained from the probability of the data (x) under assumption of the parameters ($\vec{\theta}$) of the hypothesis. For a set of N Poisson measurements, the likelihood equation is given by [102];

$$L(\mu, \vec{\theta}) = \prod_{i=1}^{N} \frac{(\mu s_i + b_i)^{n_i}}{n_i!}e^{-(\mu s_i + b_i)} \times \prod_{\theta \in \vec{\theta}} \text{Pois}(\theta_0 - \theta), \tag{6.5}$$

where n_i ($\mu s_i + b_i$) is number of observed (expected) events in the ith measurement bin. The yields are calculated by

$$s_i = s_{\text{tot}} \int_{\text{bin},i} f_s(x;\vec{\theta})dx \ \text{ and } \ b_i = b_{\text{tot}} \int_{\text{bin},i} f_b(x;\vec{\theta})dx, \tag{6.6}$$

where $f_a(x;\vec{\theta})$ are PDFs for variable x and $\vec{\theta}$ represent parameters to characterise the shapes of

the PDFs for signal and background. Both equations depend on the rate of the signal process μ, which is called the signal strength. The signal strength directly affects the signal yield, such that $\mu = 0$ corresponds to the background-only hypothesis (i.e no signal present) and $\mu = 1$ as a nominal signal hypothesis. In the general likelihood equation, this parameter is known as the parameter of interest (POI) because it is measured when performing the likelihood fit.

To reflect the imperfect nature of performing a measurement, Equation 6.5 is a function of nuisance parameters (NPs, $\vec{\theta}$), where NPs are included to parameterise systematic uncertainties. The final term in Equation 6.5 is additional Poisson (or Gaussian in large n limit) constraint term. For each systematic uncertainty, the evaluation of a NP is performed by assessing the expectation between the varied (typically $\theta_i = \pm 1$ standard deviation) and nominal values $\theta_i = 0$ [102]. Additionally, it is preferred that NPs are constrained by data. An example of this is the data-driven background estimation of the $t\bar{t}$ background in the analysis chapters 8-9.

6.3 Hypothesis Testing

Test statistics are used in searches for new physics to determine whether the null hypothesis (H_0, typically the Standard Model expectation) is favoured or excluded by an experimental observation [103]. Often, it is desirable for the observation to be tested with respect to the expectation derived using an alternate hypothesis (typically H_1), originating from a BSM physical process called the signal-plus-background hypothesis. Therefore, the test statistic used should incorporate both the currently established theory and the model where the new physics exists. This test statistic is chosen by the Neyman-Pearson lemma [104], which states that the (profile) likelihood ratio is the optimal discriminator when comparing the compatibility of the alternate and null hypotheses with the data. The equation for the profile likelihood ratio (PLR) for a specified hypothesised value of μ is calculated by

$$\lambda(\mu) = \frac{L(\mu, \hat{\hat{\theta}})}{L(\hat{\mu}, \hat{\theta})}, \tag{6.7}$$

where the numerator is the likelihood function when using the profiled values of θ that maximises the likelihood ($\hat{\hat{\theta}}$) for the specific μ and hence is named the conditional maximum likelihood estimator (MLE) of θ [100]. The denominator is the likelihood function maximised by the estimators $\hat{\mu}$ and $\hat{\theta}$. In practise, instead of maximising the PLR, it is more convenient to minimise the negative natural logarithm of the PLR and hence, the test statistic t_μ is defined as;

$$t_\mu = -2 \ln \lambda(\mu), \tag{6.8}$$

where higher (lower) values of t_μ indicate better (lesser) agreement between data and hypothesised μ and so, one can use this as a measure of the discrepancy between data and the hypothesis by calculating the p-value under the assumption of the signal strength μ;

$$p_\mu = \int_{t_{\mu,obs}}^{\infty} f(t_\mu|\mu)dt_\mu. \tag{6.9}$$

Wilks' theorem [105] states that, in the large n limit and when certain regularity conditions are satisfied [7], Equation 6.8 asymptotically approaches a χ^2 distribution with N_{dof} degrees of freedom equal to the number of components of $\vec{\theta}$.

In the scenario where the signal region has a large number of observed events, the asymptotic approximation of the test statistic PDF ($f(t_\mu|\mu)$) can be used [106]. In the scenario of low (< 10) data events in the signal region, the test statistic distributions are obtained by sampling the likelihood function with MC simulations, named pseudo-experiments or toys, which randomises the central values of all NPs and the expected yields are computed [8, 107]. To sample the test statistic distribution the frequentist calculator of the RooStats [107] package was used.

In particle physics one usually converts the p-value (p) into an equivalent significance (Z). Defined such that a Gaussian distributed variable found Z standard deviations above its mean has an upper-tail probability equal to p [106]. The relationship between the two is calculated by

$$Z = \Phi^{-1}(1-p), \tag{6.10}$$

which is in units of Gaussian standard deviations (σ) and Φ^{-1} is the inverse of the cumulative distribution of the standard Gaussian. The rejection of the background hypothesis at $Z = 5\sigma$ (p-value$=2.85 \times 10^{-7}$) can be claimed as a discovery. For the rejection of the signal hypothesis, a maximum p-value threshold of 0.05 (95% confidence level) or $Z = 1.64\sigma$ is set [106]. The particle physics community mutually accepts that a $Z = 3\sigma$ is sufficiently statistically significant to provide "evidence" for a discovery. The remaining one-sided significance values between $Z = 1\sigma$ and $Z = 5\sigma$ and how it converts to a p-value can be seen in Table 6.1.

Significance (Z)	p-value
1σ	0.15865
1.64σ (Exclude Test Hypothesis)	0.05
2σ	2.275×10^{-2}
3σ (Evidence of New Physics)	1.35×10^{-3}
4σ	3.15×10^{-5}
5σ (Discovery of New Physics)	2.85×10^{-7}

Table 6.1: One-sided Gaussian significance values and equivalent p-values.

6.3.1 Test Statistic for Discovery

If one wants to test the presence of a new signal that can only increase the number of events observed i.e $\mu > 0$, such as the signals searched for in this thesis, one can use the test statistic;

$$q_0 = \begin{cases} -2\ln\lambda(0), & \hat{\mu} \geq 0 \\ 0, & \hat{\mu} < 0 \end{cases}. \tag{6.11}$$

An example of the distribution for this test statistic can be seen in Figure 6.1(a).
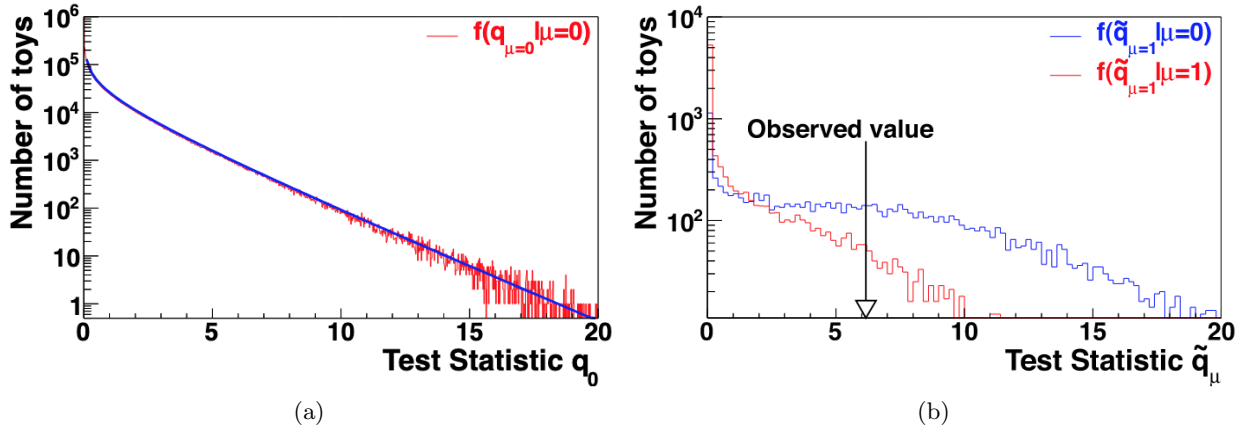
Figure 6.1: Examples of the distributions for (a) discovery and (b) exclusion test statistics used with the profile likelihood ratio. Taken from Ref. [108].

To quantify the level of disagreement between the data and the $\mu = 0$ hypothesis, the p-value is computed for the test statistic in Equation 6.9 using the observed value of q_0.

6.3.2 Test Statistic for Exclusion

If one wants to establish an upper limit on the strength parameter μ of a signal, the possibility of an increase in the mean event rate should be considered. This is factored into the test statistic [106] calculated by

$$q_\mu = \begin{cases} -2\ln\lambda(\mu), & \hat{\mu} \leq \mu \\ 0, & \hat{\mu} > \mu \end{cases}. \tag{6.12}$$

An example of the distribution for this test statistic can be seen in Figure 6.1(b). Note $q_\mu = 0$ for $\hat{\mu} > \mu$ because data would not represent less compatibility with μ than the value obtained by the data. The upper limit is obtained by testing μ against the alternate hypothesis (lower μ) and from the definition of the test statistic, one sees higher values representing greater incompatibility between data and hypothesised μ [106]. The p-value is again computed using the Equation 6.9 using the observed value of q_μ.

Note, switching discovery and exclusion test statistics is equivalent to inverting the roles of the two hypotheses. For the discovery (exclusion) test statistic, the null hypothesis is the background-only (signal-plus-background) model whereas alternate hypothesis is the signal-plus-background (background-only) model.

CL$_s$ Prescription

For a specified test statistic (q), the confidence in the signal-plus-background and background-only hypotheses is calculated by the probability that the test statistic is less than or equal to the value observed in the experiment (q_{obs}) [103];

$$\mathrm{CL}_{s+b} = p_{s+b}(q \leq q_{\mathrm{obs}}) = \int_{-\infty}^{q_{\mathrm{obs}}} \frac{dp_{s+b}}{dq} dq \text{ and}$$

$$\mathrm{CL}_b = p_b(q \leq q_{\mathrm{obs}}) = \int_{-\infty}^{q_{\mathrm{obs}}} \frac{dp_b}{dq} dq. \tag{6.13}$$

If the signal expectation is very small such that it's hard to distinguish between the signal-plus-background and background hypotheses, it is likely that the signal model will be considered excluded. The CL$_s$ value originates from normalising the confidence level for the signal-plus-background hypothesis to the confidence level for the background-only hypothesis;

$$\mathrm{CL}_s = \frac{\mathrm{CL}_{s+b}}{\mathrm{CL}_b}. \tag{6.14}$$

Because the denominator is always less than one, the criteria for exclusion is more stringent than setting a limit of $p_{s+b} \leq \alpha$, where α is a specific CL. Therefore, the CL$_s$ value is considered a conservative limit on the signal hypothesis [103]. Because of the normalisation of the two CLs, if one were to obtain two low p-values, a CL could still be obtained and hence the exclusion of a signal hypothesis is prevented due to low sensitivity.

The CL$_s$ value is not strictly a confidence level (CL), but the signal hypothesis will be considered excluded at the CL when $1 - \mathrm{CL}_s \leq \mathrm{CL}$ [103]. The threshold used in thesis is defined as 5%, i.e a 95% CL. This results in an approximation to the confidence level of the signal hypothesis (CL$_s$) one might have obtained if the experiment had been performed in the complete absence of background [103].

6.4   Likelihood Fits in ATLAS

To perform the likelihood fits introduced in the Section 6.2, the `HistFitter` [102] framework is used. The workflow of the framework for a typical ATLAS SUSY search methodology can be seen in Figure 6.2.

For N regions of phase-space or henceforth referred to as *bins*, the normalisation is measured for the pth background process in a p-enriched bin is called a p control region (CR) by performing a likelihood fit to the predicted background events. For the pth background CR processes, a transfer factor (TF) is calculated, which allows the background estimates in the CRs to be converted into background estimates in the signal-rich regions of phase-space, known as signal
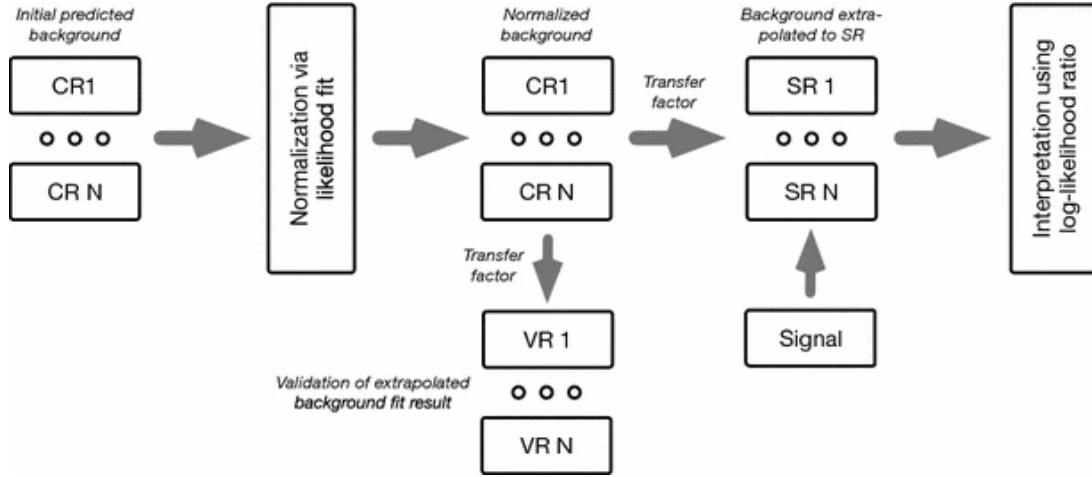
Figure 6.2: Schematic presenting the workflow of the `HistFitter` [102] framework used to perform likelihood fits.

regions (SRs) by the Equation [102];

$$N_p(\text{SR,est.}) = N_p(\text{CR,obs.}) \times \left[\frac{\text{MC}_p(\text{SR,raw.})}{\text{MC}_p(\text{CR,raw.})} \right] = N_p(\text{CR,obs.}) \times \text{TF}_p$$

$$= \left[\frac{N_p(\text{CR,obs.})}{\text{MC}_p(\text{CR,raw.})} \right] \times \text{MC}_p(\text{SR,raw.}) = \mu_p \times \text{MC}_p(\text{SR,raw.}).$$

(6.15)

For the pth background process, $N_p(\text{SR,est.})$ is the estimate for the background in the SR, $N_p(\text{CR,obs.})$ is the observed number of data events in the CR, $\text{MC}_p(\text{SR,raw.})$ ($\text{MC}_p(\text{CR,raw.})$) are the Monte Carlo SR (CR) unnormalised background estimates. The term in the square brackets of the first line of Eq. 6.15 is the transfer factor (TF_p) that quantifies the estimate from the CR to the SR. The second line of Equation 6.15 presents the actual normalisation factor in the square brackets (μ_p), which is a ratio of the observed data events to Monte Carlo in the CR which is obtained by normalising with a likelihood fit, the Monte Carlo to the data.

An important consequence of using transfer factors to estimate background processes is the cancellation of systematic uncertainties because of the ratio of MC estimates. The more kinematically similar the CR is to the SR, the greater the cancellation, however, there is a trade-off related to the statistical uncertainty in the normalisation factor becoming greater with fewer data events.

For simplicity, the previous discussions have assumed physical scenarios that are a single-bin (SB) approach, that is, an inclusive area of phase-space defined by selection thresholds on kinematic observables. However, one can increase the statistical performance of an analysis by including multiple signal region bins (MB) in a combined likelihood fit. One way to do this would be to create SR bins defined for a series of thresholds on an observable that is sensitive to a signal - examples are presented in Section 8.3.1. The combination of bins increases the statistical sensitivity to the signal because of the difference in shape between the signal and Standard Model

background, which otherwise cannot be exploited by an inclusive SB approach.

The next section will present the three likelihood fits performed by an ATLAS SUSY search.

Background-only fit - The background-only fit does not actually use a test statistic with the profile-likelihood ratio. Instead, only control regions are used in the likelihood equation in the absence of signal processes (therefore $\mu = 0$ in Equation 6.5) to obtain the background normalisation parameters, μ_p, resulting in a prediction for the post-fit background estimate which is extrapolated to the validation and signal regions. Validation regions (VRs) are designed to be kinematically close to SRs but orthogonal so that before unblinding an analysis in the SR, one can validate the background estimation methods in a region similar to the SR with real data. Consequently, this fit type is primarily used for validating the background estimation methods in the signal and validation regions. The quantity used to do this is referred to as a *pull*, which is defined by

$$\text{pull} = \frac{n_i - v_i}{\sigma_{\text{tot}}} = \frac{n_i - v_i}{\sigma_{(\text{stat. exp.})} \otimes \sigma_{(\text{syst. exp.})}}, \tag{6.16}$$

where the systematic uncertainty in the background prediction ($\sigma_{(\text{syst. exp.})}$) is added in quadrature to the statistical Poisson uncertainty in the expected number of background events ($\sigma_{(\text{stat. exp.})}$). The statistical Poisson uncertainty in the data is not accounted for in Equation 6.16 because the pull is a standardised Gaussian measure of observing data n_i, given a background distribution of $G(v_i, \sigma_{\text{tot}}^2)$. On average, if the pulls in validation regions are negative (positive), the data is overestimated (underestimated) and the background model needs to be corrected. Therefore, any pulls around zero ($< 1\sigma$) often implies a sufficient approach to the estimation of SM backgrounds. No specific signal models are used in this fit and so, this method is completely model-independent. Searches for SUSY in ATLAS use this approach to attempt to observe excesses beyond the Standard Model prediction.

The two remaining likelihood fit strategies performed by ATLAS SUSY searches are aimed towards the discovery of new physics ("discovery fit") and setting statistical limits on the presence of new physics existing ("exclusion fit"). After applying the transfer factors for the background estimation in the signal or validation regions, the results can be interpreted using the profile log-likelihood ratio with the corresponding test statistics.

Discovery fit - This strategy serves two-fold; it uses the test statistic of Equation 6.11 to measure the disagreement of data with the background-only hypothesis. Signal events are neglected in the control region and thus are only present in the signal region. The nominal strategy used by ATLAS to perform this likelihood fit uses a *dummy signal* i.e, an arbitrary signal which is chosen to have an event yield of one event in the SR, and the normalisation is allowed to float so that the background expectation plus signal is consistent with the data. The background prediction is considered conservative because any signal contribution in the control

regions is attributed to the background and thus yields a possible overestimate of the background in the signal regions.

The second purpose of this fit type is designed for the reinterpretation of the analysis regions to allow for others with a different BSM signal process to determine whether that model is excluded. This is performed by providing the 95% confidence upper limits on the number of observed and expected signal events (S_{obs}^{95} and S_{exp}^{95}), so that if any model were to predict more events in the SR, it would be excluded.

Exclusion fit   - In the event of performing the background-only or the discovery fit and no statistically significant excesses above the Standard Model expectation were observed, this fit strategy is performed. The primary purpose is to set confidence limits on the parameters of a signal model of interest, thereby quantifying whether a model can be considered statistically excluded or not. It should be performed regardless of whether an excess was observed or not in the background-only fit because it can determine whether the excess is consistent with the optimised signal.

To perform this fit, the expected number of signal events corresponding to the nominal signal hypothesis (s), are included in addition to an additional parameter, μ_s, which varies the normalisation of the signal strength and is assumed to be positive. The nuisance parameters are constrained further because of the simultaneous fit performed to both the CRs and SRs. The test statistic in Equation. 6.12 is used to perform this fit, where a p-value can be calculated using the CL_s prescription.

6.5   Conclusion

This chapter presented two statistical inference techniques, the χ^2 goodness-of-fit test and the use of the likelihood equation for hypothesis testing. For the latter, several test statistics were presented for the two main statistical goals of this thesis; the discovery of new physics and the purpose of setting statistical limits on BSM model parameters. The chapter concludes by discussing the three likelihood fit strategies used in ATLAS SUSY searches, such as those in Chapters 8-9.

Part IV

Analysis

Chapter 7

Calibration of *b*-tagging Algorithms

Jets originating from *b*-hadron decays (*b*-jets) are a common component in the final-state detector signature of many measurements and searches at the LHC because of Higgs, vector boson and top quark decays. In Section 5.2.3, the concept of identifying and classifying *b*-jets was introduced. In this chapter, the measurement of the efficiency of these algorithms that perform the *b*-jet identification is presented. The calibration is then used in physics analyses such as those in Chapters 8-9.

7.1   *b*-tagging Algorithms

The approach to *b*-tagging algorithms used by ATLAS utilises a two-level strategy where the first level targets the underlying event kinematics, primarily based on the impact parameter (IP) and secondary vertices (SV), using log-likelihood ratio discriminants. The second level combines all the outputs of the first level into a single multivariate discriminant algorithm to maximise the identification of *b*-jets.

There are two low-level algorithms used by ATLAS which are founded on the kinematics related to the impact parameter and they are; IP2D and IP3D [109]. IP2D uses the signed transverse IP significance (Equation 5.11) of tracks to construct a discriminating variable [92]. IP3D also uses the signed transverse IP significance, in addition to the longitudinal IP significance and therefore utilises a two-dimensional template to account for their correlation [92]. To enhance the discrimination power, the templates are separated into exclusive categories that depend on the hit pattern of a specific track, termed the track grade [109]. In both algorithms, probability density functions (PDFs) are derived from the histogram templates using their respective variable(s). The PDFs allow the *b*-, *c*- and *l*-jet probabilities to be calculated on a per-track basis [92] - where *b*-, *c*- and *l*-jets are jets tagged as beauty, charm and those arriving from quarks or gluons termed light flavour jets. The outputted discriminating variable from each algorithm is a log-likelihood ratio (LLR) defined, for each jet-flavour hypothesis, as the sum of per-track contributions $\sum_i^N \log\left(\frac{p_b}{p_u}\right)$, where N is the number of tracks and p_b, p_c and p_u are probability of being a *b*-jet, *c*-jet and light-jet [92]. Additional outputs based on the LLR are created to distinguish *b*-jets from *c*-jets

and *c*-jets from light-jets [92]. It is these outputs that are used as input to the *high*-level taggers.

Compared to the previously published measurement of the efficiency of *b*-tagging algorithms for ATLAS data collection periods 2015+2016+2017 [92], a further low-level track-based NN algorithm has been introduced. IP3D assumes that the flavour probabilities of different tracks in a jet are independent and studies [109] have shown the use of a Recurrent Neural Network (RNN) track-based algorithm can overcome the limiting ability of IP3D and can be used to sequentially learn the track dependency in a jet. For each selected track, the transverse (longitudinal) IP, the fraction of p_T carried by the track relative to the jet p_T (p_T^{frac}), the angular distance between the track and the jet axis ($\Delta R(\text{track}, \text{jet})$) and the track grade is passed to a NN cell where again the *b*-, *c*-, *l*- and τ-jet probabilities are outputted for use in the high-level taggers [109].

ATLAS uses two low-level algorithms to exploit behaviour related to secondary vertices, which are SV1 [110] and JETFITTER [111]. The former aims to reconstruct a single displaced SV in a jet, while the latter aims to reconstruct the full *b*-hadron decay by exploiting the topological structure of the weak *b*- and *c*-hadron decays inside a jet [92].

SV1 starts by identifying possible two-track vertices associated with the jet whilst rejecting tracks compatible with long-lived particle decays, photon conversions, or hadronic interactions with the detector material [92]. Then, running iteratively on all tracks, tries to fit one SV from the reduced list of two-track vertices. For each iteration, a Pearson's χ^2 test is performed to evaluate the track-to-vertex association [92]. The track with the largest χ^2 is removed from the fit and this is repeated until a sufficient χ^2 is obtained in addition to requiring the vertex invariant mass being less than 6 GeV [92]. The outputs of this algorithm are the vertex mass, energy fraction and number of two-track vertices, all of which are used in the high-level taggers.

JETFITTER uses a modified Kalman Filter [112] to find a common line in which the primary *b*- and *c*-vertices lie. This is achieved by approximating the *b*-hadron flight path from the intercepts of the particle tracks with the jet axis and vertex positions [92, 109]. The outputs of this algorithm are the track multiplicity at the JETFITTER vertex, the invariant mass of tracks of these vertices, energy fraction, average 3D decay length significance, all of which enter the high-level taggers.

The second stage of maximising the *b*-tagging performance in ATLAS is to combine the outputs from the low-level taggers into a single multivariate algorithm. Two high-level algorithms relevant to this thesis are MV2 [109] and DL1R [109] where the first of those uses a boosted decision tree (BDT) and the latter is a deep feed-forward NN [92]. The inputs to each of these high-level multivariate algorithms can be seen in Table B.3 in Appendix B.1.

MV2 is trained using a BDT with the ROOT Toolkit for Multivariate Data Analysis (TMVA) [113] software on a simulated background dataset. The dataset is composed of $t\bar{t}$ production and Z' decays for increased sensitivity to low- and high-p_T jets, respectively. To avoid the differences between jet flavours, in the p_T and $|\eta|$ distributions, being used for discrimination by the BDT, *b*-jets and *c*-jets are weighted to match light-jets [92]. The BDT hyperparameters, that can be seen in Table B.1 in Appendix B.1, are optimised to provide the greatest separation between the signal (*b*-jets) and the background (*c*-jets and light-jets) [92]. The distribution of the output

discriminant from MV2 can be seen in Figure 7.1(a).

(a)   (b)
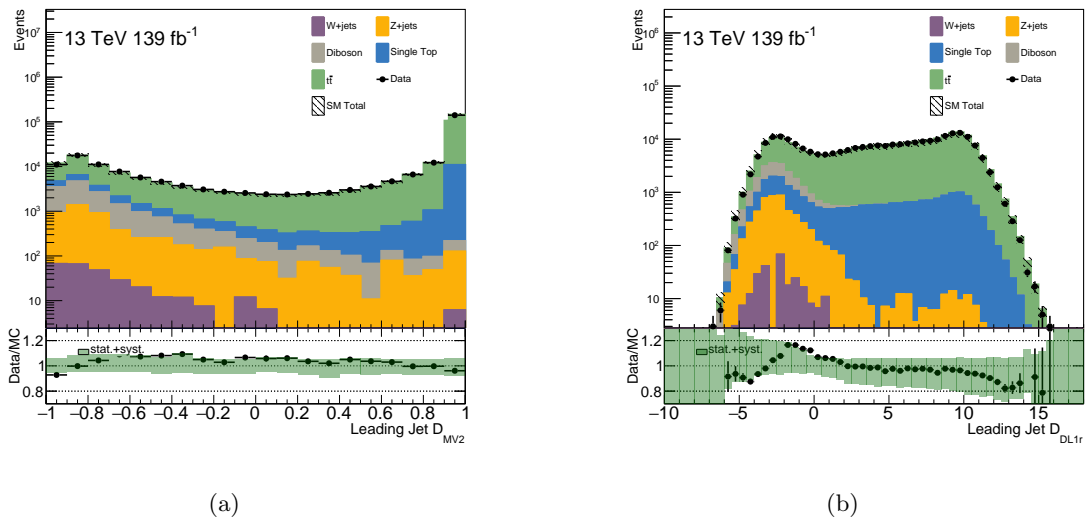
Figure 7.1: The distribution of the output discriminant for the *b*-tagging algorithms (a) MV2 and (b) DL1R. The hashed green background on the SM total is the sum in quadrature of the difference between the up (down) and nominal background of each systematic uncertainty and the straight black lines represent the statistical uncertainty. (a) was produced using a superseded iteration of ATLAS software in addition to not using the same systematic configuration included in Section 7.5.

The DL1R neural network is trained using Keras [114] with the Theano [115] backend and the Adam optimiser [92, 116] and again, a reweighting of the p_T and $|\eta|$ distributions for *b*-jets and *c*-jets is performed. The hyperparameters of the network, that can be seen in Table B.2 in Appendix B.1, are optimised for maximising *b*-tagging performance [92]. The output discriminant for the DL1R algorithm is calculated by

$$D_{\mathrm{DL1R}} = \ln\left(\frac{p_b}{f_c \cdot p_c + (1 - f_c) \cdot p_l}\right), \tag{7.1}$$

where p_x for $x = b, c, l$ is the probability of being a *b*-jet, *c*-jet and light-jet, respectively, and f_c is the *c*-jet fraction in the background, which is chosen by the analyser and typically has a value of 8% [92]. Similarly, the distribution of the output discriminant, given these parameters, can be seen in Figure 7.1(b).

The evaluation of a *b*-tagging algorithm is performed using single-cut operating points (OP), which are defined by a selection threshold of the algorithm discriminant, resulting in a specific *b*-tagging efficiency for *b*-jets and rejection rates for *c*-, $l-$, and $\tau-$jets [92]. An alternate approach is to divide the algorithm discriminant into five pseudo-continuous (PC) bins [92]. These five bins arise from the four standard *b*-tagging efficiency operating points; 85%, 77%, 70% and 60% and the highest (lowest) is bounded by 100% (0%). Then, the *b*-tagging efficiency can be calculated for the entire range of the algorithm discriminant.

7.2   Object Definitions

The next section will detail the definitions of the reconstructed physics objects used in this calibration.

Trigger   - Event recording is triggered by a logical OR between the single lepton triggers for electrons and muons, such that the event is recorded if either the electron or the muon triggers have been activated.

Electrons   - Electrons are reconstructed and required to pass the electron Fixed-cut Tight identification and isolation criteria. Candidates must fall into the fiducial area of the EM calorimeter ($|\eta| < 1.37$ or $1.52 < |\eta| < 2.47$) and have $p_\mathrm{T} > 28$ GeV to avoid large trigger efficiency uncertainties in the turn-on region of the lowest-p_T unprescaled trigger. The isolation criteria removes electrons for which there are significant energy deposits, either in the calorimeter or from high-momentum tracks.

Scale factors (SFs) of the order of unity derived in $Z \to \ell\ell$ events are applied to account for differences in reconstruction, trigger, identification and isolation efficiencies between data and simulated events. Electron calorimeter energies are calibrated to the true electron energy in simulation, and residual discrepancies between the energy scale and resolution in the simulation with respect to the data are corrected using the $Z \to \ell\ell$ mass peak.

Muons   - Muons must pass the muon Tight isolation and identification criteria in addition to being central ($|\eta| < 2.5$) and in the efficient region of the trigger ($p_\mathrm{T} > 28$ GeV) [80]. In the instance of a poorly reconstructed muon, i.e., a muon reconstructed from high hit multiplicities in the muon spectrometer because of highly energetic punch-through jets or from badly measured inner detector tracks in jets wrongly matched to muon spectrometer segments, the whole event is vetoed. Additional corrections to the muon p_T are also applied.

Jets   - Jets were reconstructed using the ParticleFlow (PFlow) algorithm. Under the PFlow Jet reconstruction scheme, calorimeter clusters are associated with reconstructed tracks and removed if their impact parameters are not compatible with tracks originating from the event primary vertex. The final energy of these PFlow objects is then determined through a combination of the measured cluster (calibrated at the EM scale) and track energy, parameterised as a function of the track p_T to take the maximum benefit from the better track p_T resolution at low energies.

PFlow objects are then clustered into jets using the anti-k_t algorithm with $R = 0.4$ [91, 117]. The transverse momenta of the jets were further corrected to the corresponding particle-level jet p_T [118]. After these calibrations, all jets in the event ($p_\mathrm{T} > 20$ GeV, $|\eta| < 4.5$) must satisfy the LooseBad jet cleaning criteria [119]. Because b-tagging is based on the tracks associated with the jets, jets with $p_\mathrm{T} < 20$ GeV or $|\eta| > 2.5$ are removed. To reduce the number of jets with large energy fractions from pileup collision vertices, the Medium operating point of

the JetVertexTagger (JVT) algorithm is used [120]. This OP determines PFlow jets with p_T ≤ 60 GeV and $|\eta| < 2.4$ as pileup if the JVT discriminator is < 0.5.

Resolving Overlapping Objects   - In the instance of candidate objects overlapping with each other, all but one object must be removed from the event. The distance metric used to define overlapping objects is $\Delta R = \sqrt{\Delta\phi^2 + \Delta y^2}$. To prevent double-counting of electron energy deposits as jets, jets within $\Delta R < 0.2$ of a reconstructed electron are removed. If the nearest jet surviving the selection is within $\Delta R < 0.4$ of the electron, the electron is discarded, to ensure it is cleanly separated from nearby jet activity. To reduce the background from muons from heavy flavour decays inside jets, muons were required to be separated by $\Delta R > 0.4$ from the nearest jet, removing the muon if the jet had at least three associated tracks, and removing the jet otherwise. This avoids the inefficiency for high-energy muons to undergo significant energy losses in the calorimeter.

Jet Truth Labeling   - Truth-level information is used to classify jets, which is necessary in this calibration technique to correctly study the flavour fraction composition in simulated events. Four different classifications are used; b-, c-, l- or $\tau-$jets. The labeling procedure for a jet is performed in three steps:

1. Select all the B-hadrons, D-hadrons and τ-leptons with $p_\mathrm{T} > 5$ GeV.

2. For each hadron or lepton, find all the jets satisfying $\Delta R(\mathrm{jet}, \mathrm{hadron}) < 0.3$. If two or more jets are matched to the hadron or lepton, keep the closest.

3. For each jet, remove the association to any hadron that is a daughter of another hadron attached to the jet.

After this algorithm is applied, jets associated with B-hadrons (D-hadrons, τ-lepton) are called b-jets (c-jets, τ-jet). If they are not associated with any previous truth particle, they are deemed light-jets.

7.3   Event Selection and Categorisation

To measure the identification performance of b-tagging algorithms in Monte Carlo simulation, a high-purity simulated dataset of b-jets is required. For one of several reasons, this motivates the targeting of the $t\bar{t}$ production detector signature. The leptonic decay of the W boson in each top quark decay[1] provides a clean detector signature, where exclusively two b-jets can be identified in addition to two well-identified leptons.

Fake events occur typically when only one W boson decays leptonically and the remaining *fake* lepton arises from non-prompt leptons produced from b- and c-hadron decays, electrons arising from photon conversions, jets misidentified as electrons and muons produced from in-flight pion

---

[1] This is referred to as the deleptonic decay of $t\bar{t}$.

or kaon decays [92]. The number of events with two fake leptons is negligible. The remaining SM processes are sub-dominant for this detector signature, however, it is useful to classify them further into those with two real prompt leptons from vector boson decays and those where at least one reconstructed lepton is fake [92]. The former consists of single top production in association with a W boson (Wt), the production of two vector bosons, referred to as *diboson* (WW, WZ, ZZ), where at least two leptons are produced in electroweak decays and Z+jets with Z decaying into leptons [92]. The latter, which is sub-dominant compared to the former, is mainly composed of t- and s-channel single top production and W+jets with the W boson decaying leptonically.

Plots of the Feynman diagrams for the contributing Standard Model (SM) background processes used in this measurement and in the analysis Chapters 8-9 can be found in Figures 7.2-7.5. The corresponding table of the MC generators used for the SM background processes used in this measurement can be found in Table 7.1.
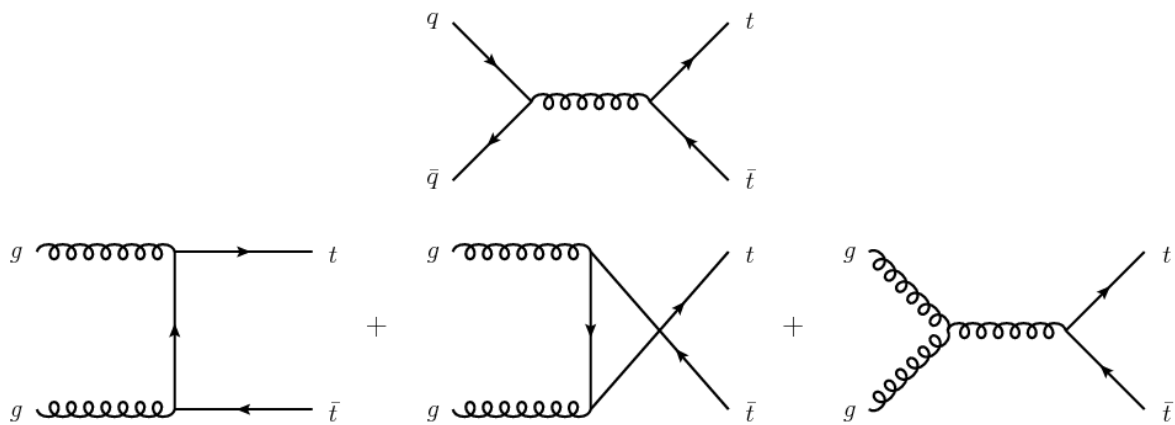
Figure 7.2: The dominant pair-production mechanisms of the top quark; gluon-gluon fusion and quark-antiquark annhilation. Taken from Ref. [121].
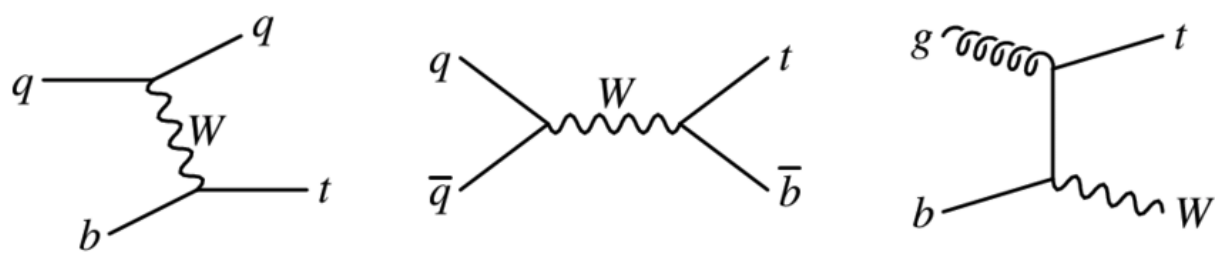
Figure 7.3: Dominant electroweak single top production mechanisms at hadron colliders. Taken from Ref. [122].

The event selection is restricted further to reduce backgrounds from non-prompt decays. To reduce backgrounds with less than two prompt leptons, the two leptons must have opposite charges. Backgrounds originating from Z boson decays are reduced by requiring one lepton to be an electron and the other a muon [92]. The remaining Z boson contribution, from $Z \to \tau\tau$, is reduced by selecting on the invariant mass of the lepton pair; $m_{e\mu} \geq 50$ GeV. The exclusive two jet selection reduces $t\bar{t}$ backgrounds where the jets originate from ISR or FSR. For the remainder
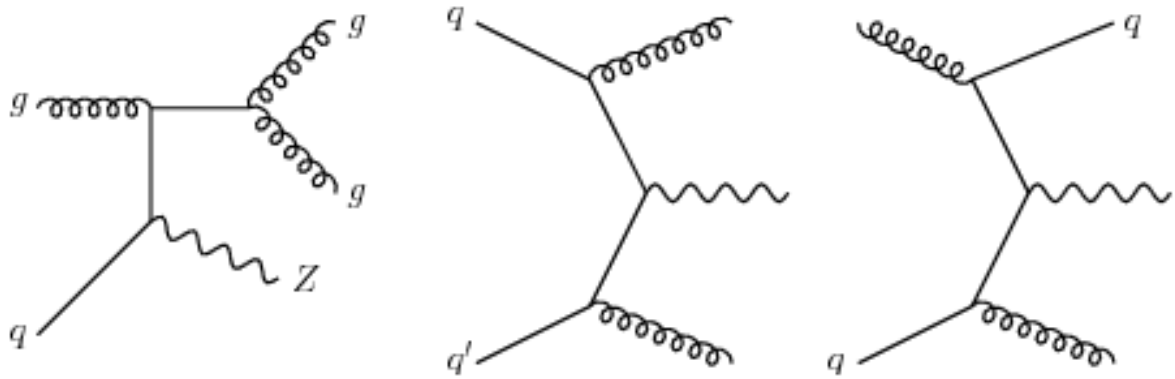
Figure 7.4: Production mechanisms for Z boson plus two jet events. Taken from Ref. [123].
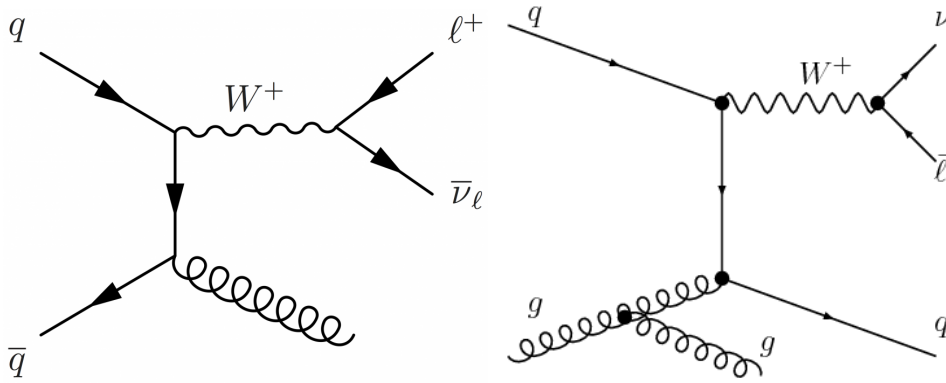
Figure 7.5: Left (right) - production mechanism for W boson plus one (two) jet events. Taken from Ref. [124].

Process	Generator + fragmentation/hadronisation	Tune	PDF set	Cross section order
$t\bar{t}$	Powheg-Boxv2 + Pythia-8.230	A14	NNPDF3.0	NNLO+NNLL [125]
Single top $Wt + s/t$-channel (DR [126] [127])	Powheg-Boxv2 + Pythia-8.230	A14	NNPDF3.0	NNLO [125]
Diboson WW, WZ, ZZ	Sherpa-2.2.1(2) 1(2) for 1(0) hadronic V decay	Default	NNPDF3.0	NLO [128, 129]
W/Z+jets	Sherpa-2.2.1	Default	NNPDF3.0	NNLO [130]
Alternate Generators				
$t\bar{t}$	Powheg-Boxv2 + Herwig-7.0.4	H7-UE-MMHT	NNPDF3.0	NNLO+NNLL [125]
Single top $Wt + s/t$-channel	Powheg-Boxv2 + Herwig-7.0.4	H7-UE-MMHT	NNPDF3.0	NNLO [125]
Single top $Wt + s/t$-channel (DS [126] [127])	Powheg-Boxv2 + Pythia-8.230	A14	NNPDF3.0	NNLO [125]

Table 7.1: List of nominal and alternate generators used for the different processes. Information is provided for the tuned set of underlying event and hadronisation parameters (tune), the PDF sets and the perturbative QCD highest-order accuracy used for the normalisation of the different simulation processes. For the single top simulation, DR (DS) abbreviations are the diagram removal (subtraction) schemes.

of this chapter, the simulated dataset will be discussed in terms of the two jet flavours (b, c, l) instead of the SM background contribution because the focus of this study is to measure the b-tagging efficiency. This classification for the events will therefore be described as either two b-jets (bb), two non-b-jets (ll), b-jet plus non-b-jet (bl) where b-jet p_T > non-b-jet p_T and lb for the reverse scenario to bl.

Large $t\bar{t}$ modelling uncertainties dominated the first ATLAS b-tagging calibration publication [131]. The subsequent ATLAS b-tagging calibration publication [92] introduced signal (SR) and control regions (CR) to constrain the flavour fractions in the extraction of the b-jet efficiency and resulted in a dramatic reduction of these uncertainties. Therefore, this strategy is also used in this measurement. The regions are enriched for each jet flavour combination by pairing each of the two leptons with a jet that determines whether they originated from the same top quark decay [92]. The pairing is achieved by

$$\min(m_{j_1 l_i}^2 + m_{j_2 l_j}^2), \tag{7.2}$$

where $j_{1(2)}$ is the (sub-)leading p_T jet and $l_{i(j)}$ are the two leptons and $m_{j_1 l_i}(m_{j_2 l_j})$ is the invariant mass of the system for the jet and associated lepton [92]. Plots of the distribution for the leading and sub-leading jets can be seen in Figure 7.6.

(a)   (b)
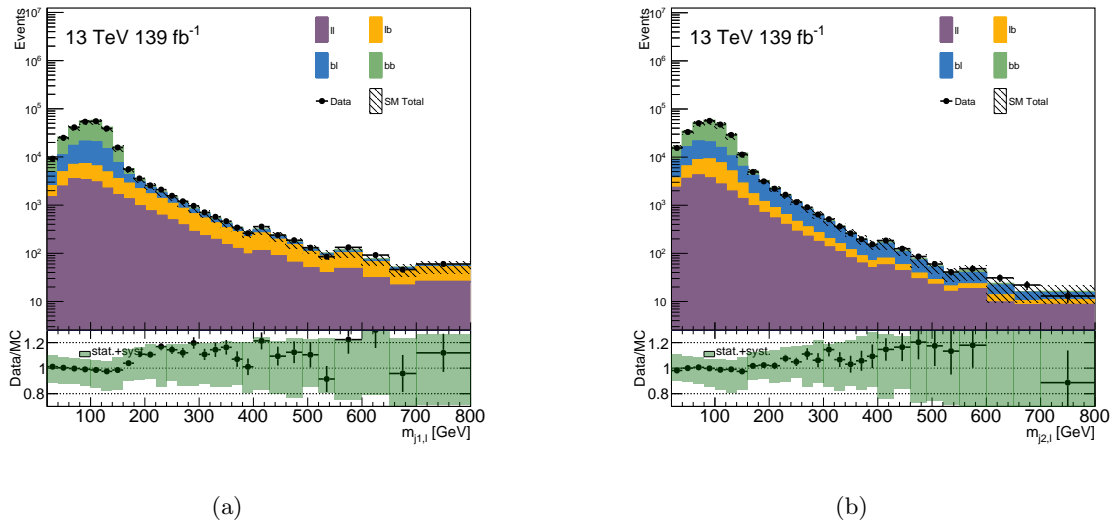
Figure 7.6: Distribution of the invariant mass of the leading and sub-leading jet and lepton pair as a function of the jet flavour. The hashed green background on the SM total is the sum in quadrature of the difference between the up (down) and nominal background of each systematic uncertainty and the straight black lines represent the statistical uncertainty.

In Figure 7.6(a), a discrepancy in the data-to-MC agreement is observed between the 160-380 GeV bins, albeit is consistent with unity when considering the total uncertainty. The discrepancy appears highly correlated with the top quark mass due to observing an agreement between the data and simulation within statistical uncertainties up to 175 GeV. Proceeding this, a sharp increase in the disagreement is observed to be 1.1-1.2 for the 175-380 GeV bins. This could

suggest the cause of the discrepancy originates from the inability of the dominant background generator (dileptonic $t\bar{t}$) to correctly replicate the number of events in data where an additional jet is produced.

If the pairs of objects are from the same particle decay, they are expected to have similar mass and therefore the quantity would be minimised [92]. The quantity penalises events where one lepton-jet pair has an asymmetrically high mass and penalises combinations with two very high invariant masses, which are unlikely to originate from top quark decays [92]. An additional requirement on $m_{j1(2)l} \geq 20$ GeV was used to remove soft nearby jets and leptons, which are not described well by MC [92].

In terms of the final MC composition, $\sim 86\%$ of the events originate from dileptonic $t\bar{t}$ production, of which $\sim 65\%$ are *bb*. The next dominant SM background is Wt associated single top production with 8%, $\sim 28\%$ of which are *bb*. Diboson and Z+jets are approximately 4 and 2% respectively, 86 and 82% of which are *ll* respectively. W+jets production is negligible ($< 0.02\%$). In terms of jet flavours, the final *bb* composition of the total MC is $\sim 60\%$. The non *b*-jet background is dominated by light-jets and the remainder is *c*-jets. The predicted fraction of τ-jets is negligible. Therefore, the dominant source of non-*b*-jet contributions originates from $t\bar{t}$ *bl* or *lb* events i.e, the dileptonic $t\bar{t}$ with a high-p_T light-jet from ISR or FSR [92]. The distributions of the leading jet p_T and η for the MC background surviving the selection criteria can be seen in Figures 7.7.

(a)	(b)
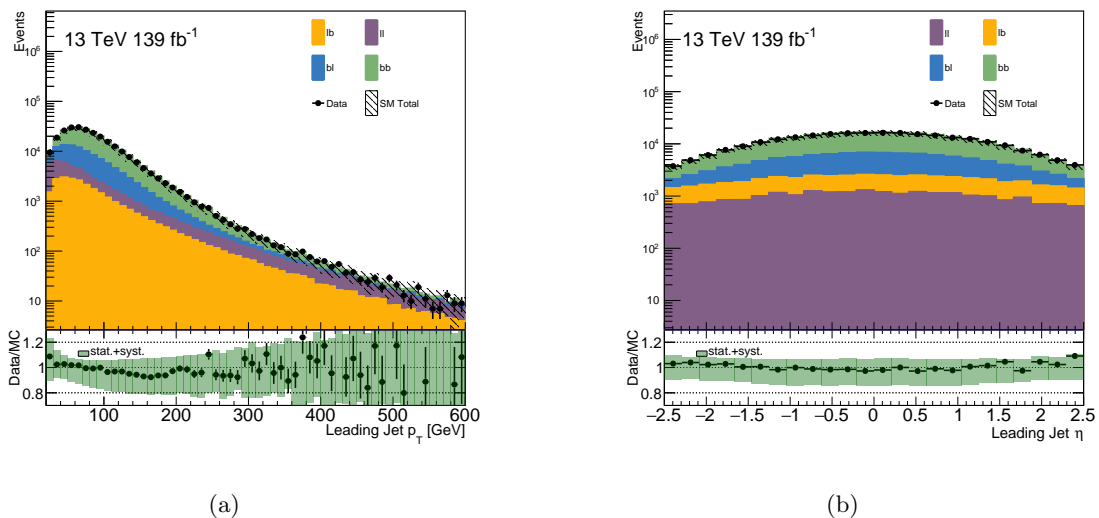
Figure 7.7: Distributions of the leading jet (a) p_T and (b) η for the MC backgrounds that surpass the selection criteria. The hashed green background on the SM total sum in quadrature of the difference between the up (down) and nominal background of each systematic uncertainty and the straight black lines represent the statistical uncertainty.

For the pseudorapidity observable, the MC is consistent with the predicted data within the total uncertainty[2]. In terms of the p_T observable, there is a downward trend between 100 and 300 GeV suggesting the MC is over-predicting the data. When considering all systematic uncertainties, the modelling is deemed sufficient to measure the *b*-tagging efficiency in bins of jet p_T. The

---

[2]In this scenario, the simulation is considered to be sufficiently "modelling" the data.

origin of the poor modelling has been suggested to possibly arise from the modelling of the top quark [92, 132]. Using the explicit p_T bins defined in Table 7.2 for the two jets, results in 45 orthogonal bins.

Bin Number	0	1	2	3	4	5	6	7	8
Jet p_T [GeV]	[20, 30]	[30, 40]	[40, 60]	[60 ,85]	[85, 110]	[110, 140]	[140, 175]	[175, 250]	[250, 600]

Table 7.2: Analysis binning for the leading and sub-leading jet p_T.

Examining Figure 7.6, the *bb* fraction is well correlated with on-shell top decays and thus, the *bb* fraction is kinematically reduced beyond 175 GeV. The invariant mass of the jet-lepton system is also uncorrelated with the *b*-tagging discriminants and hence why this quantity is used to define the *bb*-enriched SR and the *bl*-, *lb*-, *ll*-enriched CRs. The explicit regions are defined as follows:

- **SR** - $m_{j1,l}, m_{j2,l} < 175$ GeV, a high *bb* purity signal region.

- **CR$_{\textbf{LL}}$** - $m_{j1,l}, m_{j2,l} > 175 GeV$, a high *ll* purity control region.

- **CR$_{\textbf{BL}}$** - $m_{j1,l} < 175$ GeV, $m_{j2,l} > 175$ GeV, a high *bl* purity control region.

- **CR$_{\textbf{LB}}$** - $m_{j1,l} > 175$ GeV, $m_{j2,l} < 175$ GeV, a high *lb* purity control region.

The SR events are further classified as a function of the PC binned *b*-tagging discriminant of the two jets, denoted as w_1 and w_2 [92]. These three classifications result in a total of 1260 orthogonal bins [92] and to assist the reader with the visualisation of the binning, a schematic showing the definitions can be seen in Figure 7.8.

(a)
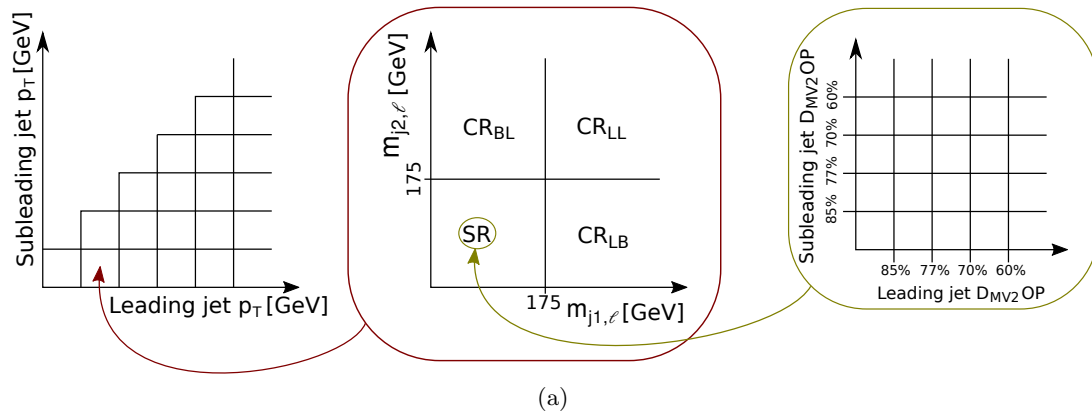
Figure 7.8: Schematic showing the complete binning used for the *b*-tagging efficiency measurement. First, split as a function of leading and sub-leading jet p_T, then into signal and control regions and finally, the signal region is a function of the *b*-tagging discriminant [133]. Taken from Ref [92].

Figure 7.9 shows each flavour fraction in the respective control and signal regions for this measurement.

Using these definitions, Figure 7.9(a) shows an overall very high *bb* fraction. The fraction is at a minimum in the $p_{\text{T},1}, p_{\text{T},2} = [20-30, 20-30]$ GeV bin with 17.5% before quickly rising to $\sim 31\%$ for the next $p_{\text{T},1}$ bin and tending towards an average value of $\sim 41\%$ for the remainder

(a) *bb*

(b) *bl*

(c) *lb*

(d) *ll*
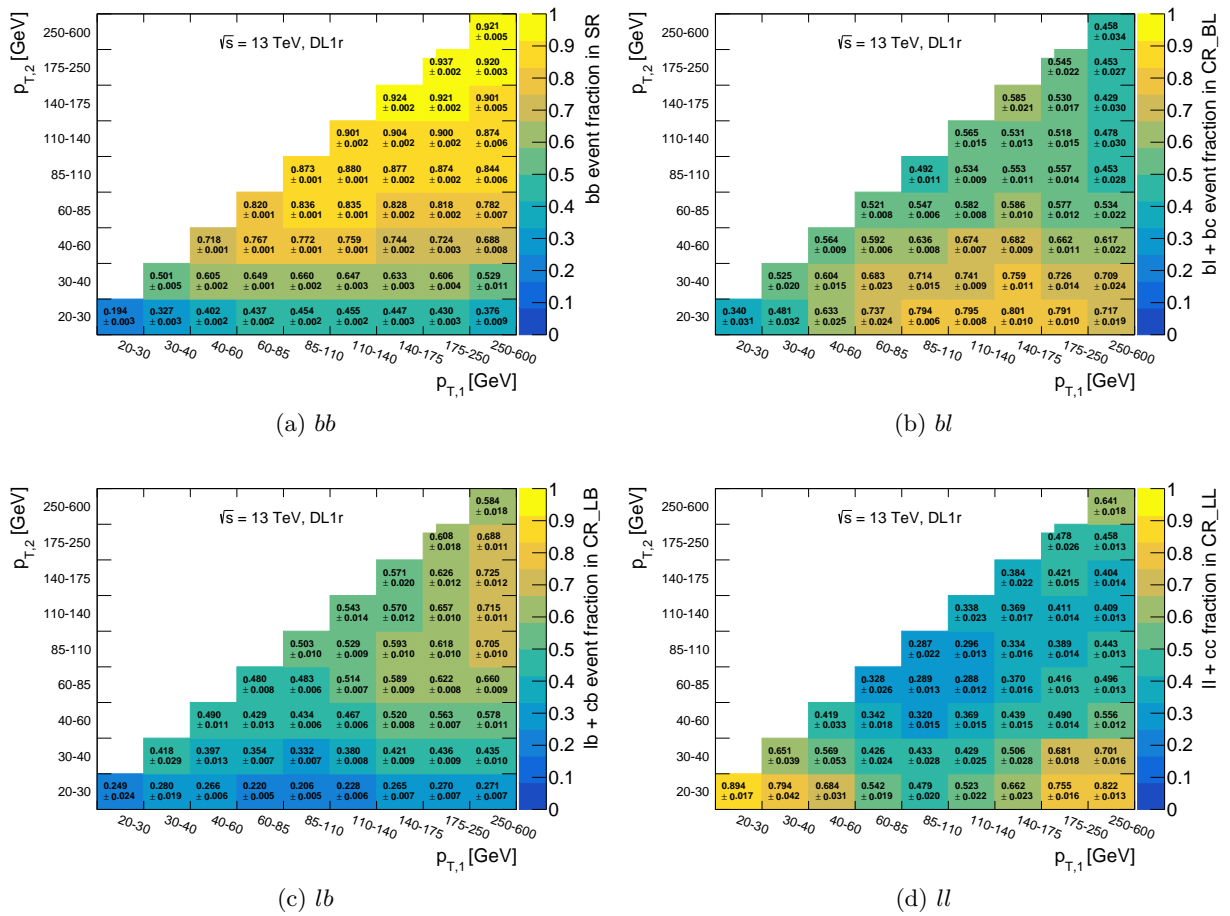
Figure 7.9: The jet flavour fraction for the targeted fraction in each respective control region and the signal region for the DL1r tagger.

$p_{T,1}$ bins. As both bins of jet p_T increase, so does the *bb* fraction as expected where it reaches a maximum of $\sim 93\%$. Moving onto the control regions, Figure 7.9(b) shows the *bl* fraction in the corresponding CR. Generally, this CR has the lowest enrichment of the flavour fractions. The fraction is particularly low when the leading jet is above 175 GeV and is similarly very low, for the $p_{T,1}, p_{T,2} = [20-30, 20-30]$ GeV bin. The remaining bins, in the intermediate range of the p_T distribution, averages around 30% with a maximum of $\sim 54\%$. The *lb* fraction is seen to be particularly sensitive for leading (sub-leading) jets over 110 (60) GeV, however, although the fractions are roughly consistent, the values are not as high, being $\mathcal{O}(30-40)\%$ with a maximum of $\sim 42\%$. The lowest purity can be seen for the $p_{T,2} = [20, 30]$ GeV where it is $< 10\%$, the purity then slightly improves for $p_{T,2} = [30, 40]$ GeV where it is $< 19\%$. The *ll* fraction is observed to peak in the three extremities of the two-dimensional binning; $p_{T,1}, p_{T,2} = [20-30, 20-30]$, $p_{T,1}, p_{T,2} = [250-600, 20-30]$ and $p_{T,1}, p_{T,2} = [250-600, 250-600]$ GeV where the purity is 90%, $\sim 84\%$ and 67% respectively. The purity then decreases linearly for bins surrounding these corners of phase-space before reaching a minimum at $p_{T,1}, p_{T,2} = [110-140, 30-40]$ GeV where it is $\sim 22\%$.

7.4   Extraction of *b*-jet Tagging Efficiency

A joint log-likelihood (LLH) function is defined to use both signal and control region data to estimate the *b*-jet tagging probability in Monte Carlo and the jet flavour composition [92]. The general form of that LLH function, after dropping terms that do not depend on the parameters to be estimated, is calculated by

$$\log \mathcal{L}(\nu_{\text{tot}}, \hat{\Theta}) = -\nu_{\text{tot}} + \sum_{i}^{N} n_i \log \nu_i(\nu_{\text{tot}}, \hat{\Theta}), \tag{7.3}$$

where ν_{tot} is the total number of expected events, $\hat{\Theta}$ is the list of parameters to be estimated, therefore containing both parameters of interest (POI) and nuisance parameters and $\nu_i(n_i)$ is the number of expected (observed) events in bin i for N bins [92]. The POIs for the likelihood fit are the *b*-jet tagging probability ($\mathcal{P}$) which are defined per p_T bin and thus, can be defined as the conditional probability for a *b*-jet with a p_T falling in one of the nine p_T bins (T^m for $m = 1, \ldots, 9$) defined in Table 7.2 to have a *b*-tagging discriminant w falling in one of five PC bins (O^k for $k = 1, \ldots, 5$.) [92]. From this, the *b*-jet tagging efficiency (termed *b*-efficiency, ϵ_b) for a single-cut OP point, X, in a jet p_T bin T^m, relates to the POIs [92] by

$$\epsilon_b(X|T^m) = \sum_{O^k \subset X} \mathcal{P}_b(O^k|T^m). \tag{7.4}$$

Having measured the *b*-efficiency for simulation (ϵ_b^{MC}) and one already knowing the *b*-efficiency in data (ϵ_b^{data}), scale factors can be calculated to correct the measured MC *b*-efficiency by

$$\text{SF}(X|T^m) = \frac{\epsilon_b^{\text{data}}(X|T^m)}{\epsilon_b^{\text{MC}}(X|T^m)}. \tag{7.5}$$

In each CR, the number of events in a specified $p_{\text{T},1}$, $p_{\text{T},2}$ bin (T^m, T^n) is written as the sum of the flavour fractions $(\nu_i^{m,n})$ adjusted by a correction factor $(c_i^{m,n}$ for $i = bb, bl, lb, ll)$ which forms the nuisance parameters [92];

$$\nu_{\text{CR}}(T^m, T^n) = \sum_{i \text{ for } i=bb,lb,bl,ll} c_i^{m,n} \nu_{\text{CR},i}^{m,n}. \tag{7.6}$$

Equivalently, the number of events expected in the SR can also be defined by additionally considering the *b*-tagging discriminants of the two jets with the p_{T} bins [92]; $p_{\text{T},1}$, $p_{\text{T},2}$, w_1, w_2 (T^m, T^n, O^k, O^p) which is calculated by

$$
\begin{aligned}
\nu_{\text{SR}}(T^m, T^n, O^k, O^p) = {} & c_{bb}^{m,n} \nu_{\text{SR},bb}^{m,n} \cdot \mathcal{P}_b(O^k|T^m) \cdot \mathcal{P}_b(O^p|T^n) \\
& + c_{bl}^{m,n} \nu_{\text{SR},bl}^{m,n} \cdot \mathcal{P}_b(O^k|T^m) \cdot \mathcal{P}_l(O^p|T^n) \\
& + c_{lb}^{m,n} \nu_{\text{SR},lb}^{m,n} \cdot \mathcal{P}_l(O^k|T^m) \cdot \mathcal{P}_b(O^p|T^n) \\
& + c_{ll}^{m,n} \nu_{\text{SR},ll}^{m,n} \cdot \mathcal{P}_l(O^k|T^m) \cdot \mathcal{P}_l(O^p|T^n),
\end{aligned}
\tag{7.7}
$$

where $\mathcal{P}_l$ is the effective *b*-jet tagging probability for *c*- and *l*-jets predicted by simulation in a given p_{T} bin. All the POIs and correction factors are estimated as free parameters by minimising the negative LLH function defined in Equation 7.3 using the MINUIT algorithm [134].

7.5   Uncertainties

This section will summarise the methodology of how all statistical and systematic uncertainties impacting the measurement were evaluated.

7.5.1   Method-related

One assumption when deriving the likelihood functions of Equation 7.3 is that the *b*-tagging discriminant w of a *b*-jet only depends on the p_{T} bin. In practice, this is not completely true because of different kinematic effects of the leading and the sub-leading jets within a specific p_{T} bin. To evaluate the impact of this assumption on the measurement, data generated with a known flavour composition, termed *pseudo-data*, is used in the measurement for a test scenario. The pseudo-data is created using the nominal generators for the SM background expectation and the uncertainty is derived by fluctuating a Poisson distribution. The *b*-efficiency is measured and the results of this test are shown in Figure 7.10.
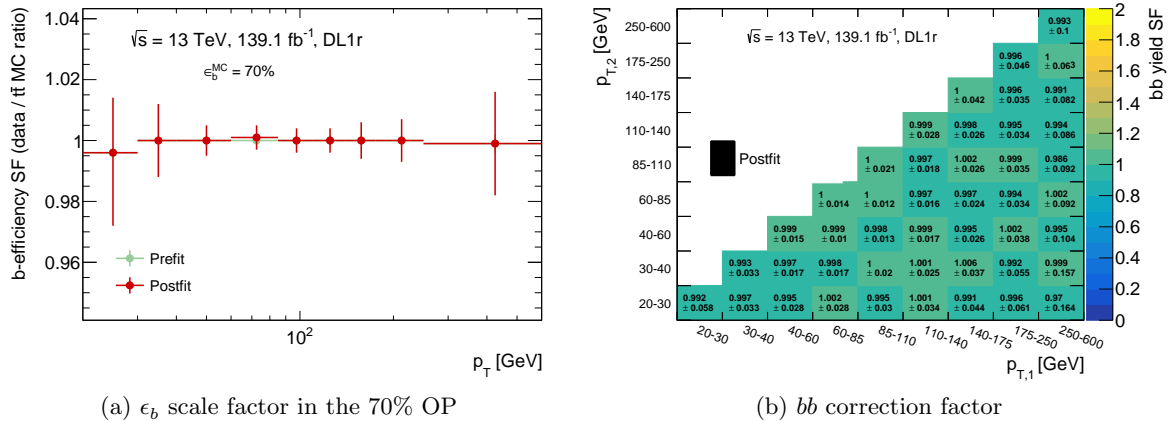
(a) ϵ_b scale factor in the 70% OP

(b) bb correction factor

Figure 7.10: Results of the measurement when the nominal simulated processes are used as pseudo-data for the DL1r tagger at a 70% OP.

A deviation from unity with a maximum of 0.05% is observed in the scale factors as a function of p_T. However, the deviations are always much smaller with respect to the Poisson uncertainty originating from limited data statistics. The impact on the results is therefore negligible and a non-closure uncertainty originating from the method is not justified by this test.

Another test designed to estimate the dependency of the b-tagging efficiency extraction method on the MC background, called the *stress test*, is performed. This test creates two sets of pseudo-data using the nominal $t\bar{t}$ MC and an alternate $t\bar{t}$ simulation generated with SHERPA[3] respectively. Again, the statistical uncertainty is fluctuated according to a Poisson distribution to replicate *real* data statistics. The SHERPA generator is chosen as the alternate $t\bar{t}$ process for three reasons; firstly it creates a known inconsistency between pseudo-data and MC background in the likelihood function, secondly, it is not used in the estimation of the $t\bar{t}$ theoretical uncertainties and finally, the SHERPA generator configuration includes processes with more than one additional parton in the matrix element. Therefore, one naively expects an increase in the accuracy of the modelling of the additional light jet kinematics. The two models are then fitted to the nominal MC background expectation and the measured ϵ_b is compared with the true b-tagging efficiency obtained from using the nominal MC, $\epsilon_b^{\text{truth}}$. The results of this test can be seen in Fig. 7.11.

The alternate model is consistent with the nominal model within the statistical uncertainties and follows the trend of the central values throughout the p_T distribution. It is therefore said that the likelihood fit behaves as expected and no additional non-closure uncertainty is needed from this test.

7.5.2 Statistical Data

The data statistical uncertainties in the b-jet tagging probabilities and the bin-to-bin correlations are obtained from the error matrix returned by MINUIT and propagated to the measurement via a basis transformation [92]. The uncertainties are correlated with the various parameters

---

[3]More details on the alternate $t\bar{t}$ MC generator can be seen in Table 7.1.
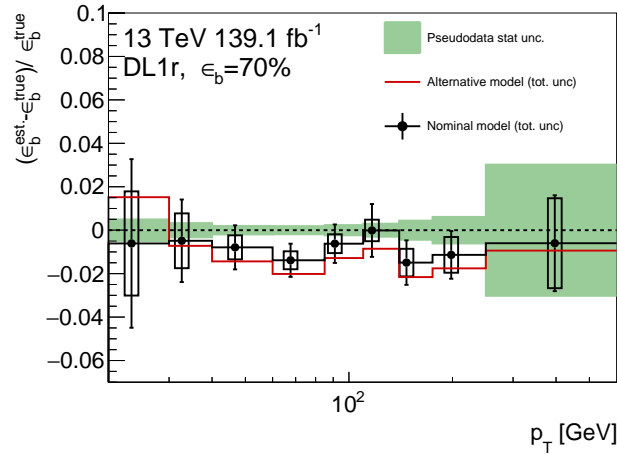
(a)

Figure 7.11: Results of the *stress test* showing the comparison of ϵ_b with the $\epsilon_b^{\text{truth}}$ for the nominal and an alternate $t\bar{t}$ MC generator used as pseudo-data for the DL1r tagger.

because of the usage of two-dimensional p_{T} bins (T^m, T^n) and the conservation of probability for the *b*-tagging discriminant density function ($\int \epsilon_b(w)dw = 1$).

To correctly obtain a consistent set of uncorrelated data statistical uncertainties, principal component analysis (PCA) is used [135]. The error matrix is diagonalised and the data statistical uncertainty is split into 36 uncorrelated components, originating from the nine p_{T} bins ($N_{p_{\text{T}}} = 9$) and the number of *b*-tagging discriminant bin related to probability conservation ($N_w - 1 = 4$). The total data statistical uncertainty for a specified parameter is obtained by summing in quadrature the 36 components.

The data statistical uncertainty has a maximum impact of 2.5%. At $p_{\text{T}} \sim 70$ GeV, the uncertainty is at a minimum with an impact of $\sim 0.5\%$. The data statistical uncertainty only significantly impacts the precision of the measurement at high p_{T} because of systematic uncertainties dominating at low p_{T}.

7.5.3   Theoretical

The remaining systematic uncertainties are assessed by deriving the *b*-efficiency measurement using the same procedure, but the simulated processes include $\pm 1\sigma$ variations on parameters related to the uncertainty and comparing the outcome of the varied measurement to the nominal measurement.

Top quark   - There are several sources of uncertainty in the ability to correctly model the top quark decay in simulated events that affects both $t\bar{t}$ and single top processes. The parton shower and hadronisation generator are varied from PYTHIA 8 to HERWIG 7, both interfaced to the POWHEG matrix-element generator. ISR and FSR are varied using the nominal POWHEG+PYTHIA8 A14 tune [136] and POWHEG+PYTHIA8. For uncertainties related to the

proton structure, the parton distribution functions (PDF) are varied following PDF4LHC recommendations [137]. An additional uncertainty is considered for the interference between single top (Wt) and $t\bar{t}$ production by adjusting the nominal generator with the diagram removal (DR) scheme to the diagram subtraction (DS) scheme for single top production [138]. The quadrature sum of the $t\bar{t}$ (single top) modelling uncertainties ranges from $\sim$3.2(2.4)% at low p_T, down to 0.8(1.8)% at high p_T. The constraining of the flavour fractions in the fit assists in constraining the parton shower and hadronisation uncertainties, particularly at low p_T. The $t\bar{t}$ (single top) modelling is dominated at low p_T by PDF (parton shower and hadronisation) uncertainties, while at high p_T the choice of parton shower and hadronisation model and the DR vs DS schemes for single top also significantly contributes.

Z+jets and diboson - The modelling of diboson and Z+jets simulated events is evaluated by varying the total cross section and factorisation and renormalisation scales as well as varying the PDFs. The total cross section remains constant when varying the scale and PDF, such that only kinematic distributions are impacted [92]. The diboson modelling uncertainties are negligible for almost the entire p_T range. Z+jets modelling uncertainties are significant in the [20, 30] GeV jet p_T bin being $\sim 2.4\%$.

7.5.4 Experimental

Uncertainties related to the imperfect understanding of the detector and the inability to perfectly model physics in data are considered and these are listed explicitly in this section.

Jet Reconstruction - Has several components that contribute to significant uncertainties in the measurement. The jet energy scale (resolution) (JES, JER) [118] of hadronic jets includes both the modelling of the detector response and the analysis techniques used to derive the calibration [92]. The impact of the JES calibration is assessed by evaluating a $\pm 1\sigma$ variation with respect to the calibration prediction. This results in a (sub-)dominant uncertainty in the [20, 30] GeV ([30, 40] GeV) jet p_T bin with an impact of $\sim 5\%$ ($\sim 2\%$). The impact of the JER uncertainty is evaluated from $\pm 1\sigma$ variations in the detector reconstruction for jets. The JER uncertainty is the largest systematic uncertainty in the [20, 30] GeV jet p_T bin with an impact of $\sim 5.5\%$. Therefore, both the JES and JER are dominant uncertainties in the lowest p_T bins of the calibration. Thirdly is the jet vertex fraction efficiency [139], which is negligible.

c/l-jet tagging efficiencies - Light-jet and c-jet mis-tagging efficiencies [140] [141] impact the measurement. The uncertainty originating from light-jet tagging efficiencies is negligible, whereas those originating from c-jet tagging is a sub-dominant uncertainty in the two lowest p_T bins ranging from $\sim 2.2\%$ down to $\sim 0.9\%$.

Lepton reconstruction - The electron and muon energy/momentum scale, resolution, identification, isolation and trigger efficiencies are taken into account. For electrons also the recon-

struction efficiency is considered and for muons only, the track-to-vertex association efficiency is considered. These uncertainties are negligible.

Remaining - Pileup modelling is non negligible only in the lowest p_T bin, reaching typically $\sim 0.9\%$. The uncertainty for background processes with fewer than two prompt leptons (fakes) is evaluated directly from data contributions from events with non-prompt leptons (0NPL) and one non-prompt muon (1NPmu), which are negligible and therefore directly taken from MC without additional uncertainties. The data-to-MC agreement for the one non-prompt electron component (1NPel) is assessed in a region enriched in misidentified leptons by requiring two same-charge (SC) leptons instead of opposite charge (OC). After subtracting the remaining zero non-prompt components from data based on MC predictions, the data-to-MC ratio is extracted in three bins of electron p_T ([28−150, 150−300, 300−∞] GeV) and used as scale factors to reweight the 1NPel component to correctly predict it in the OS region. The 1NPel scale factors are not applied for the nominal results but only for systematic evaluation. The impact of the measurement in the lowest p_T bins (20-100 GeV), up to $\sim 0.9\%$ in all OPs, however, becomes negligible beyond 80 GeV.

7.6 Results

7.6.1 Goodness-of-fit

To evaluate the agreement between the data and Monte Carlo as well as the goodness-of-fit, a Pearson's global χ^2 test is computed and compared to the number of degrees of freedom (N_{dof}) of the fit. This test confirms that the remaining differences between the observed and expected post-fit yields originate only from the limited size of the dataset [92]. One should note that this estimator accounts only for data statistical uncertainties and neglects any other sources of uncertainty.

Because the minimisation procedure is implemented as the simultaneous minimisation of several likelihood functions, each of them being defined for a specific p_T bin (T^m, T^n) and SR/CR bin, the global χ^2 is defined as the sum of Pearson's χ^2_{SR}, χ^2_{CR} estimators computed in each (T^m, T^n) bin [142] calculated by

$$\chi^2_{\mathrm{SR}}(T^m, T^n) = \sum_{O^{k,l} \subset X} \frac{(n^{k,l}_{\mathrm{SR}} - \nu^{k,l}_{\mathrm{SR}})^2}{\nu^{k,l}_{\mathrm{SR}}} \ \text{ and } \ \chi^2_{\mathrm{CR}}(T^m, T^n) = \sum_{\mathrm{CR}} \frac{(n_{\mathrm{CR}} - \nu_{\mathrm{CR}})^2}{\nu_{\mathrm{CR}}}, \qquad (7.8)$$

where the notations follow the conventions introduced in Section 7.4. The final estimators can then be written by

$$\chi^2(T^m, T^n) = \sum_i \left[\chi^2_{\mathrm{SR}}(T^m, T^n) + \chi^2_{\mathrm{CR}}(T^m, T^n) \right]. \qquad (7.9)$$

The number of degrees of freedom (N_{dof}) for the final simultaneous fit is computed as the sum of the N_{dof} of the fits bound to each likelihood presented in Section 7.4, minus the number of POIs and nuisance parameters (Θ), calculated by

$$N_{\mathrm{dof}} = \underbrace{N_k \cdot N_w^2}_{\mathrm{SR}} + \underbrace{N_k \cdot N_{\mathrm{CR}}}_{\mathrm{CRs}} - \underbrace{N_k \cdot N_{f_1,f_2}}_{\mathrm{Correction\ factors}} - \underbrace{N_{p_{\mathrm{T}}} \cdot (N_w - 1)}_{\mathrm{POIs}}, \tag{7.10}$$

where N_k is calculated from

$$N_k = \frac{N_{p_{\mathrm{T}}} \cdot (N_{p_{\mathrm{T}}} + 1)}{2}. \tag{7.11}$$

Using $N_{p_{\mathrm{T}}} = 9$ in the equation for N_k, results in $N_k = 45$. Consequently with $N_{f_1,f_2} = 4$, originating from the four different flavour fractions (bb, bl, lb and ll), and $N_w = 5$, results in $N_{\mathrm{dof}} = 1044(1260)$ post-fit (pre-fit). The nominal measurement then has a χ^2/N_{dof} of 1.01 (1.26) post-fit (pre-fit), therefore the data-to-MC agreement improves post-fit and with a corresponding post-fit p-value of 0.404, it confirms the strong agreement between the data and simulation. To further investigate where the remaining significant data-to-MC disagreements originate, if any, the χ^2 percentage as a function of the jet p_{T} bins (T^m, T^n) is used, which is calculated by

$$\%(\chi^2)(T^m, T^n) = \frac{\chi^2_{\mathrm{SR}}(T^m, T^n) + \chi^2_{\mathrm{CR}}(T^m, T^n)}{\chi^2(T^m, T^n)}. \tag{7.12}$$

Given that $N_k = 45$, it is expected on average Equation 7.12 would be $= 1/45 \sim 0.022$ in the scenario the (dis)agreement between the data and MC is uniform across all p_{T} bins. Figure 7.12 presents the $\%(\chi^2)$ for the DL1r tagger.
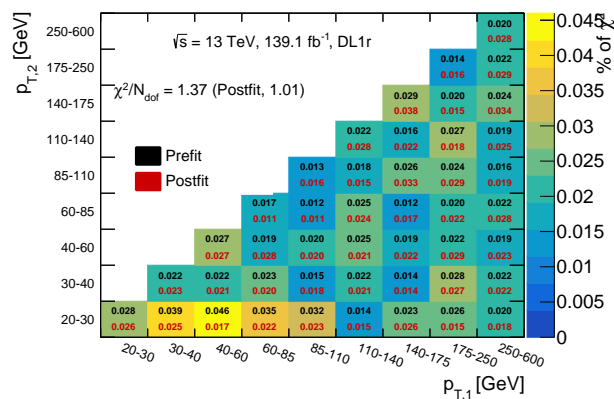
Figure 7.12: Percentage of χ^2 in each jet p_{T} bin (T^m, T^n) pre-fit (post-fit) in black (red) for the DL1r tagger.

Some significant spikes in this distribution post-fit are observed, for example, in the bin ($p_{\mathrm{T},1}$, $p_{\mathrm{T},2}$)= [140−175, 140−175] GeV with bin value 0.038%. The remaining values range from 0.011% to 0.034%. This is an additional indicator of sufficient agreement between the data and simulation and that the fit is behaving correctly.

7.6.2   Correction Factors

The flavour fractions are constrained in the LLH fit as a function of the leading and sub-leading jet p_T. Figure 7.13 presents the correction factors as a function of the jet p_T bins.
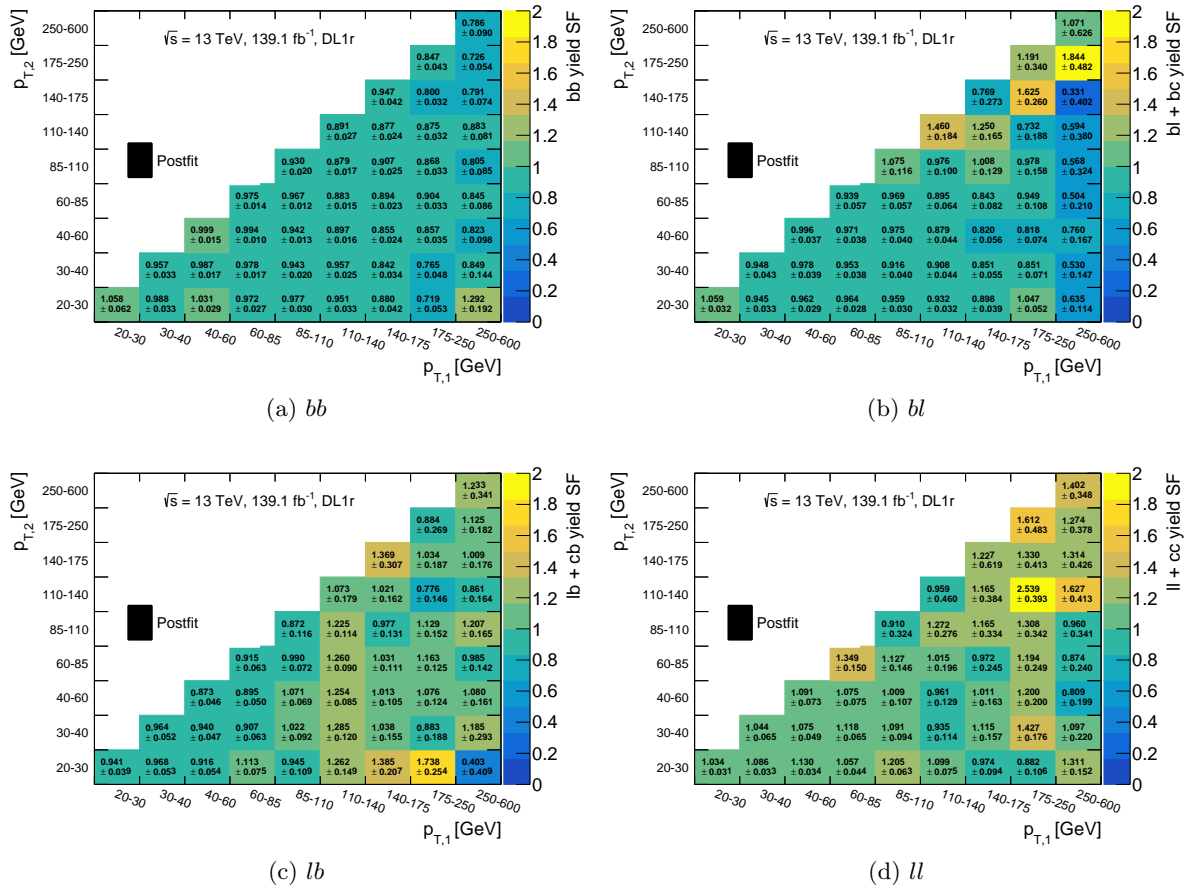
Figure 7.13: Each (post-fit) flavour correction factor is a function of the leading and sub-leading jet p_T for the DL1r tagger.

The *bb* fraction not only has most central values near unity but it is also the flavour with the greatest level of uniformity across the two jet p_T bins. The *bl* fraction shares a similar pattern however for $p_{T,1} > 250$ GeV, the majority of $p_{T,2}$ bins are of the $\mathcal{O}(0.5)$ except for the highest p_T bin, where it is of the order of unity and $(p_{T,1}, p_{T,2}) = [250-600, 175-250]$ GeV where there is a spike of 1.844. The *lb* fraction is still somewhat uniform, albeit with central values closer to 1.2 and shares some large deviations away from unity in large p_T bins, as observed with *bl* too. The *ll* fraction shares a similar pattern to *lb*, however, the average is closer to 1.2. Even though there are spikes in the flavour fractions, typically at high p_T bins, overall the correction fractions are close to unity and, especially for of the *bb* fraction, are well constrained.

7.6.3   Single-cut *b*-jet Tagging Efficiency Measurements

The POIs of the fit that correspond to the calibration of the so-called pseudo-continuous OPs, defined in Ref. [92] and mentioned in Section 7.4, are (100%-85%, 85%-77%, 77%-70%, 70%-60%,

60%-0%) and the results from these measurements will be presented in Section 7.6.4. The single-cut OP calibration that uses 85%, 77%, 70% and 60% fixed b-jet tagging efficiency is deduced by adding the relevant POI b-efficiency and by changing the basis of the correlation matrix returned by the fit. The results from this single-cut OP calibration will be discussed in this section. The final b-efficiency measurement and the corresponding data-to-MC scale factors for the DL1r tagger and the 70% cumulative OP are presented in Figure. 7.14.

(a) b-efficiency for MC

(b) Data-to-MC scale factors
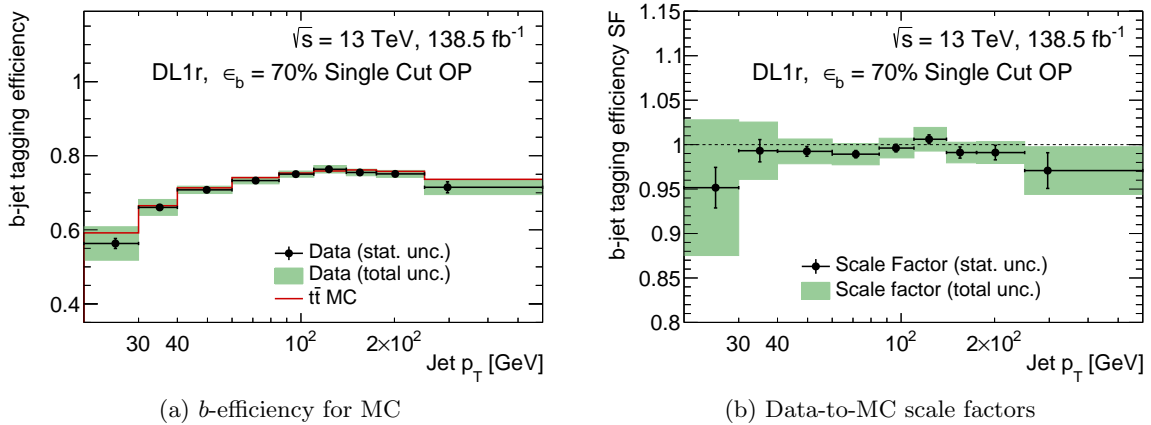
Figure 7.14: Measured b-jet tagging efficiency and corresponding data-to-MC scale factors for the DL1r tagger and 70% single-cut OP. Vertical error bars include data statistical uncertainties only, whereas the green band corresponds to the sum in quadrature of all uncertainties.

The OP definition, the NN training and the tracking performance of the ATLAS detector shape the performance of the b-efficiency as a function of p_{T}. For the DL1r tagger and the 70% cumulative OP, it ranges from 59% to approximately 76%. It smoothly increases to reach a plateau at $p_{\mathrm{T}} \sim 80$ GeV. It drops slightly starting from $p_{\mathrm{T}} \sim 250$ GeV. When taking the ratio of the data-to-MC b-efficiency, the scale factors for each bin are compatible with unity within the total uncertainty band across the entire p_{T} range. In all but the lowest and highest jet p_{T} bins ([$20-30, 250-600$] GeV) the scale factors are consistent with unity within the data statistical uncertainty, suggesting good modelling of the b-jet tagging performance by the algorithm. The related data statistical, total systematic and total uncertainties, are presented in Figure 7.15 for the measurement. Similar plots for other taggers and OPs, including those for the pseudo-continuous calibration, are available in Appendix B.2.

The total uncertainty in the measurement ranges from $\sim 7.5\%$ at low p_{T}, down to about 1.25% at $p_{\mathrm{T}} \sim 100$ GeV and increases again at high p_{T} to reach about 2.5%. Systematic uncertainties dominate up to $p_{\mathrm{T}} \sim 200$ GeV. The dominant systematic uncertainties include jet energy scale and resolution, modelling of $t\bar{t}$ and single top events (PDF/ISR/FSR, parton shower and hadronisation). In the first two p_{T} bins, various other contributions originating from pileup reweighting and c/l-jet mis-tagging. The dominant systematic uncertainties, including the contribution from each nuisance parameter to the uncertainty group for the calibration of the DL1r tagger with a 70% cumulative OP, are presented in Figure 7.16. At high p_{T}, the data statistical uncertainty becomes dominant.

A breakdown of all systematic uncertainties for the 70% OP for the DL1r can be seen in Table 7.3,
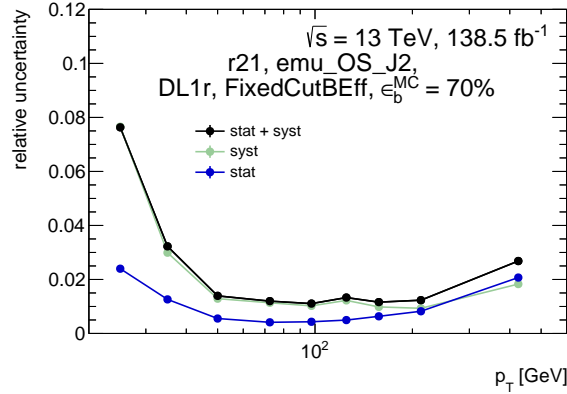
(a)

Figure 7.15: Data statistical (blue), total systematic (green) and total uncertainty (black) in the *b*-jet tagging efficiency measurement for the DL1r tagger.

where the systematics are grouped into their respective categories. All the remaining single-cut OP and taggers can be found in Appendix B.2.

Grouped Uncertainty / p_T [GeV]	20-30	30-40	40-60	60-85	85-110	110-140	140-175	175-250	250-600
Jet Energy Resolution	5.34	0.87	0.49	0.53	0.37	0.15	0.14	0.28	0.28
Jet Energy Scale	4.94	2.16	0.29	0.18	0.27	0.11	0.17	0.26	0.25
$t\bar{t}$ PS+Hadronisation+PDF	2.47	0.99	0.71	0.50	0.71	0.94	0.73	0.67	0.61
Z+jets Cross section+PDF	2.34	0.75	0.04	0.25	0.04	0.11	0.01	0.05	0.22
Flavour Tagging	2.26	0.86	0.28	0.10	0.09	0.12	0.05	0.10	0.23
$t\bar{t}$ ISR+FSR	1.80	1.02	0.46	0.40	0.30	0.60	0.33	0.28	0.46
Single top PS+Hadronisation+PDF	1.74	0.63	0.53	0.29	0.13	0.05	0.04	0.04	0.05
Single top ISR+FSR+Interference	1.74	0.71	0.56	0.74	0.54	0.46	0.54	0.45	1.56
Pileup Reweighting	1.41	0.13	0.11	0.03	0.05	0.04	0.03	0.05	0.01
Lepton Reconstruction	0.88	0.27	0.13	0.07	0.06	0.06	0.03	0.03	0.07
Fake leptons modelling	0.75	0.47	0.45	0.05	0.06	0.10	0.06	0.04	0.06
VV Cross section+PDF	0.14	0.41	0.21	0.08	0.06	0.07	0.02	0.03	0.10
Remaining	0.02	0.01	0.01	0.00	0.01	0.02	0.01	0.00	0.01
Total Systematic Uncertainty [%]	9.07	3.18	1.41	1.20	1.07	1.24	1.00	0.95	1.81

Table 7.3: Tabular breakdown of the percentage uncertainties summed in quadrature into physically-motivated groups for the DL1r tagger for a 70% operating point.

All uncertainties introduced in Section 7.5 that are not included in Table 7.3 are negligible and therefore removed from the table. The lowest p_T bin has the largest total systematic uncertainty, where the largest contributor to that is the JER (5.34%). The next dominant systematics in the lowest p_T bin, in descending order, are JES (4.94%), $t\bar{t}$ modelling (2.47%) and Z+jets modelling (2.34%). The next p_T bin ([30, 40] GeV) has the second-largest total systematic uncertainty. The three main contributors to this, with more than 1% uncertainty each and in descending order again, are JES (2.16%) and $t\bar{t}$ initial and final-state radiation (1.02%). Proceeding this p_T bin and going towards the highest p_T bin, the total systematic uncertainty ranges between $\sim 1.0 - 1.8\%$. Diboson modelling and JVT efficiency-related uncertainties are almost-negligible. The uncertainties for differing OPs follow similar behaviour and are of a similar magnitude.

(a) Jet energy resolution

(b) Jet energy scale

(c) $t\bar{t}$ modelling

(d) Single top modelling

(e) Z+jets modelling

(f) Eigenvector Charm
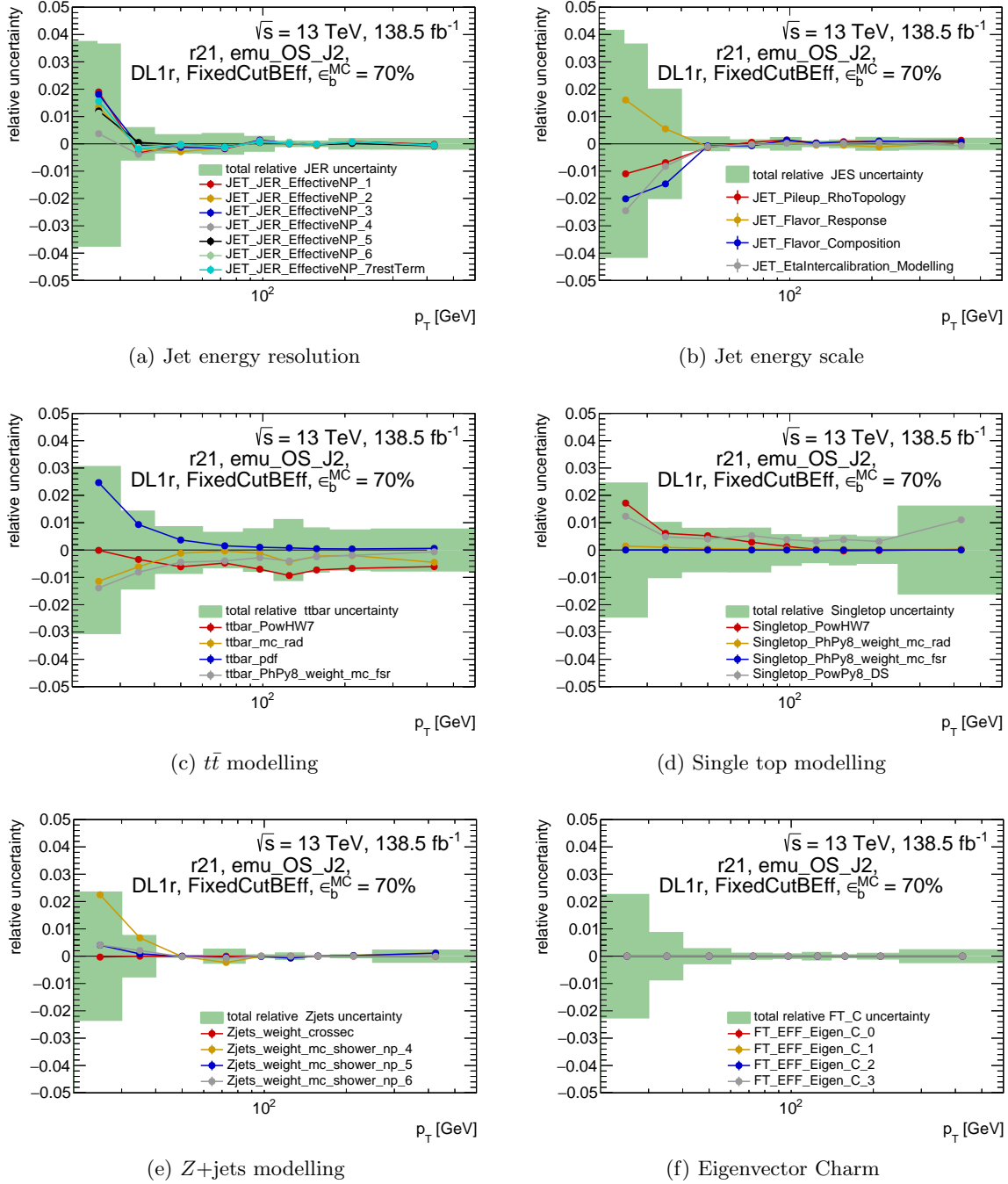
Figure 7.16: Dominant systematic uncertainties in the b-jet tagging efficiency measurement for the DL1r tagger and 70% cumulative OP. The impact of (a) jet energy resolution, (b) jet energy scale, (c) $t\bar{t}$ modelling, (d) single top modelling, (e) Z+jets modelling and (f) c-jet mis-tagging as a function of jet p_T are shown.

7.6.4   Pseudo-continous *b*-jet Tagging Efficiency Measurements

The measurement of the *b*-jet tagging probabilities in the DL1r algorithm discriminant bins was also performed. An example of the results for the p_T bin $[110, 140]$ GeV along with the corresponding data-to-MC scale factors can be seen in Figure 7.17. All *b*-jet tagging probabilities and data-to-MC scale factors for each of the remaining p_T bins can be found in Appendix B.2. The $[110, 140]$ GeV p_T range was chosen to demonstrate the measurement because, as observed in Figure 7.15, jets with p_T of this magnitude are in an optimal region of being not too low p_T that the systematic uncertainties are high but not too high p_T that there are limited data events in the region resulting in a high statistical uncertainty.

(a) *b*-efficiency for MC

(b) Data-to-MC scale factors
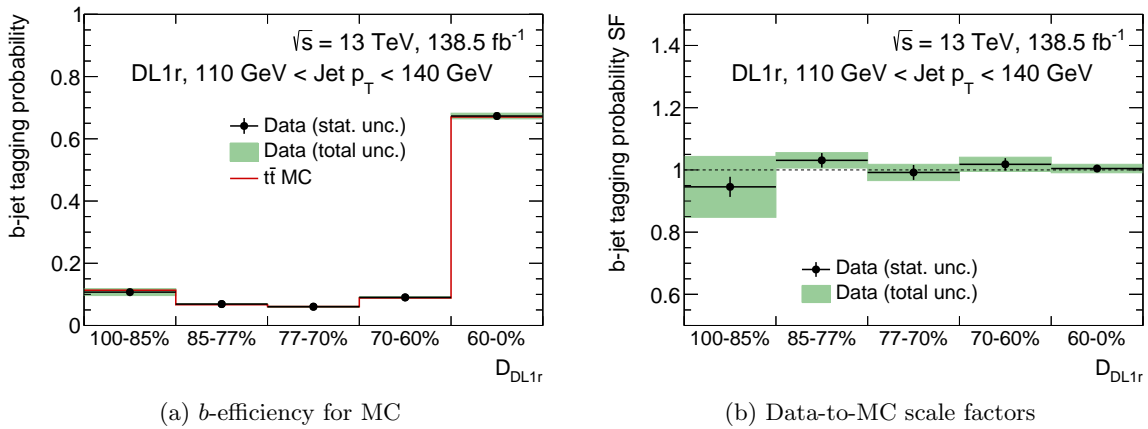
Figure 7.17: Measured *b*-efficiency for $t\bar{t}$ Monte Carlo and corresponding data-to-MC scale factors as a function of pseudo-continuous discriminant bins for the p_T range $[110, 140]$ GeV and the DL1r tagger.

All scale factors are of the order of unity within the total uncertainty band. The breakdown of the uncertainties for each *b*-tagging discriminant bin can be seen in Table 7.4. Again, the tables corresponding to the remaining p_T bins can be found in Appendix B.2.

The PC operating point with the largest total systematic uncertainty, as can be seen in Figure 7.17, is the $[100, 85]\%$ bin, where it is $\mathcal{O}(\pm 10\%)$. Theoretical $t\bar{t}$ uncertainties dominate the bin, shortly followed by theoretical single top uncertainties and jet modelling. The remainder of the total systematic uncertainty for each PC operating point ranges from $\sim 0.8\%$ to $\sim 1.3\%$ with $t\bar{t}$ modelling dominating.

Before ATLAS physics analyses use the derived scale factors, these results are smoothed and extrapolated into a high p_T range with the number of uncertainties reduced while preserving bin-to-bin correlations [92]. These scale factors are then applied to physics analyses (such as Chapters 8-9) by correcting the *b*-jet tagging response in MC and applying the associated uncertainties to the correction [92].

Grouped Uncertainty / w_1, w_2	100-85%	85-77%	77-70%	70-60%	60-0%
$t\bar{t}$ PS+Hadronisation+PDF	7.48	0.52	0.75	0.85	0.95
$t\bar{t}$ ISR+FSR	4.71	0.44	0.39	0.58	0.60
Single top ISR+FSR+Interference	3.70	0.23	0.47	0.36	0.47
Jet Energy Resolution	1.08	0.18	0.44	0.11	0.17
Flavour Tagging	1.06	0.20	0.09	0.12	0.12
Jet Energy Scale	1.00	0.23	0.32	0.21	0.12
Z+jets Cross section+PDF	0.90	0.05	0.15	0.11	0.12
Fake leptons modelling	0.89	0.08	0.21	0.10	0.10
VV Cross section+PDF	0.61	0.07	0.06	0.08	0.07
Lepton Reconstruction	0.51	0.06	0.06	0.06	0.06
Single top PS+Hadronisation+PDF	0.43	0.12	0.03	0.09	0.05
Pileup Reweighting	0.34	0.09	0.02	0.04	0.04
Remaining	0.13	0.01	0.01	0.02	0.02
Total Systematic Uncertainty [%]	9.88	0.83	1.15	1.15	1.26

Table 7.4: Tabular breakdown of the percentage uncertainties joined into physically-motivated groups for the DL1r tagger for the p_{T} range $[110, 140]$ GeV.

7.7 Conclusion

This chapter presents the results from the calibration of the DL1r b-tagging algorithm for jets reconstructed with the ParticleFlow algorithm and using the Run 2 dataset collected by the ATLAS experiment at $\sqrt{s} = 13$ TeV. Scale factors relating the efficiency of the b-tagging algorithm in data to the efficiency measured in Monte Carlo are all observed to be compatible with unity when considering all systematic and statistical uncertainties. The calibration is performed for a series of fixed b-tagging efficiency operating points and a series of pseudo-continuous bins of the DL1r discriminant distribution(s). The dominant uncertainties throughout the results are related to the reconstruction of jets and the theoretical understanding of the $t\bar{t}$ and single top processes.

Chapter 8

Search for Gluino Pair Production With Multiple *b*-jets

If R-Parity Conserving (RPC) supersymmetry (SUSY) were to exist, gluino and squark production would dominate at the Large Hadron Collider (LHC) [143]. This chapter searches for pair-produced gluinos decaying into third-generation squarks and the LSPs, where the LSP is assumed to be the lightest neutralino ($\tilde{\chi}_1^0$), a linear superposition of the superpartners of the neutral electroweak and Higgs bosons. This translates to final states with high *b*-jet multiplicity and a large amount of missing transverse momentum ($E_\mathrm{T}^\mathrm{miss}$).

8.1   Multiple *b*-jets+$E_\mathrm{T}^\mathrm{miss}$

The spectrum of the squark masses determines the flavour structure of the final-state quarks [38]. Since the first and second generations are expected to be much heavier than the third[1], gluinos will dominantly decay into top or bottom squarks via $\tilde{g} \to \tilde{t}t$ or $\tilde{g} \to \tilde{b}b$ (the so-called Gtt and Gbb signals Figures 8.1(b) and 8.1(a) respectively) [144]. Each stop (sbottom) is then assumed to decay via $\tilde{t} \to t\tilde{\chi}_1^0$ ($\tilde{b} \to b\tilde{\chi}_1^0$), or to a bottom (top) quark and the lightest chargino via $\tilde{t} \to b\tilde{\chi}_1^\pm$ ($\tilde{b} \to t\tilde{\chi}_1^\pm$) resulting in a three-body decay. In the latter instance, the chargino is assumed to subsequently decay to the LSP and Standard Model fermions by an off-shell W-boson; $\tilde{\chi}_1^\pm \to \tilde{\chi}_1^0(W^\pm \to f\bar{f}')$ (the so-called Gtb signals in Figure 8.2). The mass splitting between the chargino and the LSP is assumed to be small and hence nearly degenerate, such that the additional fermions f and $\bar{f}'$ are very soft and effectively invisible in the final state. These decays dominate when either the LSP is a higgsino or when squarks of the first two generations are heavy as per this instance [38]. The masses of the SUSY particles not involved in these processes are set to very high values.

The search is optimised for the discovery of the Gbb, Gtt and Gtb simplified models that each assumes a 100% gluino branching ratio. The simplified models are defined as follows:

---

[1]All squarks are set to 5 TeV in these models because all squark masses can be as heavy as 5 TeV without significant fine-tuning [7]
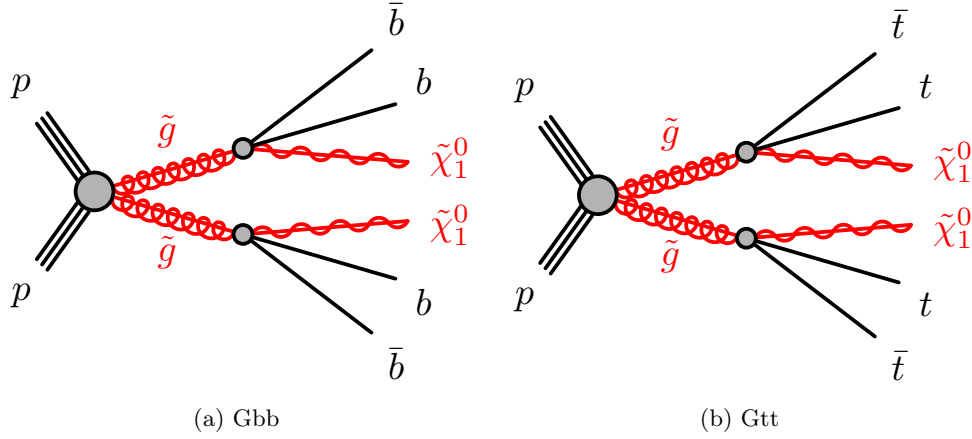
(a) Gbb (b) Gtt

Figure 8.1: The decay topologies in the (a) Gbb and (b) Gtt simplified models.

- **"Gtt"** - $\mathrm{Br}(\tilde{g} \to \tilde{t}_1 t \tilde{\chi}_1^0) = 100\%$.

- **"Gbb"** - $\mathrm{Br}(\tilde{g} \to \tilde{b}_1 b \tilde{\chi}_1^0) = 100\%$.

- **"Gtb"** - $\mathrm{Br}(\tilde{g} \to \tilde{t}_1 t \tilde{\chi}_1^0) + \mathrm{Br}(\tilde{g} \to \tilde{b}_1 b \tilde{\chi}_1^0) + \mathrm{Br}(\tilde{g} \to \tilde{t}_1 b (t \tilde{b}_1) \tilde{\chi}_1^0) = 100\%$. For the process $\tilde{g} \to \tilde{t}_1 b (t \tilde{b}_1) \tilde{\chi}_1^0$, only one gluino can decay to $\tilde{t}t$ or $(\tilde{b}b)$ as shown in Figure 8.2.

The results are also interpreted where each gluino in a single event is allowed to decay to $t\bar{t}\tilde{\chi}_1^0$, $bb\tilde{\chi}_1^0$ or $t\bar{b}\tilde{\chi}_1^-$ / $\bar{t}b\tilde{\chi}_1^+$ to set 95% confidence limits on the gluino mass in the $\mathrm{Br}(\mathrm{Gtt}) - \mathrm{Br}(\mathrm{Gbb}) - \mathrm{Br}(\mathrm{Gtb})$ plane for a specified LSP mass.

The $\tilde{\chi}_1^0$ interacts only weakly, resulting in final states with substantial missing transverse momentum of magnitude $E_{\mathrm{T}}^{\mathrm{miss}}$. The Gtt and Gbb signatures consist of large $E_{\mathrm{T}}^{\mathrm{miss}}$, and four energetic _b_-jets. To achieve high signal purity, at least three of the four required jets must be identified as _b_-jets (_b_-tagged). This requirement is highly effective in rejecting top pair production events, which constitute the main Standard Model background in this analysis, and which contain only two _b_-jets unless they are produced with additional heavy-flavour jets. Additionally, the Gtt experimental signatures contain four W bosons originating from the top quark decays $t \to Wb$. Each W boson can either decay leptonically ($W \to l\nu$) or hadronically ($W \to q\bar{q}'$). A Gtt event can therefore contain as many as 12 jets in the final state originating from the decay of the top quark, or isolated charged leptons.

This chapter will present the results using the Run 2 dataset recorded by the ATLAS experiment. The search for pair-produced gluinos decaying to multiple _b_-jets and large $E_{\mathrm{T}}^{\mathrm{miss}}$ has been previously performed using 36fb^{-1}of data, corresponding to data periods of 2015 plus 2016 and 79fb^{-1}corresponding to 2015, 2016 and 2017, both used a cut-based single bin approach and a multi-bin fit strategy [1]. No statistically significant excesses were observed so the largest 95% CL exclusion limits on each of the Gtt and Gbb signal processes can be seen in Figure 8.3. The largest observed gluino mass limit for 1 GeV LSP is ~2.25 TeV for the Gtt signal and the LSP mass limit is ~ 1.2 TeV for a gluino mass of 2.15 TeV.
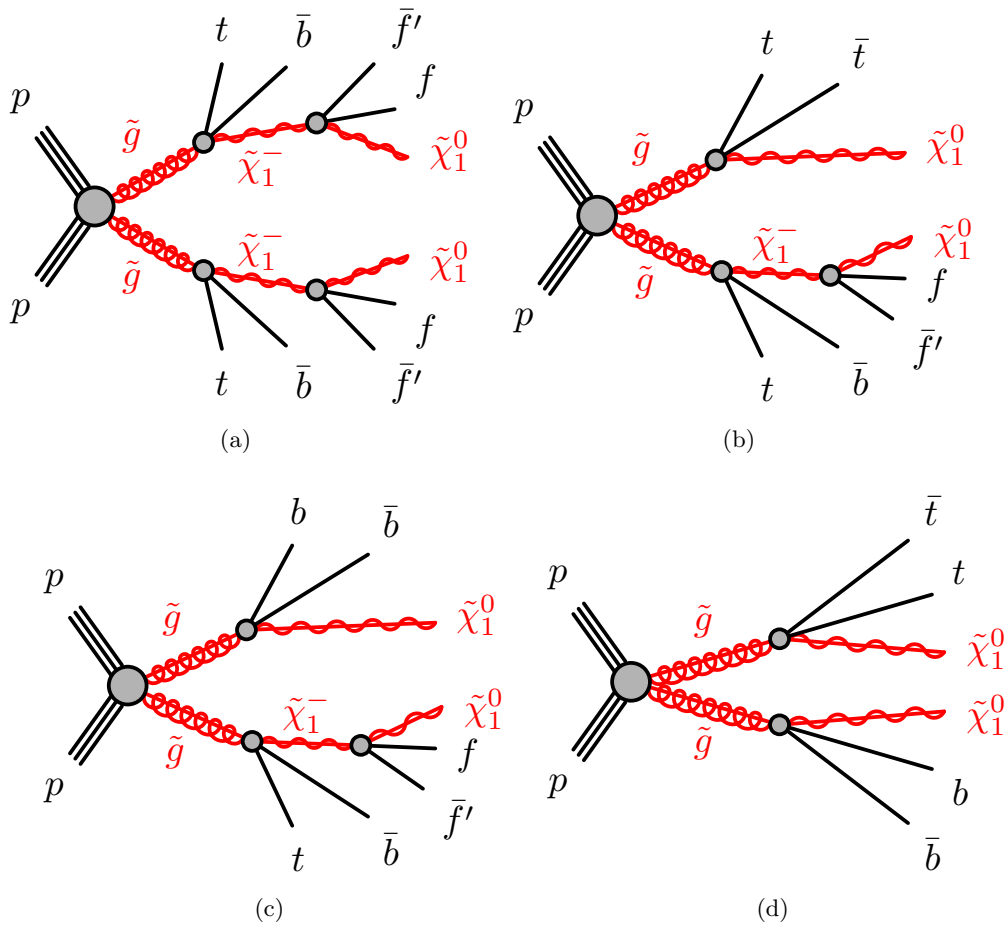
Figure 8.2: The decay topologies allowed for the Gtb simplified model.
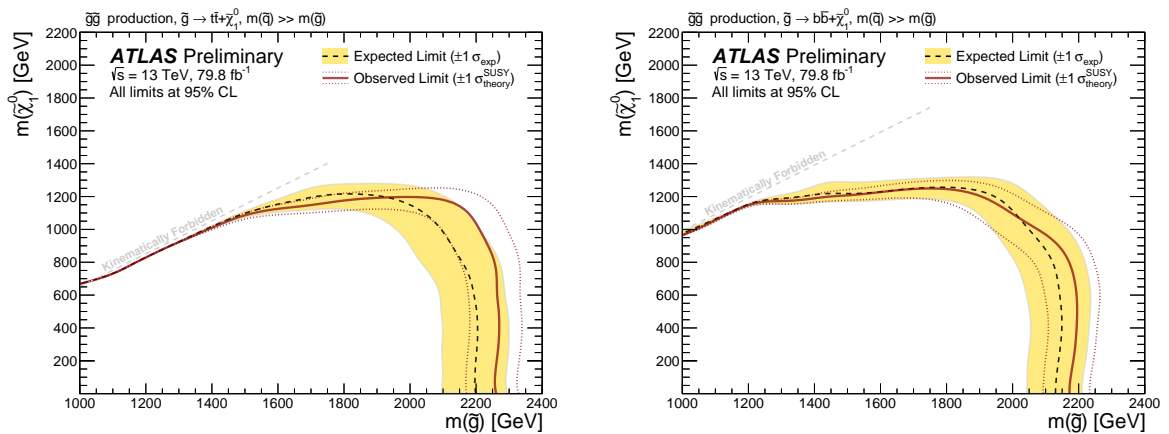
Figure 8.3: Exclusion limits in the $\tilde{\chi}_1^0$-$\tilde{g}$ mass plane for the (a) Gtt and (b) Gbb models obtained from the multi-bin strategy from the 79.8fb^{-1} version of the search [1]. The dashed and solid bold lines show the 95% CL expected and observed limits, respectively.

8.2   Object Definitions

This section will define the reconstructed physics objects used in this, and the subsequent search chapter. Two types of objects are considered; baseline and signal. Baseline (signal) refers to a looser (tighter) series of selection requirements for a specified object, such as the isolation criteria or the p_T of the object.

Jets   - Jets are reconstructed with the anti-k_T algorithm using $R_C = 0.4$ with the jet energy and mass scale calibration and are calibrated at the electromagnetic scale. Jets reconstructed with this radius are typically referred to as small-radius jets. Baseline jets must have $p_T > 30$ GeV and $|\eta| < 2.8$. To suppress pile-up jets, the "medium" JVT requirement and JVT $\gtrsim 0.59$ are applied to jets in the range $20 < p_T < 120$ GeV and $|\eta| < 2.4$. While for jets in the range $2.4 < |\eta| < 2.5$, they must have JVT $\gtrsim 0.11$. The MV2 algorithm is used to b-tag jets with $p_T > 30$ GeV and $|\eta| < 2.5$. Several operating points, corresponding to approximate efficiencies in $t\bar{t}$ of 70%, 77% and 85%, were analysed in the previous iteration of this analysis [1]. The 77% efficiency point was found to be optimal for most points of the signal model parameter-space and is considered nominal in the following results[2]. This OP corresponds to an efficiency of 77.60% for b-jets and to a rejection factor of 4, 15 and 109 for c-jets, τ-jets and light-jets respectively.

Large-radius jets are created using small-radius jets passing the overlap removal procedure, which are used as inputs for further jet (re-)clustering [145] by using the anti-k_t algorithm with $R_C = 0.8$. The calibration from the input small-R jets propagates directly to the re-clustered jets. These re-clustered jets are then trimmed by removing sub-jets (i.e., the constituent small-R jets) whose p_T falls below 10% of the p_T of the original re-clustered jet [146, 147]. The resulting large-R jets are selected by requiring them to have $p_T > 100$ GeV and $|\eta| < 2.0$. When it is not explicitly stated otherwise, the term "jets" in this thesis refers to small-R jets.

Leptons   - The choice of the lepton isolation and overlap removal settings target an improved reconstruction of leptonic boosted top quarks. Baseline electrons must pass the loose likelihood identification criteria and contain B-layer hits (LooseAndBLayerLLH), have $p_T > 20$ GeV, $|\eta| < 2.47$, $|s_{d_0}| < 5$ and $z_0 \sin\theta < 0.5$mm. Signal electrons must pass the medium likelihood identification criteria and be isolated using the Fixed cut Loose requirement. Baseline muons must pass the medium identification and to have $p_T > 20$ GeV, $|\eta| < 2.5$, $|s_{d_0}| < 3$ and $z_0 \sin\theta < 0.5$mm. They also require $d_0 > 0.2$ mm or $|z_0| > 1$ mm to suppress muons coming from cosmic rays. Signal muons must be isolated using the FixedCutTightTrackOnly requirement.

Both the muon and electron definition choices were optimised in the previous iteration of this search [1]. In this search, all lepton vetoes are implemented using the baseline definitions, whereas leptonic selections use the signal definitions. Because of the difficult reconstruction of the τ-lepton, only electrons and muons are treated as leptons and taus are reconstructed as jets instead.

---

[2]While the optimisation occasionally favours the 85% OP, the 77% OP is not significantly worse, and presents some advantages in terms of the background estimation because of the enhanced purity of the b-tagging.

Resolving Overlapping Objects - Overlaps between candidate objects are removed sequentially. Firstly, electron candidates that share a track with a muon candidate are removed to suppress contributions from muon bremsstrahlung. Overlaps between electron and jet candidates are resolved next, and finally, overlaps between remaining jets and muon candidates are removed.

Overlap removal between electron and jet candidates removes jets that are formed primarily from the showering of a prompt electron and electrons that are produced in the decay chains of hadrons. Consequently, any jet whose axis lies $\Delta R < 0.2$ from an electron is discarded. Electrons with $E_\mathrm{T} < 50$ GeV are discarded if they are within $\Delta R < 0.4$ of the axis of any remaining jet and the corresponding jet is kept. For higher-E_T electrons, the latter removal is performed using a threshold of $\Delta R = \min(0.4, 0.04 + 10\ \mathrm{GeV}/p_\mathrm{T})$ to increase the acceptance for boosted events. This p_T dependent requirement provides high lepton selection efficiency in the high-p_T regime, where *b*-jets and leptons originating from top decays become collimated.

The overlap removal procedure between muon and jet candidates is designed to remove those muons that are expected to have originated from the decay of hadrons and to retain the overlapping jet. Jets and muons may also be detected in close proximity when the jet results from high-p_T muon bremsstrahlung, and in such instances, the jet should be removed and the muon retained. These jets are characterised by very few matching inner detector tracks. Therefore, if the angular distance ΔR between a muon and a jet is lower than 0.2, the jet is removed if it has fewer than three matching inner detector tracks. After resolving overlaps with electrons and muons, selected jets must satisfy the stricter requirement of $p_\mathrm{T} > 30$ GeV.

$\boldsymbol{E_\mathrm{T}^{\mathbf{miss}}}$ - The missing transverse energy ($E_\mathrm{T}^{\mathrm{miss}}$) in the event is defined as the magnitude of the negative vector sum p_T of all selected and calibrated physics objects in the event (the baseline jets, electrons and muons, after overlap removal and application of the JVT threshold), with an extra term added to account for soft energy if it is not associated with any selected object. This soft term is calculated from inner detector tracks matched to the primary vertex to make it more resilient to pile-up contamination.

8.3   Monte Carlo Simulation and Event Selection

In previous iterations of the search, $t\bar{t}$ production was found to be the dominant SM process in most signal regions [1]. For this reason, $t\bar{t}$ is normalised with dedicated CRs and the remaining backgrounds - single top production (single top), $W(Z)$-boson production in association with an ISR jet(s) (termed $W(Z)$+jets), the production of a vector boson pair (named *diboson*, VV), rare top processes ($t\bar{t}V, t\bar{t}H, t\bar{t}t\bar{t}$), are all estimated directly from MC simulation. The remaining SM process expected to contribute to regions where leptons are absent, is multiple jets originating from QCD interactions between colliding partons (termed multi-jet). Multi-jet events are the most commonly produced events in LHC collisions. Two incoming partons scatter to create a high-p_T jet pair (di-jet), and additional jets may be generated via hard gluon emissions or gluon splittings [148]. Because of the difficulty of simulating QCD events, the multi-jet background is

estimated with a data-driven method. A kinematic correction is also applied to the one-lepton regions because of a disagreement in the data-to-MC ratio for several analysis observables.

8.3.1 Discriminating Variables

To enhance the sensitivity to the various signal processes, the signal and control regions (SR, CR) are defined using the following discriminating variables. The effective mass (m_{eff}) is calculated by

$$m_{\text{eff}} = \sum_i p_T^{\text{jet}_i} + \sum_j p_T^{\ell_j} + E_T^{\text{miss}}, \tag{8.1}$$

where the first and second sums are over the selected jets (N_{jet}) and leptons (N_{lepton}), respectively [143]. SM backgrounds are expected to have smaller values of m_{eff} because of their smaller (real) E_T^{miss} and lower jet multiplicity as opposed to RPC SUSY events that contain large E_T^{miss} from the undetected LSPs. In regions with at least one selected lepton, the transverse mass (m_T) [149, 150] composed of the p_T of the leading selected lepton (ℓ) and E_T^{miss} is defined as,

$$m_T = \sqrt{2 p_T^{\ell} E_T^{\text{miss}} \{1 - \cos[\Delta\phi(\vec{p}_T^{\text{miss}}, \vec{p}_T^{\ell})]\}}. \tag{8.2}$$

It is used to reduce the $t\bar{t}$ and W+jets background events in which the W boson decays leptonically. The m_T distribution for these backgrounds has an upper bound corresponding to the W boson mass and typically has higher values for Gtt events. Additionally, the minimum transverse mass formed by E_T^{miss} and any of the three highest-p_T b-tagged jets in the event is used;

$$m_{T,\text{min}}^{b-\text{jets}} = \min_{i \leq 3} \left(\sqrt{2 p_T^{b-\text{jet}_i} E_T^{\text{miss}} \{1 - \cos[\Delta\phi(\vec{p}_T^{\text{miss}}, \vec{p}_T^{b-\text{jet}_i})]\}} \right). \tag{8.3}$$

The $m_{T,\text{min}}^{b-\text{jets}}$ distribution has an upper bound corresponding to the top quark mass for semi-leptonic $t\bar{t}$ events, while peaking at higher values for Gbb and Gtt events. Another discriminating variable is the sum of the four highest p_T large-radius jet masses, defined as the following;

$$M_J^{\Sigma} = \sum_{i \leq 4} m_{J,i}. \tag{8.4}$$

where $m_{J,i}$ is the mass of the large-radius re-clustered jet i in the event. The decay products of a hadronically decaying boosted top quark are reconstructed in a single large-radius re-clustered jet, resulting in a jet with a high mass. This variable typically has larger values for Gtt events than for background events because Gtt events contain as many as four hadronically decaying top quarks, while $t\bar{t}$ events dominate the background.

The requirement of a selected lepton with the additional requirements on E_T^{miss}, and remaining event observables described in this section, results in the multi-jet background being negligible

for regions with at least one lepton. For the zero-lepton signal regions, the minimum azimuthal angle $\Delta\phi_{\text{min}}^{4j}$ between $\vec{p}_{\text{T}}^{\text{miss}}$ and the p_{T} of the four leading small-*R* jets in the event, defined as,

$$\Delta\phi_{\text{min}}^{4j} = \min_{i \leq 4} \left(|\phi_{\text{jet}_i} - \phi_{\vec{p}_{\text{T}}^{\text{miss}}}| \right), \tag{8.5}$$

is required to be greater than 0.4. This requirement suppresses the multi-jet background, which can produce events with large $E_{\text{T}}^{\text{miss}}$ if jets are poorly measured or neutrinos are emitted close to the jet axis.

8.3.2 Data and Simulated Events

This analysis uses the ATLAS Run 2 dataset from data-taking periods 2015, 2016, 2017 and 2018, resulting in 139.9fb^{-1} of integrated luminosity. Events must have a reconstructed primary vertex with at least two associated tracks with $p_{\text{T}} > 0.4$ GeV, consistent with the beamspot envelope. If multiple primary vertices are reconstructed, the one with the highest sum of the p_{T}^2 of the associated tracks is selected as the primary vertex [151]. Additionally, the dataset must satisfy all detector and data event cleaning requirements and the *GoodForPhysics* requirement. A $E_{\text{T}}^{\text{miss}}$ trigger with thresholds of 70 GeV, 100 GeV and 110 GeV at the HLT level for 2015, early 2016 and late 2016, 2017 and 2018 datasets, respectively, is also required. These triggers are fully efficient for events passing the preselection.

The dominant Standard Model background for this analysis is top pair production ($t\bar{t}$), which originates predominantly from gluon-gluon fusion ($gg \rightarrow t\bar{t}$, 90%) and the remaining contribution is from $q\bar{q} \rightarrow t\bar{t}$ [7]. Because of the very short lifetime of the top quark, it is expected to decay before it hadronises and consequently decays with an $\sim 100\%$ branching ratio to a real *W* boson; $t \rightarrow Wb$[7]. There are three further classifications of the decay of $t\bar{t}$ that depend on the decay of the *W* boson; $\text{Br}(W \rightarrow q\bar{q}) = 67\%$ and $\text{Br}(W \rightarrow l_i\nu_i) = 10.9\%$ where $i = e, \mu$ and τ. These can be categorised as a fully hadronic ($t\bar{t} \rightarrow W^+W^-b\bar{b} \rightarrow q\bar{q}q\bar{q}b\bar{b}$, 45.7% contribution), leptons plus jets (sometimes called semi-leptonic, $t\bar{t} \rightarrow W^+W^-b\bar{b} \rightarrow q\bar{q}b\bar{b}l^-\bar{\nu}_l + q\bar{q}b\bar{b}l^+\nu_l$, 43.8% cotribution) and di-leptonic ($t\bar{t} \rightarrow W^+W^-b\bar{b} \rightarrow l^-\bar{\nu}_l l^+\nu_l b\bar{b}$, 10.5%) final states. Feynman diagrams for the two leading processes can be seen in Figure 7.2.

The sub-dominant backgrounds in this analysis are single top production (single top) and jets produced in association with a *Z* boson (Z+jets). Single top originates from electroweak production mechanisms; $q\bar{q} \rightarrow tb$ and $qb \rightarrow qt$, mediated by virtual s- and t-channel *W* bosons. Wt-associated production originates through $bg \rightarrow W^-t$, albeit with a smaller cross section [7]. Feynman diagrams for the three processes can be seen in Figure 7.3. The *Z* boson decays primarily to hadrons ($\sim 70\%$), invisible (i.e neutrinos, 20%) and lepton pairs ($l = 3.36\%$) for $l = e, \mu$ and τ[7]. Because of this, *Z* boson production in association with jet(s), can be a significant background in fully hadronic channels because of the high $E_{\text{T}}^{\text{miss}}$ selection. Feynman diagrams for two jet events can be seen in Figure 7.4.

W-boson associated production with jet(s) is not a dominant background for the analysis, however,

it can be identified by a high p_T charged lepton from its decay (therefore only affecting leptonic channels) and missing energy from the neutrino. For this reason, the transverse mass variable is used. Feynman diagrams for these processes can be seen in Figure 7.5. The remaining backgrounds are predominantly electroweak ($t\bar{t}Z, t\bar{t}W, WW, WZ, ZZ$) and other rare processes ($\bar{t}tH, tttt$) which are categorised into "topEW", for those involving tops, and diboson for pair-produced vector boson processes.

All SM Monte Carlo simulated events are normalised using the best available theoretical calculation for their respective cross sections and a summary of the generators can be found in Table 8.1. The modelling of the dominant backgrounds in the signal regions, such as the production of $t\bar{t}$ pairs with additional high transverse momentum (p_T) jets is simulated using the Powheg [60] v2 event generator using the NNPDF3.0 [152] PDF set. The parton shower, fragmentation, and the underlying event are simulated using Pythia v8.230 [153]. The h_{damp} parameter in Powheg, which controls the p_T of the first additional emission beyond the Born level and thus regulates the p_T of the recoil emission against the $t\bar{t}$ system, is set to 1.5 times the mass of the top quark ($m_t = 172.5$ GeV).

The signal simulation is normalised using the best cross section calculations at NLO in the strong coupling constant, adding the resummation of soft gluon emission at the next-to-leading-logarithm (NLL) accuracy [154–158]. The mass difference between the $\tilde{\chi}_1^{\pm}$ and the $\tilde{\chi}_1^0$ is fixed at 2 GeV. The nominal cross section and the uncertainty are taken from an envelope of cross section predictions using different PDF sets and factorisation and renormalisation scales, as described in Ref. [159].

Process	Generator + fragmentation/hadronisation	Tune	PDF set	Cross section order
Gbb/Gtb/Gtt	MadGraph5_aMC@NLO-2.2.2 + Pythia v8.186	A14	NNPDF2.3	NLO+NLL [154–159]
$t\bar{t}$	Powheg-Boxv2 + Pythia-8.230	A14	NNPDF3.0	NNLO+NNLL [125]
Single top Wt-channel (s/t)	Powheg-Boxv2 + Pythia-8.230	PERUGIA2012	NNPDF3.0	NNLO+NNLL [125]
$t\bar{t}W$/$t\bar{t}Z$	MadGraph5_aMC@NLO-2.3.3 + Pythia-8.186	A14	NNPDF3.0	NLO [59]
4-tops	MadGraph-2.3.3 + Pythia-8.186	A14	NNPDF2.3	NLO [59]
$t\bar{t}H$	Powheg-Box (v2) + Pythia-8.186	A14	NNPDF2.3	NLO [59]
Dibosons WW, WZ, ZZ	Sherpa-2.2.1	Default	NNPDF3.0	NLO [128, 129]
W/Z+jets	Sherpa-2.2.1	Default	NNPDF3.0	NNLO [130]

Table 8.1: List of the Monte Carlo generators used for the different processes. Information is given for the tuned set of underlying event and hadronisation parameters (Tune), the PDF sets and the perturbative QCD highest-order accuracy used for the normalisation of the different processes.

8.3.3   Data-driven Multi-jet Estimate

The combination of a high E_T^{miss} requirement ($E_T^{\text{miss}} \geq 200$ GeV) and the presence of an isolated signal lepton results in a negligible multi-jet contribution to the leptonic regions. In the zero-lepton regions, multi-jet events are minimised by the large E_T^{miss} selection and imposing a minimum ϕ separation between the E_T^{miss} and the four leading jets, which suppresses events with a large amount of fake E_T^{miss} because of badly reconstructed jets. Therefore, the multi-jet background is expected to be small in the zero-lepton CC regions only, but is estimated using a template fit to this $\Delta\phi_{\text{min}}^{4j}$ observable because of the difficult modelling of QCD by simulation.

The multi-jet background prediction in the zero-lepton CC regions follows the method performed in Ref. [160]. The strategy estimates the background process for each SR from an equivalent SR but with modified $\Delta\phi_{\text{min}}^{4j}$ ($\Delta\phi_{\text{min}}^{4j} > 0.4 \to \Delta\phi_{\text{min}}^{4j} < 0.1$) selection, such that the region has similar kinematic properties but is enriched in multi-jet events. The multi-jet estimate is obtained by extrapolating the yield in the multi-jet-enriched region to the corresponding SR by the use of an exponential function in the $\Delta\phi_{\text{min}}^{4j}$ distribution. Excellent closure is observed for $0.1 < \Delta\phi_{\text{min}}^{4j} < 0.2$, however, it is not possible to validate this prediction closer to the analysis regions. Because of this and to conservatively describe the differences in the shapes between the $\Delta\phi_{\text{min}}^{4j} < 0.1$ and > 0.4 bins, a 300% uncertainty is applied to this prediction.

8.3.4   One-Lepton Event Reweighting

Discrepancies in the shapes of p_T-dependent observables, such as, m_{eff}, M_J^{Σ} and E_T^{miss}, show a negative slope between the preselected data and the expected background in the one-lepton channels, whereas no similar discrepancies are visible in the zero-lepton channel. This disagreement therefore impacts all CC CRs and the 1 lepton Gtt SRs. The disagreement is thought to originate from the modelling of the top quark, which can be corrected with the inclusion of electroweak corrections at NLO [161]. To correct for these discrepancies, a background-dependent kinematic reweighting is applied to events containing greater than one signal lepton. The correction is derived in dedicated reweighting regions (RR) designed to target the $t\bar{t}$ background, single top, $t\bar{t} + W/Z/H$ and 4-tops processes, W+jets and finally, Z+jets and electroweak diboson processes, as defined in Table 8.2. Figures presenting the data-to-SM ratio for each RR as a function of the effective mass observable can be seen in Figure 8.4.

The method begins by normalising the simulation to the data in each reweighting region. The ratio of data and normalised simulation is then computed as a function of the m_{eff} distribution and for a specified N_{jet} selection where for the $t\bar{t}$ and W+jets RRs only, an exclusive N_{jet} selection ($N_{\text{jet}} = 4, 5, 6, \geq 7$) is used or for the remaining RRs, $N_{\text{jet}} \geq 4$. A decreasing exponential function is performed to this ratio in the m_{eff} distribution, where the reweighting factor is determined per event. The reweighting factors typically take values between $\sim$1.17 and $\sim$0.19 for low and high values of m_{eff} for the $t\bar{t}$ and W+jets processes, and between $\sim$1.7 and $\sim$0.43 for low and high values of m_{eff} for the single top, $t\bar{t} + W/Z/H$ and 4-tops processes, and the Z+jets and electroweak diboson processes. The statistical uncertainty propagated from the exponential fit

Criteria common to all regions: $N_{\text{jet}} \geq 4$, E_T^{miss} or $\hat{E}_T^{\text{miss}} \geq 200$ GeV				
Reweighting Region	N_{lepton}	$N_{b-\text{jet}}$	$m_{T,\text{min}}^{b-\text{jets}}$ [GeV]	$M_{\ell\ell}$ [GeV]
$t\bar{t}$	$= 1$	$= 2$	≤ 350	-
Single top, $t\bar{t} + W/Z/H$, 4-tops	$= 1$	$= 2$	> 350	-
W+jets	$= 1$	$= 0$	-	-
Z+jets, VV	$= 2$ Opposite charge	$= 0$	-	$\in [60,120]$

Table 8.2: Definitions of the reweighting regions used to derive the m_{eff} reweighting factors applied to all simulation. The N_{lepton} requirements apply to signal leptons. The $N_{b-\text{jet}}$ requirements ensure the reweighting regions (RR) are orthogonal to all analysis signal regions. The Z and VV RR uses a definition of E_T^{miss} ($\hat{E}_T^{\text{miss}}$) that adds the lepton pair transverse momentum to the missing transverse momentum, to simulate $Z \to \nu\nu$ events.
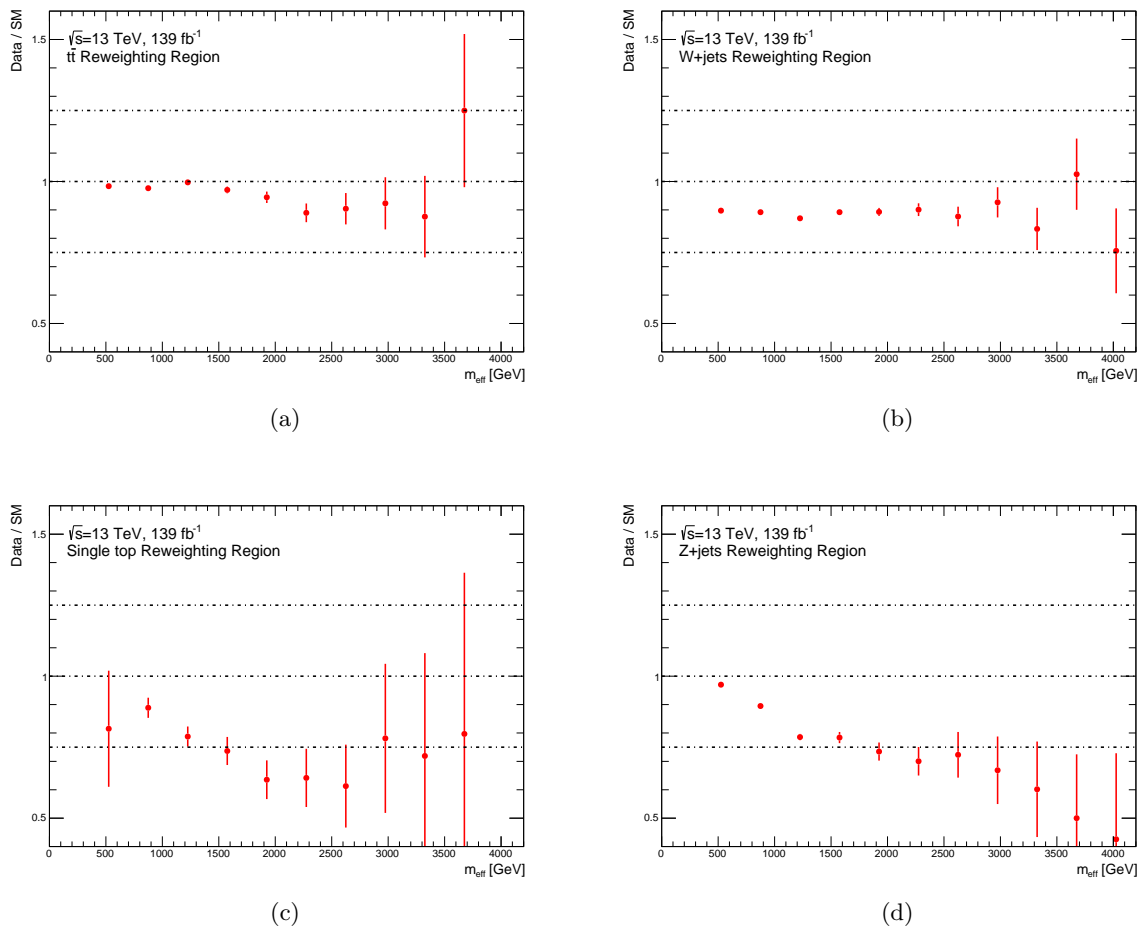
Figure 8.4: Ratio of the data to the total Standard Model background for the (a) $t\bar{t}$, (b) W+jets, (c) single top and (d) Z+jets reweighting regions. The total Standard Model background is formed from $t\bar{t}$, single top, W/Z+jets, diboson and $t\bar{t} + X$ Monte Carlo simulation. The background category $t\bar{t} + X$ includes $t\bar{t}W/Z$, $t\bar{t}H$ and $t\bar{t}t\bar{t}$ events.

parameters is included as systematic uncertainty related to this method.

8.3.5   Event Preselection

Two sets of preselection criteria are used, targeting two different final states; one containing no leptons and one with at least one lepton, referred to as zero-lepton (0L) and one-lepton (1L) channels throughout the rest of the text. Events must pass the $E_\mathrm{T}^\mathrm{miss}$ trigger and are preselected by requiring at least four jets of which at least three must be *b*-tagged and requiring that $E_\mathrm{T}^\mathrm{miss} > 200$ GeV, which ensures that the efficiency for the $E_\mathrm{T}^\mathrm{miss}$ triggers used in this analysis is close to $\sim 100\%$.

Plots of the Monte Carlo background processes, the data-driven multi-jet estimate, benchmark Gtt and Gbb signal processes as well as the data, with the one-lepton kinematic correction applied, at a preselection level for zero- and one-lepton channels can be seen in Figures 8.5 and 8.6, respectively. No significant issues in the modelling of analysis variables used in the SR definitions in zero- or one-lepton channels are observed.

Nearly all the p_T-related variables used in SR definitions (Section 8.4) have much improved data-to-MC agreement after applying the kinematic correction. The reweighting negatively affects the data-to-MC agreement for the N_jet observable. Although, the impact is small and the data-to-MC ratio is still in argeement within the total uncertainty. Therefore, when considering the improved performance for the other main analysis variables and the proceedure can be justified.

8.4   Analysis Regions

The search strategy is a set of partially overlapping selection-based, or referred to as *cut-and-count* (CC), regions that are optimised with a discovery-oreintated approach. The objective of the strategy is to have a set of easily interpretable regions in the instance of observing an excess of events above the SM background and thus, the observables chosen for optimisation are multiplicative quantities of detector signatures (such as the number of jets or leptons) or well motivated by their physical discrimination (such as $\mathrm{m}_\mathrm{T,min}^{b-\mathrm{jets}}$ with a motivated threshold of 175 GeV because of the *kinematic endpoint* for $t\bar{t}$). The final motivation for this strategy was to use these SRs to be able to obtain model-independent upper limits on the number of beyond-the-Standard Model (BSM) events at a 95% confidence level. Signal regions are designed to specifically target the Gtt, Gbb and Gtb signatures and to cover different ranges of gluino and lightest neutralino masses. The Gtt signal regions are categorised into those containing zero leptons or at least one identified charged lepton. Control and validation regions are defined by inverting one selection to remain close to the SRs whilst being mutually orthogonal to each other.

The search also uses another technique that utilises a neural network (NN) to improve the model-dependent sensitivity to the Gbb and Gtt signal processes. The neural network is trained on the four-vectors of the ten largest p_T small-radius jets, four largest p_T large-radius jets, four
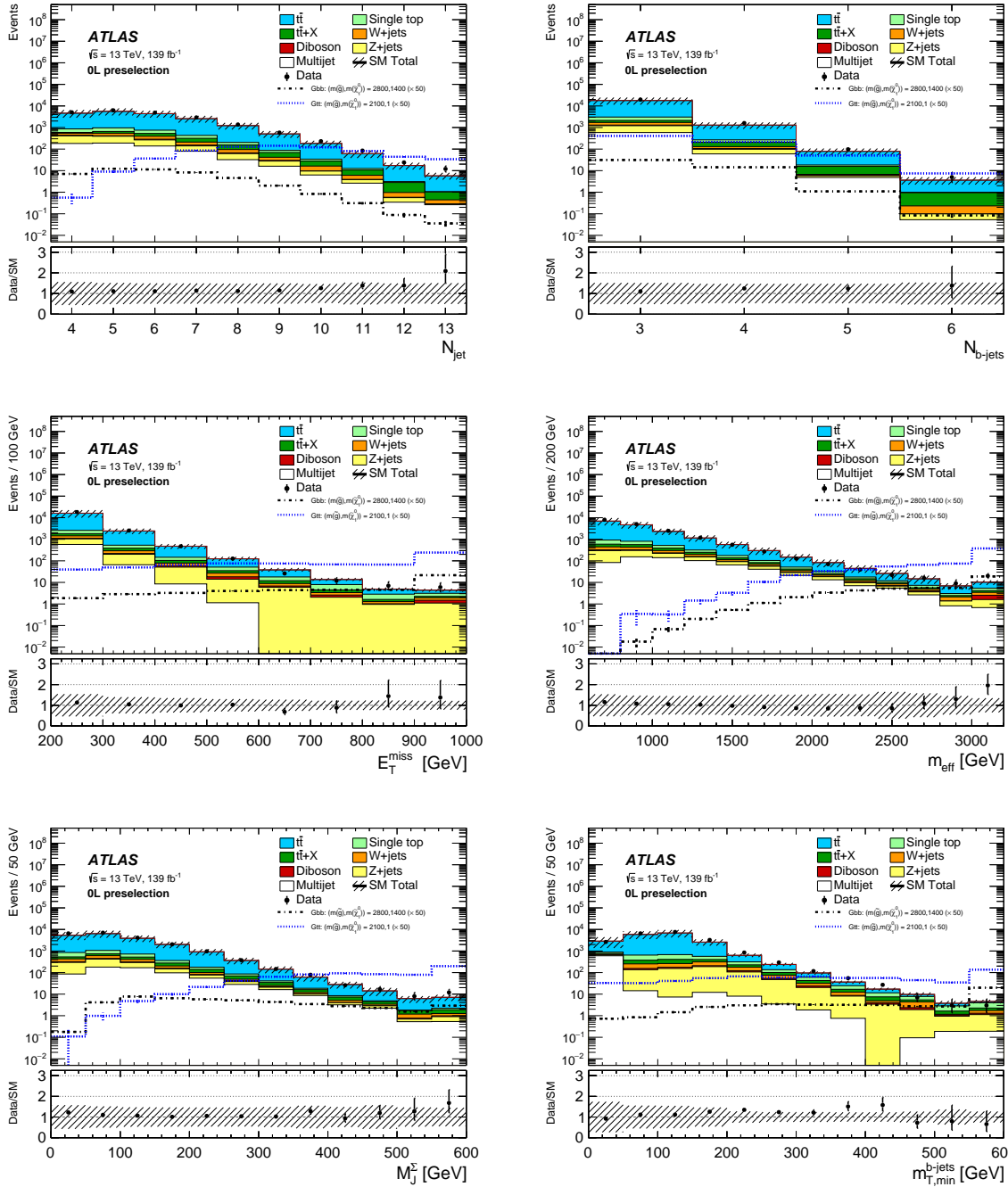
Figure 8.5: Distributions of (top-left) the number of selected jets (N_{jet}), (top-right) the number of selected b-tagged jets, (middle-left) $E_{\text{T}}^{\text{miss}}$, (middle-right) m_{eff}, (bottom-left) M_J^{Σ} and (bottom-right) $m_{\text{T,min}}^{b-\text{jets}}$ for events passing the zero-lepton preselection criteria. The statistical and experimental systematic uncertainties (as defined in Section 8.5) are included in the uncertainty band. The last bin includes overflow events. The lower part of each figure shows the ratio of data to the background prediction. All backgrounds (including $t\bar{t}$) are normalised using the best available theoretical calculation described in Section 8.3. The background category $t\bar{t} + X$ includes $t\bar{t}W/Z$, $t\bar{t}H$ and $t\bar{t}t\bar{t}$ events. Example signal models with cross sections enhanced by a factor of 50 are overlaid for comparison. Taken from Ref. [162].
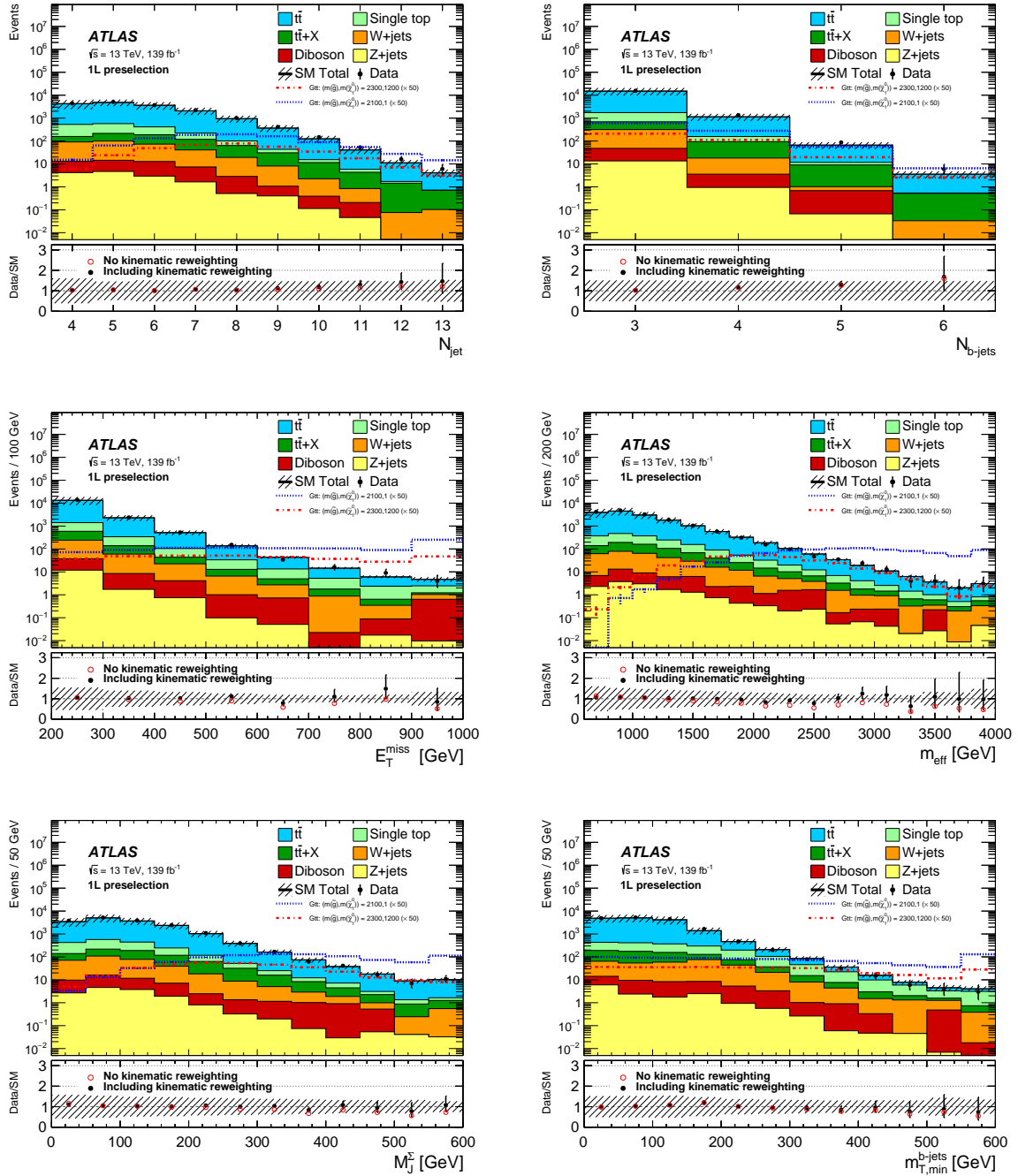
Figure 8.6: Distributions of (top-left) the number of selected jets (N_{jet}), (top-right) the number of selected *b*-tagged jets, (middle-left) $E_{\text{T}}^{\text{miss}}$, (middle-right) m_{eff}, (bottom-left) M_J^{Σ} and (bottom-right) $m_{\text{T,min}}^{b-\text{jets}}$ for events passing the one-lepton preselection criteria. The statistical and experimental systematic uncertainties (as defined in Section 8.5) are included in the uncertainty band. The last bin includes overflow events. The lower part of each figure shows the ratio of data to the background prediction. All backgrounds (including $t\bar{t}$) are normalised using the best available theoretical calculation described in Section 8.3. The background category $t\bar{t} + X$ includes $t\bar{t}W/Z$, $t\bar{t}H$ and $t\bar{t}t\bar{t}$ events. Example signal models with cross sections enhanced by a factor of 50 are overlaid for comparison. Taken from Ref. [162].

largest p_T leptons and the magnitude and azimuthal angle of the missing transverse energy for Gbb and Gtt processes as well as for SM background processes. The outputs of the NN are probabilities for an event to be Gtt, Gbb, $t\bar{t}$, single top, electroweak-top processes, W/Z+jets and diboson. A detailed discussion of this analysis has not been included in this thesis because the author made a non-significant contribution. The NN analysis, however, contributes significantly to the model-dependent 95% CLs set on the Gbb and Gtt simplified scenarios, and these will be presented later for comparisons to the results obtained by the CC regions.

As in the previous iterations of the analysis, dedicated regions are provided for Gtt in the zero-lepton channel and one-lepton channel and for Gbb in the zero-lepton channel only. For the first time, a set of regions optimised to be sensitive to Gtb models are provided. As illustrated in Figure 8.7, for each Gtt-0L, Gtt-1L, Gbb and Gtb processes, SRs are defined for a representative area of phase-space based on the kinematics of the model. The quantity used to do this is referred to as the *mass splitting* calculated by $\Delta m = m(\tilde{g}) - m(\tilde{\chi}_1^0)$, which is a function of the two model parameters. Since in practice one cannot define a SR for every signal in the model-space, the clear classification of groups in the optimisation process decided the number of SRs. Ultimately this leads to three regions:

- A "Boosted" (B) SR that targets signals with a large mass splitting between the gluino and the $\tilde{\chi}_1^0$; $m(\tilde{g}) \gg m(\tilde{\chi}_1^0)$. For these signals, the decay products are boosted and the events are characterised by high values for all energy-related variables (E_T^{miss}, m_{eff}, M_J^Σ, ...).

- A "Moderate" (M) SR that targets signals with intermediate mass splitting; $m(\tilde{g}) > m(\tilde{\chi}_1^0)$.

- A "Compressed" (C) SR that targets signals close to the limit for the production of the final-state particles; $m(\tilde{g}) \approx m(\tilde{\chi}_1^0) + 2 \times m_{t/b}$.
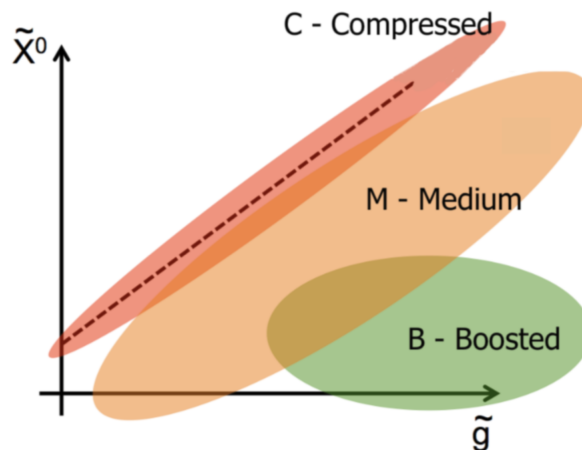
Figure 8.7: Representation of the three targeted sets of kinematics; boosted (B), moderate (M) and compressed (C) as a function of the two SUSY signal parameters $(\tilde{g}, \tilde{\chi}_1^0)$.

To define the selection criteria for each of these areas of phase-space an optimisation framework [163] was used for each of the Gtt, Gbb and Gtb signal processes. Given a set of possible selections, for example, $E_T^{\text{miss}} >$ in the range [300,400] GeV in steps of 50 GeV and $m_{\text{eff}} >$ [1500,2000] GeV in steps of 250 GeV; the optimisation code considers all the possible combinations. It would then

choose the combination that has the highest expected significance[3], require ≥ 0.5 background events and $t\bar{t}$ MC statistical uncertainty $< 30\%$. While there is no requirement on the minimum number of expected SM events in the SRs, all the candidate-SRs where the total background expectation has a MC statistical uncertainty larger than 30% are discarded. This is included to ensure that the SRs are not optimised based on statistical fluctuations in the background.

Each SR has a corresponding control region (CR) defined for a data-driven estimate of the dominant $t\bar{t}$ background. To ensure that the region is kinematically similar to the SR but orthogonal to it, a lepton requirement is used. To ensure sufficient purity of the targeted SM background, a reversed m_T is also used, which selects events with a leptonic W decay to enhance the semi-leptonic $t\bar{t}$ background in the region. The m_T requirement also reduces the contamination from the Gbb signal and other SM backgrounds, such as WW and fully leptonic $t\bar{t}$. Adjacent to this is ensuring, for a benchmark signal point, that the region is not sensitive to that signal as to potentially unblind a signal-sensitive region of phase-space. To do this is a threshold on the *signal contamination* is required - quantified by the ratio of the yield of the signal in that region to the total SM background. For this optimisation, the signal contamination in the CRs is required to be lower than 1%. The regions also require a high $t\bar{t}$ purity (minimum $\geq 40\%$ $t\bar{t}$ of the total background composition and no large contributions from rare processes) for an accurate measurement of the $t\bar{t}$ background normalisation. It is also beneficial for control regions to have a high number of data events ($O(100)$) however, a minimum of 20 data events was required in the optimisation. With a higher number of data events, the measurement of the $t\bar{t}$ normalisation can be constrained with greater certainty and hence, the statistical uncertainty in the normalisation is not limiting the sensitivity of the corresponding SR and VR.

Validation regions (VR) are used to validate the analysis strategy before unblinding the data in the SR. Similar to the CR design procedure, each VR is required to be kinematically similar but orthogonal to the corresponding SR and mutually orthongal to the corresponding CR. To ensure orthogonality for the VRs, only variables with sufficient data-to-MC agreement and kinematically well-understood variables were chosen to be inverted. This resulted in E_T^{miss}, m_{eff} and M_J^{Σ} being acceptable for inversion. The signal contamination from a benchmark model is also required to be low $< O(10\%)$. The relaxation of one or more selection thresholds was permitted to allow for more data events.

8.4.1 Region Optimisation - Gbb

This section describes the optimisation of the Gbb signal, control and validation regions. The variables used in the optimisation of the Gbb signal regions are; $m_{\text{T,min}}^{b-\text{jets}}$, $\Delta\phi_{\text{min}}^{4j}$, E_T^{miss}, m_{eff}, N_{jet}, $N_{b-\text{jet}}$, p_T^{1j}, N_{lepton} and the range was motivated by previous versions of the analysis as well as the physical kinematics of the observable.

The SR optimisation procedure is extremely time consuming and so, the strategy of performing the optimisation over several iterations with fewer degrees of freedom (DoF) as opposed to a

---

[3]Calculated from a binomial distribution for a specified signal yield s, background yield b, and a fixed uncertainty size ($\sigma_b = 30\%$) using the RooStats [107] function `Roostats::BinomialExpZ(s, b, 30%)` [76].

single optimisation with many DoF was favoured. The strategy enabled the quick determination of key analysis variables (such as the number of leptons) and an initial an estimate of the selection threshold. Once this was performed, further iterations of the optimisation were performed with finer ranges of selection thresholds because some variables already have their optimised values, such as the lepton requirement or $\Delta\phi^{4j}_{\min} \geq 0.4$. An example of one of the finer optimisations performed is shown in Table 8.3. The results of the nominal variable scan for each signal in the model parameter-space can be seen in Figure 8.8.

Parameters	$N_{\text{b-jet}} \geq$	$N_{\text{jet}} \geq$	$m^{b-\text{jets}}_{\text{T,min}} >$	$E^{\text{miss}}_{\text{T}} >$	$m_{\text{eff}} >$	$p^{1j}_{\text{T}} >$
Min value	3	4	70	300	1500	20
Max value	4	6	150	600	2700	80
Step size	1	1	20	50	100	15

Table 8.3: Ranges of selection thresholds used in the final iteration of the Gbb SR optimisation, where all kinematic variables are expressed in GeV.

If one uses for each signal point of the Gbb mass plane the corresponding optimised selections for each variable, the resulting expected significance can be seen in Figure 8.9. To achieve the goals of having only a limited number of SRs and at the same time having good sensitivity across the entire Gbb signal model-space, three SRs are defined: Boosted, which targets $\Delta m \geq 1.5$ TeV, Moderate, which targets $0.3 \leq \Delta m \leq 1.5$ TeV, and Compressed, which targets $\Delta m \leq 0.3$ TeV. The definitions of Gbb SRs are summarised in Table 8.4.

Targeted kinematics	Type	N_{lepton}	p^{1j}_{T} [GeV]	m_{eff} [GeV]	$E^{\text{miss}}_{\text{T}}$ [GeV]	$m^{b-\text{jets}}_{\text{T,min}}$ [GeV]	m_{T} [GeV]
Region B (Boosted, Large Δm)	SR	$= 0$	> 65	> 2600	> 550	> 130	
	CR	$= 1$	> 65	> 2600	> 450		< 150
	VR	$= 0$	> 65	< 2400	> 550	> 130	
Region M (Moderate Δm)	SR	$= 0$	> 30	> 2000	> 550	> 130	
	CR	$= 1$	> 30	> 2000	> 550		< 150
	VR	$= 0$	> 30	> 1600	< 500	> 80	
Region C (Compressed, small Δm)	SR	$= 0$	> 30	> 1600	> 550	> 130	
	CR	$= 1$	> 30	> 1600	> 550		< 150
	VR	$= 0$	> 30	> 1500	< 450	> 130	

Table 8.4: Definitions of the Gbb SRs, CRs and VRs of the analysis regions. The jet p_{T} requirement is also applied to b-tagged jets.

The CRs for the Gbb regions require exactly one signal lepton because the main background is expected to be semi-leptonic $t\bar{t}$. Being a zero-lepton channel, one would expect fully hadronic $t\bar{t}$ to be dominant but because of the $E^{\text{miss}}_{\text{T}}$ requirement, leptonic decays of the W boson with a misidentified e or μ as jets or a hadronic τ reconstructed as a jet as well as the potential for them to be out-of-acceptance[4] means semi-leptonic dominates the $t\bar{t}$ composition. The selected number

---

[4]Out-of acceptance is consdiered when the objects p_{T} or η is out of the detection and therefore reconstruction range.
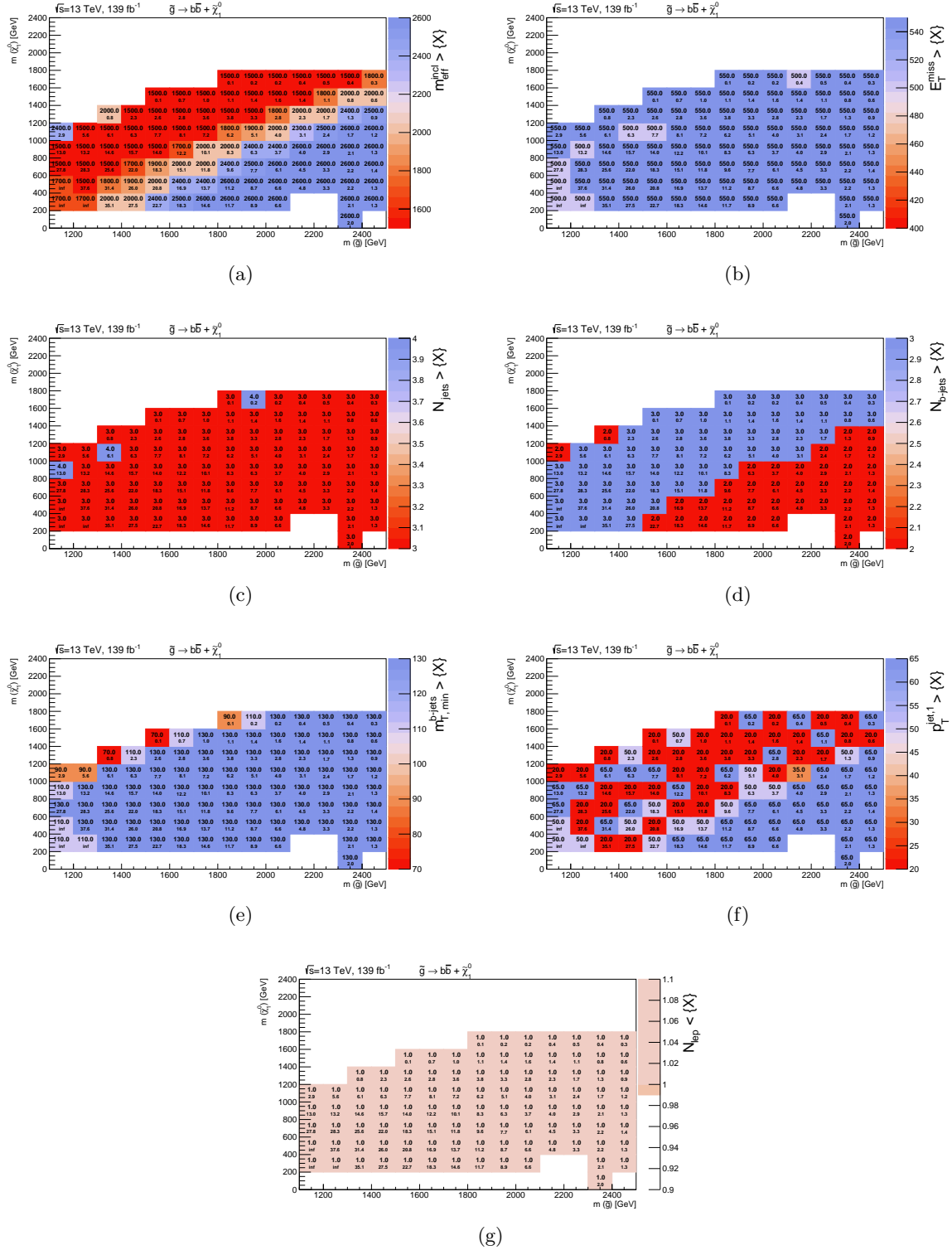
Figure 8.8: Optimal selection thresholds for each model in the parameter-space in the Gbb zero-lepton channel for variables. (a) m_{eff} GeV, (b) E_T^{miss} GeV, (c) N_{jet}, (d) $N_{\text{b-jet}}$, (e) $m_{T,\text{min}}^{b-\text{jets}}$ GeV, (f) p_T^{1j} GeV (g) N_{lepton}.
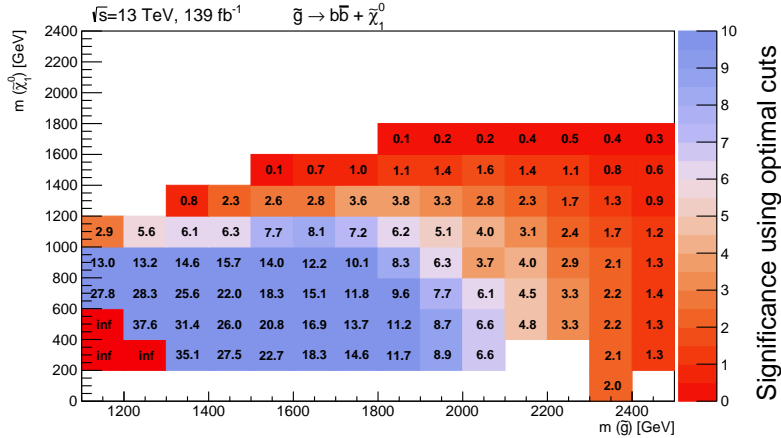
Figure 8.9: The expected significance for each model of the Gbb signal grid.

of jets in the optimisation is already low ($N_{\text{jet}} \geq 4$, as expected because the Gbb signal model has a lower number of jets with respect to the Gtt model). Other than the lepton multiplicity and the selection on m_T, the main differences between the CRs and the SRs are; the selection on E_T^{miss} is relaxed in Gbb-M and Gbb-C and the selection on $m_{T,\text{min}}^{b-\text{jets}}$ is removed across all regions. Plots for all control regions for Gbb binned in m_{eff} are shown in Figure 8.10 and the definitions of the CRs can be found in Table 8.4.

In each Gbb region, a VR is defined to validate the extrapolation of the number of leptons between the CR and the SR. VRs require a lepton veto, and the variable that is used to achieve orthogonality between each VR and the corresponding SR is m_{eff} in Gbb-B and E_T^{miss} in Gbb-M and Gbb-C. The selections on the other kinematic variables are loosened to ensure the uncertainty in the number of data events is not significant. Plots of the corresponding validation regions binned in m_{eff} can be found in Figure 8.11 and the definitions of the regions can be found in Table 8.4.

8.4.2   Region Optimisation - Gtb

This section describes the optimisation of the Gtb signal, control and validation regions. Gtb models share an intermediate final state between the Gbb and Gtt signal processes that depends on the number of stops and sbottoms produced. When the mass splitting between the gluino and neutralino is large, the top quarks tend to be highly boosted and their decay products become collimated. A topological observable, built from the mass of large-radius jets re-clustered from small-radius jets, M_J^{Σ}, is used to enhance the signal discrimination for Gtt and thus is powerful for this decay too. The remaining variables used in the optimisation of the Gtb signal regions follow similar to those used in the Gbb optimisation with the addition of those used for Gtt; $m_{T,\text{min}}^{b-\text{jets}}$, $\Delta\phi_{\text{min}}^{4j}$, E_T^{miss}, m_{eff}, M_J^{Σ}, N_{jet}, $N_{b-\text{jet}}$, p_T^{1j}, N_{lepton}. This is included to create SRs sensitive to those signals which are not considered in the optimisation of the Gbb and Gtt SRs.

The final iteration of the optimisation performed for a range of selection thresholds for the Gtb optimisation is shown in Table 8.5. The results of this optimisation can be seen in Figure
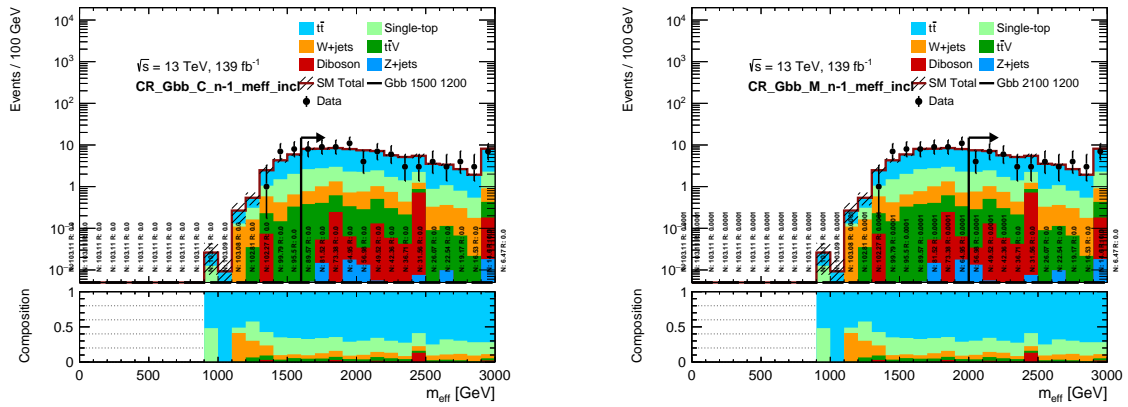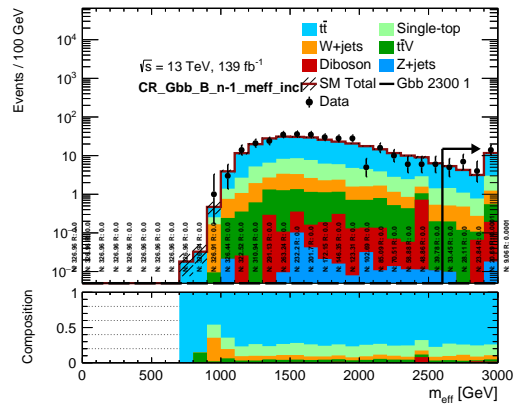
Figure 8.10: The m$_{\text{eff}}$ distributions of the one-lepton $t\bar{t}$ control regions of the Gbb channel: (a) Compressed, (b) Moderate and (c) Boosted.
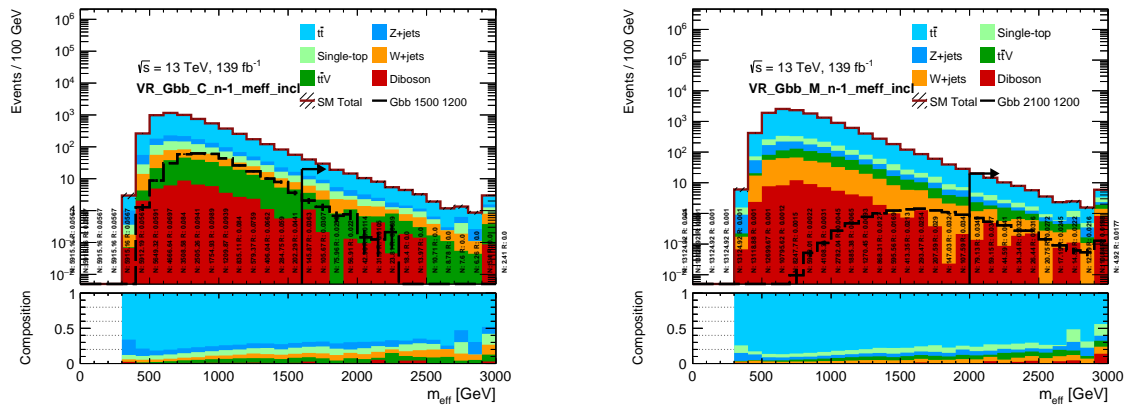
(a)

(b)
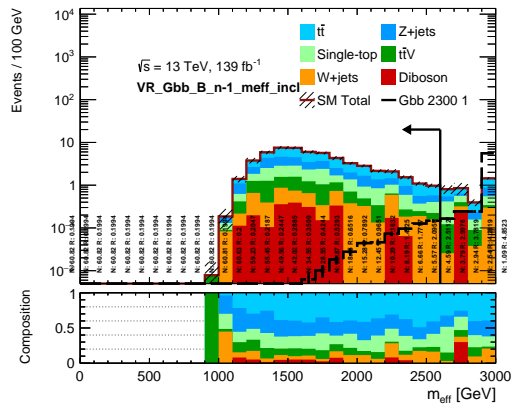
(c)

Figure 8.11: The m_{eff} distributions for the validation regions of the Gbb channel: (a) Compressed, (b) Moderate and (c) Boosted.

8.12. Figure 8.12 presents a much coarser granularity in neutralino masses compared to the corresponding Figures for Gbb. This reflects the different structure of the experimentally available signal models, which in turn is motivated by the different strategy for interpreting the analysis results. While for Gtt and Gbb, the main interpretation will indeed be in the $\tilde{g} - \tilde{\chi}_1^0$ mass plane, the Gtb signals are used only as benchmark models for the analysis to define further discovery regions and as part of the signals that constitute a reinterpretation. This difference in granularity has no impact on the optimisation. It does, however, have an effect only for the interpretation of the results.

Parameters	$N_{b-jet} \geq$	$N_{jet} \geq$	$m_{T,min}^{b-jets} >$	$E_T^{miss} >$	$m_{eff} >$	$M_J^{\Sigma} >$	$p_T^{1j} >$
Min value	3	4	100	300	1300	0	30
Max value	4	6	140	600	2600	350	50
Step size	1	1	10	50	100	50	10

Table 8.5: Ranges of selection thresholds used in the final iteration of the Gbb SR optimisation, where all kinematic variables are expressed in GeV.

If one uses the optimised selections for each variable for the signal in the parameter-space, the expected significance for that model can be seen in Figure 8.13.

As per the Gbb SR strategy, three Gtb SRs are defined, targeting Boosted, Moderate and Compressed regions, with the same mass splitting definitions as those from Gbb. A summary of the signal region definitions can be found in Table 8.6.

Targeted kinematics	Type	N_{lepton}	N_{jet}	N_{b-jet}	m_{eff} [GeV]	E_T^{miss} [GeV]	$m_{T,min}^{b-jets}$ [GeV]	m_T [GeV]	M_J^{Σ} [GeV]
Region B (Boosted, Large Δm)	SR	$= 0$	≥ 4	≥ 3	> 2500	> 550	> 130		> 200
	CR	$= 1$	≥ 4	≥ 3	> 2200	> 400		< 150	> 200
	VR	$= 0$	≥ 4	≥ 3	< 2500	> 450	> 130		> 200
Region M (Moderate Δm)	SR	$= 0$	≥ 6	≥ 4	> 2000	> 550	> 130		> 200
	CR	$= 1$	≥ 6	≥ 4	> 1700	> 300		< 150	> 200
	VR	$= 0$	≥ 6	≥ 4	> 1600	< 550	> 110		> 200
Region C (Compressed, small Δm)	SR	$= 0$	≥ 7	≥ 4	> 1300	> 500	> 130		> 50
	CR	$= 1$	≥ 7	≥ 4	> 1300	> 350		< 150	> 50
	VR	$= 0$	≥ 7	≥ 4	> 1300	< 500	> 80		> 50

Table 8.6: Definitions of the Gtb SRs, CRs and VRs.

CRs for the Gtb regions are defined with the same strategy as for the Gbb CRs. They require exactly one signal lepton, have an upper selection on m_T to reduce signal contamination and have the same requirement on the number of jets and number of *b*-jets as the SRs. Other than the lepton multiplicity and the selection on m_T, the main differences between the CRs and the SRs are; the selection on m_{eff} is relaxed in Gtb-M and Gtb-B, the selection on E_T^{miss} is relaxed and $m_{T,min}^{b-jets}$ is removed for all regions. Plots of the Gtb CRs binned in m_{eff} can be found in Figure 8.14 and the definitions of the regions can be found in Table 8.6.

In each Gtb region, a VR is defined to validate the extrapolation of the number of leptons
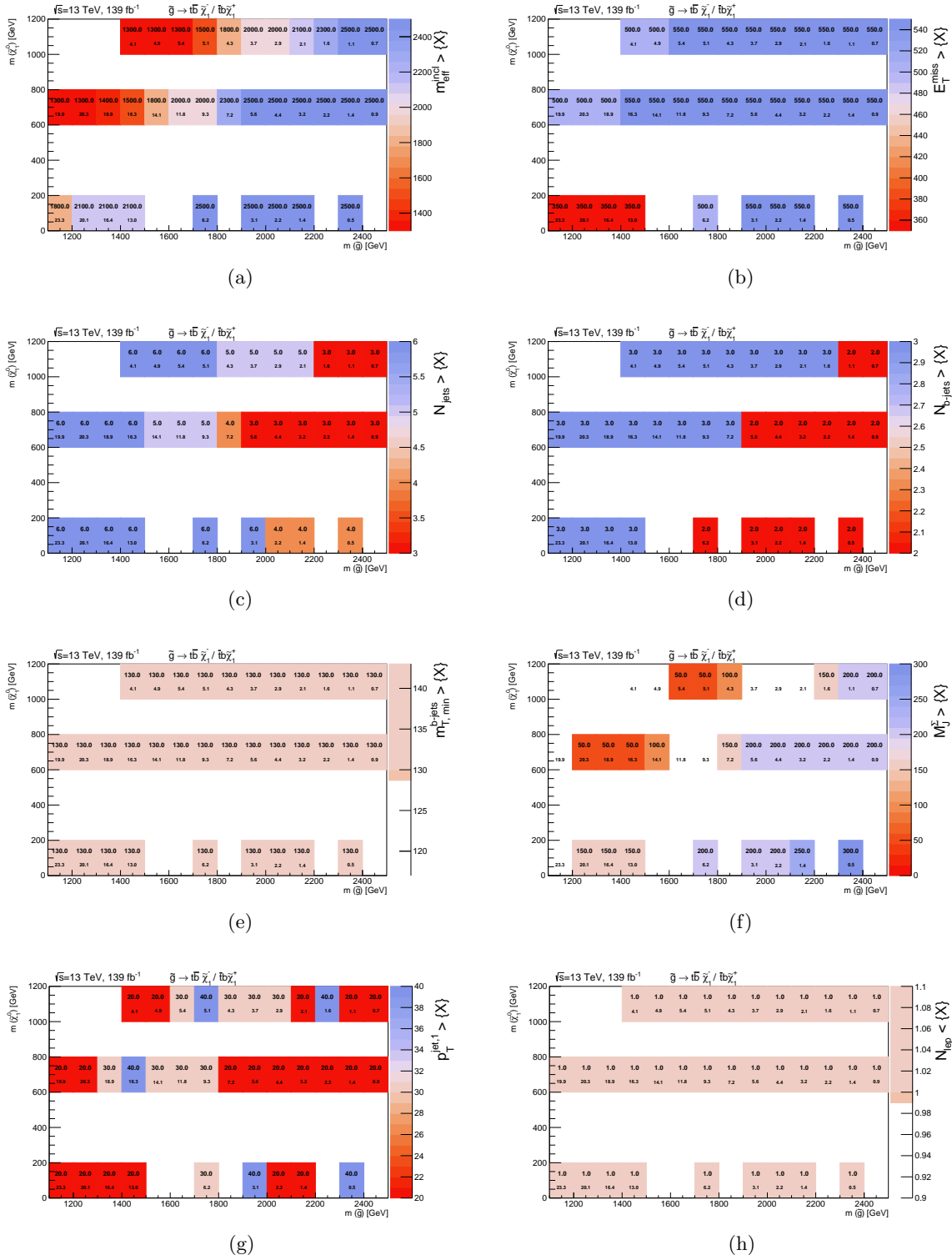
Figure 8.12: Optimal selection thresholds for each model in the parameter-space in the Gtb zero-lepton channel for variables; (a) m_{eff} GeV, (b) E_T^{miss} GeV, (c) N_{jet}, (d) $N_{\text{b-jet}}$, (e) $m_{T,\text{min}}^{b-\text{jets}}$ GeV, (f) M_J^{Σ} GeV, (g) p_T^{1j} GeV (h) N_{lepton}.
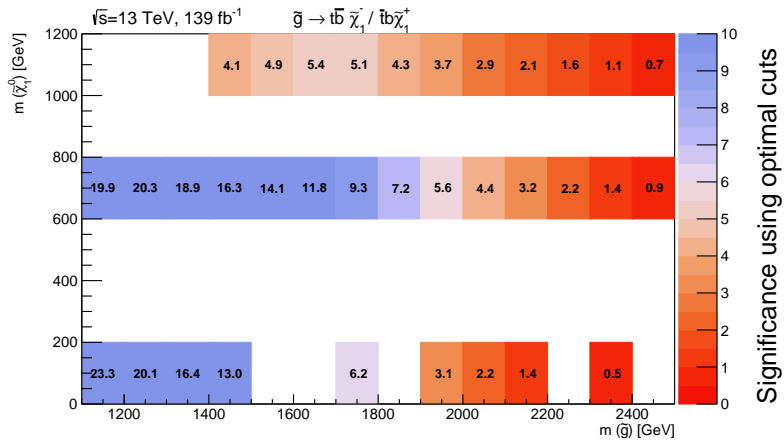
Figure 8.13: The expected significance for mass point of the Gtb signal grid.

(a)

(b)

(c)
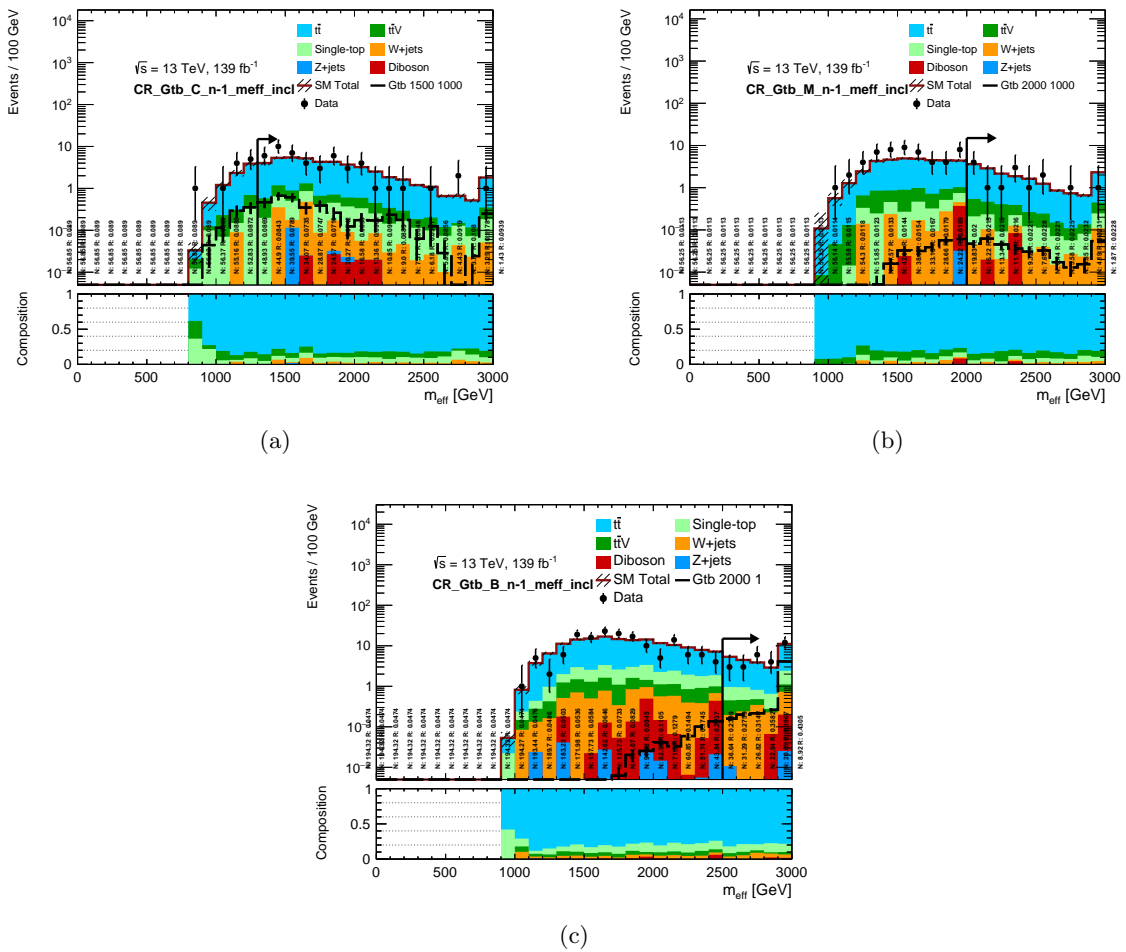
Figure 8.14: The m$_{\text{eff}}$ distributions for the one-lepton $t\bar{t}$ control regions of the Gtb channel: (a) Compressed, (b) Moderate and (c) Boosted.

between the CR and the SR. VRs require a lepton veto, and the variable that is used to achieve orthogonality between each VR and the corresponding SR is m_{eff} in Gtb-B and E_T^{miss} in Gtb-M and Gtb-C. The selections of other kinematic variables are loosened to ensure adequate statistics. Plots of the corresponding validation regions binned in m_{eff} can be found in Figure 8.15 and the definitions of the regions can be found in Table 8.6.
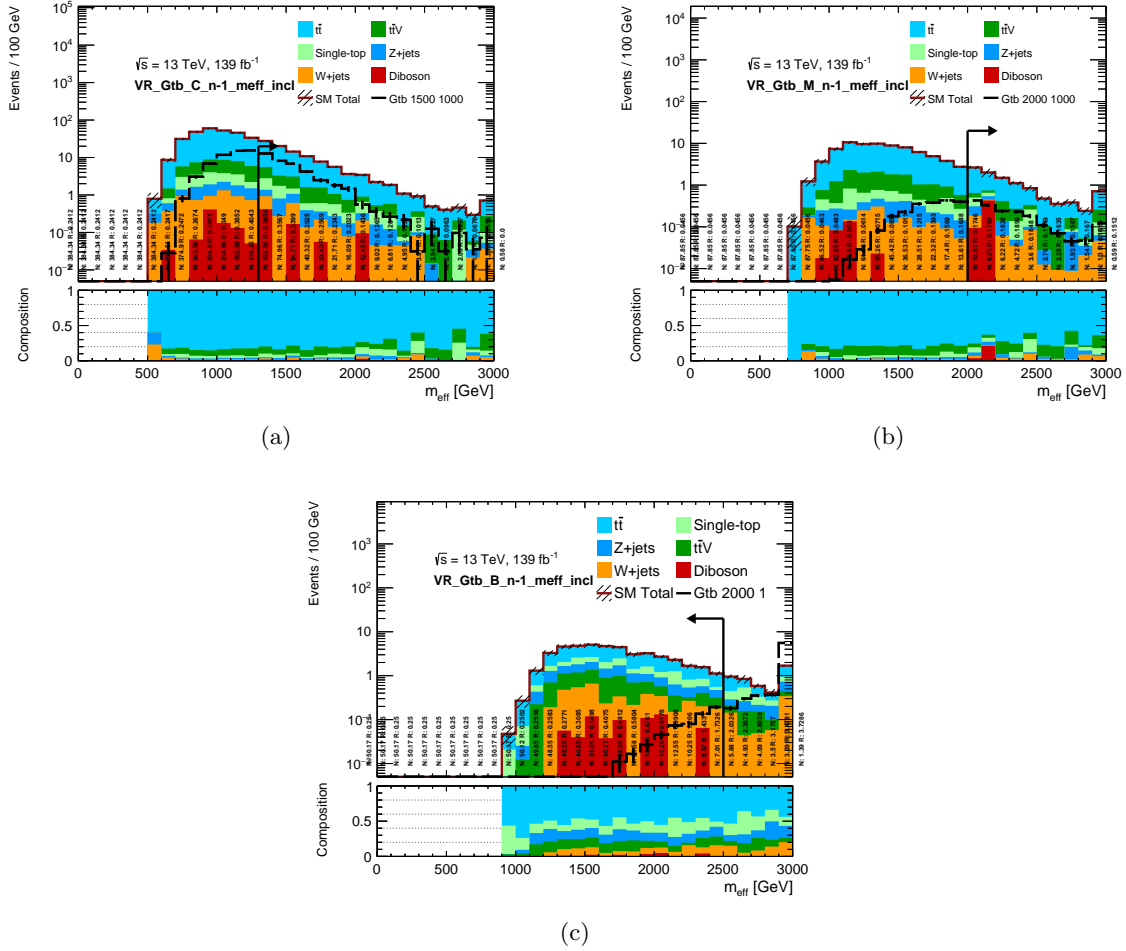
Figure 8.15: The m_{eff} distributions for the validation regions of the Gtb channel: (a) Compressed, (b) Moderate and (c) Boosted.

8.4.3 Remaining Regions

The author of this thesis did not perform the optimisation of the zero and one-lepton Gtt signal regions, however, they are key components of the analysis strategy and hence, their definitions can be found in Tables 8.7-8.8, respectively. The same optimisation strategy was performed, however, it was noticed a second moderate region was beneficial and thus, there are four SRs for the Gtt channels instead of the three for Gbb and Gtb.

Targeted kinematics	Type	N_{lepton}	N_{jet}	$N_{\text{b-jet}}$	E_T^{miss} [GeV]	$\Delta\phi_{\text{min}}^{4j}$	m_{eff} [GeV]	m_T [GeV]	$m_{T,\text{min}}^{b-\text{jets}}$ [GeV]	M_J^{Σ} [GeV]
Region B (Boosted, Large Δm)	SR	$= 0$	≥ 5	≥ 3	≥ 600	≥ 0.4	≥ 2900	–	≥ 120	≥ 300
	CR	$= 1$	≥ 4	≥ 3	≥ 200	–	≥ 2000	< 150	–	≥ 150
	VR	$= 0$	≥ 5	≥ 3	≥ 250	≥ 0.4	≥ 2000	–	–	< 300
Region M1 (Moderate Δm)	SR	$= 0$	≥ 9	≥ 3	≥ 600	≥ 0.4	≥ 1700	–	≥ 120	≥ 300
	CR	$= 1$	≥ 8	≥ 3	≥ 200	–	≥ 1100	< 150	–	≥ 150
	VR	$= 0$	≥ 9	≥ 3	≥ 300	≥ 0.4	≥ 1400	–	–	< 300
Region M2 (Moderate Δm)	SR	$= 0$	≥ 10	≥ 3	≥ 500	≥ 0.4	≥ 1100	–	≥ 120	≥ 200
	CR	$= 1$	≥ 9	≥ 3	≥ 200	–	≥ 800	< 150	–	≥ 100
	VR	$= 0$	≥ 10	≥ 3	≥ 300	≥ 0.4	≥ 800	–	–	< 200
Region C (Compressed, small Δm)	SR	$= 0$	≥ 10	≥ 4	≥ 400	≥ 0.4	≥ 800	–	≥ 180	≥ 100
	CR	$= 1$	≥ 9	≥ 4	≥ 200	–	≥ 800	< 150	–	≥ 100
	VR	$= 0$	≥ 10	≥ 4	≥ 200	≥ 0.4	≥ 800	–	–	< 100

Table 8.7: Definitions of the Gtt zero-lepton SRs, CRs and VRs, which depend on the difference between the gluino and neutralino masses (Δm).

Targeted kinematics	Type	N_{jet}	E_T^{miss} [GeV]	m_{eff} [GeV]	m_T [GeV]	$m_{T,\text{min}}^{b-\text{jets}}$ [GeV]	M_J^{Σ} [GeV]
Region B (Boosted, Large Δm)	SR	≥ 4	≥ 600	≥ 2300	≥ 150	≥ 120	≥ 200
	CR	$= 4$	≥ 200	≥ 1500	< 150	–	–
	VR-m_T	≥ 4	≥ 200	≥ 1500	≥ 150	–	< 200
	VR-$m_{T,\text{min}}^{b-\text{jets}}$	≥ 5	≥ 200	≥ 1200	< 150	≥ 120	≥ 200
Region M1 (Moderate Δm)	SR	≥ 5	≥ 600	≥ 2000	≥ 200	≥ 120	≥ 200
	CR	$= 5$	≥ 200	≥ 1200	< 200	–	–
	VR-m_T	≥ 5	≥ 200	≥ 1200	≥ 200	–	< 200
	VR-$m_{T,\text{min}}^{b-\text{jets}}$	≥ 6	≥ 200	≥ 1000	< 200	≥ 120	≥ 100
Region M2 (Moderate Δm)	SR	≥ 8	≥ 500	≥ 1100	≥ 200	≥ 120	≥ 100
	CR	$= 8$	≥ 200	≥ 800	< 200	–	–
	VR-m_T	≥ 8	≥ 200	≥ 800	≥ 200	–	< 100
	VR-$m_{T,\text{min}}^{b-\text{jets}}$	≥ 9	≥ 200	≥ 800	< 200	≥ 120	≥ 100
Region C (Compressed, small Δm)	SR	≥ 9	≥ 300	≥ 800	≥ 150	≥ 120	–
	CR	$= 9$	≥ 200	≥ 800	< 150	–	–
	VR-m_T	≥ 9	≥ 200	≥ 800	≥ 150	< 120	–
	VR-$m_{T,\text{min}}^{b-\text{jets}}$	≥ 10	≥ 200	≥ 800	< 150	≥ 120	–

Table 8.8: Definitions of the Gtt one-lepton SRs, CRs and VRs, which depend on the difference between the gluino and neutralino masses (Δm). All regions require an inclusive $N_{\text{lepton}} \geq 1$ selection.

8.5 Uncertainties

This section will summarise all the theoretical and experimental uncertainties associated with this and the subsequent chapter search strategies. The systematic configuration is implemented for the results described in Section 8.6.

8.5.1 Theoretical

The uncertainties in the modelling of the SM background and signal processes are taken into account by assessing their generation in Monte Carlo as well as the theoretical cross section.

$t\bar{t}$ - Hadronisation and parton showering model uncertainties of the $t\bar{t}$ background are evaluated by comparing two simulation processes generated with POWHEG and showered by either HERWIG++ v2.7.1 or PYTHIA v6.428 [164]. Additionally, systematic uncertainties in the modelling of initial- and final-state radiation are explored with POWHEG simulation, showered with two alternative settings of PYTHIA v6.428 [165]. The uncertainty caused by the choice of generator for the matrix element calculation is estimated by comparing the expected yields obtained using $t\bar{t}$ processes generated with MADGRAPH5_aMC@NLO and POWHEG. The total theoretical uncertainty in the $t\bar{t}$ background estimation is taken as the sum in quadrature of these individual components and has a maximum impact of 37%. Moreover, an additional uncertainty is assigned to the fraction of $t\bar{t}$ events produced in association with additional heavy-flavour jets [164] (i.e. $t\bar{t}+ \geq 1b$ and $t\bar{t}+ \geq 1c$) is found to impact no larger than 6%.

Single top - Modelling uncertainties affecting the single top processes arise especially from the interference between the $t\bar{t}$ and Wt processes. This uncertainty is estimated using inclusive $WWbb$ events, generated using MADGRAPH5_aMC@NLO, which are compared with the sum of $t\bar{t}$ and Wt processes. Furthermore, as with the $t\bar{t}$ modelling uncertainties, variations of PYTHIA v6.428 settings to increase or decrease the amount of radiation are also evaluated. An uncertainty is included for the cross section of single top processes, which has a maximum impact of 5% [166]. The overall impact of single top theoretical uncertainties varies between 2.9 and 11.2%.

V**+jets** - Uncertainties related to factorisation and renormalisation scales and those affecting the matching procedure between the matrix element and parton shower in the W/Z+jets backgrounds are taken into account [164]. These are found to impact no larger than 7%. Additional uncertainties related to the heavy and light flavour composition of jets are estimated by varying the yields of events containing at least one b-jet or c-jet with an uncertainty of 30%. These uncertainties have a maximum impact of 7%.

Remaining - A 50% uncertainty is assigned to $t\bar{t}+W/Z/H$, $t\bar{t}t\bar{t}$ and diboson backgrounds, and is assumed uncorrelated across all SRs. For electroweak top (diboson) processes, these have

a maximum impact of 12% (3%). The uncertainties in the cross sections of signal processes are determined from a series of different cross section predictions using an alternate MC event generator. These are no larger than 30%.

8.5.2   Experimental

Uncertainties related to the imperfect nature of the detector and our reconstruction methods are also taken into account.

Jet Reconstruction   - Seven components associated with the jet energy are scaled up and down to evaluate a $\pm 1\sigma$ uncertainty in the jet energy scale (JES) calibration of jets. The largest JES uncertainty component has a maximum impact of 12%. The impact of the jet energy resolution (JER) systematic uncertainty is evaluated from $\pm 1\sigma$ variations. JER has eight components related to detector reconstruction of jets. The largest JER uncertainty component has a maximum impact of 16%. Six components related to our understanding of statistics, modelling and tracking with respect to the scale of the jet mass are varied up and down by the total 1σ. The largest JMS uncertainty component has a maximum impact of 12%. The uncertainties related to the large-radius re-clustered jets are obtained on the basis of the propagation of the small-R jets systematic uncertainties.

b-tagging and mis-tagging rates   - The *b*-tagging uncertainty is evaluated by varying up and down the η-, p_T- and flavour-dependent jet scale factors. An additional uncertainty for the extrapolation of the scale factors to high p_T jets is included. Additionally, an uncertainty related to the usage of *c*-jets scale factors for τ-jets. The uncertainties related to this vary between 0.3 and 12%.

Background estimation   - The statistical uncertainty from the reweighting scale factors enter the likelihood fit as a systematic uncertainty. Additionally, to better reflect the impact of kinematic reweighting on the one-lepton regions, an uncertainty was implemented to assess the difference between the inclusion/removal of the kinematic reweighting. The reweighting-related uncertainties have a combined maximum impact of 15%. A 300% uncertainty in the multi-jet background in all regions is applied, as motivated from the data-driven closure estimate in Section 8.3.3.

Remaining   - The electron and muon energy/momentum scale and resolution uncertainties are taken into account. Additionally, systematic uncertainties affecting the lepton efficiencies and isolation requirements are also accounted for. These uncertainties were negligible in previous versions of this search. The soft term of the $E_\mathrm{T}^\mathrm{miss}$ calculation was also evaluated. The uncertainties related to the $E_\mathrm{T}^\mathrm{miss}$ soft term were also negligible.

The magnitudes of the total combined uncertainties in the background estimates for the various signal regions are summarised in Figure 8.16.

(a)
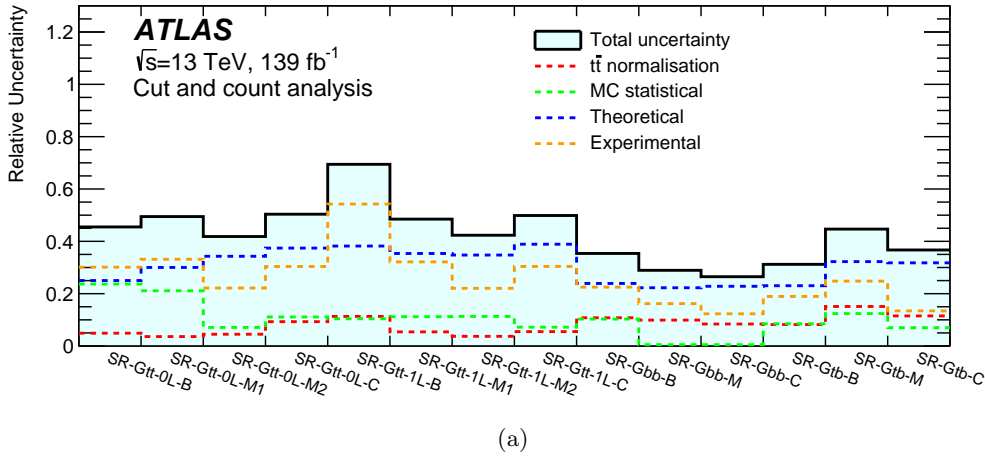
Figure 8.16: The total relative uncertainties for each signal region. All uncertainties are assumed to be fully uncorrelated so they can be summed in quadrature. Taken from Ref. [162].

8.6 Statistical Interpretation

This section presents the unblinded results of the statistical analysis performed for each likelihood fit introduced in Section 6.4.

8.6.1 Background-only Fit

In this section, the results of the background-only fit for the analysis regions are presented. The results are obtained following the strategy defined in Section 6.4 and are presented in Figures 8.17 to 8.19. Figure 8.17 presents the pre-fit data-to-MC agreement in the CRs and, in the bottom panel, the post-fit $t\bar{t}$ normalisation factors, which are explicitly stated in Table 8.9.

The $t\bar{t}$ normalisation factors range from 0.858 to 1.309 with no discernible patterns between regions and almost all are consistent with unity within its respective total error. Applying these scale factors in the VRs and SRs, Figures 8.18-8.19 present the post-fit total event yields for data and simulation along with the corresponding pull.

In the VRs, the data-to-MC ratio indicates sufficient agreement with all pulls within $< 1\sigma$ validating the overall fit strategy. Even though the Gbb and Gtb signal and validation regions require exclusively zero final-state leptons, because the control regions have at least one lepton present, all post-fit VRs and SRs benefit from the reweighting in the m_{eff} distribution. It is specifically beneficial for the leptonic Gtt regions. Figure 8.19 presents the agreement between the data and post-fit event yields in the SRs, where the pull is shown for each region in the lower panel.
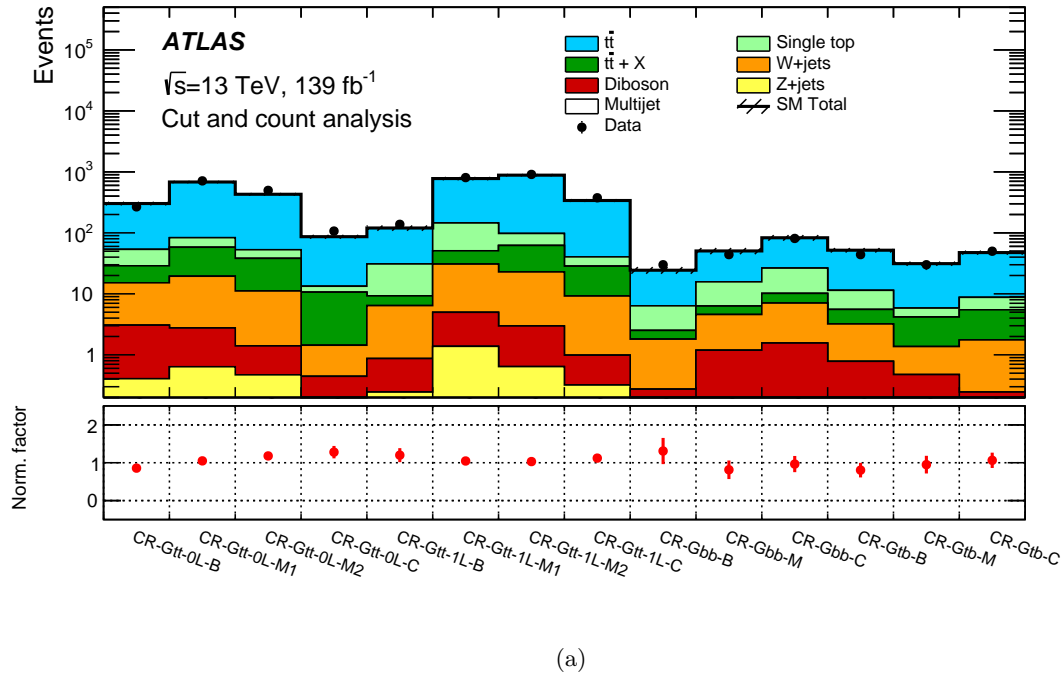
(a)

Figure 8.17: Pre-fit event yield in control regions and the related post-fit $t\bar{t}$ normalisation factors after the background-only fit. The upper panel presents the observed number of events and the predicted background yield before the fit. The background category $t\bar{t} + X$ includes $t\bar{t}W/Z$, $t\bar{t}H$ and $t\bar{t}t\bar{t}$ events. All of these regions require at least one signal lepton, for which the multi-jet background is negligible. All uncertainties described in Section 8.5 are included in the uncertainty band. The $t\bar{t}$ normalisation is obtained from the fit and is displayed in the bottom panel. Taken from Ref. [162].

Region	$\mu_{t\bar{t}}$	Symmetrical error
Gbb-B	1.309	0.346
Gbb-M	0.814	0.246
Gbb-C	0.965	0.214
Gtb-B	0.805	0.193
Gtb-M	0.95	0.234
Gtb-C	1.064	0.202
Gtt-0L-B	0.858	0.101
Gtt-0L-M1	1.049	0.066
Gtt-0L-M2	1.18	0.08
Gtt-0L-C	1.28	0.164
Gtt-1L-B	1.2	0.185
Gtt-1L-M1	1.046	0.085
Gtt-1L-M2	1.031	0.059
Gtt-1L-C	1.122	0.084

Table 8.9: Post-fit normalisation parameter for the $t\bar{t}$ background ($\mu_{t\bar{t}}$) for each region in the search.
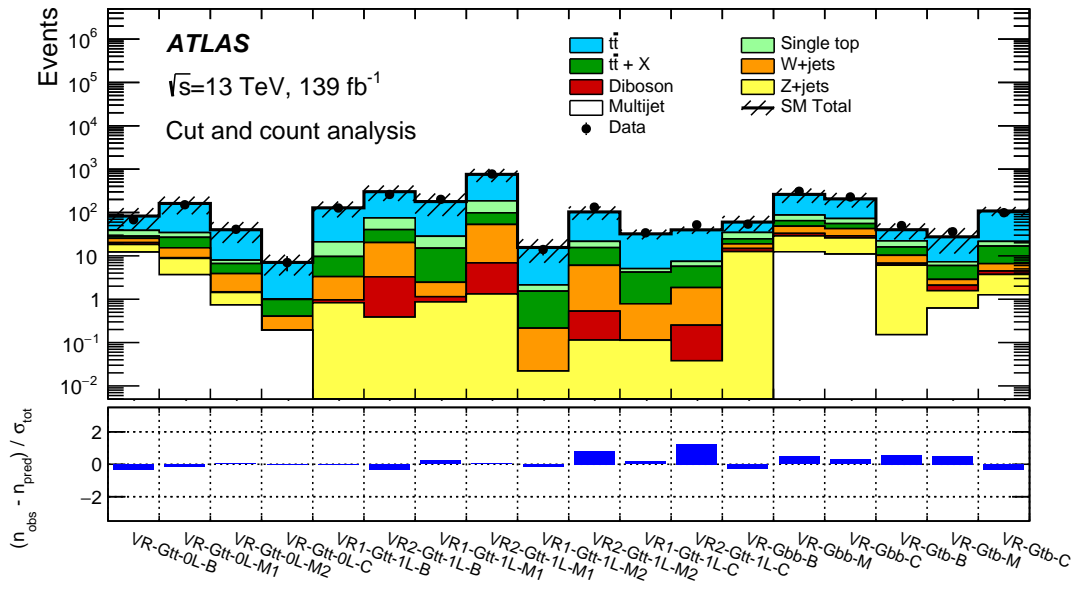
(a)

Figure 8.18: Results of the background-only fit extrapolated to the VRs. The upper panel shows the observed number of events and the predicted background yield. All uncertainties defined in Section 8.5 are included in the uncertainty band. The background category $t\bar{t} + X$ includes $t\bar{t}W/Z$, $t\bar{t}H$ and $t\bar{t}t\bar{t}$ events. The lower panel shows the pulls in each VR. Taken from Ref. [162].
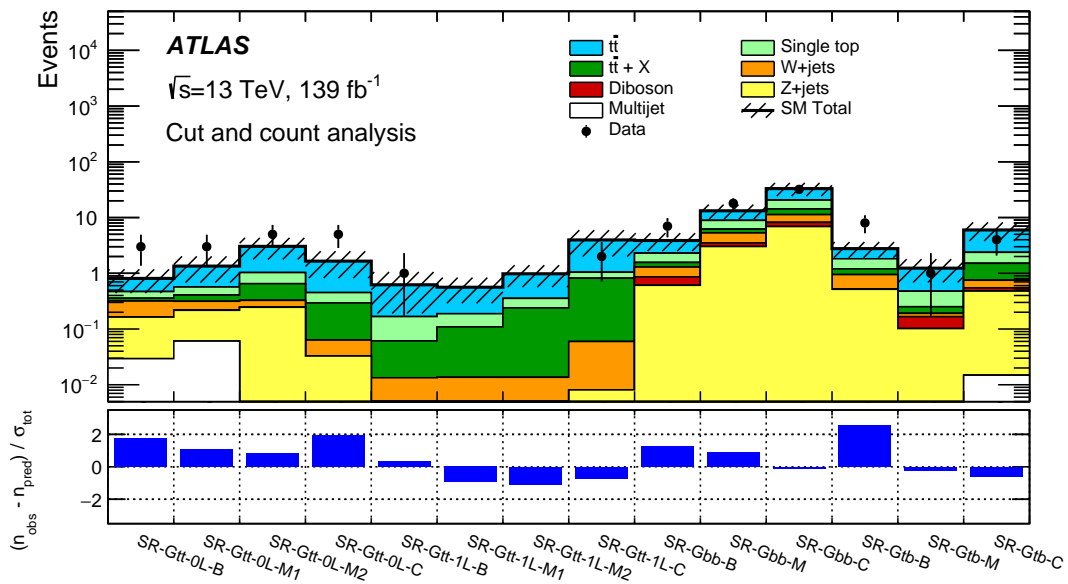
(a)

Figure 8.19: Results of the background-only fit extrapolated to the SRs. The upper panel shows the observed number of events and the predicted background yield. All uncertainties defined in Section 8.5 are included in the uncertainty band. The background category $t\bar{t} + X$ includes $t\bar{t}W/Z$, $t\bar{t}H$ and $t\bar{t}t\bar{t}$ events. The lower panel shows the pull in each SR. Taken from Ref. [162].

No significant excesses are found above the predicted background in any SR. The $t\bar{t}$ background dominates all SRs, as expected. The sub-dominant background contributions in the zero-lepton regions are $Z(\to \nu\nu)$+jets and $W(\to \ell\nu)$+jets events, where for W+jets events, the lepton is an unidentified electron or muon, or a hadronically decaying τ-lepton. In the one-lepton SRs, the sub-dominant backgrounds are single top, $t\bar{t}W$ and $t\bar{t}Z$. Tables 8.10- 8.11 present the observed number of events and predicted number of background events from the background-only fit in the Gtt one-lepton, Gtt zero-lepton and Gbb regions.

| Region | SR-Gbb | | |
	B	M	C
Observed events	7	18	32
Fitted background	3.9 ± 1.4	13 ± 4	33 ± 9
$t\bar{t}$	1.6 ± 1.0	4.3 ± 3.0	12 ± 7
Single top	0.7 ± 0.4	2.7 ± 1.4	6.3 ± 3.4
$t\bar{t} + X$	0.27 ± 0.16	0.9 ± 0.5	3.0 ± 1.5
Z+jets	0.61 ± 0.26	3.0 ± 1.0	6.9 ± 2.3
W+jets	0.43 ± 0.21	1.8 ± 1.2	3.1 ± 1.6
Diboson	$0.3^{+0.4}_{-0.3}$	0.5 ± 0.4	1.3 ± 0.8
Multijet	< 0.01	< 0.01	< 0.01
Pre-fit background	3.5	14	33

| Region | SR-Gtb | | |
	B	M	C
Observed events	8	1	4
Fitted background	2.8 ± 0.9	1.2 ± 0.6	6.0 ± 2.2
$t\bar{t}$	0.9 ± 0.6	0.8 ± 0.5	3.6 ± 2.1
Single top	0.62 ± 0.35	0.23 ± 0.12	0.9 ± 0.5
$t\bar{t} + X$	0.25 ± 0.15	0.06 ± 0.04	0.8 ± 0.4
Z+jets	0.52 ± 0.26	0.10 ± 0.10	0.46 ± 0.17
W+jets	0.43 ± 0.23	$0.02^{+0.07}_{-0.02}$	0.21 ± 0.11
Diboson	< 0.01	$0.06^{+0.16}_{-0.06}$	$0.06^{+0.16}_{-0.06}$
Multijet	< 0.01	< 0.01	$0.01^{+0.64}_{-0.01}$
Pre-fit background	3.0	1.3	5.8

Table 8.10: Results of the background-only fit extrapolated to the Gbb and Gtb SRs, for the total background prediction and breakdown of the main background sources. The uncertainties shown include all systematic uncertainties. The data in the SRs are not included in the fit. The background category $t\bar{t} + X$ includes $t\bar{t}W/Z$, $t\bar{t}H$ and $t\bar{t}t\bar{t}$ events. The row "MC-only background" provides the total background prediction when the $t\bar{t}$ normalisation is obtained from a theoretical calculation [125]. Yields are obtained for large Δm ("B"), moderate Δm ("M") and small Δm ("C") scenarios. Taken from Ref. [162].

Region	SR-Gtt-0L			
	B	M1	M2	C
Observed events	3	3	5	5
Fitted background	0.81 ± 0.32	1.3 ± 0.6	3.0 ± 1.3	1.7 ± 0.8
$t\bar{t}$	0.34 ± 0.21	0.8 ± 0.5	2.0 ± 1.2	1.2 ± 0.8
Single top	0.11 ± 0.10	0.16 ± 0.10	0.38 ± 0.23	0.16 ± 0.11
$t\bar{t} + X$	$0.04^{+0.05}_{-0.04}$	$0.09^{+0.13}_{-0.09}$	0.32 ± 0.20	0.23 ± 0.16
Z+jets	0.13 ± 0.08	0.16 ± 0.08	0.25 ± 0.14	$0.03^{+0.08}_{-0.03}$
W+jets	0.15 ± 0.11	0.10 ± 0.09	0.08 ± 0.05	0.03 ± 0.02
Diboson	< 0.01	< 0.01	< 0.01	< 0.01
Multijet	$0.03^{+0.20}_{-0.03}$	$0.06^{+0.25}_{-0.06}$	< 0.01	< 0.01
Pre-fit background	0.87	1.3	2.7	1.4

Region	SR-Gtt-1L			
	B	M1	M2	C
Observed events	1	0	0	2
Fitted background	0.6 ± 0.4	0.56 ± 0.27	1.0 ± 0.4	4.0 ± 2.0
$t\bar{t}$	0.5 ± 0.4	0.37 ± 0.23	0.63 ± 0.34	2.9 ± 1.8
Single top	0.11 ± 0.08	0.08 ± 0.07	0.12 ± 0.08	0.23 ± 0.15
$t\bar{t} + X$	0.05 ± 0.04	0.10 ± 0.06	0.23 ± 0.15	0.8 ± 0.5
Z+jets	< 0.01	< 0.01	< 0.01	< 0.01
W+jets	$0.013^{+0.021}_{-0.013}$	< 0.01	< 0.01	0.052 ± 0.034
Diboson	< 0.01	< 0.01	< 0.01	< 0.01
Multijet	< 0.01	< 0.01	< 0.01	< 0.01
Pre-fit background	0.55	0.55	1.0	3.7

Table 8.11: Results of the background-only fit extrapolated to the Gtt zero-lepton and Gtt one-lepton SRs, for the total background prediction and breakdown of the main background sources. The uncertainties shown include all systematic uncertainties. The data in the SRs are not included in the fit. The background category $t\bar{t} + X$ includes $t\bar{t}W/Z$, $t\bar{t}H$ and $t\bar{t}t\bar{t}$ events. The row "MC-only background" provides the total background prediction when the $t\bar{t}$ normalisation is obtained from a theoretical calculation [125]. Yields are obtained for large Δm ("B"), moderate-1 Δm ("M1"), moderate-2 Δm ("M2") and small Δm ("C") scenarios. Taken from Ref. [162].

8.6.2   Model-Independent Fit

Since no significant excesses were observed above the expected background from SM processes, the analysis proceeds to set limits on the signal processes to allow for reinterpretation where the data are used to derive one-sided upper limits at 95% confidence level (CL). Two levels of interpretation are provided in the next section: model-independent exclusion limits (Section 8.6.2) and model-dependent exclusion limits set on the Gbb, Gtt (Section 8.6.3) and gluino variable branching ratio models (Section 8.6.4).

The analysis regions are also used to place model-independent limits on the presence of beyond-the-SM (BSM) events for each SR. These limits are derived using the CL_s prescription [167], neglecting a possible signal contamination in the control regions. The results of this fit with the use of 10,000 pseudo-experiments are presented in Table 8.12 [107]. The expected upper limit on the presence of BSM events in each region follows the pattern expected given the yields in each signal region: it is, in general, higher in regions with a higher number of background events.

Signal region	p_0 (Z)	$\sigma^{95}_{\rm vis}$ [fb]	$S^{95}_{\rm obs}$	$S^{95}_{\rm exp}$
SR-Gbb-B	0.11 (1.22)	0.07	9.5	$6.2^{+2.6}_{-1.4}$
SR-Gbb-M	0.18 (0.93)	0.11	16.0	$11.4^{+5.0}_{-2.7}$
SR-Gbb-C	0.5 (0.0)	0.14	19.4	$19.5^{+5.5}_{-4.6}$
SR-Gtb-B	0.01 (2.30)	0.08	11.3	$5.4^{+2.2}_{-1.3}$
SR-Gtb-M	0.5 (0.0)	0.03	3.7	$3.8^{+1.5}_{-0.5}$
SR-Gtb-C	0.5 (0.0)	0.04	5.7	$6.7^{+2.6}_{-1.8}$
SR-Gtt-0L-B	0.03 (1.82)	0.05	6.4	$3.7^{+1.2}_{-0.4}$
SR-Gtt-0L-M1	0.13 (1.13)	0.04	6.1	$4.3^{+1.6}_{-1.0}$
SR-Gtt-0L-M2	0.18 (0.91)	0.06	7.7	$5.7^{+2.2}_{-1.2}$
SR-Gtt-0L-C	0.03 (1.83)	0.06	8.5	$4.9^{+2.0}_{-1.0}$
SR-Gtt-1L-B	0.29 (0.56)	0.03	3.9	$3.3^{+1.2}_{-0.2}$
SR-Gtt-1L-M1	0.5 (0.0)	0.02	3.0	$3.1^{+1.2}_{-0.1}$
SR-Gtt-1L-M2	0.5 (0.0)	0.02	3.0	$3.4^{+1.3}_{-0.4}$
SR-Gtt-1L-C	0.5 (0.0)	0.03	4.6	$5.3^{+2.2}_{-1.5}$

Table 8.12: The p_0-values and equivalent significance (Z), the 95% CL upper limits on the visible cross section ($\sigma^{95}_{\rm vis}$), and the observed and expected 95% CL upper limits on the number of BSM events ($S^{95}_{\rm obs}$ and $S^{95}_{\rm exp}$). The maximum allowed p_0-value is truncated to 0.5. Taken from Ref. [162].

8.6.3   Model-Dependent Fit

While the main goal of the analysis regions is to provide discovery regions and to present model-independent upper limits, the results are also interpreted in terms of model-dependent

limits, to allow a direct comparison with the performance to the 79.9fb^{-1} public result. The results were obtained using the CL_s prescription with 10,000 pseudo-experiments. The signal contamination is considered in the CRs as well as systematic uncertainties related to the signal models. Because the SRs overlap, the exclusion contour is built by selecting, for each signal point, the result corresponding to the SR with the lowest expected CL_s value. The 95% CL observed and expected exclusion limits for the Gtt and Gbb models are shown in the LSP and gluino mass plane in Figures 8.20.
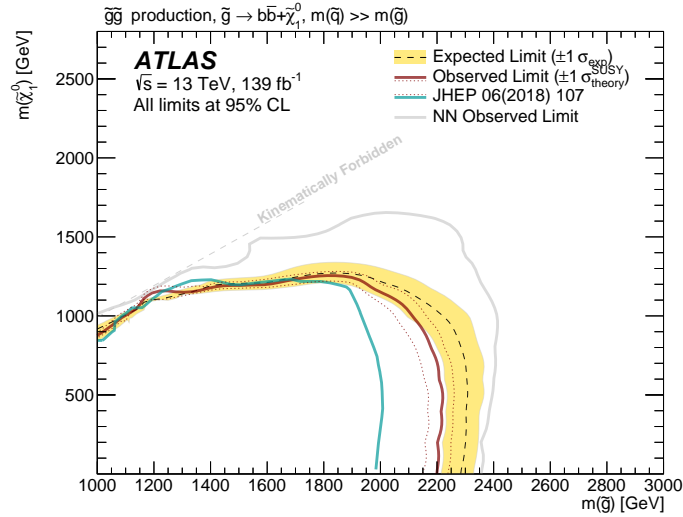
(a)
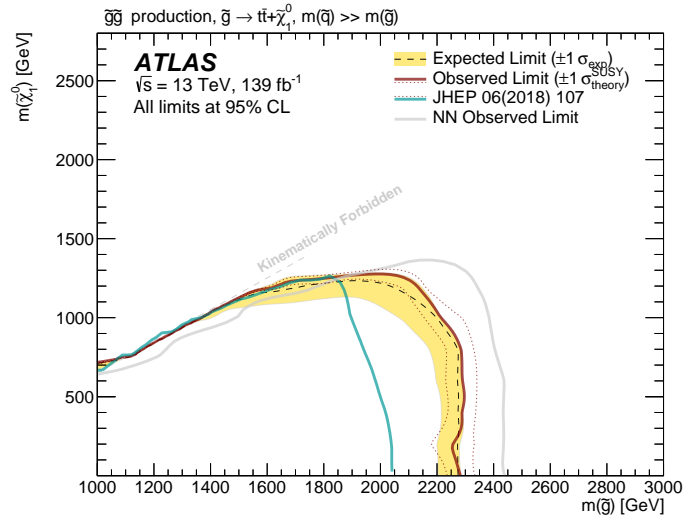
(b)

Figure 8.20: Result of exclusion fit for the analysis regions for the (a) Gbb and (b) Gtt model-space. The dashed line shows the 95% CL expected limit. The shaded bands around the expected limits show the impact of the experimental and background-modelling systematic uncertainties. The grey line presents the observed limit from SRs defined using a neural network (NN). Taken from Ref. [162].

The $\pm 1\sigma_{\text{theory}}^{\text{SUSY}}$ contours around the observed limits are obtained by running the fit with the SUSY production cross section adjusted by one standard deviation ($\pm 1\sigma$), as described in Section 8.3.2. The yellow band around the expected limit shows the $\pm 1\sigma$ uncertainty originating from

all statistical and systematic uncertainties except the theoretical uncertainties in the SUSY cross section.

Compared to the previous results of Ref. [164], the sensitivity in the gluino mass plane of the current search (assuming massless LSPs) have improved by 200 and 250 GeV for the Gbb and Gtt models, respectively. LSP with masses below 700 (800) GeV are excluded at 95% CL for gluino masses lower than 2.2 (2.27) TeV for the Gbb (Gtt) model. The best exclusion limits on the LSP mass are approximately 1.25 TeV, reached for a gluino mass of approximately 1.85 and 2.05 TeV for Gbb and Gtt models, respectively. As introduced in Section 8.1, the neural network (NN) training results in increased model sensitivity and thus strong observed limits, which can also been observed in grey Figure 8.20. The 95% CL on the Gbb (Gtt) simplified model is observed to reach a gluino mass of 2.4 (2.44) TeV for a 1.0 TeV (massless) lightest neutralino from the NN analysis. The limit on the maximum lightest neutralino mass was observed to be 1.65 ($\sim$ 1.35) TeV for the maximum gluino mass of 2.0 (2.17) TeV for Gbb (Gtt).

8.6.4   Reinterpretation

The results of the analysis will also be interpreted for a model with a variable branching ratio (BR) of the gluino, where it is permitted to decay to $tt\tilde{\chi}_1^0$, $bb\tilde{\chi}_1^0$, or $tb\tilde{\chi}_1^{\pm}$ (and the $\tilde{\chi}_1^{\pm}$ then decays to $\tilde{\chi}_1^0$ and soft fermions). All the combinations of these three decays are considered, with the constraint that the sum of the three BRs must be 100%. The inclusion of the gluino BR makes it impossible to display the results in the two-dimensional mass plane, as is presented for the Gtt and Gbb models. Instead, the limits are shown in the BR plane. The two BRs used to define the plane are the one to $tt\tilde{\chi}_1^0$ and $bb\tilde{\chi}_1^0$, with the assumption that the BR to $tb\tilde{\chi}_1^{\pm}$ equals one minus the sum of these two. Each plot considers a single LSP mass, and for each BR point the highest excluded gluino mass is shown. The expected (observed) results are presented in the instance of m($\tilde{\chi}_1^0$)=1, 600 and 1000 GeV in Figures 8.21(a) (8.21(b)), 8.22(a) (8.22(b)) and 8.23(a) (8.23(b)), respectively.

For each of the three expected limit planes, the Br($\tilde{g} \to$ Gbb) = 100% provides the highest excluded gluino mass in the BR plane. This is in contrast to the observed limit plane, where it is observed to be Br($\tilde{g} \to$ Gtt) = 100%. This can be related back to the limits observed in Figure 8.20, where the observed (expected) limit is weaker (stronger) than the expected (observed) for Gbb (Gtt). For all LSP masses, the previous results of Ref. [164] had a strong bias towards the Br($\tilde{g} \to$ Gtt) = 100% BR for the largest excluded gluino mass. This seems to originate from the particularly strong sensitivity to boosted models up to a LSP mass of 400 GeV in the Gtt limit of Ref. [164], and not a lack of sensitivity to Gbb (Figure 8.20). However, there is an overall observed minima in the Br($\tilde{g} \to$ Gtb) = 100% BR, which is not observed in the results obtained from this section. This is most likely because of the improved sensitivity originating from the dedicated Gtb signal regions.

The greatest observed gluino mass limit for a LSP up to 600 GeV LSP, is observed to be $\sim$ 2.25 TeV corresponding to the Br($\tilde{g} \to$ Gtt) = 100% BR. For a LSP with mass 1.0 TeV, the gluino
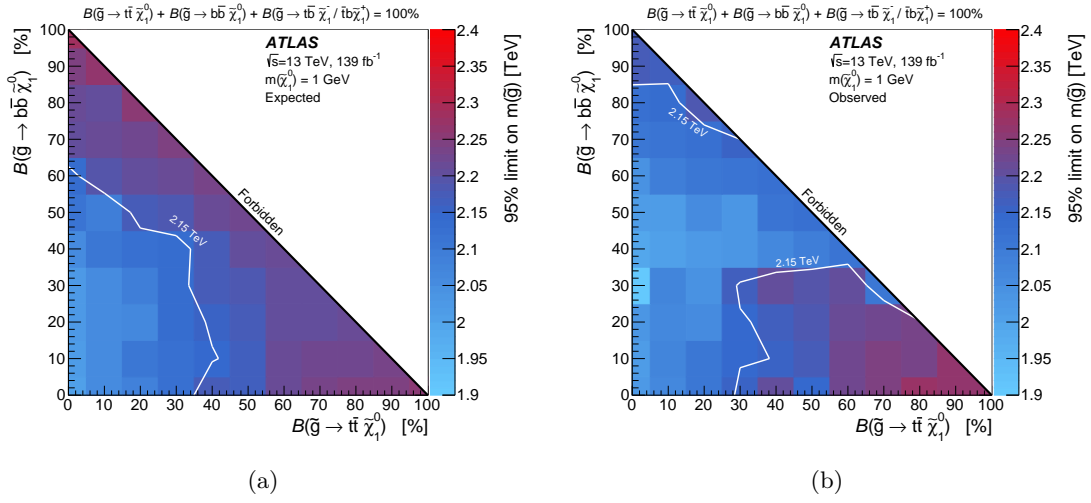
Figure 8.21: The (a) expected and (b) observed 95% CL exclusion limits on the gluino mass as a function of the gluino branching ratio to Gbb (vertical) and Gtt (horizontal) models. Gluinos not decaying to either the Gtt or Gbb mode are assumed to decay via Gtb instead. In this figure, the neutralino mass is fixed at 1 GeV. The z-axis indicates the maximum excluded gluino mass for each point in the branching ratio phase-space. The white lines indicate contours at mass intervals of 50 GeV. Taken from Ref. [162].
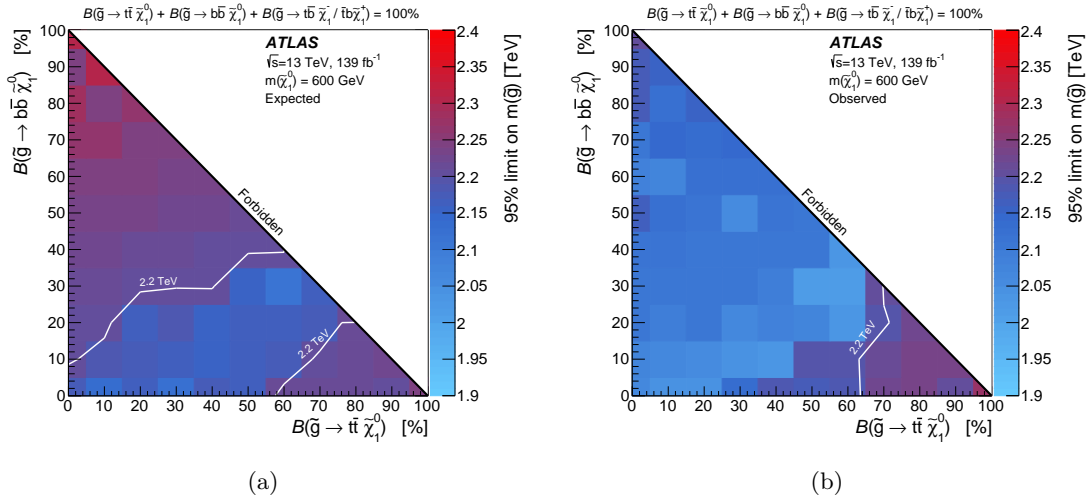
Figure 8.22: The (a) expected and (b) observed 95% CL exclusion limits on the gluino mass as a function of the gluino branching ratio to Gbb (vertical) and Gtt (horizontal) models. Gluinos not decaying to either the Gtt or Gbb mode are assumed to decay via Gtb instead. In this figure, the neutralino mass is fixed at 600 GeV. The z-axis indicates the maximum excluded gluino mass for each point in the branching ratio space. The white lines indicate contours at mass intervals of 50 GeV. Taken from Ref. [162].
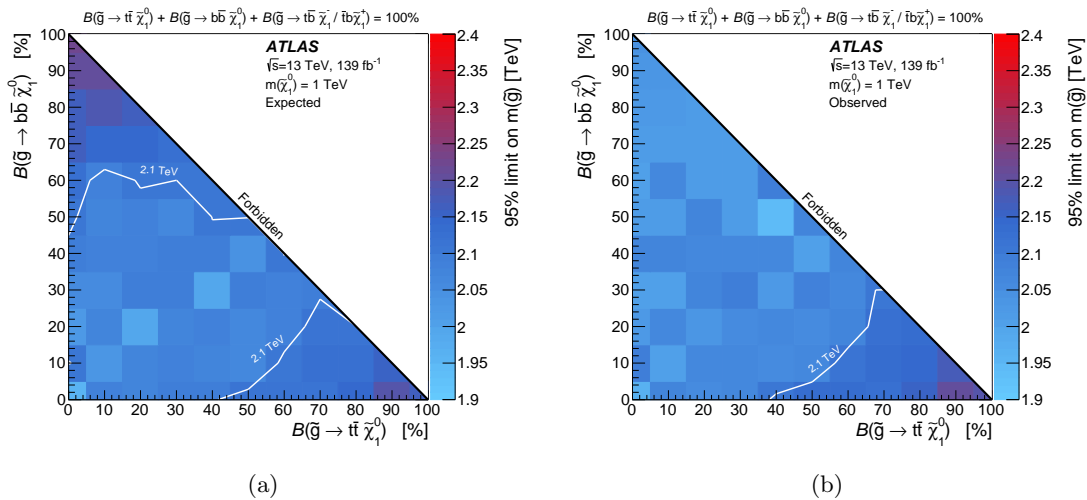
Figure 8.23: The (a) expected and (b) observed 95% CL exclusion limits on the gluino mass as a function of the gluino branching ratio to Gbb (vertical) and Gtt (horizontal) models. Gluinos not decaying to either the Gtt or Gbb mode are assumed to decay via Gtb instead. In this figure, the neutralino mass is fixed at 1000 GeV. The *z*-axis indicates the maximum excluded gluino mass for each point in the branching ratio space. The white lines indicate contours at mass intervals of 50 GeV. Taken from Ref. [162].

mass of 2.2 TeV corresponding to the $\mathrm{Br}(\tilde{g} \to \mathrm{Gtt}) = 100\%$ BR can be considered excluded at 95% CL.

8.7   Conclusion

This chapter presents the results from the search for supersymmetry in final states containing multiple *b*-jets and large quantities of $E_\mathrm{T}^\mathrm{miss}$. The search follows a strategy of defining a series of signal-enriched regions where selections are required on kinematic quantities. The thresholds of the selections are optimised to maximise the statistical sensitivity in the gluino-lightest neutralino mass plane. Each signal region has a corresponding $t\bar{t}$ control region, that is for the data-driven normalisation of the dominant background contribution. Additionally, at least one validation region has been defined for validating the extrapolation from a lepton-absent signal region to a leptonic control region. No statistically significant deviations are observed in the validation regions and thus, the background expectation techniques are deemed sufficient.

No statistically significant excesses were observed in the background-only or discovery fit strategies and consequently model-dependent limits were set. For the Gbb (Gtt) simplified models, the 95% confidence limit on the gluino mass, for a massless LSP, is 2.2 (2.27) TeV and the maximum limit on the LSP mass is 1.25 TeV for a gluino mass of 1.85 (2.05) TeV. The final result from this chapter is obtained from the model-dependent limits in the branching-ratio plane for the decays of gluino to $b\bar{b}\tilde{\chi}_1^0, t\bar{t}\tilde{\chi}_1^0$ and $t\bar{b}\tilde{\chi}_1^\pm/\bar{t}b\tilde{\chi}_1^\pm$. The maximum exclusion limit is reached from $\mathrm{Br}(\tilde{g} \to \mathrm{Gtt}) = 100\%$ branching-ratio resulting in a limit on the gluino mass of 2.25 (2.2) TeV for a LSP mass up to 600 (1000) GeV.

Chapter 9

Search for SUSY Using a Gaussian Signal Shape

This chapter presents a novel methodology for searching for supersymmetry (SUSY). It makes use of an arbitrary mathematical function to search for discrepancies in the data with respect to the Standard Model (SM) expectation. The binned likelihood fit is performed for an observable sensitive to beyond the SM processes. The results are then reinterpreted for events originating from pair-produced gluinos decaying to multiple b-jets and E_T^{miss} final state.

9.1 Motivation

ATLAS SUSY searches are typically comprised of two components. *Discovery* - the search targets the discovery of new physics. *Exclusion* - in the event of no statistically significant excesses being observed in the SM prediction, the search will proceed with setting limits on the SUSY signal searched. To perform these, a series of signal regions (SRs) are defined by either using a single bin (SB) or multiple bins (*multi-bin*, MB) of a distribution of an observable.

The SB defines a SR by a series of inclusive selections on kinematic observables, where the threshold is commonly determined by the value that results in the highest expected significance. Typically, this would result in the optimal selection being in the tail of the distribution, which particularly benefits models with large mass splitting. Because of the lack of sensitivity to models with small mass splitting, a SB approach is not optimal for excluding the greatest area of signal phase-space. In ATLAS SUSY searches, the discovery strategy is performed only by the SB approach. Ultimately, this results in a search with greater model independence, even though the selection criteria are optimised for the specific SUSY signal.

The SRs of a MB approach are defined as the bins of an observable that is sensitive to BSM processes. In ATLAS, the MB strategy is used only for exclusion because a signal shape would be required to search for new physics in the SRs and because the choice of signal shapes is arbitrary, it would be model-dependent. One way this can be rectified is by using a generic signal

shape that describes a broad range of BSM models, termed "universal". The MB approach is better suited for exclusion than the SB because the differences in the shape of the signal and background from the MBs of the distribution enhance sensitivity to softer events. It is for this reason the MB has improved sensitivity to a broader range of models with small mass splitting.

Evidently, the SB and MB approaches seem best suited to discovery and exclusion, respectively, however, there are further limitations to be considered. Firstly, when searching for new physics with a SB in ATLAS, it is possible that any deviation, irrespective of whether it reflects the expectation of a signal process, could contribute to a low p-value. This can be improved upon by using a universal signal shape. This would require an excess of events to follow the signal shape distribution and therefore, is more likely to have originated from a signal process.

When setting model-dependent limits on BSM signal processes, it is the process of how such limits are derived that could be improved upon. For each BSM model in the available phase-space, a likelihood fit calculates whether the model is expected to be excluded or not given the experimental configuration, from which an exclusion contour is derived. This can be simplified by setting the limit as a function of the shape parameter(s) and model-dependent limits on the signal model phase-space can be interpolated from this. To do this, a universal signal shape would be required.

Additionally, although the MB increases the model dependence with respect to the SB, the use of the universal signal shape means that the analysis would be sensitive to any BSM signal that can be described by the shape. Therefore, this would somewhat rectify the loss in model independence and hence, could be classified as a semi-model independent strategy, whereas most ATLAS SUSY exclusion limits have strong model dependence.

This chapter focuses on a novel method of using multiple SR bins with a binned shape fit for both discovery and exclusion. To motivate this, Section 9.2 introduces the concept of mass determination and how it relates to observables calculable for detecting SUSY signals. This is then related to the effective mass (m_{eff}) distribution, which is the observable chosen to define the multiple SR bins. Also within Section 9.2, is a proof of the universality of the Gaussian signal shape for pairs of strongly-produced gluinos SUSY models. The shape is characterised by a two-parameter Gaussian distribution where the width is set to a constant value of 0.125.

The results of this search are interpreted with the models from the pair-produced gluinos decaying to a multiple b-jet plus E_T^{miss} final state, referred to as the *strong multi-b analysis*, presented in Chapter 8. Hence, the results are compared to those obtained from a SB cut-based approach (CC) and using the default ATLAS search strategy. Additionally, the same MC and data events are used as well as the same background estimation methods, systematic uncertainty configuration and analysis observables. Any differences with respect to the strong multi-b analysis are stated explicitly where relevant. Section 9.3 defines the analysis regions (signal, control and validation) in which the novel method will be performed. Section 9.4 clarifies the differences in the systematic configuration between the strategy used in this section and the CC search. Finally, Section 9.5 presents the results of searching for new physics and setting cross section limits on the Gaussian signal as well as the reinterpreted limits on pair-produced gluino decays. Comparisons are made

with the SB strategy of the strong multi-b analysis.

9.2 Universal Shape of Strongly-produced SUSY Signals

If R-Parity Conserving (RPC) SUSY particles were to exist, one would want a model-independent way to measure their properties. Made more complicated by the missing energy from two LSPs, direct reconstruction of the SUSY event is not possible and hence, a technique to do that is required. One such way would be to measure the SUSY mass scale (M_{susy}) [143, 168]. One way this can be defined is by summing over the initial sparticles (p) in the event and taking the mean of the SUSY particle masses (m_p) weighted by their production cross section of each state (σ_p) [168];

$$M_{\text{susy}}^{\text{true}} = \frac{1}{\sigma_{\text{tot}}} \sum_{p \ni \text{sparticles}} m_p \cdot \sigma_p. \tag{9.1}$$

In the limit of squarks or gluinos of a single mass dominating the production cross section,

$$M_{\text{susy}}^{\text{true}} = \min(m_{\tilde{g}}, m_{\tilde{u}R}) \tag{9.2}$$

can also be used, which can be seen to equal Equation 9.1 [143]. Because the LSP remains undetected, experimental observables can be insensitive to the true mass scale. Equation 9.1 was found to break down for events when the mass difference between the parent and daughter SUSY particles was similar. One way to solve this is to use the analogous relation for the transverse momentum of a heavy SUSY particle (1) cascade decay, in the lab frame, to a lighter SUSY particle (2) and a massless SM particle [168]. This is given by

$$p_{\text{T}} \propto \frac{1}{2}\left(m_1 - \frac{m_2^2}{m_1}\right). \tag{9.3}$$

Using Equation 9.3, the effective SUSY mass scale ($M_{\text{susy}}^{\text{eff}}$) for a non zero LSP mass can be defined by

$$M_{\text{susy}}^{\text{eff,2-body}} = \underbrace{\frac{M_{\text{susy}}^{\text{true}2} - m_{\tilde{\chi}_1^0}^2}{M_{\text{susy}}^{\text{true}}}}_{\text{General}} = \underbrace{\frac{m_1^2 - m_2^2}{m_1}}_{\text{2-parameter Model}} \equiv \underbrace{\frac{m_{\tilde{g}}^2 - m_{\tilde{\chi}_1^0}^2}{m_{\tilde{g}}}}_{\text{RPC Gluino}}, \tag{9.4}$$

for an arbitrary SUSY decay and for the simplified RPC gluino decay model used in this thesis. Equation 9.4 accurately describes the $M_{\text{susy}}^{\text{true}}$ for two-body squark decays, however, it was not sufficient for three-body gluino decays [148]. Ref. [148] successfully extended the equation for the effective SUSY mass scale to accommodate a $n > 2$ body decays, calculated by

$$M_{\text{susy}}^{\text{eff,n-body}} = \left.\frac{(n-1)M_{\text{susy}}^{\text{true}} - \sqrt{M_{\text{susy}}^{\text{true}2} + (n^2 - 2n)m_{\tilde{\chi}_1^0}^2}}{n-2}\right\} \text{General}$$

$$\left. = \frac{(n-1)m_1 - \sqrt{m_1^2 + (n^2 - 2n)m_2^2}}{n-2}.\right\} \text{2-parameter Model}$$

(9.5)

Equation 9.5 assumes that the decay products are distributed isotropically. In the event of three-body decay, such as simplified RPC gluino decays, Equation 9.6 can be used;

$$M_{\text{susy}}^{\text{eff,3-body}} = 2m_1 - \sqrt{m_1^2 + 3m_2^2}$$

$$\left. = 2m_{\tilde{g}} - \sqrt{m_{\tilde{g}}^2 + 3m_{\tilde{\chi}_1^0}^2}.\right\} \text{RPC Gluino}$$

(9.6)

The Gtt and Gbb signal processes of Section 8.1 are three-body decays and so Figure 9.1 presents the values of $M_{\text{susy}}^{\text{eff,3-body}}$ for the Gtt and Gbb model phase-space respectively.

(a)   (b)
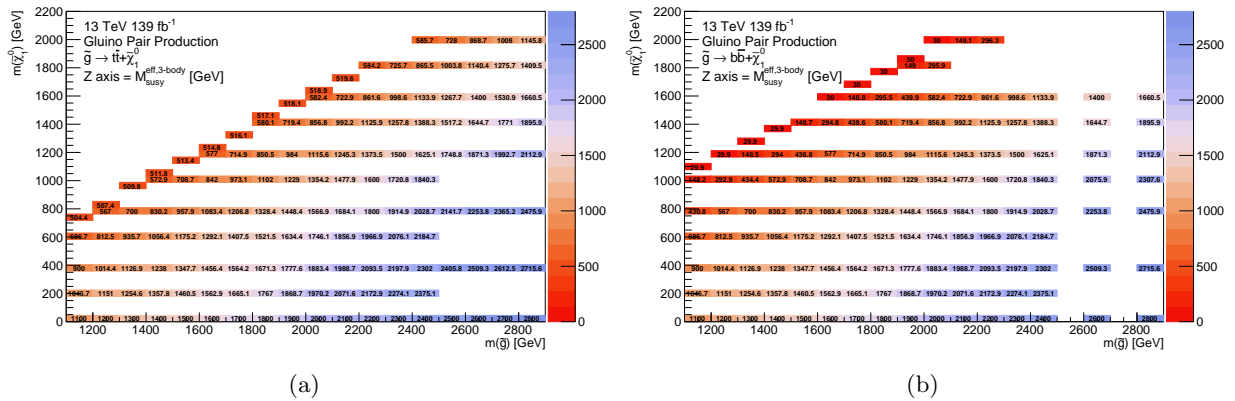
Figure 9.1: Distribution of the $M_{\text{susy}}^{\text{eff,3-body}}$ as a function of the SUSY model parameters for the (a) Gtt and (b) Gbb signal processes.

The distributions present the lowest effective SUSY mass scales are those where the gluino and LSP mass are similar and peaks for models with a massless LSP and the highest gluino mass in the parameter-space. Between these two regions, the values transition linearly from the diagonal, describing the kinematically forbidden region, to the boosted signals with a massless LSP.

With the LSP always escaping the detector, true invariant mass peaks are not possible in RPC SUSY [24]. However, the Gaussian nature of the m_{eff} has previously been observed for constrained MSSM and individual simplified squark and gluino models in Refs. [148, 169]. For this reason, it was expected that a Gaussian signal shape could describe the gluino signals introduced in Section 8.1 for the m_{eff} observable. The m_{eff} is also of interest because of its particular sensitivity to inclusive gluino production and hence why it was used for the multiple SR bins of the search performed in Ref. [164].

Note, all figures presented until Section 9.3, where specific analysis regions are defined, are produced with the event preselection defined in Section 8.3.5 without a requirement on the lepton multiplicity. Each Figure will also indicate whether it includes all the signal models introduced in Section 8.1, i.e, inclusive gluino production, or a specific gluino decay process, such as Gtt.

By plotting all the off-shell strong SUSY signals named Gbb, Gtt and Gtb, introduced in Section 8.1, for the m_{eff} distribution and subtracting the mean for each histogram, it was observed that the signal shape was in fact log-normal. Subsequently, for each gluino signal, a three-parameter Gaussian function was fitted to the $\log 10(m_{eff})$ distribution in the absence of SM backgrounds. Figure 9.2 shows the $\log 10(m_{eff})$ ditribution after normalising it to unity and subtracting the fitted Gaussian mean (μ_G) from each entry in the histogram to centre the peak of each signal to zero. The figure is shown for an assortment of kinematic scenarios of Gtt and inclusive gluino production processes.

(a)   (b)
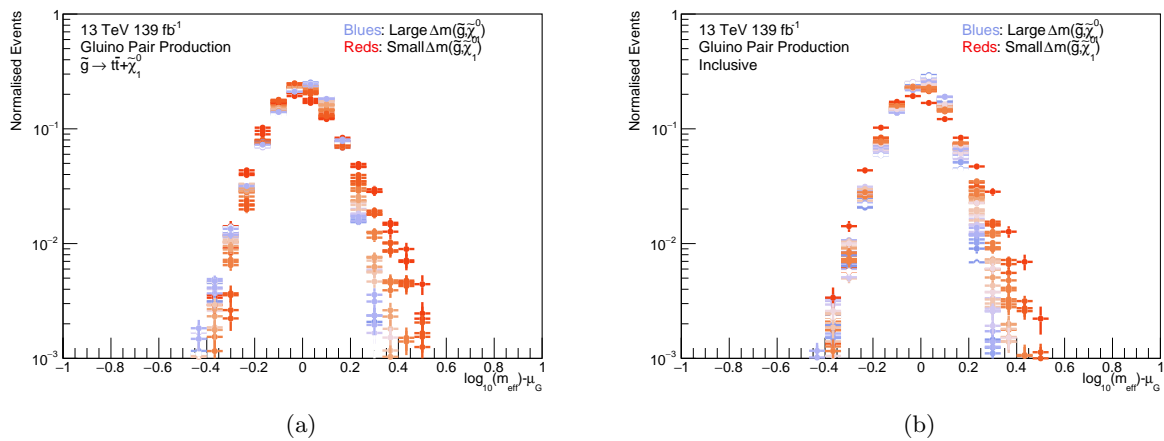
Figure 9.2: The $\log 10(m_{eff})$ distribution normalised to unity and centred by the fitted Gaussian mean. The signals included are an assortment of forty signal processes of varying mass differences between the gluino and lightest neutralino from the (a) Gtt (b) inclusive (Gtt, Gtb, Gbb) phase-space in Section 8.1. The minimum mass splitting included is $\Delta m = 2m_{top} = 355$ GeV. Each signal follows a normal distribution with a similar Gaussian width (σ_G).

Evidently, one can visually observe the universal Gaussian shape for various strong production processes and for various event kinematics (labelled boosted, moderate and compressed following the terminology used in Chapter 8). It is for this reason that the quantity used for the multiple SR bins of this search is $\log 10(m_{eff})$. However, the deviations originating from the compressed signals in the tails of the right-hand-side of Figure 9.2 warrant further discussion. For these models, the ISR jet becomes significant compared with the gluino decay products in the m_{eff} distribution. Consequently, the detector signature of the signal seems similar to $Z(\to \nu\nu)$+jets, which falls monotonically with increasing m_{eff}. This process explains the small deviations observed in the tails of the distributions. This is exacerbated for compressed Gbb signals because the process can have a minimum mass splitting much lower than for Gtt; $\Delta m = 20$ GeV compared to $\Delta m = 2m_{top} = 355$ GeV. Figure D.1 of Appendix D.1 shows an equivalent distribution for Gbb signal processes with $\Delta m = 20$ GeV. Not only is the shape affected by the event kinematics but these models also predict very few events and thus large fluctuations occur.

Figures of the fitted Gaussian mean (10^{μ_G}) and the three-body effective SUSY mass scale and the fitted Gaussian width (σ_G) and fitted Gaussian mean can be seen in Figure 9.3.

(a)　　　　　　　　　　　　　　　　　　　　(b)
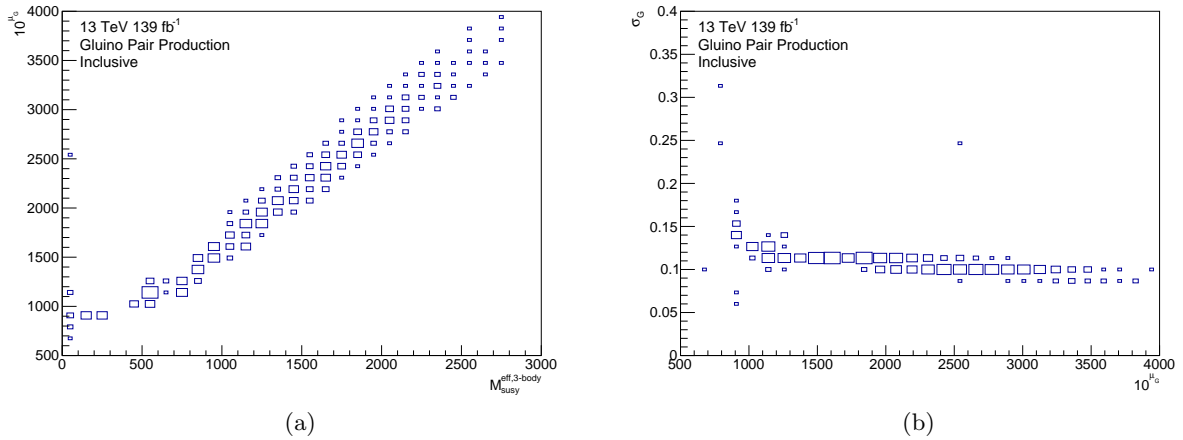
Figure 9.3: (a) Shows the fitted Gaussian mean as a function of the three-body effective SUSY mass scale and (b) shows the fitted Gaussian width as a function of fitted Gaussian mean. The model points used are all Gbb, Gtb and Gtt signals from Section 8.1. The size of the squares represent the event count in each bin.

Figure 9.3(a) shows a strong positive correlation between the three-body effective SUSY mass scale and the fitted mean of the Gaussian. It is therefore said to be a quantity that is sufficiently accurate for mass determination [148]. Figure 9.3(b) shows an almost-constant value for the fitted Gaussian width and thus, for this model phase-space, the Gaussian width can be approximated by a single value. The significant deviations from the strong linear patterns in both figures originate from the very compressed[1] models. So it can be concluded that the Gaussian shape in the $\log 10(\mathrm{m_{eff}})$ distribution is approximately universal for a fixed width for gluino-produced SUSY scenarios with this detector signature, except for those with extremely small mass splitting ($\Delta m \leq 20$ GeV).

Earlier in this section, it was stated only Equation 9.6 was applicable to estimate the SUSY mass scale for three-body decays [148]. To assess the differences between the mass reconstruction equations for two- and three-body decays, Figure 9.4 shows the fitted Gaussian mean plotted for the two equations in addition to linear regression been performed to the signal MC, following what was performed in Ref. [148].

It is observed in Figure 9.4(a) that the two-body equation does sufficiently reconstruct the mass of the SUSY particles in contrast to what was observed in Ref. [148]. However, visually, the three-body equation produces a smaller variation around the fitted linear function and consequently has an improved χ^2/N_{dof}. For this reason, $M_{\mathrm{susy}}^{\mathrm{eff}}$ will only refer to $M_{\mathrm{susy}}^{\mathrm{eff,3\text{-}body}}$ from this section onward.

To extract a chosen value of the fixed Gaussian width from Figure 9.3(b) to be used in the likelihood fits in Section 9.5, linear regression was performed to the 10^{μ_G}-σ_G plane for all signal

---

[1]Naming originates from the region definition used in Ref. [1] to target Gbb models with mass splitting ≤ 20 GeV.
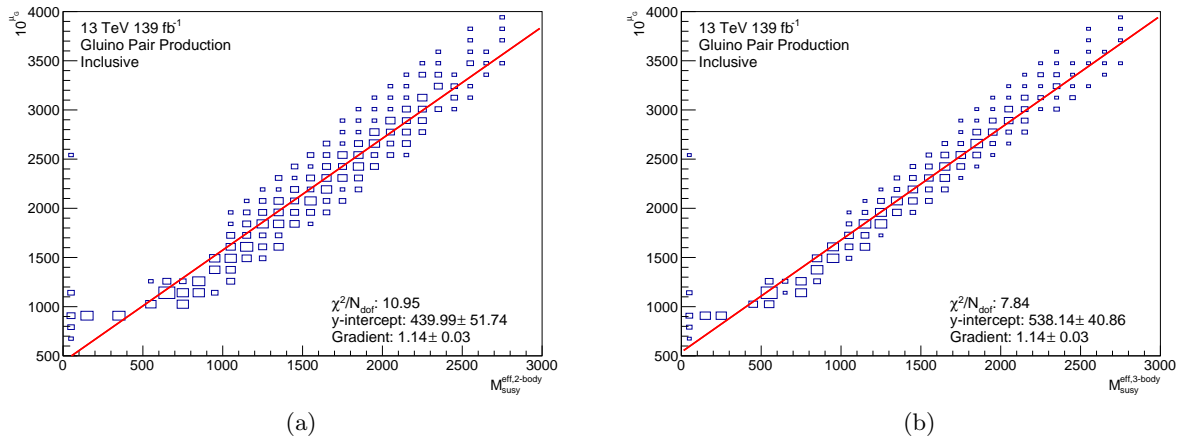
Figure 9.4: A comparison of the fitted Gaussian mean against the (a) two- and (b) three-body effective SUSY mass scales with linear regression performed to the MC. The size of the squares represent the event count in each bin.

from Section 8.1. These can be observed in Figure 9.5 with signal combinations of varying mass splitting scenarios, inclusive or only Gtt SUSY signals, in addition to those motivated by pure-higgsino LSP [2] signals.

In the first instance, one would expect the y-intercept of the linear function to be the best descriptor of the universal width. Figure 9.5(a) presents the 10^{μ_G}-σ_G plane for inclusive strong gluino production signals with no restrictions on the event kinematics. It is evident that the anomalies decrease the quality of the fit with an observed poor χ^2/N_{dof} and a y-intercept that visually seems too high to describe most of the data. This can be improved by first removing the very compressed models, which the Gaussian approximation is expected to break down for. The result of this can be seen in Figure 9.5(b). Secondly, it can be improved by reducing it to only Gtt models, which the Gaussian approximation is expected to best describe and can be seen in Figure 9.5(c). Here, the y-intercept is observed to be 0.131 ± 0.003 that still visually seems too high to represent the average of MC. Instead, a better representation seems to be the average of the fitted Gaussian widths, $\langle \sigma_G \rangle$, which across all Figures in Figure 9.5, is roughly ~ 0.11. In this instance, compressed SUSY models with smaller fitted Gaussian means are not accurately described by this and therefore, it was justified that a value of 0.125 would be best to describe most of these RPC gluino models. Additionally, a non-optimal width for a given set of models does not invalidate the method but is instead reflected in the reduced statistical sensitivity to them.

To further validate the Gaussian approximation with the chosen fixed width, the χ^2/N_{dof}, originating from a Gaussian fit with a fixed width of 0.125 to each signal MC, is plotted as a function of the SUSY mass scale. This can be seen in Figure 9.6 for inclusive and Gtt RPC SUSY gluino decays.

---

[2] Allowed to have a gluino mass between 2200–2600 GeV and LSP mass between 1000–1200 GeV, as motivated by Section 3.8.3.

(a) Inclusive

(b) Inclusive, VC removed

(c) Gtt only

(d) Pure higgsino-like signals
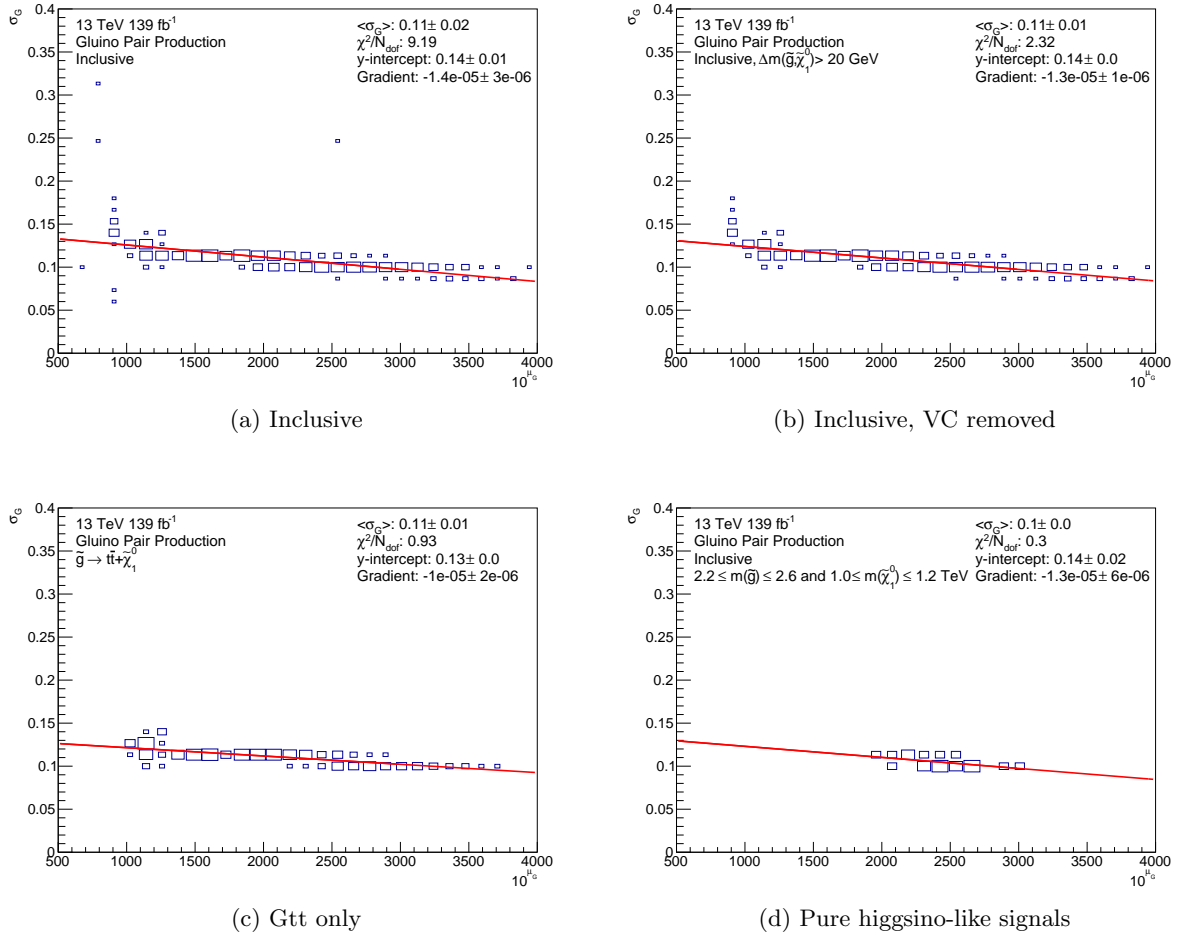
Figure 9.5: Plots of the fitted Gaussian width (σ_G) against fitted Gaussian mean (10^{μ_G}) with a linear fit performed for a combination of signal and kinematic scenarios. The plot will be either inclusive gluino SUSY production (Gtt, Gtb and Gbb) or Gtt only. Because the Gaussian approximation breaks down for very compressed (VC, $\Delta m \leq 20$ GeV) models, Figure 9.5(b) removes these models. In Figure 9.5(d), only signals motivated by pure higgsino dark matter are included. The pure higgsino-motivated signals were allowed to have a gluino mass between $[2200-2600]$ GeV and LSP mass between $[1000-1200]$ GeV. The size of the squares represent the event count in each bin.

(a)   (b)
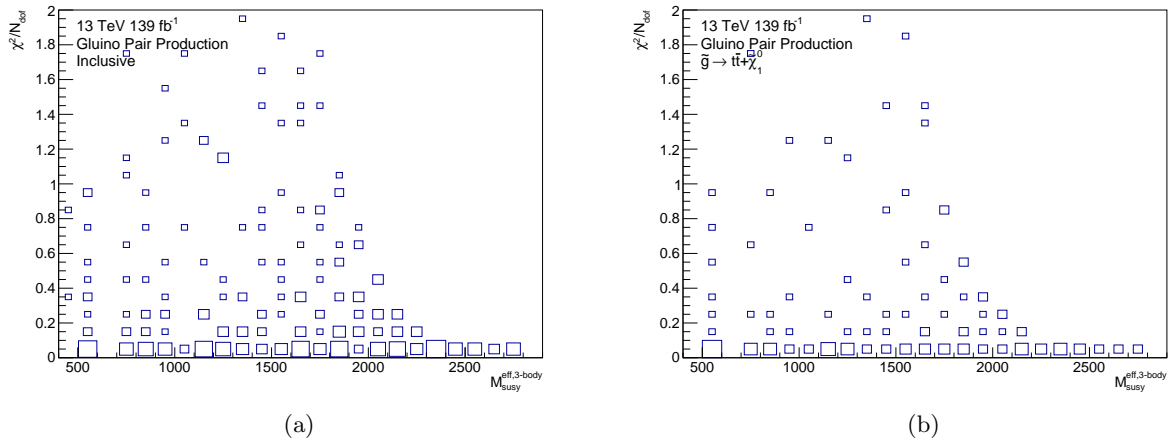
Figure 9.6: The χ^2/N_{dof} from the fitting a two-parameter Gaussian function (floating mean and normalisation and a fixed width with value 0.125) to each (a) inclusive and (b) Gtt RPC SUSY gluino signals as a function of the SUSY mass scale. The size of the squares represent the event count in each bin.

The expected χ^2/N_{dof} for each model should be between zero and one because the signal MC was produced with a luminosity greater than that used in the analysis[3]. For a given signal model, the statistical uncertainty assigned to each bin in the $\log 10(m_{\mathrm{eff}})$ distribution will be smaller due to the scaling of the event count to the analysis luminosity. When calculating the χ^2, each bin of the distribution contributes a term with the correct denominator for $139\mathrm{fb}^{-1}$ but a smaller numerator if the Gaussian model is a good approximation to the signal MC. This is because of the reduced scatter of the MC around the Gaussian function for $139\mathrm{fb}^{-1}$ and hence, a χ^2 value would be expected to be < 1.

Few signals have high (i.e $\gg 1.0$) χ^2/N_{dof} and the majority are between 0.0 and 0.2 suggesting the fitted Gaussian function with the chosen fixed width is a sufficient approximation to the signal simulation. Table 9.1 presents an explicit breakdown of signals with $\chi^2/N_{\mathrm{dof}} > 3$. It is noticeable that the gluino mass does not exceed 1.6 (1.5) TeV for Gbb (Gtt) however, Gbb seems to have the largest composition of signals with large χ^2/N_{dof}.

9.3 Analysis Regions and Background Estimation

The largest contributing factor to the statistical sensitivity of a CC approach is the signal region optimisation procedure. With this being a novel method, the primary goal of this chapter was to validate the strategy and hence a series of highly optimised SRs was not performed. However, the expected increase in statistical performance from the MB approach permitted the use of a simplified SR selection criteria. The selection criteria were chosen to include observables that are physically well understood and have kinematically motivated properties whilst preferably using "low-scale" thresholds, that is, selection thresholds on observables that are not selecting

---

[3]See Figure C.1 of Appendix C.1.

Gtt	Gbb	Gtb
$m(\tilde{g}, \tilde{\chi}_1^0)$ [GeV] ($M_{\mathrm{susy}}^{\mathrm{eff}}$ [GeV])	$m(\tilde{g}, \tilde{\chi}_1^0)$ [GeV] ($M_{\mathrm{susy}}^{\mathrm{eff}}$ [GeV])	$m(\tilde{g}, \tilde{\chi}_1^0)$ [GeV] ($M_{\mathrm{susy}}^{\mathrm{eff}}$ [GeV])
1100,1 (1100)	1100,1 (1100)	1100,1 (1100)
1100,200 (1045)	1100,1000 (148.2)	1100,600 (686.7)
1100,400 (900.0)	1100,200 (1047)	1200,1 (1200)
1100,600 (686.7)	1100,400 (900.0)	1200,600 (812.5)
1100,745 (504.4)	1100,600 (686.7)	1300,1 (1300)
1200,1 (1200)	1100,800 (430.8)	1300,600 (935.7)
1200,200 (1151)	1200,1 (1200)	1400,1 (1400)
1200,400 (1014)	1200,1000 (292.9)	1500,1 (1500)
1200,600 (812.5)	1200,200 (1151)	1600,1 (1600)
1200,800 (567.0)	1200,400 (1014)	
1200,845 (507.4)	1200,600 (812.5)	
1300,1 (1300)	1200,800 (567.0)	
1300,200 (1255)	1300,1 (1300)	
1300,400 (1127)	1300,1000 (434.4)	
1300,600 (935.7)	1300,200 (1255)	
1300,800 (700.0)	1300,400 (1127)	
1400,1 (1400)	1300,600 (935.7)	
1400,200 (1358)	1300,800 (700.0)	
1400,400 (1238)	1400,1 (1400)	
1500,1 (1500)	1400,1000 (572.9)	
	1400,1200 (294.0)	
	1400,200 (1358)	
	1400,400 (1234)	
	1400,600 (1056)	
	1500,1 (1500)	
	1500,200 (1461)	
	1500,400 (1348)	
	1500,600 (1175)	
	1600,1 (1600)	
	1600,200 (1563)	
	1600,400 (1456)	

Table 9.1: Strongly produced SUSY models and their corresponding $M_{\mathrm{susy}}^{\mathrm{eff}}$, which resulted in a $\chi^2/N_{\mathrm{dof}} > 3$ from fitting a two-parameter Gaussian function with a fixed width. The signals are classified by the decay of the gluino.

deep into the tail of the distributions. An example of an observable satisfying these requirements would be the $m_{T,min}^{b-jets}$. Because of the kinematic endpoint of the top quark, $m_{T,min}^{b-jets}$ has a physically-motivated threshold and thereby does not require optimisation, in addition to being highly effective at reducing the dominant $t\bar{t}$ background. One could also include dimensionless quantities, which avoid sculpting the signal shape. Observables where large increases in the sensitivity to compressed signal models are particularly beneficial, but validation of the Gaussian approximation in this subsequent region should be performed. The signal regions of this search were defined with this philosophy.

Because this is a research and development (R&D) study, only signal regions where leptons are absent were considered. However, as will be shown later, the leptonic CC Gtt regions have greater sensitivity to the Gtt model-space than the zero-lepton and so, this is an area for improvement in this search. In addition to the zero-lepton preselection requirements introduced in Section 8.3.5 and the $m_{T,min}^{b-jets}$ selection, the remaining observables used in the signal region optimisation were N_{jet}, N_{b-jet} and E_T^{miss}/m_{eff}. Figures presenting each of these observables for a zero-lepton preselection can be seen in Figure 9.7.
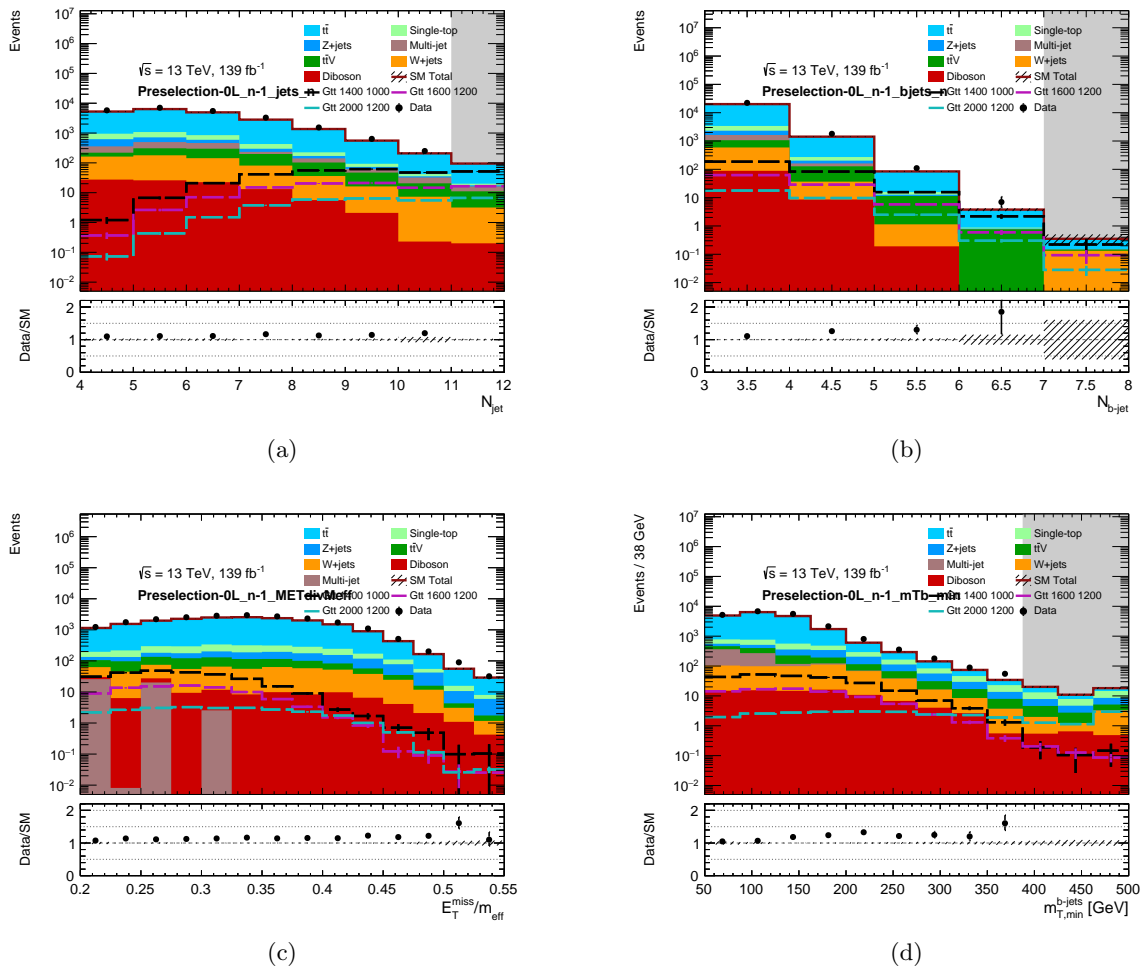
Figure 9.7: Plots of the quantities used to define the signal regions with a zero-lepton preselection with Gtt signals $m(\tilde{g}, \tilde{\chi}_1^0) = (1400,1000), (1600,1200), (2000,1200)$ overlayed. Only statistical uncertainties are included and the plots are blinded in bins of low data statistics.

The selections on E_T^{miss}/m_{eff} and N_{b-jet} were chosen to be > 0.25 and ≥ 4, respectively, to increase the sensitivity to the signal whilest remaining low-scale. One notable exception to the low-scale selection strategy is the relatively high threshold chosen for the jet multiplicity (≥ 10) for one signal region. This has been implemented because of the dramatic increase in sensitivity to compressed Gtt models, which is the main kinematic phase-space of interest for this method. The closure tests, presented in Section 9.7, show that the Gaussian signal approximation holds with this selection. An additional signal region with a looser jet multiplicity selection (≥ 4 jets), named "SR-4j", which is sensitive to the Gbb signals, has also been defined. The definitions of the optimised signal regions can be seen in Table 9.2.

Signal, Control and Validation Regions

Criteria common to all regions: $N_{b-jet} \geq 4$, $E_T^{miss}/m_{eff} > 0.25$

Region Type	$N_{baseline,\ leptons}$	$N_{signal,\ leptons}$	$\Delta\phi_{min}^{4j}$	N_{jet}	m_T [GeV]	$m_{T,min}^{b-jets}$ [GeV]
SR	$= 0$	$-$	> 0.4	≥ 10	$-$	≥ 175
SR-4j	$= 0$	$-$	> 0.4	≥ 4	$-$	≥ 175
CR	$-$	≥ 1	$-$	≥ 4	≤ 80	≤ 175
VR-0L-MTB	$= 0$	$-$	> 0.4	≥ 7	$-$	≤ 175
VR-1L-MT	$-$	≥ 1	$-$	≥ 7	≤ 80	≥ 175
VR-1L-MTB	$-$	≥ 1	$-$	≥ 7	$-$	≤ 175
VR-4j-0L-MTB	$= 0$	$-$	> 0.4	≥ 4	$-$	≤ 175
VR-4j-1L-MT	$-$	≥ 1	$-$	≥ 4	≤ 80	≥ 175
VR-4j-1L-MTB	$-$	≥ 1	$-$	≥ 4	$-$	≤ 175

Table 9.2: The definitions of the shape fit analysis regions, all of which are binned in $\log 10(m_{eff})$. The regions can effectively be categorised into high and low (given the name "4j") N_{jet} regions, which are sensitive to the Gtt and Gbb signal processes, respectively. The selections for each equivalent high and low N_{jet} SR and VR are the same except for the threshold on the N_{jet}. Only one control region is defined, which is used for normalisation of the $t\bar{t}$ background in each signal and validation region.

The selection criteria of each analysis region is applied to events binned in the $\log 10(m_{eff})$ distribution with the binning defined in Table 9.3. The range of the binning was optimised in accordance with the requirement on the number of data events in each bin for the CR.

Bin Number	0	1	2	3	4	5	6	7	8
$\log 10(m_{eff}/GeV)$	[2.9, 2.95]	[2.95, 3.0]	[3.0, 3.05]	[3.05, 3.1]	[3.1, 3.15]	[3.15, 3.2]	[3.2, 3.25]	[3.25, 3.3]	[3.3, ∞]

Table 9.3: All analysis regions are binned in the $\log 10(m_{eff})$ distribution, where the binning is defined in this table. Each region has a total of nine bins, ranging from 2.9 to 3.3 $\log 10(m_{eff}/GeV)$, where the final bin is inclusive beyond 3.3 $\log 10(m_{eff}/GeV)$.

The background estimation strategy is almost the same as Chapter 8. For each SM background process, the same background estimation technique is used except for the multi-jet background. The multi-jet background is estimated with di-jet MC because of the almost-negligible contribution in the zero-lepton SRs of Chapter 8 and the inability to implement the method. The kinematic reweighting of events including leptons is also used because of the improvement in the modelling

of the m_{eff} distribution. The reweighting scale factors are derived in dedicated reweighting regions where $m_{T,min}^{b-jets} < 350$ GeV and because the CR of this analysis also occupies an area of this phase-space, it has been argued this reweighting is still valid.

The $t\bar{t}$ background is estimated using a dedicated 1L control region (CR), which ensures orthogonality with the SR. The likelihood fit has nine $t\bar{t}$ normalisation factors for the nine SR (CR) bins and are fitted simultaneously. Compared to the SB strategy, using multiple SR bins particularly benefits when using the transfer factor method for background estimation [102]. This is because a MB analysis can use the difference in the shape of data and MC which the single-bin cannot. Therefore, any shape-dependent background systematic uncertainties can be constrained. A minimum of one data event was required in each of the CR bins. A selection on m_T and an inverted selection with respect to the SR requirement on $m_{T,min}^{b-jets}$ are included to enhance the $t\bar{t}$ purity in the region. Figures of the post-fit $\log 10(m_{eff})$ distribution for the SR and CR analysis regions can be seen in Figure 9.8. An additional figure presenting the CR pre-fit is also included. All post-fit yields were obtained from a background-only fit and extrapolated into the relevant signal or validation region. The results of this fit are presented in Appendix D.6.

It could be argued, the data-to-MC ratio in the CR has sufficient agreement within the total uncertainty band except for the $[3.05, 3.1]$ $\log 10(m_{eff}/GeV)$ bin. An investigation into this disagreement found discrepancies originating from the highest p_T jet ($225 \leq p_T \leq 250$ GeV, $2 \leq \phi \leq 3$ rads, $|\eta| \leq 1$), highest p_T lepton ($25 \leq p_T \leq 90$ GeV, $|\eta| \leq 0.3$) and the MC generally underpredicting the data for the E_T^{miss} observable. The origin of the cause is yet to be determined. Figures presenting the investigation into this discrepancy can be found in Appendix D.2. Because the remainder of the background expectation is in agreement with the data within the total uncertainty, this discrepancy is considered an anomaly and therefore, it has been argued to justify the CR definition. As expected, the $t\bar{t}$ background dominates all the CR bins. The signal contamination is low in most bins except for the final inclusive bin $[> 3.3, \infty]$ $\log 10(m_{eff}/GeV)$, where it is $\sim 30\%$.

Three validation regions (VRs) were defined with a high (low) N_{jet} selection; VR-0L-MTB (VR-4j-0L-MTB), VR-1L-MT (VR-4j-1L-MT) and VR-1L-MTB (VR-4j-1L-MTB), corresponding to the high (low) N_{jet} SRs. The naming convention indicates the number of leptons required (nL), whether there is a reduced $N_{jet} \geq 7 \rightarrow \geq 4$ threshold (inclusion of "4j"), and the observable which is inverted relative to the SR definition, where MT and MTB are the quantities m_T and $m_{T,min}^{b-jets}$, respectively. The zero-lepton VR is designed to validate the extrapolation from the one-lepton CR to the zero-lepton SR. The remaining two one-lepton VRs validate the extrapolation of the additional two inverted observables used in the CR, m_T and $m_{T,min}^{b-jets}$, respectively. No requirements were placed on the number of data events in the VRs; however, it was preferable that the majority of VR bins had at least one data event whilst maximising the N_{jet} threshold to be as close to the SR as possible. Figures of each VR for the $\log 10(m_{eff})$ distribution can be seen in Figures 9.9.

The data-to-MC ratio is in agreement in most bins of the $\log 10(m_{eff})$ distribution, in particular for all high N_{jet} VRs, of which the VR-1L-MT has the lowest background expectation. The

(a) SR

(b) SR-4j

(c) CR pre-fit

(d) CR post-fit
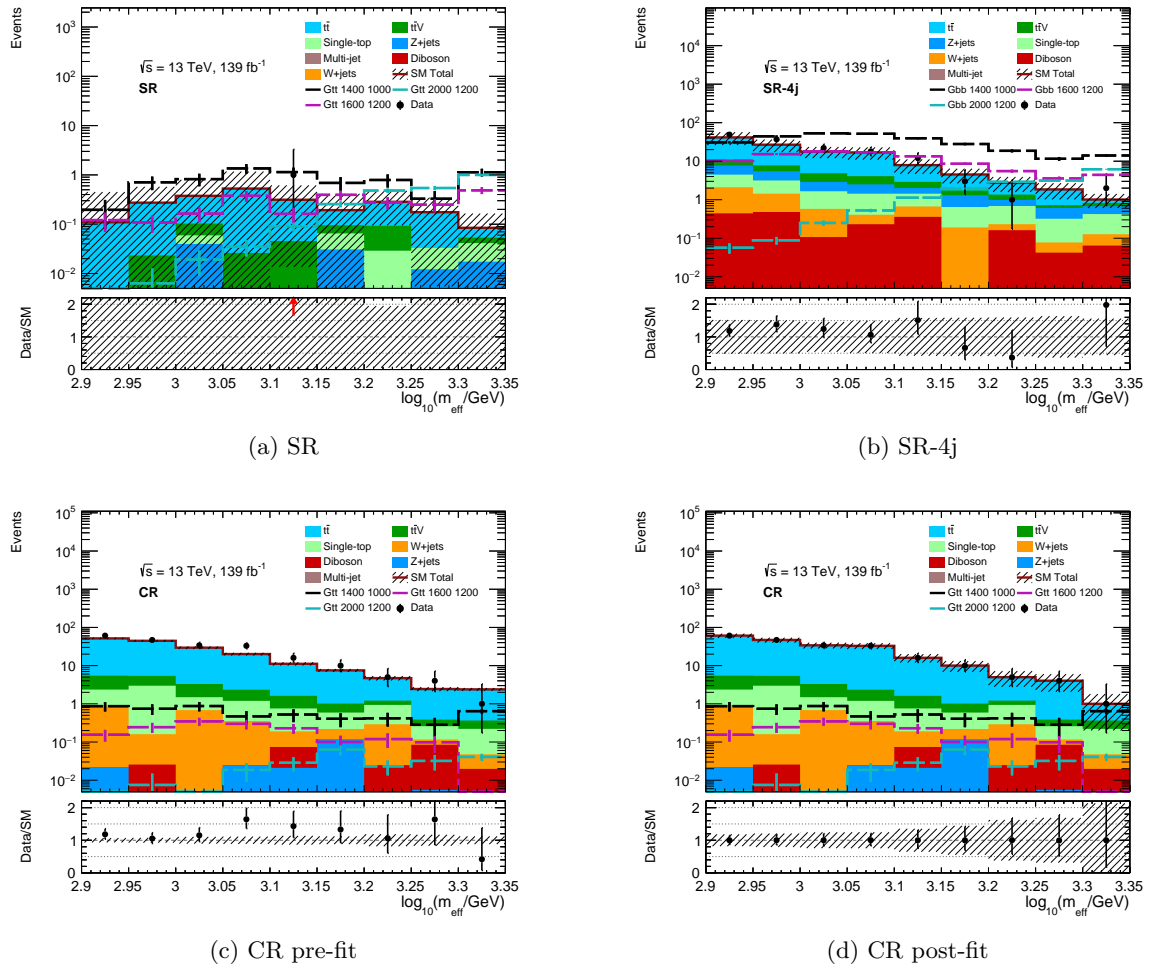
Figure 9.8: All the post-fit signal and control regions - SR, SR-4j and CR (as defined in Table 9.2) plotted in the $\log 10(m_{\text{eff}})$ distribution with the binning defined in Table 9.3. An additional plot for the pre-fit CR is also included. All regions have Gtt $m(\tilde{g}, \tilde{\chi}_1^0) = (1400,1000)$, (1600,1200), (2000,1200) overlayed, except SR-4j, which has Gbb signals with the same mass parameters. The bottom pad indicates the ratio of the data to total Standard Model background in each bin. For (d) the bottom pad corresponds to the $t\bar{t}$ normalisation factors for each bin. The systematic configuration of Section 9.4, which includes all systematic and statistical uncertainties, is included.

(a) VR-0L-MTB

(b) VR-4j-0L-MTB

(c) VR-1L-MT

(d) VR-4j-1L-MT

(e) VR-1L-MTB
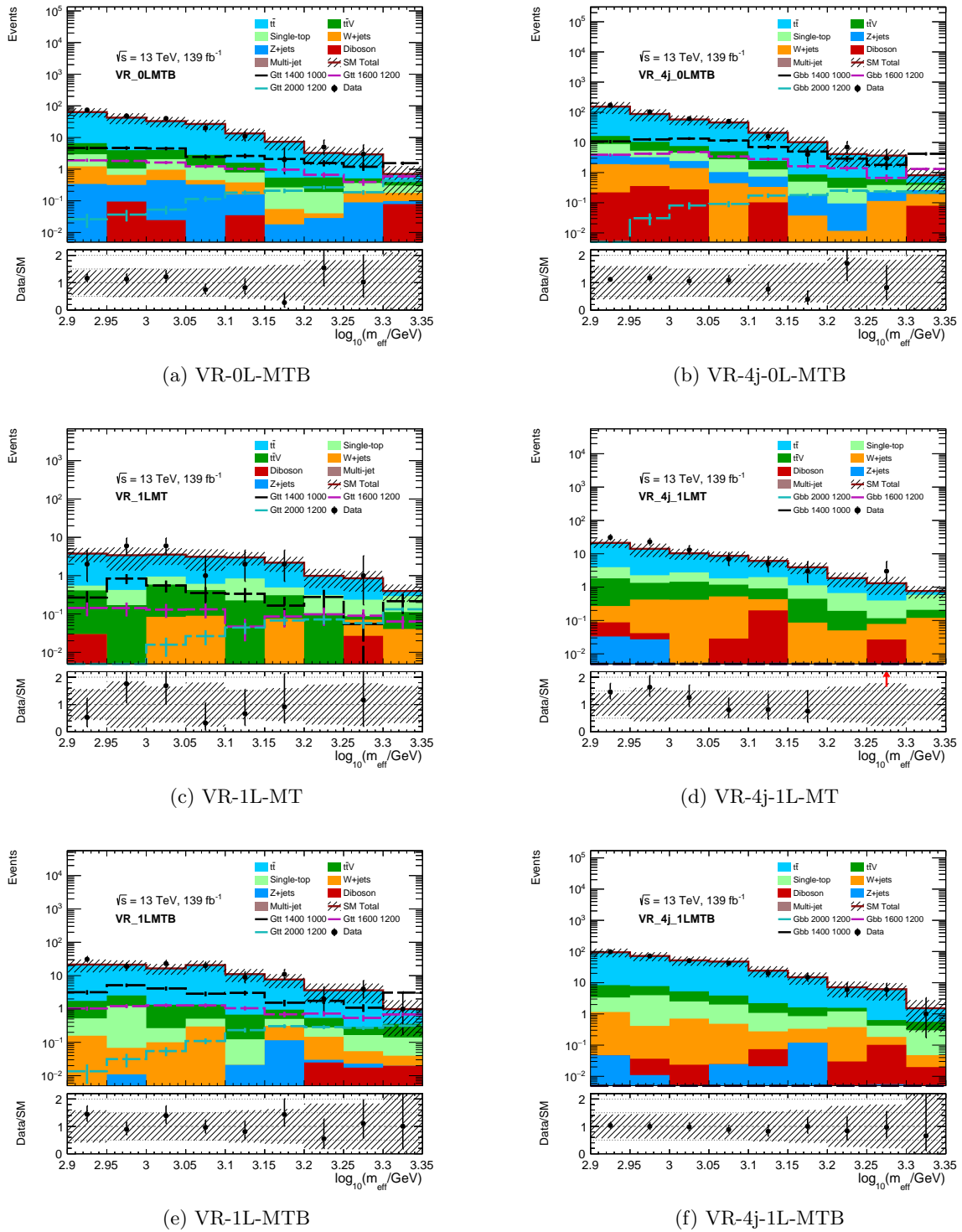
(f) VR-4j-1L-MTB

Figure 9.9: All the post-fit validation regions - VR-0L-MTB, VR-1L-MT, VR-1L-MTB, VR-4j-0L-MTB, VR-4j-1L-MT and VR-4j-1L-MTB (as defined in Table 9.2) plotted in the $\log 10(\mathrm{m_{eff}})$ distribution with the binning defined in Table 9.3. All regions have Gtt $m(\tilde{g}, \tilde{\chi}_1^0) = (1400,1000)$, (1600,1200), (2000,1200) overlayed except 4j VRs, which have equivalent signals but for the Gbb final state. The bottom pad indicates the ratio of the data to total Standard Model background in each bin. The systematic configuration of Section 9.4, which includes all systematic and statistical uncertainties, is included.

$\log 10(m_{\mathrm{eff}}/\mathrm{GeV})$	[2.9,2.95]	[2.95,3.0]	[3.0,3.05]	[3.05,3.1]	[3.1,3.15]	[3.15,3.2]	[3.2,3.25]	[3.25,3.3]	[3.3 → ∞]
Observed events	0	0	0	0	1	0	0	0	0
Fitted background	$0.12^{+0.34}_{-0.12}$	$0.27^{+0.30}_{-0.27}$	$0.38^{+0.42}_{-0.38}$	$0.53^{+0.64}_{-0.53}$	0.32 ± 0.30	$0.19^{+0.22}_{-0.19}$	0.29 ± 0.19	0.18 ± 0.17	0.08 ± 0.08
$t\bar{t}$	$0.12^{+0.34}_{-0.12}$	$0.25^{+0.27}_{-0.25}$	$0.27^{+0.42}_{-0.27}$	$0.51^{+0.63}_{-0.51}$	$0.27^{+0.32}_{-0.27}$	$0.10^{+0.24}_{-0.10}$	0.19 ± 0.16	$0.14^{+0.15}_{-0.14}$	$0.03^{+0.05}_{-0.03}$
Single top	< 0.01	< 0.01	$0.02^{+0.07}_{-0.02}$	< 0.01	< 0.01	$0.03^{+0.04}_{-0.03}$	$0.03^{+0.04}_{-0.03}$	$0.02^{+0.03}_{-0.02}$	0.02 ± 0.01
$t\bar{t} + X$	< 0.01	$0.02^{+0.04}_{-0.02}$	$0.04^{+0.05}_{-0.04}$	$0.03^{+0.03}_{-0.03}$	$0.04^{+0.08}_{-0.04}$	$0.03^{+0.05}_{-0.03}$	0.06 ± 0.05	< 0.01	$0.01^{+0.02}_{-0.01}$
W+$jets$	< 0.01	< 0.01	< 0.01	< 0.01	< 0.01	< 0.01	< 0.01	< 0.01	< 0.01
Z+$jets$	< 0.01	< 0.01	$0.04^{+0.04}_{-0.04}$	< 0.01	< 0.01	$0.03^{+0.06}_{-0.03}$	< 0.01	$0.01^{+0.02}_{-0.01}$	$0.02^{+0.02}_{-0.02}$
Diboson	< 0.01	< 0.01	< 0.01	< 0.01	< 0.01	< 0.01	< 0.01	< 0.01	< 0.01
Multijet	< 0.01	< 0.01	< 0.01	< 0.01	< 0.01	< 0.01	< 0.01	< 0.01	< 0.01
Pre-fit background	0.10	0.26	0.34	0.32	0.22	0.17	0.27	0.11	0.15

Table 9.4: The table presents the observed number of events and the predicted background yield after the fit for the signal region SR. The values are obtained from extrapolating the background-only fit results (Appendix D.6) to this region. The background category $t\bar{t} + X$ includes $t\bar{t}W/Z$, $t\bar{t}H$ and $t\bar{t}t\bar{t}$ events.

$\log 10(m_{\mathrm{eff}}/\mathrm{GeV})$	[2.9,2.95]	[2.95,3.0]	[3.0,3.05]	[3.05,3.1]	[3.1,3.15]	[3.15,3.2]	[3.2,3.25]	[3.25,3.3]	[3.3 → ∞]
Observed events	49	37	22	18	12	3	1	0	2
Fitted background	41.57 ± 15.15	26.82 ± 9.61	17.72 ± 5.70	16.95 ± 5.91	7.93 ± 3.24	4.53 ± 1.87	2.75 ± 1.15	1.85 ± 0.83	1.01 ± 0.40
$t\bar{t}$	30.54 ± 14.82	19.02 ± 9.10	12.82 ± 5.37	12.86 ± 5.97	5.01 ± 3.09	2.79 ± 1.73	1.39 ± 1.07	1.13 ± 0.78	$0.19^{+0.26}_{-0.19}$
Single top	2.38 ± 1.06	1.72 ± 0.55	1.08 ± 0.65	1.03 ± 0.34	0.77 ± 0.19	0.46 ± 0.15	0.46 ± 0.13	0.24 ± 0.08	0.30 ± 0.18
$t\bar{t} + X$	3.29 ± 1.75	2.32 ± 1.28	2.00 ± 1.07	1.59 ± 0.85	0.91 ± 0.48	0.43 ± 0.24	0.37 ± 0.23	0.11 ± 0.08	0.15 ± 0.14
W+$jets$	1.67 ± 1.11	0.95 ± 0.66	0.47 ± 0.32	$0.18^{+0.29}_{-0.18}$	0.31 ± 0.17	0.19 ± 0.10	0.07 ± 0.03	$0.04^{+0.04}_{-0.04}$	$0.06^{+0.07}_{-0.06}$
Z+$jets$	3.26 ± 1.17	2.32 ± 1.08	1.24 ± 0.68	1.07 ± 0.40	0.57 ± 0.30	0.66 ± 0.31	0.30 ± 0.13	0.29 ± 0.22	0.26 ± 0.11
Diboson	0.44 ± 0.24	0.48 ± 0.27	$0.11^{+0.14}_{-0.11}$	0.23 ± 0.14	0.36 ± 0.18	< 0.01	$0.16^{+0.18}_{-0.16}$	0.04 ± 0.02	0.06 ± 0.04
Multijet	< 0.01	< 0.01	< 0.01	< 0.01	< 0.01	< 0.01	< 0.01	< 0.01	< 0.01
Pre-fit background	36.33	25.79	15.83	11.52	6.24	3.75	2.64	1.36	1.41

Table 9.5: The table presents the observed number of events and the predicted background yield after the fit for the signal region SR-4j. The values are obtained from extrapolating the background-only fit results (Appendix D.6) to this region. The background category $t\bar{t} + X$ includes $t\bar{t}W/Z$, $t\bar{t}H$ and $t\bar{t}t\bar{t}$ events.

equivalent VRs with looser N_{jet} thresholds show similar trends in the data-to-MC ratio, albeit with increased data statistics as expected. Mismodelling is present in the first two bins and $[3.05, 3.1]$ $\log 10(m_{\mathrm{eff}}/\mathrm{GeV})$ bin of VR-4j-1L-MT, albeit compatible within the total uncertainty. The observed signal contamination in each region follows similar to what was observed for the CR, however, in general, the signal contamination is higher - reaching a maximum in the final inclusive bin $[> 3.3, \infty]$ $\log 10(m_{\mathrm{eff}}/\mathrm{GeV})$, where it is $> 100\%$.

The final important selection to validate is the $N_{\mathrm{jet}} \geq 10$ threshold in the SR. To do this, the three high N_{jet} VRs, defined in Table 9.2, were adjusted to require this jet multiplicity. These VRs are plotted for the $\log 10(m_{\mathrm{eff}})$ distribution in Figure D.6 in Appendix D.3. These predict, as expected, very few Monte Carlo and data events and hence, why the selection was not used. However, the data-to-MC ratio could be argued to be satisfactory in the zero-lepton VR given the extremely low data statistics. Whereas, there are too few events in the one-lepton VRs to comment on the modelling of the data by the MC.

The numerical values for the post-fit expectation from each SM background and the data for each signal and validation region in Figures 9.8(a)-9.9(f) can be seen Tables 9.4-9.11.

$\log 10(m_{\text{eff}}/\text{GeV})$	[2.9,2.95]	[2.95,3.0]	[3.0,3.05]	[3.05,3.1]	[3.1,3.15]	[3.15,3.2]	[3.2,3.25]	[3.25,3.3]	[3.3 → ∞]
Observed events	74	48	40	20	11	2	5	3	0
Fitted background	63.70 ± 20.57	42.39 ± 15.88	32.81 ± 11.55	26.75 ± 9.61	13.44 ± 5.57	7.32 ± 3.36	3.25 ± 1.88	2.92 ± 1.70	0.70 ± 0.55
$t\bar{t}$	57.07 ± 20.58	38.42 ± 15.04	28.79 ± 11.46	23.92 ± 9.45	11.85 ± 5.53	6.78 ± 3.36	2.70 ± 1.86	2.41 ± 1.67	$0.31^{+0.42}_{-0.31}$
Single top	1.73 ± 1.29	$0.38^{+0.82}_{-0.38}$	1.11 ± 0.46	0.84 ± 0.20	0.41 ± 0.13	0.21 ± 0.06	0.15 ± 0.05	$0.16^{+0.18}_{-0.16}$	0.13 ± 0.07
$t\bar{t} + X$	3.68 ± 1.95	2.93 ± 1.57	1.96 ± 1.05	1.53 ± 0.82	0.81 ± 0.48	$0.27^{+0.29}_{-0.27}$	0.36 ± 0.27	0.14 ± 0.12	0.08 ± 0.06
$W + jets$	0.89 ± 0.74	$0.34^{+0.41}_{-0.34}$	0.51 ± 0.34	$0.13^{+0.40}_{-0.13}$	$0.22^{+0.28}_{-0.22}$	$0.04^{+0.06}_{-0.04}$	$0.01^{+0.02}_{-0.01}$	$0.12^{+0.26}_{-0.12}$	$0.08^{+0.19}_{-0.08}$
$Z + jets$	$0.34^{+0.77}_{-0.34}$	$0.22^{+0.39}_{-0.22}$	0.43 ± 0.17	$0.33^{+0.35}_{-0.33}$	0.13 ± 0.10	$0.02^{+0.04}_{-0.02}$	0.03 ± 0.02	0.09 ± 0.03	0.02 ± 0.01
Diboson	< 0.01	0.09 ± 0.05	$0.02^{+0.07}_{-0.02}$	< 0.01	0.04 ± 0.02	< 0.01	< 0.01	< 0.01	$0.08^{+0.17}_{-0.08}$
Multijet	< 0.01	< 0.01	< 0.01	< 0.01	< 0.01	< 0.01	< 0.01	< 0.01	< 0.01
Pre-fit background	54.04	40.25	28.64	16.69	9.45	5.44	3.04	1.87	1.39

Table 9.6: The table presents the observed number of events and the predicted background yield after the fit for the validation region VR-0L-MT. The values are obtained from extrapolating the background-only fit results (Appendix D.6) to this region. The background category $t\bar{t} + X$ includes $t\bar{t}W/Z$, $t\bar{t}H$ and $t\bar{t}t\bar{t}$ events.

$\log 10(m_{\text{eff}}/\text{GeV})$	[2.9,2.95]	[2.95,3.0]	[3.0,3.05]	[3.05,3.1]	[3.1,3.15]	[3.15,3.2]	[3.2,3.25]	[3.25,3.3]	[3.3 → ∞]
Observed events	2	6	6	1	2	2	0	1	0
Fitted background	3.76 ± 1.51	3.41 ± 2.05	3.56 ± 1.65	3.10 ± 1.77	2.99 ± 1.13	2.18 ± 0.92	0.99 ± 0.51	0.85 ± 0.47	0.40 ± 0.19
$t\bar{t}$	3.21 ± 1.40	2.99 ± 2.03	2.61 ± 1.49	2.49 ± 1.56	2.14 ± 1.03	1.69 ± 0.87	0.68 ± 0.49	0.62 ± 0.45	$0.10^{+0.14}_{-0.10}$
Single top	$0.14^{+0.17}_{-0.14}$	0.26 ± 0.17	0.36 ± 0.27	$0.19^{+0.37}_{-0.19}$	0.62 ± 0.49	0.18 ± 0.11	0.21 ± 0.07	0.15 ± 0.08	0.18 ± 0.09
$t\bar{t} + X$	0.38 ± 0.25	$0.17^{+0.18}_{-0.17}$	0.50 ± 0.32	0.33 ± 0.20	0.23 ± 0.15	0.23 ± 0.15	0.10 ± 0.07	$0.02^{+0.03}_{-0.02}$	0.07 ± 0.05
$W + jets$	< 0.01	< 0.01	0.08 ± 0.04	0.09 ± 0.08	< 0.01	0.08 ± 0.04	$0.00^{+0.01}_{-0.00}$	0.04 ± 0.03	0.04 ± 0.02
$Z + jets$	< 0.01	< 0.01	< 0.01	< 0.01	< 0.01	< 0.01	< 0.01	< 0.01	< 0.01
Diboson	0.03 ± 0.02	< 0.01	< 0.01	< 0.01	< 0.01	< 0.01	< 0.01	$0.03^{+0.05}_{-0.03}$	< 0.01
Multijet	< 0.01	< 0.01	< 0.01	< 0.01	< 0.01	< 0.01	< 0.01	< 0.01	< 0.01
Pre-fit background	3.22	3.25	3.17	2.06	2.27	1.71	0.94	0.59	0.62

Table 9.7: The table presents the observed number of events and the predicted background yield after the fit for the validation region VR-1L-MT. The values are obtained from extrapolating the background-only fit results (Appendix D.6) to this region. The background category $t\bar{t} + X$ includes $t\bar{t}W/Z$, $t\bar{t}H$ and $t\bar{t}t\bar{t}$ events.

$\log 10(m_{\text{eff}}/\text{GeV})$	[2.9,2.95]	[2.95,3.0]	[3.0,3.05]	[3.05,3.1]	[3.1,3.15]	[3.15,3.2]	[3.2,3.25]	[3.25,3.3]	[3.3 → ∞]
Observed events	31	19	23	20	9	11	2	4	1
Fitted background	21.47 ± 8.94	21.30 ± 7.48	16.47 ± 5.83	20.71 ± 7.57	11.10 ± 4.64	7.65 ± 3.43	3.65 ± 2.15	3.62 ± 2.15	0.99 ± 0.84
$t\bar{t}$	19.72 ± 8.79	18.75 ± 7.38	15.13 ± 5.80	19.35 ± 7.48	10.43 ± 4.61	6.69 ± 3.32	3.11 ± 2.14	3.33 ± 2.15	$0.63^{+0.83}_{-0.63}$
Single top	0.36 ± 0.33	1.17 ± 0.65	$0.16^{+0.62}_{-0.16}$	0.21 ± 0.16	0.10 ± 0.05	0.19 ± 0.17	0.14 ± 0.12	0.11 ± 0.05	0.10 ± 0.05
$t\bar{t} + X$	1.23 ± 0.73	1.31 ± 0.82	1.07 ± 0.62	0.84 ± 0.49	0.56 ± 0.38	0.45 ± 0.26	0.26 ± 0.19	0.12 ± 0.07	0.22 ± 0.13
$W + jets$	$0.16^{+0.29}_{-0.16}$	$0.06^{+0.06}_{-0.06}$	$0.10^{+0.11}_{-0.10}$	0.30 ± 0.24	< 0.01	0.20 ± 0.09	0.12 ± 0.09	0.03 ± 0.02	0.02 ± 0.01
$Z + jets$	< 0.01	0.01 ± 0.01	< 0.01	< 0.01	$0.02^{+0.07}_{-0.02}$	0.12 ± 0.09	0.01 ± 0.00	0.01 ± 0.00	< 0.01
Diboson	< 0.01	< 0.01	< 0.01	< 0.01	< 0.01	< 0.01	0.02 ± 0.01	$0.02^{+0.04}_{-0.02}$	0.02 ± 0.01
Multijet	< 0.01	< 0.01	< 0.01	< 0.01	< 0.01	< 0.01	< 0.01	< 0.01	< 0.01
Pre-fit background	18.16	20.24	14.26	12.57	7.59	5.79	3.41	2.17	2.38

Table 9.8: The table presents the observed number of events and the predicted background yield after the fit for the validation region VR-1L-MTB. The values are obtained from extrapolating the background-only fit results (Appendix D.6) to this region. The background category $t\bar{t} + X$ includes $t\bar{t}W/Z$, $t\bar{t}H$ and $t\bar{t}t\bar{t}$ events.

$\log 10(m_{\text{eff}}/\text{GeV})$	[2.9,2.95]	[2.95,3.0]	[3.0,3.05]	[3.05,3.1]	[3.1,3.15]	[3.15,3.2]	[3.2,3.25]	[3.25,3.3]	[3.3 → ∞]
Observed events	172	103	61	50	16	4	7	3	0
Fitted background	154.07 ± 65.75	87.47 ± 37.14	57.61 ± 20.62	45.81 ± 17.10	20.93 ± 9.82	10.18 ± 5.19	4.12 ± 2.65	3.66 ± 2.15	0.81 ± 0.59
$t\bar{t}$	137.68 ± 65.69	77.04 ± 35.67	50.03 ± 20.45	40.72 ± 17.05	18.50 ± 9.55	9.32 ± 5.19	3.44 ± 2.63	3.05 ± 2.13	$0.35^{+0.48}_{-0.35}$
Single top	4.87 ± 1.57	2.06 ± 1.43	2.20 ± 0.66	1.74 ± 0.67	$0.54^{+0.62}_{-0.54}$	0.33 ± 0.13	0.22 ± 0.07	$0.16^{+0.18}_{-0.16}$	0.13 ± 0.07
$t\bar{t} + X$	7.53 ± 3.91	5.12 ± 2.65	2.97 ± 1.59	2.31 ± 1.25	1.16 ± 0.65	$0.36^{+0.38}_{-0.36}$	0.36 ± 0.22	0.21 ± 0.13	0.08 ± 0.07
W+jets	1.68 ± 0.69	1.48 ± 1.06	1.13 ± 0.78	$0.45^{+0.84}_{-0.45}$	$0.23^{+0.28}_{-0.23}$	$0.04^{+0.06}_{-0.04}$	$0.01^{+0.02}_{-0.01}$	$0.12^{+0.26}_{-0.12}$	$0.12^{+0.20}_{-0.12}$
Z+jets	2.08 ± 0.86	1.41 ± 0.95	1.01 ± 0.40	0.60 ± 0.37	$0.40^{+0.74}_{-0.40}$	0.13 ± 0.08	0.08 ± 0.05	0.11 ± 0.05	0.07 ± 0.03
Diboson	$0.22^{+0.30}_{-0.22}$	0.36 ± 0.25	$0.28^{+0.28}_{-0.28}$	< 0.01	0.10 ± 0.09	< 0.01	< 0.01	< 0.01	$0.08^{+0.17}_{-0.08}$
Multijet	< 0.01	< 0.01	< 0.01	< 0.01	< 0.01	< 0.01	< 0.01	< 0.01	< 0.01
Pre-fit background	130.51	83.29	50.28	28.65	14.68	7.57	3.85	2.32	1.58

Table 9.9: The table presents the observed number of events and the predicted background yield after the fit for the validation region VR-4j-0L-MT. The values are obtained from extrapolating the background-only fit results (Appendix D.6) to this region. The background category $t\bar{t} + X$ includes $t\bar{t}W/Z$, $t\bar{t}H$ and $t\bar{t}t\bar{t}$ events.

$\log 10(m_{\text{eff}}/\text{GeV})$	[2.9,2.95]	[2.95,3.0]	[3.0,3.05]	[3.05,3.1]	[3.1,3.15]	[3.15,3.2]	[3.2,3.25]	[3.25,3.3]	[3.3 → ∞]
Observed events	31	23	13	7	5	3	0	3	0
Fitted background	21.23 ± 6.18	14.04 ± 6.09	10.34 ± 3.69	8.64 ± 3.00	6.11 ± 2.15	3.94 ± 1.47	1.86 ± 0.86	1.30 ± 0.72	0.77 ± 0.31
$t\bar{t}$	17.26 ± 6.22	11.78 ± 5.87	7.58 ± 3.24	6.82 ± 2.85	4.11 ± 1.89	2.80 ± 1.42	1.20 ± 0.88	0.91 ± 0.63	$0.18^{+0.24}_{-0.18}$
Single top	2.14 ± 0.80	0.93 ± 0.61	1.31 ± 0.58	0.63 ± 0.61	1.09 ± 0.58	0.69 ± 0.22	0.47 ± 0.16	0.28 ± 0.12	0.38 ± 0.16
$t\bar{t} + X$	1.56 ± 1.08	0.92 ± 0.71	1.03 ± 0.65	0.66 ± 0.50	0.48 ± 0.30	0.36 ± 0.22	0.14 ± 0.12	$0.04^{+0.05}_{-0.04}$	0.09 ± 0.07
W+jets	$0.18^{+0.19}_{-0.18}$	$0.38^{+0.44}_{-0.38}$	$0.42^{+0.61}_{-0.42}$	0.50 ± 0.44	$0.23^{+0.30}_{-0.23}$	0.09 ± 0.05	0.05 ± 0.03	0.05 ± 0.05	0.12 ± 0.06
Z+jets	$0.03^{+0.09}_{-0.03}$	$0.03^{+0.04}_{-0.03}$	< 0.01	< 0.01	< 0.01	< 0.01	< 0.01	< 0.01	< 0.01
Diboson	0.05 ± 0.03	$0.01^{+0.06}_{-0.01}$	< 0.01	0.02 ± 0.01	0.20 ± 0.11	< 0.01	< 0.01	$0.03^{+0.18}_{-0.03}$	< 0.01
Multijet	< 0.01	< 0.01	< 0.01	< 0.01	< 0.01	< 0.01	< 0.01	< 0.01	< 0.01
Pre-fit background	18.30	13.43	9.22	5.78	4.72	3.15	1.77	0.91	1.15

Table 9.10: The table presents the observed number of events and the predicted background yield after the fit for the validation region VR-4j-1L-MT. The values are obtained from extrapolating the background-only fit results (Appendix D.6) to this region. The background category $t\bar{t} + X$ includes $t\bar{t}W/Z$, $t\bar{t}H$ and $t\bar{t}t\bar{t}$ events.

$\log 10(m_{\text{eff}}/\text{GeV})$	[2.9,2.95]	[2.95,3.0]	[3.0,3.05]	[3.05,3.1]	[3.1,3.15]	[3.15,3.2]	[3.2,3.25]	[3.25,3.3]	[3.3 → ∞]
Observed events	98	72	51	42	20	15	6	6	1
Fitted background	94.60 ± 29.18	71.88 ± 22.74	51.98 ± 17.09	47.56 ± 15.82	24.33 ± 9.46	14.97 ± 6.34	7.13 ± 3.77	6.20 ± 3.50	1.52 ± 1.26
$t\bar{t}$	86.21 ± 29.36	64.07 ± 22.97	46.69 ± 16.98	43.66 ± 15.79	22.11 ± 9.55	13.35 ± 6.35	5.56 ± 3.78	5.56 ± 3.50	$0.96^{+1.26}_{-0.96}$
Single top	2.21 ± 1.13	3.58 ± 1.36	1.80 ± 1.19	1.52 ± 0.60	0.80 ± 0.26	0.51 ± 0.26	0.83 ± 0.35	0.24 ± 0.12	0.25 ± 0.15
$t\bar{t} + X$	5.01 ± 3.06	3.82 ± 2.49	2.78 ± 1.60	1.89 ± 1.08	1.13 ± 0.94	0.77 ± 0.47	0.36 ± 0.30	0.21 ± 0.15	0.26 ± 0.16
W+jets	1.11 ± 0.53	0.38 ± 0.33	0.69 ± 0.38	$0.46^{+0.51}_{-0.46}$	$0.20^{+0.24}_{-0.20}$	0.21 ± 0.08	0.35 ± 0.18	$0.08^{+0.08}_{-0.08}$	0.03 ± 0.02
Z+jets	$0.05^{+0.12}_{-0.05}$	0.01 ± 0.01	< 0.01	$0.02^{+0.15}_{-0.02}$	$0.02^{+0.11}_{-0.02}$	0.12 ± 0.08	0.01 ± 0.00	0.01 ± 0.00	< 0.01
Diboson	< 0.01	$0.02^{+0.19}_{-0.02}$	$0.02^{+0.51}_{-0.02}$	< 0.01	0.05 ± 0.03	< 0.01	0.02 ± 0.01	0.10 ± 0.07	0.02 ± 0.01
Multijet	< 0.01	< 0.01	< 0.01	< 0.01	< 0.01	< 0.01	< 0.01	< 0.01	< 0.01
Pre-fit background	80.05	68.38	45.14	29.19	16.88	11.25	6.72	3.77	3.62

Table 9.11: The table presents the observed number of events and the predicted background yield after the fit for the validation region VR-4j-1L-MTB. The values are obtained from extrapolating the background-only fit results (Appendix D.6) to this region. The background category $t\bar{t} + X$ includes $t\bar{t}W/Z$, $t\bar{t}H$ and $t\bar{t}t\bar{t}$ events.

9.4   Uncertainties

Because this is a R&D study, the implementation of the systematic uncertainties is as close as possible to Chapter 8. However, where it has not been possible to implement such uncertainties, physically-motivated approximations have been made that are detailed next. Only the systematic uncertainties that differ from Chapter 8 will be presented here, but note, a complete systematic uncertainty configuration is employed covering both theoretical and experimental uncertainties.

$t\bar{t}$ **and single top theoretical uncertainties**   - Because the analyser was unable to implement the methods performed in Chapter 8, it was not possible to calculate the impact of the $t\bar{t}$ and single top theoretical uncertainties. To approximate this, the average of the relative uncertainties for the zero-lepton Gtt CC regions was used. This resulted in a relative uncertainty of 30% (6%) for $t\bar{t}$ (single top). In the CC region that targets compressed signals, Gtt-0L-C, the $t\bar{t}$ uncertainty is 33%. It could be argued that this would be overly conservative to apply to the entire phase-space and thus a difference of 3% should not greatly impact the results.

Multi-jet method   - Because the multi-jet background has not been estimated from a data-driven method and instead uses Monte Carlo, an approximation for the uncertainty must be made. The maximum multi-jet composition from the zero-lepton Gtt CC SRs is 4.6% with a total relative uncertainty of 8%. The compressed (C) and moderate (M2) regions have zero multi-jet events in the SR, whereas the kinematically higher-energy moderate (M1) and boosted (B) regions are those with the non-negligible multi-jet contributions. The di-jet Monte Carlo also yields zero events in the SR of the $\log 10(m_{\text{eff}})$ histogram, and because the more precise data-driven approach would have also applied a 300% uncertainty to this estimation, it has been argued that this would also be sufficient for the uncertainty in this search.

Gaussian width   - An uncertainty associated to the width would be derived from the variation in fitted widths across a range of particular BSM models. However, this choice of models is arbitrary and the resulting uncertainty is by definition model-dependent. It is for that reason that it is not included and the resulting impact will be reflected in the statistical sensitivity for discovery and exclusion on the BSM model.

9.5   Statistical Interpretations

The idea of a model-independent multi-bin shape fit (MB SF) was introduced at the start of this chapter, motivated by Section 9.2 and defined in Section 9.3. In this section, a series of likelihood fits for n Gaussian signals with mean y are performed and henceforth will be referred to as a *scan*. Effectively, this approach replicates a resonance search strategy similar to those used in the Higgs discovery [3], for a series of discrete bins, which has never been performed for an ATLAS SUSY search.

The signal processes are chosen to have a cross section of 1.0fb and are generated with 30,000 Gaussian-distributed events, where the mean is set to a range of SUSY mass scale (M_{susy}) values and the width of the Gaussian is fixed to 0.125. The range of means varies from $10^{\mu_G} = [800, 3500]$ GeV in 75 GeV intervals that corresponds to a minimum (maximum) Gaussian mean of 2.903 (3.544). The events are also assumed to have 100% acceptance of the SR and VR selections and 0% acceptance in the CR. Model-dependent acceptance and efficiency corrections are applied later when reinterpreting the results in the context of the Gtt and Gbb models.

The first scan performed searches for new physics, where the primary goal is to improve the statistical sensitivity to models with small mass splitting with respect to using the current ATLAS SUSY discovery strategy. The current ATLAS SUSY discovery strategy is the model-independent likelihood fit discussed in Section 6.4. A p-value is calculated for the null hypothesis to search for discrepancies between the data and the estimated background. The discovery strategy proposed in this chapter is effectively the same, however, a model independent fit would be performed with each Gaussian model and the distribution of obtained p-values results in a scan for discrepancies in the background expectation consistent with a Gaussian function. This strategy will henceforth be known as the discovery scan.

The objective of the second scan is to set limits on BSM processes. A 95% confidence level (CL) on the Gaussian normalisation as a function of the Gaussian mean is obtained. This strategy will henceforth be known as the exclusion scan. This results in improved ease of reinterpretation by allowing for any BSM signal, that could have an acceptance of events in the SR and can be described by a Gaussian with width 0.125, to interpolate a visible[4] cross section limit with the Gaussian mean of the signal. The model-dependent exclusion contours from this method are an approximation to those that might be obtained by performing an exclusion fit with the BSM models. The validation of this approximation for the Gtt exclusion contour can be found in Section 9.7.2. The difference in the limits arises if there are shape differences in the $\log 10(\text{m}_{\text{eff}})$ distribution between the Gaussian signal model and the Gtt/Gbb model.

9.5.1   Search for New Physics

The first strategy this method can be utilised for is in the search for new physics. If the events of a pair-produced simplified gluino model, such as Gtt $m(\tilde{g}, \tilde{\chi}_1^0) = 2000, 1200$ GeV, were included in the blinded[5] data and a discovery scan was performed to the SR using the Gaussian signal models, the results of the p-values obtained for the background-only hypothesis can be seen in Figure 9.10.

Figure 9.10 is a proof of concept of the general fit strategy. By effectively scanning over the data in the SR $\log 10(\text{m}_{\text{eff}})$ distribution with the Gaussian signals, one can evidently see how the p-value evolves over the range of Gaussian means. As the Gaussian mean tends towards the

---

[4]Visible meaning, the cross section limit assuming the experimental conditions imposed in this search. To obtain a true cross section limit, one would need to correct for the acceptance and efficiency of the search.

[5]The blinded data is equivalent to the post-fit background estimate throughout this section, however, as per this scenario, signal processes are also sometimes included to test the sensitivity of the method to the data to replicate the existence of the BSM signal. The inclusion of signal in the blinded data is termed *signal injection*.

Figure 9.10: The resulting background-only hypothesis p-values when performing a model independent fit for a range of Gaussian signals when Gtt $m(\tilde{g}, \tilde{\chi}_1^0) = 2000, 1200$ GeV is included in the blinded data for the SR defined in Figure 9.8(a). Note the $M_{\mathrm{susy}}^{\mathrm{eff,3\text{-}body}}$ of the Gtt signal process is 1115.6 GeV and has a fitted Gaussian mean of 3.219.

fitted Gaussian mean of the signal (3.219), the p-value tends towards a minimum ($\mu_G = 3.284$). Because the Gaussian mean of the Gtt signal is before the inclusive bin of the SR, the p-value increases as the Gaussian mean tends toward the inclusive bin. Approximately 84% (97.5%) events of the Gaussian signal are contained in the inclusive bin when the Gaussian mean is $\mu_G = 3.363$ ($\mu_G = 3.488$). Therefore, beyond $\mu_G = 3.3$, the likelihood fit can no longer exploit the shape information in all bins of the signal region and will decrease to an approximately constant minimum as more of the Gaussian events are contained in the inclusive bin.

An example of the pulls and constraining of the fit parameters as well as the correlation matrix for one of the Gaussian discovery fits from this scan can be seen in Figure 9.11.

There are no strong positive (or anti-)correlations between any POI or nuisance parameter. The nuisance parameters associated with the theoretical systematic uncertainties are all well constrained. Slight pulling and constraining of nuisance parameters associated with several jet-related uncertainties are observed. The $t\bar{t}$ normalisation factors are all > 1, indicating that the MC is underpredicting the data, except for the final bin, where it is < 1. The uncertainty in these parameters increases as the bin in the $\log 10(\mathrm{m_{eff}})$ distribution increases because of the decrease in data events. It is the yield in the second to final bin that has the largest uncertainty because the final bin is inclusive. For the same likelihood fit, the tabular breakdown of the contribution from the systematic uncertainties for each SR bin can be found in Table D.1 in Appendix D.5. The jet energy scale and resolution provide the largest contribution to the total systematic uncertainty. The uncertainties associated with the $t\bar{t}$ normalisation factors are largely sub-dominant and in certain instances, such as the $\mu_{t\bar{t}}(\mathrm{B2})$, it is almost negligible.

By performing discovery scans for each unblinded validation region defined in Section 9.3, the resulting p-values as a function of the Gaussian signal mean can be seen in Figure 9.12. Note that 10,000 pseudo-experiments have been used.

No statistically significant fluctuations or trends are present in the scans of any VR. This indicates
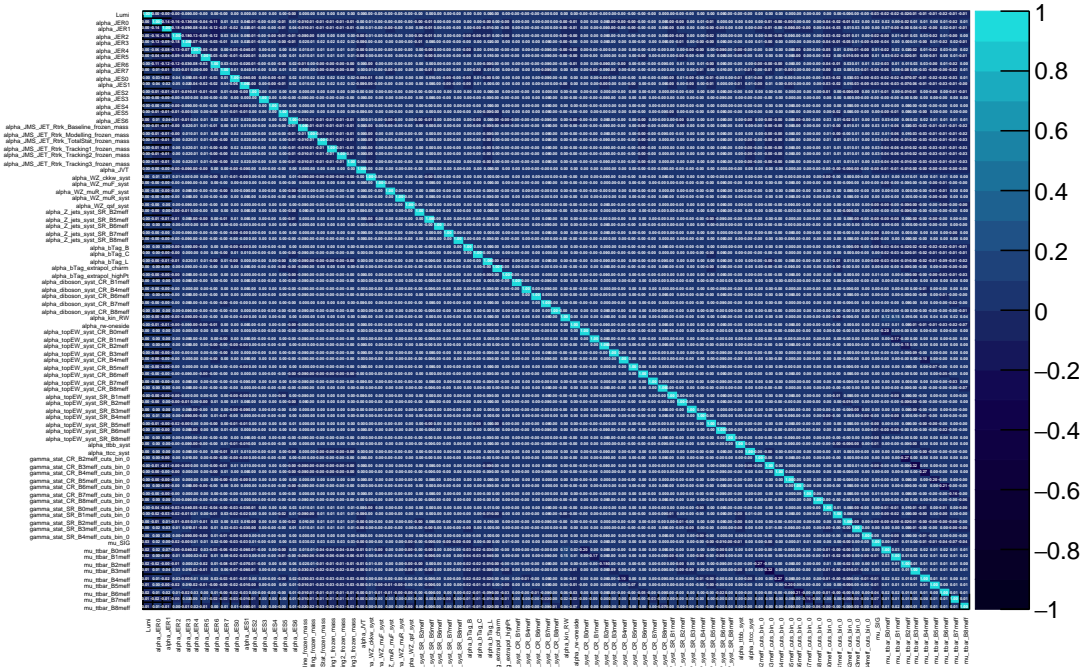
(a) Correlation Matrix
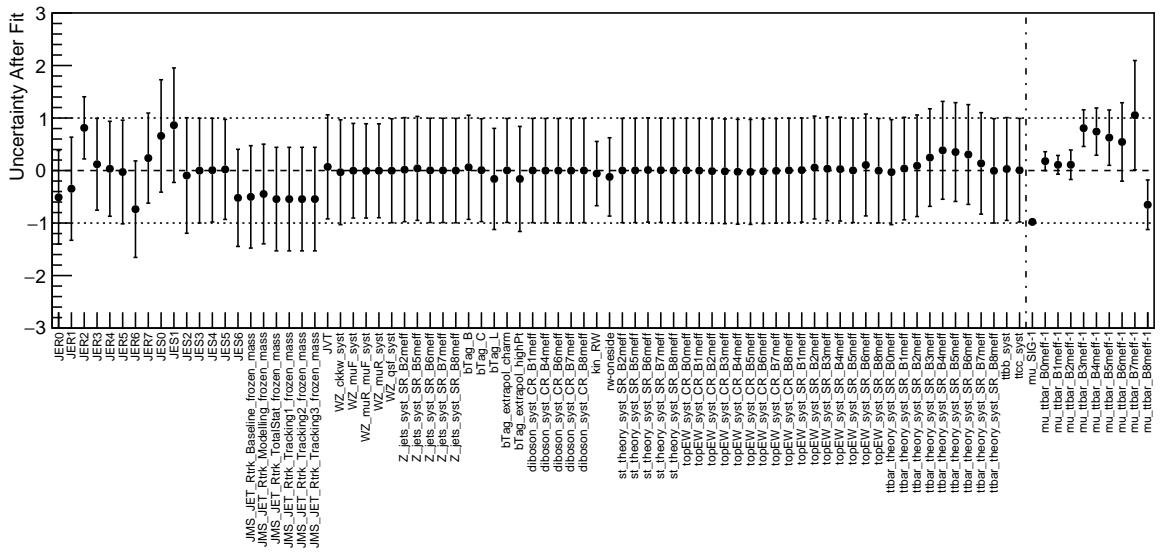
(b) Fit Parameter Constraints

Figure 9.11: The correlation matrix and constraining of the fit parameters from the model independent fit with the $\mu_G = 3.427$ Gaussian signal when Gtt $m(\tilde{g}, \tilde{\chi}_1^0) = 2000, 1200$ GeV is included in the blinded data.
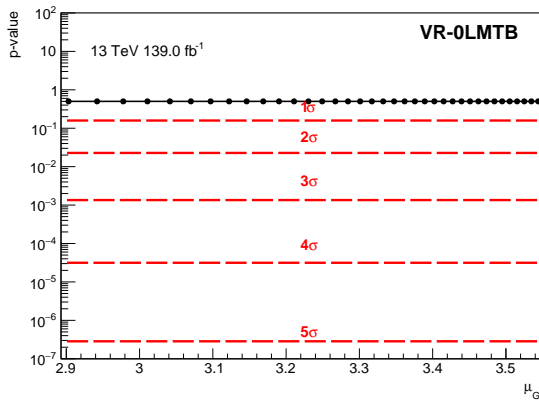
(a) VR-0L-MTB
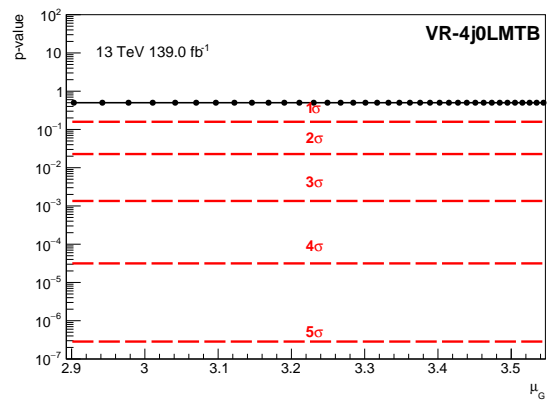
(b) VR-4j-0L-MTB
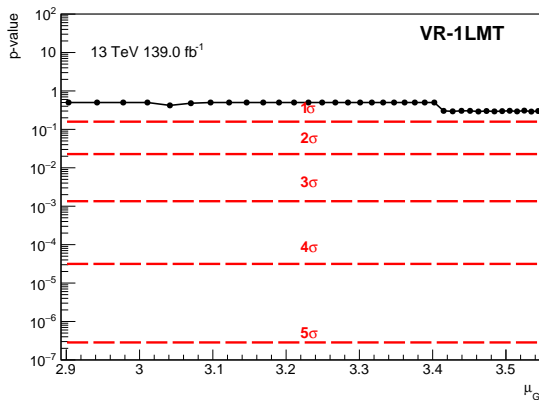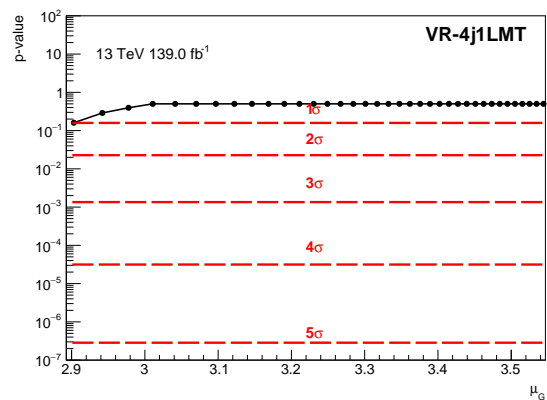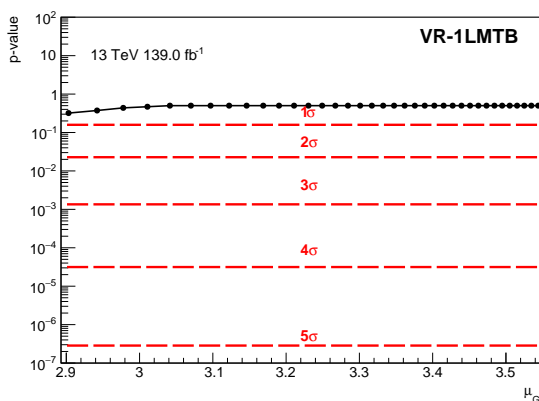
(c) VR-1L-MT

(d) VR-4j-1L-MT

(e) VR-1L-MTB
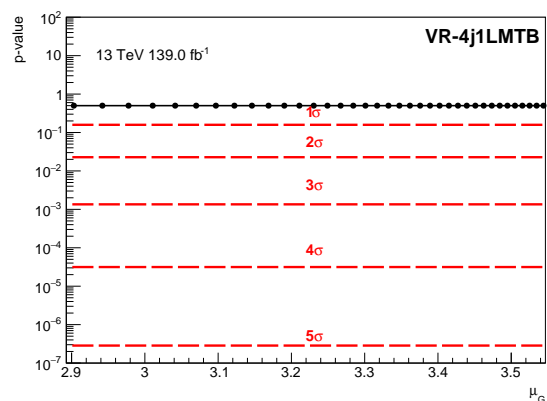
(f) VR-4j-1L-MTB

Figure 9.12: The resulting null hypothesis p-values when performing a model independent fit for a range of Gaussian signals for the six validation regions (a)-(f). All the results are produced with 10,000 pseudo-experiments and the p-values are truncated to 0.5.

a sufficient modelling of the data by the MC background in these regions and the presence of a *fake*[6] signal that could exist in the unblinded SRs would be unprobable.

First, let us discuss the VRs associated to the SR with a high N_{jet} threshold. For VR-0L-MTB in particular, all the p-values are 0.5[7] indicating that the background estimation methods are sufficient for this region. For VR-1L-MTB, the p-values are < 0.5 for the opening range of Gaussian signal means up to and including $\mu_G = 3.011$. These p-values correspond to significances $< 0.5\sigma$ and therefore can be considered statistically insignificant. Consequently, the extrapolation of the inverted $m_{\text{T,min}}^{b-\text{jets}}$ threshold in the CR with respect to the SR is considered valid.

The validation region with the greatest number of p-values that are not 0.5 is VR-1L-MT. In this region, all p-values are 0.5 except a small deviation between $\mu_G = [3.041, 3.070]$ and an almost-constant p-value of ~ 0.3 beyond 3.4. A small discrepancy in the data-to-MC ratio can be seen in the bin $[3.0, 3.05]$ $\log 10(m_{\text{eff}}/\text{GeV})$ in Figure 9.9(c) that explains the first of those deviations. The second is much harder to explain because the discrepancy originates beyond the inclusive 3.3 $\log 10(m_{\text{eff}}/\text{GeV})$ bin boundary of the analysis, but that does however, explain why it is almost constant. In Figure 9.9(c) over the range of the three bins $[3.2, \infty]$ $\log 10(m_{\text{eff}}/\text{GeV})$, only one data event is predicted and thus the latter bins of this region could be susceptible to binning effects and a lack of statistical power. Again, all deviations are $\mathcal{O}(< 0.5\sigma)$ and thus the extrapolation of this observable can be considered valid.

In terms of the 4-jet VRs, 0L-MTB and 1L-MTB have p-values at 0.5 for each Gaussian mean, suggesting excellent validation of the background expectation in these regions. For the 4-jet VR using the 1L-MT selection, the p-value scan follows similar to Figure 9.12(e), where the lowest Gaussian mean corresponds to the lowest p-value in the discovery scan before tending to 0.5 at the Gaussian mean of $\mu_G = 3.011$. The likelihood fit with the Gaussian signal with the lowest mean, $\mu_G = 2.903$, results in a significance of approximately 1σ. For the VR-4j-MT histogram of Figure 9.9(d), the underprediction of the data by MC can be seen in the $\log 10(m_{\text{eff}})$ bins $[2.9, 3.0]$ $\log 10(m_{\text{eff}}/\text{GeV})$ but is in agreement within the total uncertainty. This being the largest deviation observed among all VRs defined, with a value $\mathcal{O}(1\sigma)$, the modelling across all VRs can be considered sufficient.

With the VRs providing sufficient validation of the extrapolated observables used to define the control and signal regions, the next results presented are the discovery scans with the unblinded signal regions - SR and SR-4j. Figures for these scans can be seen in Figure 9.13.

No statistically significant excesses were observed in either of the signal regions. In terms of Figure 9.13(a), the p-values seem erratic compared with Figure 9.13(b). However, the erratic behaviour could have originated from the extremely small background expectation and therefore, cause more fluctuations when using toys compared to SR-4j and the VRs. Most p-values for this region correspond to a significance $< 1\sigma$ and consequently can be considered statistically

---

[6]A fake signal would be events that indicate an excess of data events above the background expectation, consistent with a BSM signal, but originates from mis-measured objects or a consequence of the finite detector acceptance for example.

[7]The analyser has truncated the p-values to 0.5 to reflect only where positive increases in the number of data events with respect to the background expectation are observed.
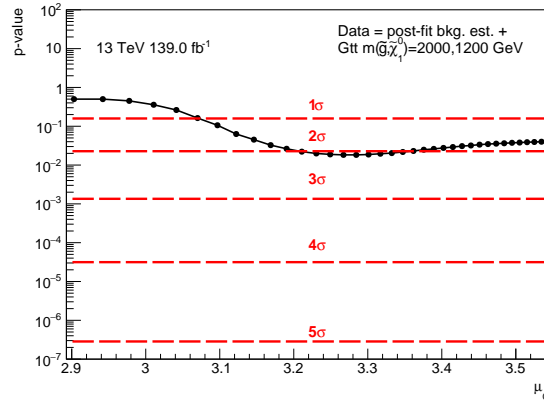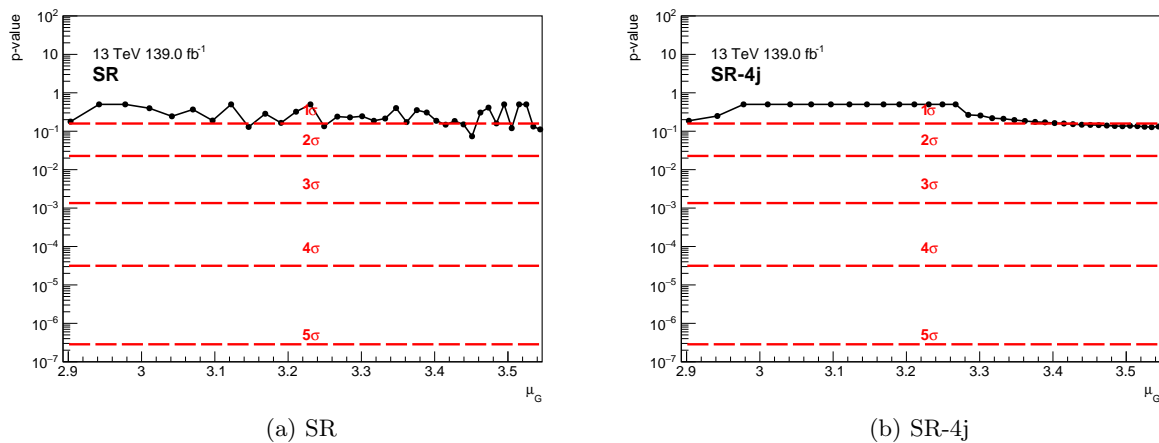
Figure 9.13: The resulting null hypothesis p-values when performing a model independent fit for a range of Gaussian signals for the signal regions (a) SR (b) SR-4j. All the results are produced with 10,000 pseudo-experiments and the p-values are truncated to 0.5.

insignificant. In terms of Figure 9.13(b), the background expectation of the SR-4j distribution seems to be well-modelled by the data up to $\mu_G = 3.27$ before a gradual underprediction of the simulation occurs. The resulting maximum discrepancy of $\mathcal{O}(1\sigma)$ is observed.

9.5.2 Setting Signal Cross section Limits

This section presents the 95% confidence limits on the Gaussian signal cross section using the CL_s prescription with the test statistic of Equation 6.12. To set limits on the signal strength, the *hypothesis test inversion* approach is performed - that is, finding the signal strength that corresponds to a p-value < 0.05 (95% CL). Classically, supersymmetry results are obtained in a model-dependent method and therefore are presented as a function of the simplified model parameters. In contrast, this method obtains the 95% CL limits in a semi-model-independent method, where the signal is parameterised by the Gaussian mean μ_G.

By performing exclusion scans with the two SRs, Figure 9.14 presents the 95% CL limit for the Gaussian visible cross section as a function of the Gaussian mean for each SR.

The tighter N_{jet} SR, improves on the limit obtained from the looser N_{jet} SR for the entire range of Gaussian means. The minimum Gaussian mean ($\mu_G = 2.903$) corresponds to the weakest observed limit, where it is ~ 0.05fb. Tending towards $\mu_G = 3.28$, the limit becomes approximately constant with a value of ~ 0.025fb. Similar behaviour is observed for the 4-jet SR, however, the limit is weaker with respect to the tighter N_{jet} SR - especially at low values of the Gaussian mean.

(a) SR
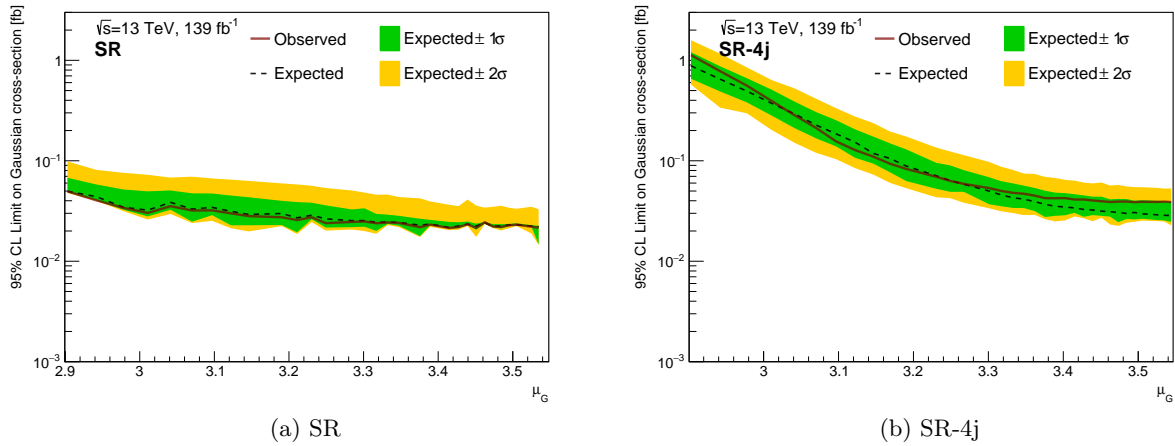
(b) SR-4j

Figure 9.14: The 95% CL limit on the visible Gaussian cross section as a function of the Gaussian mean for the signal region; (a) SR and (b) SR-4j. Both Figures include results which are produced using 10,000 pseudo-experiments.

9.6   Multiple b-jets$+E_{\mathrm{T}}^{\mathrm{miss}}$ Reinterpretation

The two main results obtained from Section 9.5, have been obtained only as a function of the Gaussian mean because of the (semi-)model-independent nature of this analysis strategy. This section reinterprets the results for events originating from the RPC gluino simplified models introduced in Section 8.1.

9.6.1   Discovery Sensitivity

To report the statistical sensitivity of discovering a BSM model using the MB SF, one performs a discovery scan with the signal injected into the blinded data prediction; following what was performed for Figure 9.10. This method replicates the existence of a BSM signal present in the data. Repeating this method for each model in the Gtt phase-space and extracting the lowest p-value (highest significance) under the background-only hypothesis for each model, the best sensitivity to discover that model (*discovery sensitivity*) can be obtained. This is shown for each Gtt model in Figure 9.15(a).

Similarly, the discovery sensitivity to the SB cut-based approach using the nominal ATLAS discovery fit strategy can be reported. The discovery sensitivity to each Gtt model is obtained by performing the same model-independent fit in Section 8.6.2 with the signal injected in the blinded data for each of the zero-lepton CC Gtt regions. For a given model, the lowest p-value from the CC regions is the best sensitivity to that model and therefore is reported as the discovery sensitivity. The results of this can be seen in Figure 9.15(b).

The results in Figures 9.15(a)-9.15(b), are effectively a comparison, quantified by the sensitivity to discovering each Gtt model, of the SB and MB region strategies and the model-independent fit approach compared to the Gaussian shape fit. It is for that reason, Figure 9.15(e) is produced,

which shows the percentage difference between the MB SF and the CC approaches. Higher, positive values show the MB SF has higher discovery sensitivity than the CC and vice versa for lower, negative values.

As expected, the MB SF approach improves upon the CC analysis in the compressed mass splitting regions of phase-space. For gluinos with mass up to 1.8 TeV, there is an approximate increase in sensitivity at 3σ, to discover models with a 50 GeV larger LSP mass with respect to the CC. As the gluino mass increases to 2.0 TeV, there is a dramatic reduction in the sensitivity to boosted signals with the MB SF. It is here in the moderate and boosted regions that the CC extends the gluino mass sensitivity, at 3σ, up to 200 GeV higher than the MB SF for a massless LSP. Examining the contour of Figure 9.15(e), one confirms that for most of the signal grid phase-space the CC strategy provides a higher discovery sensitivity than the MB SF, except for compressed signals and most models with a LSP mass beyond 1.1 TeV.

This entire procedure was repeated for the Gbb model phase-space and therefore, for the MB SF (Figure 9.15(c)) the SR-4j signal region definition was used. The repeated CC results (Figure 9.15(d)) only used the CC Gbb SR definitions from Chapter 8. Similarly, Figure 9.15(f) presents the percentage difference in the discovery sensitivity for the two results.

The MB SF 3σ contour lies significantly beyond the CC contour in the compressed and moderate regions of phase-space. The exception is a corner of phase-space corresponding to models with $M_\mathrm{susy} \gtrsim 1800$ GeV and therefore are highly boosted. For gluinos in the mass range $[1.9, 2.0]$ TeV, there is up to a 400 GeV increase in LSP mass sensitivity at 3σ using the MB SF relative to the CC. For a massless LSP, there is an approximate increase in sensitivity at 3σ, to discover models with a ~ 75 GeV larger gluino mass with respect to that obtained from the MB SF. This is most likely due to the high selection thresholds of the CC strategy.

9.6.2   Simplified Model Cross section Limits

One of the greatest advantages of this novel method is when setting model-dependent limits. If a signal model can be approximated by a Gaussian function with a width of 0.125 and kinematically satisfies the signal region selection criteria, a visible cross section limit can be obtained. This is obtained by interpolating to the relevant Gaussian cross section limit of Figure 9.14 with the Gaussian mean of a given signal process of interest. Thereby simplifying the reinterpretation process.

In doing this for the Gtt signal processes and correcting for the acceptance and efficiency for each model, a true cross section limit can be obtained for each signal in the model space. Dividing these values by the theoretically predicted cross section at NLO+NLL, an exclusion curve can be derived where for > 1 (< 1) the model can be considered not excluded (excluded) at a 95% CL limit. For the Gtt (Gbb) model parameter-space, the results can be seen in Figure 9.16(a) (9.16(b)).

Comparing Figure 9.16(a) to the observed exclusion contours of the CC analysis in Figure C.2(b) of Appendix C.2, the CC exclusion contour extends beyond the MB SF but the individual CC
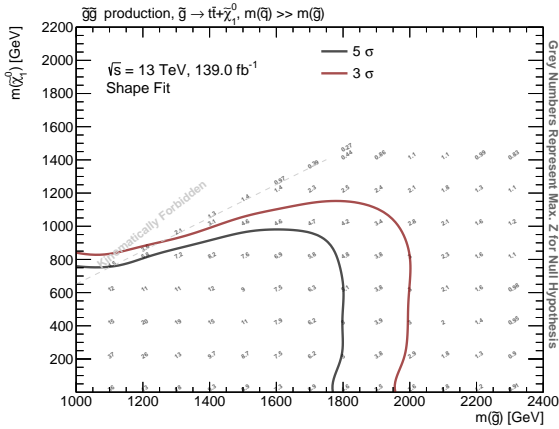
(a) Multi-bin Shape Fit - SR
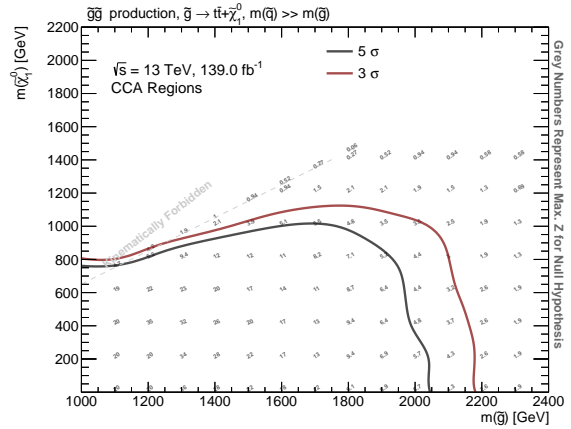
(b) CC Gtt 0-lepton
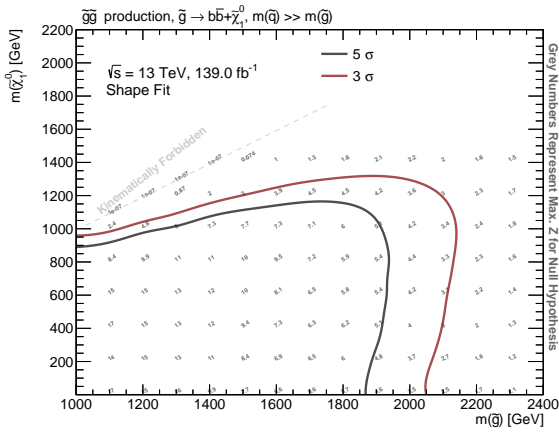
(c) Multi-bin Shape Fit - SR-4j
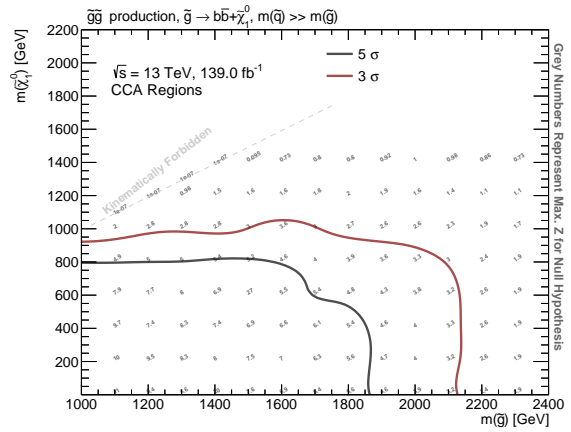
(d) CC Gbb
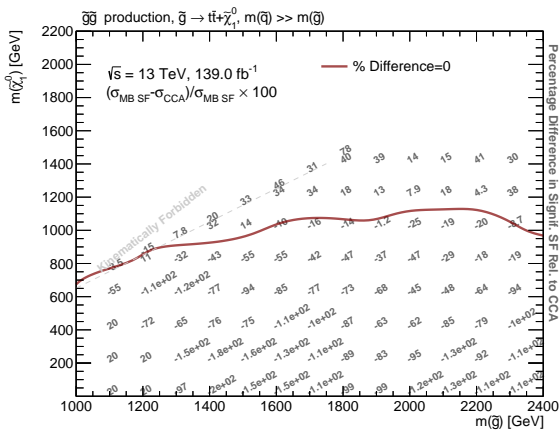
(e) Percentage Difference - Gtt
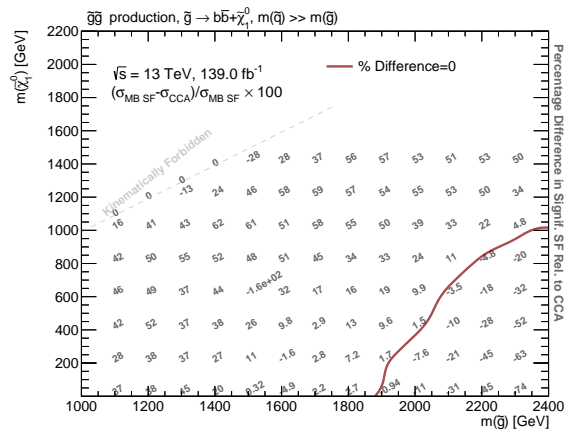
(f) Percentage Difference - Gbb

Figure 9.15: Presents the *discovery sensitivity* for the Gtt (Gbb) models using the (a) ((c)) multi-bin shape fit (MB SF) methodology utilising a Gaussian signal shape and (b) ((d)) the zero-lepton cut-and-count analysis (CC) Gtt (Gbb) regions of Chapter 8 with the nominal ATLAS model independent fit strategy. Both are obtained by including the signal expectation in the blinded data prediction. (e) ((f)) Presents the percentage difference in the results obtained by MB SF relative to CC for the Gtt (Gbb) scenario.
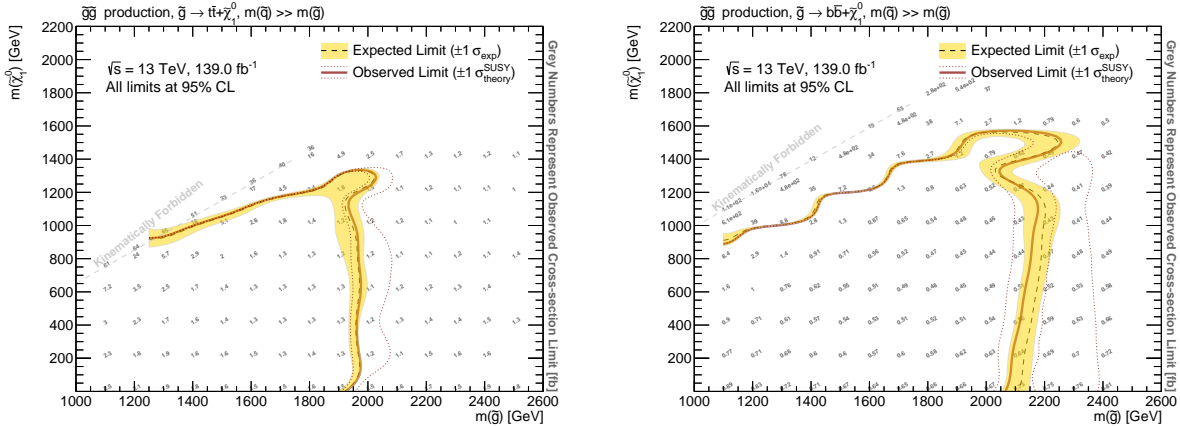
(a) Gtt 95% true cross section limit

(b) Gbb 95% true cross section limit

Figure 9.16: (a) ((b)) Exclusion contour for the 95% cross section limit for the Gtt (Gbb) signal processes using the Gaussian multi-bin shape fit with the signal region SR (SR-4j). All figures are using results produced with 10,000 pseudo-experiments.

region contours show that this originates from the Gtt 1L regions and thus could be considered not a fair comparison. Consequently, an additional figure is presented to compare the MB SF to the expected and observed results obtained from the Gtt zero-lepton CC and NN SRs in Figures 9.17(c)-9.17(d), respectively. The exclusion contours obtained for Gbb using SR-4j can be seen in Figure 9.16(b) and a comparison with the equivalent limits obtained from the Gbb CC and NN SRs is shown in Figures 9.17(a)-9.17(b), respectively.

When comparing the MB SF to the limit obtained only from the Gtt 0L SRs, the statistical sensitivity seen in Figures 9.15(a)-9.15(b) is also observed here, as expected. The MB SF and CC exclude gluino masses up to 1.97 TeV for an LSP mass of ~ 1.0 TeV at a 95% CL. However, the CC extends the gluino mass limit to 2.3 TeV for a massless LSP and the MB SF extends the LSP limit to 1.33 TeV for a gluino mass of 1.95 TeV. Therefore, the MB SF has greater sensitivity to the moderate mass splitting signal models than the CC and the CC has greater sensitivity with respect to the MB SF for signal processes with a boosted mass splitting.

Similarly, for Gbb, the general trends with respect to the statistical sensitivity observed in Figures 9.15(c)-9.15(d) are also observed here. However, two further interesting occurrences are observed. Firstly, the limit in the moderate region of the MB SF lies greatly beyond the CC as hoped - reaching a maximum LSP mass of 1.57 TeV for a gluino mass near to 2.1 TeV. The strong performance in the moderate region continues with a LSP mass of 1.5 TeV for a gluino mass up to 2.23 TeV. Secondly, the MB SF has poorer sensitivity to the very compressed region where the Gaussian approximation breaks down for these models. Therefore, the simplistic methodology of the CC strategy has increased sensitivity for some models in this area of phase-space.

The total $\pm 1\sigma$ uncertainty in the observed exclusion contour Figure 9.16(b) is in general smaller for compressed models and then much larger for boosted models. This could be because of two reasons. The first, and potentially smaller effect is that for a fixed gluino mass, as the LSP mass increases, the SUSY mass scale decreases (Figure 9.1) therefore, the corresponding limit is weaker
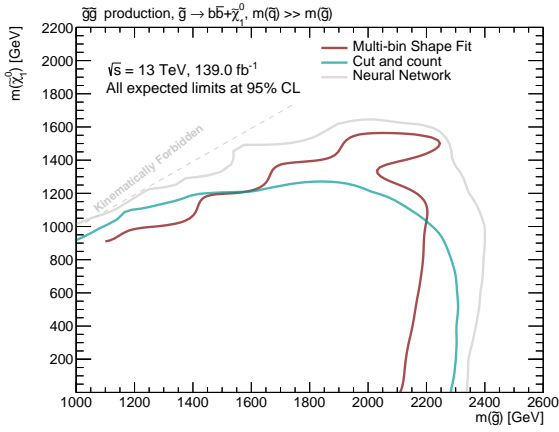
(a) Gbb Expected Limit
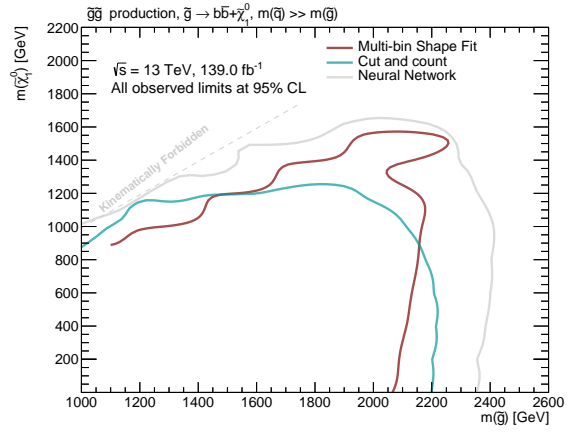
(b) Gbb Observed Limit
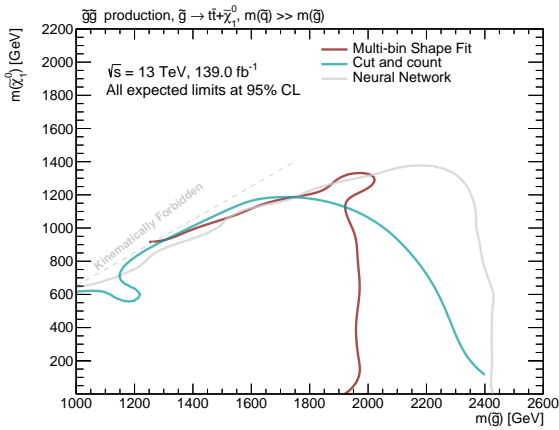
(c) Gtt Expected Limit
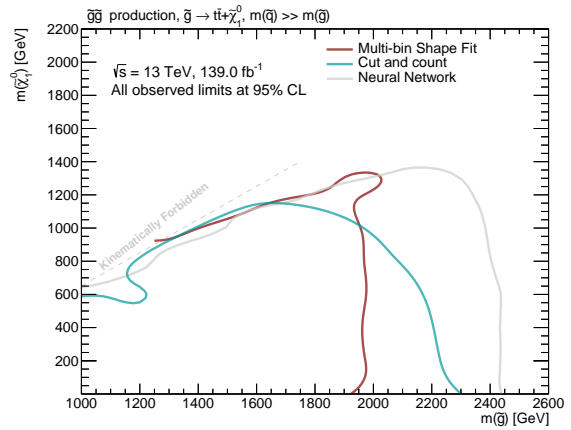
(d) Gtt Observed Limit

Figure 9.17: A comparison of the observed and expected 95% CL$_s$ limits for Gbb and Gtt signal processes for the multi-bin shape fit (MB SF), cut-and-count (CC) and neural network (NN) strategies. The exclusion contour for the 95% CL limit on the signal strength for the CC and NN signal regions contributing to the exclusion contour use their best expected CL$_s$ value for each signal model. For Gtt, only zero-lepton SRs are included for the CC limit. All figures use results produced using 10,000 pseudo-experiments.

and $\pm 1\sigma$ variations have a slightly smaller uncertainty (Figure 9.14). The second effect originates from the calculation of the acceptance and efficiency, which is used to derive the true cross section limit for each model. As the models tend towards the kinematically forbidden diagonal, the top(bottom) quarks and LSP become less boosted in the gluino rest frame, resulting in jets with lower p_{T} and smaller $E_{\mathrm{T}}^{\mathrm{miss}}$ therefore decreasing the acceptance and efficiency. This means that the resulting true cross section limits become rapidly larger as the models tend towards the diagonal and the $\pm 1\sigma$ limit curves get compressed together.

9.7 Closure Tests

9.7.1 Discovery and Exclusion Results Validation

In the Gaussian regime, exclusion contours are expected to lie significantly beyond discovery contours. As shown in Figures 9.18(a) and 9.18(b), this is not observed here.

(a) Gtt Discovery Sensitivity

(b) Gtt 95% True Cross section Limit
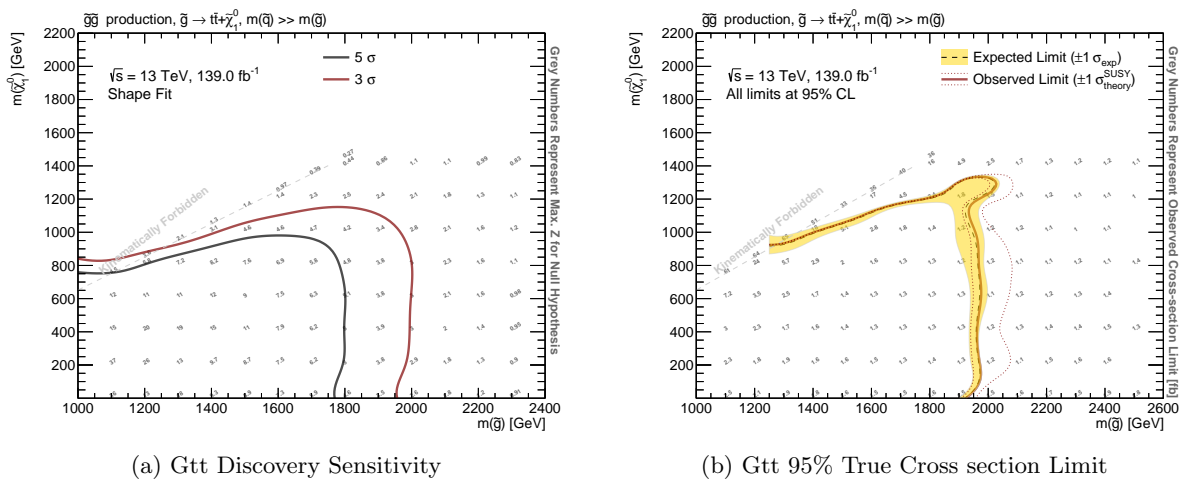
Figure 9.18: Reproduction of Figures 9.15(a) and 9.16(a) to assist the reader with a side-by-side comparison.

The reason for this is the small background estimate in the signal region (< 1 background event in each bin of Figure 9.8(a)) and consequently, the statistical regime is no longer Gaussian and is instead distributed according to a Poisson function. To demonstrate this, consider two simplified and idealised counting experiments with μ_b (μ_s), where μ_b (μ_s) is the expected number of background (signal) events and assume that μ_b (μ_s) is understood completely such that the uncertainty in their expectation is zero and no other systematic uncertainties are present.

Poisson counting experiment - Set $\mu_b = 0.0$ and $\mu_s = 1.0$ and derive the two following contours in the mass plane of the two signal model parameters.

1. The estimated discovery sensitivity contour is obtained by including the signal yield in the blinded data ($n_{\mathrm{obs}} = \mu_b + \mu_s = 1.0$) and a test of the background-only hypothesis

is performed. Given that the background expectation is $\mu_b = 0.0$, the corresponding significance[8] for this signal is infinite. Therefore, the expected 5σ discovery contour lies to the right of the signal model in the mass plane and the model can be considered as observed.

2. The expected 95% exclusion contour is obtained without the signal being included in the blinded data ($n_{\mathrm{obs}} = \mu_b$) under the test of the signal-plus-background hypothesis. Given that $\mu_b = 0$, $n_{\mathrm{obs}} = 0$. The 95% upper limit on μ_s is $\mu_s < 3.0$ [7] for a model to be allowed. The expected limit curve therefore lies to the left of the signal model in the mass plane and the model is not excluded.

Given these scenarios, the expected limit contour lies below the 5σ discovery curve and is illustrated in Figure 9.19(a).

(a)   (b)
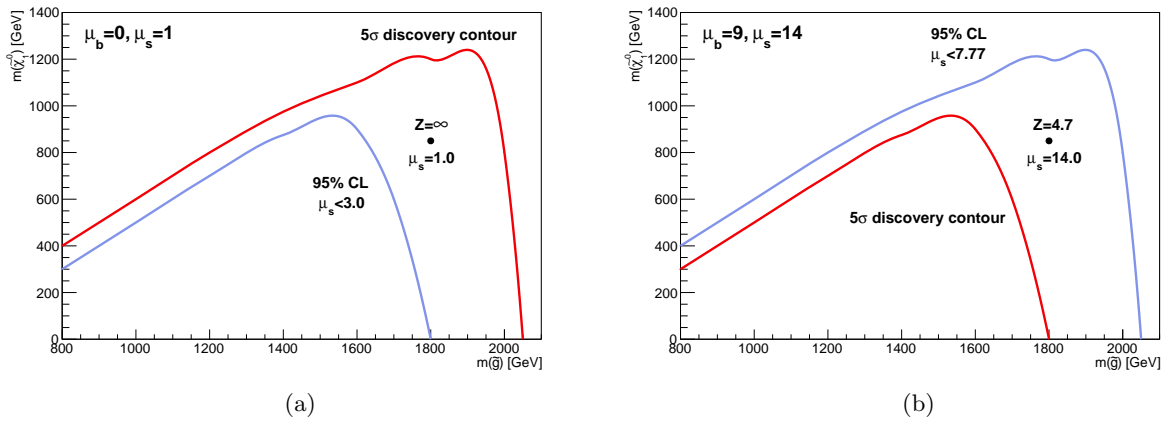
Figure 9.19: Illustrations of the estimated discovery sensitivity contours and expected 95% exclusion contours for a simplified and idealised (a) Poisson and a (b) Gaussian counting experiment. The contours do not correspond to the significance or exclusion limits expected in this experiment and are included only for illustrative purposes.

Gaussian counting experiment   - Set $\mu_b = 9.0$ and $\mu_s = 14.0$ and derive the two equivalent contours using these values in the mass plane of the two signal model parameters.

1. The estimated discovery sensitivity contour is obtained by including the signal yield in the blinded data ($n_{\mathrm{obs}} = \mu_b + \mu_s = 23.0$) and a test of the background-only hypothesis is performed. Given that the background expectation is $\mu_b = 9.0$, the significance of the signal is approximately 4.7σ. Therefore, the expected 5σ discovery contour lies to the left of the signal model in the mass plane and the model cannot be considered as observed.

2. The expected 95% exclusion contour is obtained without the signal being included in the blinded data ($n_{\mathrm{obs}} = \mu_b$) and a test of the signal-plus-background hypothesis is performed. Given that $\mu_b = 9.0, n_{\mathrm{obs}} = 9$. The 95% upper limit on μ_s is $\mu_s < 7.77$ [170] for the model

---

[8]Using the approximation of the significance; $Z = s/\sqrt{b}$.

to be allowed. The expected limit curve therefore lies to the right of the signal model in the mass plane and the model is excluded.

Given these scenarios, the expected limit contour lies above the 5σ discovery curve and is illustrated in Figure 9.19(b). Evidently, it is possible to enter a statistical scenario where a 5σ discovery contour can extend beyond a 95% CL (1.64σ) contour in the event of a very small $(< 1$ data events per signal region bin) background expectation, which appears to be the scenario for the results obtained in Figures 9.15(a).

9.7.2 Gaussian Approximation in the Likelihood Fits

To validate the use of the Gaussian signal model with width 0.125 used in the likelihood fits of Sections 9.5.1-9.5.2, the results in Figures 9.15(a) and 9.16(a) were reproduced by replacing the Gaussian signal model with the Gtt signals. Only statistical uncertainties were considered in this test. To obtain results for the discovery sensitivity using Gtt models, each discovery scan for the Gtt model-space was performed with signal injection using only its respective signal process because this would always produce the highest significance. The result of this test can be seen in Figure 9.20.

(a) Discovery Sensitivity - Gaussian signal   (b) Discovery Sensitivity - Gtt models
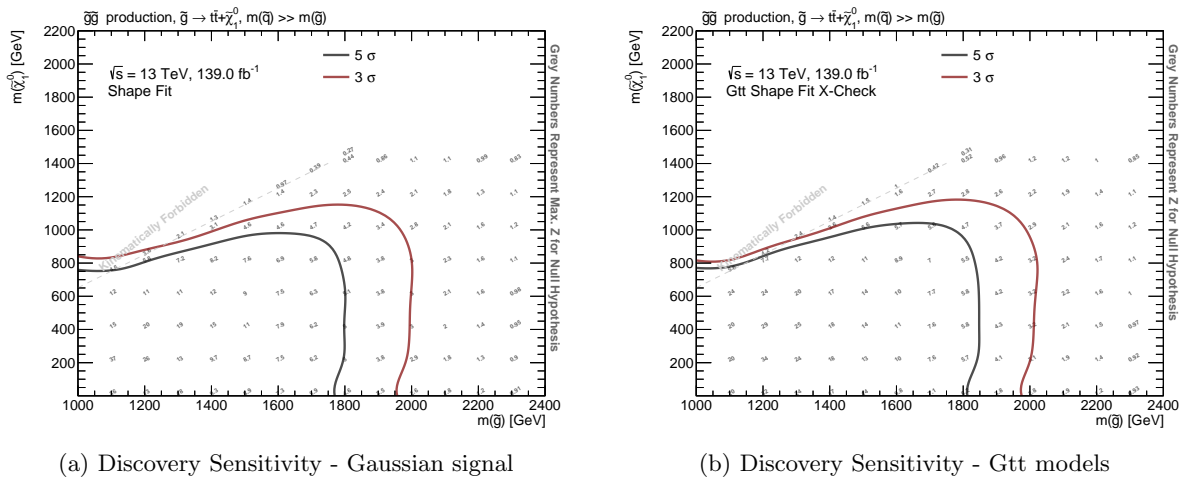
Figure 9.20: Validating the discovery sensitivity in the SR when using a (a) Gaussian signal model with width 0.125 and (b) Gtt signal processes.

Visual differences between the two figures can only be observed in the compressed region, where the results obtained from the Gtt models improve marginally on those obtained from the Gaussian approximation. In the absence of systematic uncertainties, the closure between both 3 and 5σ discovery contours is very high and thus, indicates that the Gaussian approximation in these likelihood fits performs comparable to those described using the gluino-produced signal process.

In terms of setting cross section limits for each Gtt signal model, a 95% CL limit on the signal strength for each Gtt model was obtained by performing the model-dependent fit strategy in Section 6.4. This is converted to a 95% CL limit on the visible cross section for each Gtt signal model and subsequently to a true cross section limit by correcting for the acceptance and

efficiency. The results of this test can be seen in Figure 9.21.

(a) 95% true cross section limit - Gaussian signal   (b) 95% true cross section limit - Gtt models
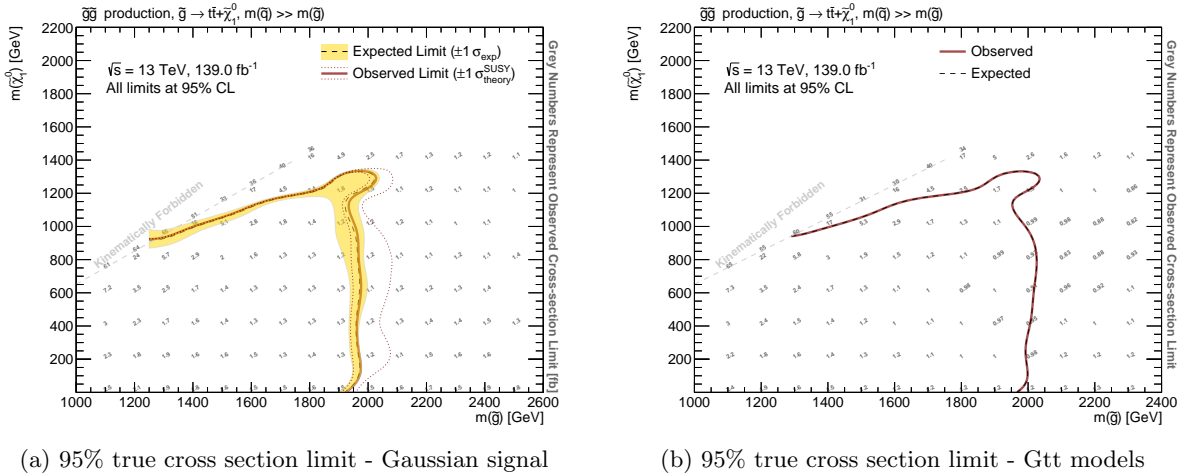
Figure 9.21: Validating the 95% true cross section limits in the SR when using a (a) Gaussian signal model with width 0.125 and (b) Gtt signal processes.

As observed with the cross-check for the discovery sensitivity, the compatibility between the results obtained using the Gaussian approximation and those from the corresponding Gtt models shows excellent closure. The largest deviation is observed in the model phase-space around $m(\tilde{g}, \tilde{\chi}_1^0) = 2000, 1000$ GeV, which originates from several weaker cross section limits obtained when using the Gaussian signal approximation - which would be expected. Considering both the results, the observed closure is consistent with our understanding of the approximation of the Gtt signals by the Gaussian function and hence the closure has been considered sufficient from these tests.

9.8   Conclusion

This chapter presents the model-independent search for Gaussian-distributed excesses above the Standard Model with the Run 2 proton-proton collision data collected at $\sqrt{s} = 13$ TeV by the ATLAS experiment. The strategy is a novel method that can be used for searching for new physics and setting cross section limits for SUSY searches. The philosophy of the strategy is to utilise multiple signal region bins along with a generic signal shape distribution. This search is binned in the $\log 10(\mathrm{m_{eff}})$ distribution because, for various kinematic scenarios of gluino decays, it is observed to be universally Gaussian and has high discriminating sensitivity to these models from the Standard Model background.

Two signal regions were defined to target high and low jet multiplicity events where zero leptons were present. Both signal regions are dominated by the $t\bar{t}$ background and therefore, a dedicated control region was used to provide a data-driven background estimate for the process. Additionally, a validation region has been defined for each differing selection observable between the signal and control region. No significant deviations are observed and thus, the extrapolation of these observables between the SRs and CR is validated.

By using this method to assess the sensitivity to discovering RPC gluino signals, an increase in sensitivity to small mass splitting models compared to a single bin cut-based strategy was observed. By using this method to search for new physics in the signal regions, no statistically significant excesses above the Standard Model are observed and thus, a limit on the Gaussian cross section is set. For the tighter (looser) signal region selection, the 95% visible cross section limit plateaus at 0.025(0.04)fb for a Gaussian mean of 3.25(3.37).

Because the 95% visible cross section limit is presented as a function of the Gaussian mean, the reinterpretation process is simplified. This chapter reinterprets the 95% CL limit on the visible Gaussian cross section for events originating from RPC gluino decays. When comparing the exclusion contour derived from this method to the single-bin approach of Chapter 8, this method increases the sensitivity beyond the cut-based approach for moderate mass splitting $\tilde{g} \to \tilde{t}t\tilde{\chi}_1^0$ signal processes. As expected, the largest improvements are for models with small and moderate mass splitting. This situation is enhanced even further when considering the process; $\tilde{g} \to \tilde{b}b\tilde{\chi}_1^0$. However, for models where $\Delta m(\tilde{g}, \tilde{\chi}_1^0) = 20$ GeV, the breakdown in Gaussian approximation highly challenges the multi-bin shape fit strategy and thus, for several specific models, the simpler cut-based approach has larger sensitivity.

Part V

Closing

Chapter 10

Summary

The predictions of the properties of the observed matter of the Universe by the Standard Model have been extremely successful for the particle physics community over the last century. However, deviations from the Standard Model predictions are arising in lepton violation measurements of B-meson decays, the measurement of the muon anomalous magnet moment and dark matter and dark energy are yet to be understood. This thesis searched for the supersymmetric extension to the Standard Model, motivated by its solution to the hierarchy problem and providing a WIMP dark matter candidate. The extension is sought in the context of large quantities of missing transverse energy and multiple b-jets in the final state from gluino pair-production, which is motivated by naturalness.

The calibration of the DL1r b-tagging algorithm for jets reconstructed using the ParticleFlow algorithm was also presented. The calibration uses the previously published method but is performed using the ATLAS Run 2 dataset on a new set of neural network-based b-tagging algorithms with ParticleFlow jets for the first time. The calibration corrects the b-tagging efficiency in the Monte Carlo simulation and provides an associated uncertainty, both based on the transverse momentum of each jet. This calibration will be essential to ATLAS measurements and beyond the Standard Model searches when b-jets are a component of the targeted detector signature.

As with all other direct searches for supersymmetry in ATLAS and CMS using the Run 2 dataset, no significant excesses above the Standard Model were observed in any search performed in this thesis. Limits were set at a 95% confidence limit on the simplified model plane extending the gluino mass limit to 2.2 TeV (2.27 TeV) for a massless lightest neutralino and the maximum excluded lightest neutralino mass is 1.25 TeV for a 1.85 TeV (2.05 TeV) gluino in a $\tilde{g} \rightarrow \bar{b}b$ ($\tilde{g} \rightarrow t\bar{t}$) scenario. The limit on the gluino mass highly challenges the principle of naturalness, albeit still within the bounds of the constraint.

Also within this thesis is a demonstration of a model-independent search strategy for events distributed according to a Gaussian function for use in ATLAS supersymmetry searches. This approach is contrary to the nominal strategy performed at ATLAS, where a specific kinematic final state is the target and the results are entirely model-dependent. In this strategy, a Gaussian

is the signal sought in the background expectation and the results can be reinterpreted in a model-dependent manner to obtain 95% confidence limits in the simplified model mass plane. For a Gaussian with a width of 0.125, signal processes can be considered excluded at a 95% CL limit with a cross section of ~ 0.05fb for a Gaussian mean up to 3.25, where beyond this, the limit is approximately constant at ~ 0.025fb. The method improves sensitivity to compressed models with respect to a cut-based approach with a maximum-excluded LSP mass of 1.57 TeV (1.33 TeV) for a gluino mass of 2.1 TeV (1.95 TeV) for the $\tilde{g} \to \bar{b}b$ ($\tilde{g} \to t\bar{t}$) signal process.

It is hoped that this strategy will become the standard search methodology because it has increased statistical sensitivity to small mass splitting signals, a simplified reinterpretation process and is less model-dependent with respect to the current ATLAS SUSY strategy. All of this is conducted whilst retaining the ability to provide nominally reported results by ATLAS from direct supersymmetry searches.

The two searches for gluino pair-production with a multiple b-jet plus $E_{\mathrm{T}}^{\mathrm{miss}}$ final state set 95% CL limits in the gluino-lightest-neutralino mass plane. Each search has differing strategies albeit can be considered somewhat complimentary. The cut-based regions have selection thresholds deep in the tails of kinematic distributions, thereby increasing sensitivity to high-p_{T} events because of the p_{T}-dependent nature of many kinematic observables. Whereas the model-independent search exploits the additional shape information of a specified kinematic observable to increase sensitivity to small mass splitting models which are better characterised by their low-p_{T} topology. The kinematics of these two strategies reflect the sensitivity observed in the model-dependent limits. The final strategy, where model-dependent limits were also presented, was for a supervised learning technique. Here, the neural network is trained to identify not only event characteristics for the signal processes but also the background, and thus has a high sensitivity to both high- and low-p_{T} signal events.

Bibliography

[1] ATLAS Collaboration,
Search for supersymmetry in final states with missing transverse momentum and multiple b-jets in proton-proton collisions at $\sqrt{s} = 13$ TeV with the ATLAS detector,
JHEP **06** (2018) 107, arXiv: 1711.01901 [hep-ex]
(cit. on pp. 4, 107–110, 148, 217, 218).

[2] ATLAS Collaboration,
Search for supersymmetry in final states with missing transverse momentum and multiple b-jets in proton-proton collisions at $\sqrt{s} = 13$ TeV with the ATLAS detector, tech. rep.,
All figures including auxiliary figures are available at
https://atlas.web.cern.ch/Atlas/GROUPS/PHYSICS/CONFNOTES/ATLAS-CONF-2018-041: CERN, 2018, URL: http://cds.cern.ch/record/2632347
(cit. on p. 4).

[3] ATLAS Collaboration, *Observation of a new particle in the search for the Standard Model Higgs boson with the ATLAS detector at the LHC*, Physics Letters B **716** (2012) 1
(cit. on pp. 9, 48, 161).

[4] CMS Collaboration,
Observation of a new boson at a mass of 125 GeV with the CMS experiment at the LHC,
Physics Letters B **716** (2012) 30 (cit. on pp. 9, 48).

[5] A. Purcell, *Go on a particle quest at the first CERN webfest*, (2012) 10,
URL: https://cds.cern.ch/record/1473657 (cit. on p. 9).

[6] M. Thomson, *Modern particle physics*, Cambridge University Press, 2013
(cit. on pp. 10–14, 39, 51, 70).

[7] P. Zyla et al., *Review of Particle Physics*, PTEP **2020** (2020) 083C01
(cit. on pp. 10–15, 23, 26, 28, 40, 41, 44–46, 70, 72, 74, 106, 112, 174).

[8] C. Rizzi, *Searches for supersymmetric particles in final states with multiple top and bottom quarks with the ATLAS detector*, PhD thesis: Barcelona, Autonoma U.
(cit. on pp. 11, 15, 24, 40, 46, 58, 74).

[9] J. Goldstone, *Field theories with Superconductor solutions*,
Il Nuovo Cimento (1955-1965) **19** (1961) 154 (cit. on p. 11).

[10] A. Pich, *The Standard Model of Electroweak Interactions; rev. version*, (2005) 48 p,
URL: https://cds.cern.ch/record/819632 (cit. on p. 12).

[11] Super-Kamiokande Collaboration, *Evidence for oscillation of atmospheric neutrinos*, Physical Review Letters **81** (1998) 1562 (cit. on p. 12).

[12] ATLAS Collaboration, *Combined measurements of Higgs boson production and decay using up to $80\mathrm{fb}^{-1}$ of proton-proton collision data at $\sqrt{s} = 13$ TeV collected with the ATLAS experiment*, Physical Review D **101** (2020) 012002 (cit. on p. 13).

[13] N. Cabibbo, *Unitary symmetry and leptonic decays*, Physical Review Letters **10** (1963) 531 (cit. on p. 13).

[14] M. Kobayashi and T. Maskawa, *CP-violation in the renormalizable theory of weak interaction*, Progress of theoretical physics **49** (1973) 652 (cit. on p. 13).

[15] D. Buttazzo et al., *Investigating the near-criticality of the Higgs boson*, Journal of High Energy Physics **2013** (2013) 1 (cit. on p. 13).

[16] V. C. Rubin and W. K. Ford Jr, *Rotation of the Andromeda nebula from a spectroscopic survey of emission regions*, The Astrophysical Journal **159** (1970) 379 (cit. on p. 14).

[17] P. Ade et al., *Planck 2013 results. XVI. Cosmological parameters*, Astronomy & Astrophysics **571** (2014) A16 (cit. on p. 14).

[18] D Larson et al., *Seven-year wilkinson microwave anisotropy probe (WMAP*) observations: power spectra and WMAP-derived parameters*, The Astrophysical Journal Supplement Series **192** (2011) 16 (cit. on p. 14).

[19] N. Aghanim et al., *Planck 2018 results-VI. Cosmological parameters*, Astronomy & Astrophysics **641** (2020) A6 (cit. on pp. 14, 28).

[20] O. Lahav and A. R. Liddle, *The cosmological parameters*, arXiv preprint astro-ph/0406681 (2004) (cit. on pp. 14, 28).

[21] D. Scott and G. F. Smoot, *Cosmic microwave background mini-review*, arXiv preprint arXiv:1005.0555 (2010) (cit. on pp. 14, 28).

[22] F. Halzen and A. D. Martin, *Quark & Leptons: An introductory course in modern particle physics*, John Wiley & Sons, 2008 (cit. on p. 15).

[23] J. Gómez-Cadenas, J. Martin-Albo, M. Mezzetto, F. Monrabal and M. Sorel, *The search for neutrinoless double beta decay*, Rivista del Nuovo Cimento **35** (2011) (cit. on p. 15).

[24] S. P. Martin, *A supersymmetry primer*, World Scientific, 2010 1 (cit. on pp. 16, 17, 19–22, 25–28, 146, 196, 197).

[25] K. G. Wilson, *Renormalization group and strong interactions*, Physical Review D **3** (1971) 1818 (cit. on p. 17).

[26] A. Borrelli and E. Castellani,
The practice of naturalness: a historical-philosophical perspective,
Foundations of Physics **49** (2019) 860 (cit. on p. 17).

[27] C. M. Macdonald, *Searches for supersymmetry in final states containing b-tagged jets
with the ATLAS detector*, PhD thesis: University of Sheffield, 2017
(cit. on pp. 20, 21, 40, 42, 46, 51, 58–60, 64, 70, 197, 198).

[28] Super-Kamiokande Collaboration, *Search for proton decay via $p \to e^+ \pi^0$ and $p \to \mu^+ \pi^0$
in 0.31 megaton years exposure of the Super-Kamiokande water Cherenkov detector*,
Physical Review D **95** (2017) 012004 (cit. on p. 22).

[29] G. Hooft, *Symmetry breaking through Bell-Jackiw anomalies*,
Physical Review Letters **37** (1976) 8 (cit. on p. 22).

[30] N. Polonsky, *Supersymmetry: structure and phenomena: extensions of the standard model*,
vol. 68, Springer Science & Business Media, 2001 (cit. on p. 23).

[31] W. De Boer, *Grand unified theories and supersymmetry in particle physics and cosmology*,
Progress in Particle and Nuclear Physics **33** (1994) 201 (cit. on p. 23).

[32] S. S. AbdusSalam, B. C. Allanach, F. Quevedo, F. Feroz and M. Hobson,
Fitting the phenomenological MSSM, Physical Review D **81** (2010) 095012 (cit. on p. 23).

[33] S. P. Martin and J. D. Wells,
Muon anomalous magnetic dipole moment in supersymmetric theories,
Physical Review D **64** (2001) 035003 (cit. on p. 23).

[34] L. J. Hall, D. Pinner and J. T. Ruderman, *A natural SUSY Higgs near 125 GeV*,
Journal of High Energy Physics **2012** (2012) 1 (cit. on p. 24).

[35] F. Brümmer, S. Kraml and S. Kulkarni, *Anatomy of maximal stop mixing in the MSSM*,
Journal of High Energy Physics **2012** (2012) 1 (cit. on p. 24).

[36] C. Brust, A. Katz, S. Lawrence and R. Sundrum,
SUSY, the Third Generation and the LHC,
Journal of High Energy Physics **2012** (2012) 1 (cit. on p. 24).

[37] I. Melzer-Pellmann and P. Pralavorio, *Lessons for SUSY from the LHC after the first run*,
Springer, 2014 29 (cit. on p. 25).

[38] D. Alves et al., *Simplified models for LHC new physics searches*,
Journal of Physics G: Nuclear and Particle Physics **39** (2012) 105005
(cit. on pp. 25, 106).

[39] M. Drees, M. M. Nojiri, D. Roy and Y. Yamada, *Light Higgsino dark matter*,
Physical Review D **56** (1997) 276 (cit. on p. 28).

[40] A. Djouadi, M. Muhlleitner and M. Spira, *Decays of supersymmetric particles: the
program SUSY-HIT (SUspect-SdecaY-HDECAY-InTerface)*,
arXiv preprint hep-ph/0609292 (2006) (cit. on p. 28).

[41] G. Belanger, F Boudjema, A. Pukhov and A Semenov,
microOMEGAs_3: A program for calculating dark matter observables,
Computer Physics Communications **185** (2014) 960 (cit. on p. 28).

[42] J. L. Feng, K. T. Matchev and F. Wilczek,
Neutralino dark matter in focus point supersymmetry, Physics Letters B **482** (2000) 388
(cit. on p. 28).

[43] ATLAS Collaboration, *SUSY Summary Plots June 2021*, tech. rep.,
All figures including auxiliary figures are available at
https://atlas.web.cern.ch/Atlas/GROUPS/PHYSICS/PUBNOTES/ATL-PHYS-PUB-
2021-019: CERN, 2021, URL: http://cds.cern.ch/record/2771785
(cit. on pp. 29, 32, 33).

[44] CMS Collaboration,
CMS Supersymmetry Physics Results - Run 2 Summaries $\sqrt{s} = 13$ TeV, 2022,
URL: https://twiki.cern.ch/twiki/bin/view/CMSPublic/PhysicsResultsSUS#Run_
2_Summaries_13_TeV (cit. on pp. 30, 34).

[45] F. Cardillo, *Search for supersymmetry in events with two same-sign leptons or three
leptons with the ATLAS detector at $\sqrt{s} = 13$ TeV*, PhD thesis: Freiburg U.
(cit. on pp. 38, 39, 44, 46, 58).

[46] J. M. Butterworth, G. Dissertori and G. P. Salam,
Hard processes in proton-proton collisions at the large hadron collider,
Annual Review of Nuclear and Particle Science **62** (2012) 387
(cit. on pp. 40–42, 44, 48, 60).

[47] Y. L. Dokshitzer, *Calculation of the structure functions for deep inelastic scattering and
e+ e-annihilation by perturbation theory in quantum chromodynamics*,
Zh. Eksp. Teor. Fiz **73** (1977) 26 (cit. on p. 40).

[48] V. Gribov and L. Lipatov, *Deep inelastic electron scattering in perturbation theory*,
Physics Letters B **37** (1971) 78 (cit. on p. 40).

[49] G. Altarelli and G. Parisi, *Asymptotic freedom in parton language*,
Nuclear Physics B **126** (1977) 298 (cit. on p. 40).

[50] H.-L. Lai et al., *New parton distributions for collider physics*,
Physical Review D **82** (2010) 074024 (cit. on p. 40).

[51] A. D. Martin, W. J. Stirling, R. S. Thorne and G Watt,
Parton distributions for the LHC, The European Physical Journal C **63** (2009) 189
(cit. on pp. 40, 41).

[52] R. D. Ball et al., *Unbiased global determination of parton distributions and their
uncertainties at NNLO and at LO*, Nuclear Physics B **855** (2012) 153 (cit. on p. 40).

[53] S. Höche, *Introduction to parton-shower event generators*, World Scientific, 2016 235
(cit. on pp. 41, 44, 52).

[54] A. Hoecker,
Physics at the LHC Run-2 and Beyond. Physics at the LHC Run-2 and Beyond,
(2016) 153, Lecture notes from the 2016 European School of High-Energy Physics, 15-28
June 2016, Skeikampen, Norway (61 pages, 56 figures), arXiv: `1611.07864`,
URL: `https://cds.cern.ch/record/2236645` (cit. on pp. 43, 49).

[55] D. Amati and G. Veneziano, *Preconfinement as a Property of Perturbative QCD*,
Physics Letters B **83** (1979) 87 (cit. on p. 44).

[56] B. Andersson, G. Gustafson, G. Ingelman and T. Sjöstrand,
Parton fragmentation and string dynamics, Physics Reports **97** (1983) 31 (cit. on p. 44).

[57] P. Nason, *A new method for combining NLO QCD with shower Monte Carlo algorithms*,
Journal of High Energy Physics **2004** (2004) 040 (cit. on p. 45).

[58] S. Frixione and B. R. Webber,
Matching NLO QCD computations and parton shower simulations,
Journal of High Energy Physics **2002** (2002) 029 (cit. on p. 45).

[59] J. Alwall et al., *The automated computation of tree-level and next-to-leading order
differential cross sections, and their matching to parton shower simulations*,
JHEP **07** (2014) 079, arXiv: `1405.0301` `[hep-ph]` (cit. on pp. 45, 46, 113).

[60] S. Alioli, P. Nason, C. Oleari and E. Re, *A general framework for implementing NLO
calculations in shower Monte Carlo programs: the POWHEG BOX*, JHEP **06** (2010) 043,
arXiv: `1002.2581` `[hep-ph]` (cit. on pp. 45, 46, 113).

[61] P. Z. Skands, *Tuning Monte Carlo generators: the perugia tunes*,
Physical Review D **82** (2010) 074018 (cit. on p. 46).

[62] T. Sjöstrand, S. Mrenna and P. Skands, *PYTHIA 6.4 physics and manual*,
Journal of High Energy Physics **2006** (2006) 026 (cit. on p. 46).

[63] T. Sjöstrand et al., *An introduction to PYTHIA 8.2*,
Computer physics communications **191** (2015) 159 (cit. on p. 46).

[64] A. Buckley et al., *General-purpose event generators for LHC physics*,
Physics Reports **504** (2011) 145 (cit. on p. 46).

[65] E. Bothmann et al., *Event generation with Sherpa 2.2*, SciPost Physics **7** (2019) 034
(cit. on p. 46).

[66] L. Evans, *The large hadron collider*,
Annual Review of Nuclear and Particle Science **61** (2011) 435 (cit. on pp. 48, 49).

[67] CERN, *Linear accelerator 2*,
`https://home.cern/science/accelerators/linear-accelerator-2`,
Accessed: 2022-03-11 (cit. on pp. 48, 49).

[68] CERN, *The Proton Synchrotron Booster*,
`https://home.cern/science/accelerators/proton-synchrotron-booster`,
Accessed: 2022-03-11 (cit. on p. 49).

[69] CERN, *The Proton Synchrotron*,
https://home.cern/science/accelerators/proton-synchrotron,
Accessed: 2022-03-11 (cit. on p. 49).

[70] CERN, *The Super Proton Synchrotron*,
https://home.cern/science/accelerators/super-proton-synchrotron,
Accessed: 2022-03-11 (cit. on p. 49).

[71] ATLAS Collaboration, *The ATLAS experiment at the CERN large hadron collider*,
Journal of instrumentation **3** (2008) (cit. on pp. 49, 50, 52, 55–58).

[72] ATLAS Collaboration, *ATLAS Luminosity Public Results Run-2*, https:
//twiki.cern.ch/twiki/bin/view/AtlasPublic/LuminosityPublicResultsRun2,
Accessed: 2022-02-21, 2018 (cit. on p. 50).

[73] ATLAS Collaboration, *Luminosity determination in pp collisions at $\sqrt{s} = 13$ TeV using the ATLAS detector at the LHC*, (2019) (cit. on p. 49).

[74] J. A. McFayden,
Searches for supersymmetric partners of third generation quarks and measurement of the $t\bar{t} + Z$ process using the ATLAS detector at the CERN Large Hadron Collider,
PhD thesis: University of Sheffield, 2013 (cit. on p. 50).

[75] I. Neutelings, *CMS coordinate system*, https://tikz.net/axis3d_cms,
Accessed: 2021-12-17, 2017 (cit. on pp. 50, 51).

[76] M. Anthony, *Search for the supersymmetric partner to the top quark in the all-hadronic final state with the ATLAS detector*, PhD thesis: University of Sheffield, 2020
(cit. on pp. 51, 58, 69, 120).

[77] J. Pequenao, *Computer generated image of the whole ATLAS detector*, (2008),
URL: https://cds.cern.ch/record/1095924 (cit. on p. 52).

[78] J. Pequenao, *Computer generated image of the ATLAS inner detector*, (2008),
URL: https://cds.cern.ch/record/1095926 (cit. on p. 53).

[79] ATLAS Collaboration,
ATLAS detector and physics performance: Technical Design Report, 1,
Technical design report. ATLAS, Geneva: CERN, 1999,
URL: https://cds.cern.ch/record/391176 (cit. on pp. 53–56, 64).

[80] ATLAS Collaboration, *Muon reconstruction and identification efficiency in ATLAS using the full Run 2 pp collision data set at $\sqrt{s} = 13$ TeV*,
The European Physical Journal C **81** (2021) 1 (cit. on pp. 53, 55, 56, 69, 70, 85).

[81] R Wigmans, *Calorimetry : energy measurement in particle physics*, eng,
International series of monographs on physics ; 107, Oxford: Clarendon, 2000,
ISBN: 0198502966 (cit. on pp. 54, 60).

[82] ATLAS Collaboration, *Jet energy scale and resolution measured in proton-proton collisions at $\sqrt{s} = 13$ TeV with the ATLAS detector*,
The European Physical Journal C **81** (2021) 1 (cit. on pp. 55, 63–65).

[83] ATLAS Collaboration,
      The superconducting magnet system for the ATLAS detector at CERN,
      Fusion engineering and design **58** (2001) 195 (cit. on p. 57).

[84] ATLAS Collaboration, *Performance of the ATLAS trigger system in 2015*,
      The European Physical Journal C **77** (2017) 1 (cit. on p. 57).

[85] ATLAS Collaboration, *The ATLAS simulation infrastructure*,
      The European Physical Journal C **70** (2010) 823 (cit. on pp. 58, 59).

[86] GEANT4 Collaboration, *GEANT4—a simulation toolkit*,
      Nuclear instruments and methods in physics research section A: Accelerators,
      Spectrometers, Detectors and Associated Equipment **506** (2003) 250 (cit. on p. 58).

[87] I. Sanderswood, *A test of Lepton Flavour Universality by comparing the decay widths of
      W bosons produced in top quark pair events with the ATLAS detector at the LHC*,
      PhD thesis: Lancaster University, 2021 (cit. on p. 59).

[88] M. Cacciari, G. P. Salam and G. Soyez, *The anti-kt jet clustering algorithm*,
      Journal of High Energy Physics **2008** (2008) 063 (cit. on pp. 60, 61).

[89] ATLAS Collaboration,
      Jet reconstruction and performance using particle flow with the ATLAS Detector,
      Eur. Phys. J. **C77** (2017) 466, arXiv: `1703.10485 [hep-ex]` (cit. on pp. 61–63).

[90] CMS Collaboration,
      Particle-Flow Event Reconstruction in CMS and Performance for Jets, Taus, and MET,
      tech. rep. CMS-PAS-PFT-09-001, CERN, 2009,
      URL: `https://cds.cern.ch/record/1194487` (cit. on p. 61).

[91] ATLAS Collaboration,
      Topological cell clustering in the ATLAS calorimeters and its performance in LHC Run 1,
      Eur. Phys. J. C **77** (2017) 490, arXiv: `1603.02934 [hep-ex]` (cit. on pp. 61, 62, 85).

[92] ATLAS Collaboration, *ATLAS b-jet identification performance and efficiency
      measurement with $t\bar{t}$ events in pp collisions at $\sqrt{s} = 13$ TeV*,
      Eur. Phys. J. C **79** (2019) 970, arXiv: `1907.05120 [hep-ex]`
      (cit. on pp. 64, 66, 82–84, 87, 89–91, 93–95, 97, 98, 100, 104, 199, 200).

[93] N. Bartosik, *Diagram showing the common principle of identification of jets initiated by
      b-hadron decays*, `https://en.wikipedia.org/wiki/File:B-tagging_diagram.png`,
      Accessed: 2022-01-18 (cit. on p. 66).

[94] R. Frühwirth and A. Strandlie, *Secondary Vertex Reconstruction*,
      Cham: Springer International Publishing, 2021 159, ISBN: 978-3-030-65771-0,
      URL: `https://doi.org/10.1007/978-3-030-65771-0_9` (cit. on pp. 64, 66).

[95] ATLAS Collaboration, *Performance of missing transverse momentum reconstruction with
      the ATLAS detector using proton-proton collisions at $\sqrt{s} = 13$ TeV*,
      arXiv preprint arXiv:1802.08168 (2018) (cit. on pp. 66, 67).

[96] ATLAS Collaboration, *Performance of algorithms that reconstruct missing transverse momentum in $\sqrt{s} = 8$ TeV proton–proton collisions in the ATLAS detector*, The European Physical Journal C **77** (2017) 1 (cit. on p. 67).

[97] ATLAS Collaboration, *Performance of missing transverse momentum reconstruction with the ATLAS detector in the first proton–proton collisions at $\sqrt{s} = 13$ TeV*, ATL-PHYS-PUB-2015-027, 2015, URL: https://cds.cern.ch/record/2037904 (cit. on p. 67).

[98] ATLAS Collaboration, *Expected performance of missing transverse momentum reconstruction for the ATLAS detector at $\sqrt{s} = 13$ TeV*, ATL-PHYS-PUB-2015-023, 2015, URL: https://cds.cern.ch/record/2037700 (cit. on p. 67).

[99] ATLAS Collaboration, *Electron reconstruction and identification in the ATLAS experiment using the 2015 and 2016 LHC proton–proton collision data at $\sqrt{s} = 13$ TeV*, The European Physical Journal C **79** (2019) 1 (cit. on pp. 67, 68).

[100] G. Cowan, *Statistical data analysis*, Oxford university press, 1998 (cit. on pp. 71–73).

[101] R. K. Bock, H Grote and D Notz, *Data analysis techniques for high-energy physics*, vol. 11, Cambridge University Press, 2000 (cit. on pp. 71, 72).

[102] M Baak et al., *HistFitter software framework for statistical data analysis*, The European Physical Journal C **75** (2015) 1 (cit. on pp. 72, 73, 76, 77, 155, 218).

[103] A. L. Read, *Modified frequentist analysis of search results (the CL_s method)*, tech. rep., CERN, 2000 (cit. on pp. 73, 76).

[104] J. Neyman and E. S. Pearson, *IX. On the problem of the most efficient tests of statistical hypotheses*, Philosophical Transactions of the Royal Society of London. Series A, Containing Papers of a Mathematical or Physical Character **231** (1933) 289 (cit. on p. 73).

[105] S. S. Wilks, *The large-sample distribution of the likelihood ratio for testing composite hypotheses*, The annals of mathematical statistics **9** (1938) 60 (cit. on p. 74).

[106] G. Cowan, K. Cranmer, E. Gross and O. Vitells, *Asymptotic formulae for likelihood-based tests of new physics*, The European Physical Journal C **71** (2011) 1 (cit. on pp. 74, 75).

[107] L. Moneta et al., *The roostats project*, arXiv preprint arXiv:1009.1003 (2010) (cit. on pp. 74, 120, 138).

[108] ATLAS Collaboration, CMS Collaboration and LHC Higgs Combination Group, *Procedure for the LHC Higgs boson search combination in Summer 2011*, (2011), URL: https://cds.cern.ch/record/1379837 (cit. on p. 75).

[109] ATLAS Collaboration, *Optimisation and performance studies of the ATLAS b-tagging algorithms for the 2017-18 LHC run*, tech. rep. ATL-PHYS-PUB-2017-013, CERN, 2017, URL: https://cds.cern.ch/record/2273281 (cit. on pp. 82, 83).

[110]   ATLAS Collaboration,
        Secondary vertex finding for jet flavour identification with the ATLAS detector, tech. rep.,
        ATL-PHYS-PUB-2017-011, 2017 (cit. on p. 83).

[111]   G. Piacquadio and C. Weiser,
        A new inclusive secondary vertex algorithm for b-jet tagging in ATLAS,
        119 (2008) 032032 (cit. on p. 83).

[112]   R. Frühwirth, *Application of Kalman filtering to track and vertex fitting*,
        Nuclear Instruments and Methods in Physics Research Section A: Accelerators,
        Spectrometers, Detectors and Associated Equipment **262** (1987) 444 (cit. on p. 83).

[113]   A. Hoecker et al., *TMVA - Toolkit for Multivariate Data Analysis*, 2009,
        arXiv: `physics/0703039 [physics.data-an]` (cit. on p. 83).

[114]   F. Chollet et al., *Keras: Deep learning library for theano and tensorflow*,
        URL: https://keras. io/k **7** (2015) T1 (cit. on p. 84).

[115]   R. Al-Rfou et al.,
        Theano: A Python framework for fast computation of mathematical expressions,
        arXiv e-prints (2016) 1605 (cit. on p. 84).

[116]   D. P. Kingma and J. Ba, *Adam: A Method for Stochastic Optimization*, 2017,
        arXiv: `1412.6980 [cs.LG]` (cit. on p. 84).

[117]   M. Cacciari, G. P. Salam and G. Soyez, *The anti-k_t jet clustering algorithm*,
        JHEP **04** (2008) 063, arXiv: `0802.1189 [hep-ph]` (cit. on p. 85).

[118]   ATLAS Collaboration, *Jet energy scale measurements and their systematic uncertainties
        in proton-proton collisions at $\sqrt{s} = 13\ TeV$ with the ATLAS detector*,
        Physical Review D **96** (2017), ISSN: 2470-0029,
        URL: `http://dx.doi.org/10.1103/PhysRevD.96.072002` (cit. on pp. 85, 97).

[119]   ATLAS Collaboration, *Selection of jets produced in $\sqrt{s} = 13\ TeV$ proton–proton
        collisions with the ATLAS detector*, ATLAS-CONF-2015-029, 2015,
        URL: `https://cds.cern.ch/record/2037702` (cit. on p. 85).

[120]   ATLAS Collaboration, *Tagging and suppression of pileup jets with the ATLAS detector*,
        ATLAS-CONF-2014-018, 2014, URL: `https://cds.cern.ch/record/1700870`
        (cit. on p. 86).

[121]   R. Lysák, *Charge Asymmetry in Top Quark Pair Production*, Symmetry **12** (2020) 1278
        (cit. on p. 87).

[122]   M. Beneke et al., *Top quark physics*, arXiv e-prints (2000),
        URL: `https://arxiv.org/abs/hep-ph/0003033` (cit. on p. 87).

[123]   M. Schott and M. Dunford,
        Review of single vector boson production in pp collisions at $\sqrt{s} = 7\ TeV$.,
        Eur. Phys. J. C **74** (2014) 60 p, Comments: 60 pages, 64 figures, For Eur. Phys. J. C,
        arXiv: `1405.1160`, URL: `https://cds.cern.ch/record/1699952` (cit. on p. 88).

[124] ATLAS Collaboration, *Measurement of hard double-parton interactions in $W \to l\nu$)+ 2 jet events at $\sqrt{s}=7$ TeV with the ATLAS detector.*, New J. Phys. **15** (2013) 033038. 23 p, arXiv: 1301.6872, URL: https://cds.cern.ch/record/1510534 (cit. on p. 88).

[125] M. Czakon and A. Mitov,
Top++: A program for the calculation of the top-pair cross-section at hadron colliders,
Comput. Phys. Commun. **185** (2014) 2930, arXiv: 1112.5675 [hep-ph]
(cit. on pp. 88, 113, 136, 137).

[126] S. Frixione, E. Laenen, P. Motylinski, C. White and B. R. Webber,
Single-top hadroproduction in association with a W boson,
Journal of High Energy Physics **2008** (2008) 029–029, ISSN: 1029-8479,
URL: http://dx.doi.org/10.1088/1126-6708/2008/07/029 (cit. on p. 88).

[127] E. Re, *Single-top Wt-channel production matched with parton showers using the POWHEG method*, The European Physical Journal C **71** (2011) 1 (cit. on p. 88).

[128] T. Gleisberg et al., *Event generation with SHERPA 1.1*, JHEP **02** (2009) 007,
arXiv: 0811.4622 [hep-ph] (cit. on pp. 88, 113).

[129] S. Höche, F. Krauss, M. Schönherr and F. Siegert,
QCD matrix elements + parton showers. The NLO case, JHEP **04** (2013) 027,
arXiv: 1207.5030 [hep-ph] (cit. on pp. 88, 113).

[130] S. Catani, L. Cieri, G. Ferrera, D. de Florian and M. Grazzini,
Vector Boson Production at Hadron Colliders: A Fully Exclusive QCD Calculation at Next-to-Next-to-Leading Order, Physical Review Letters **103** (2009), ISSN: 1079-7114,
URL: http://dx.doi.org/10.1103/PhysRevLett.103.082001 (cit. on pp. 88, 113).

[131] ATLAS Collaboration, *Measurements of b-jet tagging efficiency with the ATLAS detector using $t\bar{t}$ events at $\sqrt{s} = 13$ TeV*, JHEP **08** (2018) 089, arXiv: 1805.01845 [hep-ex]
(cit. on p. 89).

[132] ATLAS Collaboration,
Measurements of differential cross sections of top quark pair production in association with jets in pp collisions at $\sqrt{s} = 13$ TeV using the ATLAS detector,
Journal of High Energy Physics **2018** (2018), ISSN: 1029-8479,
URL: http://dx.doi.org/10.1007/JHEP10(2018)159 (cit. on p. 91).

[133] ATLAS Collaboration, *Measurement of the b-jet identification efficiency with $t\bar{t}$ events using an improved likelihood method: Calibration INT note of ANA-FTAG-2018-01*,
tech. rep. ATL-COM-PHYS-2018-1072, CERN, 2018,
URL: https://cds.cern.ch/record/2631547 (cit. on p. 91).

[134] F. James, M. Winkler et al., *Minuit user's guide*, CERN, Geneva **23** (2004)
(cit. on p. 94).

[135] I. Jolliffe, *Principal component analysis*, New York: Springer Verlag, 2002 (cit. on p. 96).

[136]   ATLAS Collaboration, *ATLAS Pythia 8 tunes to 7 TeV data*, tech. rep.,
        All figures including auxiliary figures are available at
        https://atlas.web.cern.ch/Atlas/GROUPS/PHYSICS/PUBNOTES/ATL-PHYS-PUB-
        2014-021: CERN, 2014, URL: https://cds.cern.ch/record/1966419
        (cit. on p. 96).

[137]   J. Butterworth et al., *PDF4LHC recommendations for LHC Run II*,
        J. Phys. G **43** (2016) 023001, arXiv: 1510.03865 [hep-ph] (cit. on p. 97).

[138]   A. Giammanco, *Single top quark production at the LHC*, Rev. Phys. **1** (2016) 1,
        arXiv: 1511.06748 [hep-ex] (cit. on p. 97).

[139]   ATLAS Collaboration, *Performance of the ATLAS trigger system in 2015*,
        The European Physical Journal C **77** (2017), ISSN: 1434-6052,
        URL: http://dx.doi.org/10.1140/epjc/s10052-017-4852-3 (cit. on p. 97).

[140]   ATLAS Collaboration, *Calibration of light-flavour b-jet mistagging rates using ATLAS
        proton-proton collision data at $\sqrt{s} = 13$ TeV*, tech. rep.,
        All figures including auxiliary figures are available at
        https://atlas.web.cern.ch/Atlas/GROUPS/PHYSICS/CONFNOTES/ATLAS-CONF-
        2018-006: CERN, 2018, URL: https://cds.cern.ch/record/2314418
        (cit. on p. 97).

[141]   ATLAS Collaboration,
        Calibration of the ATLAS b-tagging algorithm in $t\bar{t}$ semi-leptonic events, tech. rep.,
        All figures including auxiliary figures are available at
        https://atlas.web.cern.ch/Atlas/GROUPS/PHYSICS/CONFNOTES/ATLAS-CONF-
        2018-045: CERN, 2018, URL: https://cds.cern.ch/record/2638455
        (cit. on p. 97).

[142]   N. D. Gagunashvili, *Pearson's chi-square test modifications for comparison of unweighted
        and weighted histograms and two weighted histograms*, PoS **ACAT** (2007) 060
        (cit. on p. 98).

[143]   I. Hinchliffe, F. E. Paige, M. Shapiro, J Söderqvist and W Yao,
        Precision susy measurements at cern lhc, Physical Review D **55** (1997) 5520
        (cit. on pp. 106, 111, 145).

[144]   B. S. Acharya et al., *Identifying multi-top events from gluino decay at the LHC*,
        arXiv preprint arXiv:0901.3367 (2009) (cit. on p. 106).

[145]   B. Nachman, P. Nef, A. Schwartzman, M. Swiatlowski and C. Wanotayaroj, *Jets from
        jets: re-clustering as a tool for large radius jet reconstruction and grooming at the LHC*,
        Journal of High Energy Physics **2015** (2015) 1, ISSN: 1029-8479,
        URL: http://dx.doi.org/10.1007/JHEP02(2015)075 (cit. on p. 109).

[146]   ATLAS Collaboration, *Performance of jet substructure techniques for large-R jets in
        proton–proton collisions at $\sqrt{s} = 7$ TeV using the ATLAS detector*, JHEP **09** (2013) 076,
        arXiv: 1306.4945 [hep-ex] (cit. on p. 109).

[147] ATLAS Collaboration,
Performance of Top Quark and W Boson Tagging in Run 2 with ATLAS,
ATLAS-CONF-2017-064, 2017, URL: https://cds.cern.ch/record/2281054
(cit. on p. 109).

[148] T. J. Khoo, *The hunting of the squark: Experimental strategies in the search for supersymmetry at the Large Hadron Collider*, PhD thesis: University of Cambridge, 2013
(cit. on pp. 110, 145, 146, 148).

[149] G Arnison et al., *Experimental observation of isolated large transverse energy electrons with associated missing energy at $\sqrt{s} = 540$ GeV*, Physics letters B **122** (1983) 103
(cit. on p. 111).

[150] G Arnison et al.,
Further evidence for charged intermediate vector bosons at the SPS collider,
Physics Letters B **129** (1983) 273 (cit. on p. 111).

[151] ATLAS Collaboration,
Vertex Reconstruction Performance of the ATLAS Detector at $\sqrt{s} = 13$ TeV,
ATL-PHYS-PUB-2015-026, 2015, URL: https://cds.cern.ch/record/2037717
(cit. on p. 112).

[152] R. D. Ball et al., *Parton distributions for the LHC run II*, JHEP **04** (2015) 040,
arXiv: 1410.8849 [hep-ph] (cit. on p. 113).

[153] T. Sjöstrand, S. Mrenna and P. Skands, *A brief introduction to PYTHIA 8.1*,
Comput. Phys. Commun. **178** (2008) 852, arXiv: 0710.3820 [hep-ph] (cit. on p. 113).

[154] W. Beenakker, R. Hopker, M. Spira and P. Zerwas,
Squark and gluino production at hadron colliders, Nucl. Phys. B **492** (1997) 51,
arXiv: hep-ph/9610490 (cit. on p. 113).

[155] A. Kulesza and L. Motyka,
Threshold resummation for squark-antisquark and gluino-pair production at the LHC,
Phys. Rev. Lett. **102** (2009) 111802, arXiv: 0807.2405 [hep-ph] (cit. on p. 113).

[156] A. Kulesza and L. Motyka, *Soft gluon resummation for the production of gluino-gluino and squark-antisquark pairs at the LHC*, Phys. Rev. D **80** (2009) 095004,
arXiv: 0905.4749 [hep-ph] (cit. on p. 113).

[157] W. Beenakker and others, *Soft-gluon resummation for squark and gluino hadroproduction*,
JHEP **12** (2009) 041, arXiv: 0909.4418 [hep-ph] (cit. on p. 113).

[158] W. Beenakker and others, *Squark and gluino hadroproduction*,
Int. J. Mod. Phys. A **26** (2011) 2637, arXiv: 1105.1110 [hep-ph] (cit. on p. 113).

[159] C. Borschensky and others, *Squark and gluino production cross sections in pp collisions at $\sqrt{s} = 13, 14, 33$ and 100 TeV*, Eur. Phys. J. C **74** (2014) 3174,
arXiv: 1407.5066 [hep-ph] (cit. on p. 113).

[160] ATLAS Collaboration, *Search for pair production of up-type vector-like quarks and for four-top-quark events in final states with multiple b-jets with the ATLAS detector*,
JHEP **07** (2018) 089, arXiv: 1803.09678 [hep-ex] (cit. on p. 114).

[161] C. Gütschow, J. M. Lindert and M. Schönherr,
       Multi-jet merged top-pair production including electroweak corrections,
       The European Physical Journal C **78** (2018), ISSN: 1434-6052,
       URL: http://dx.doi.org/10.1140/epjc/s10052-018-5804-2 (cit. on p. 114).

[162] ATLAS Collaboration, *Search for supersymmetry in final states with missing transverse*
       momentum and three or more b-jets in 139 fb^{-1} of proton−proton collisions at $\sqrt{s} = 13$
       TeV with the ATLAS detector, (2022), publication submitted to Eur. Phys. Journal C,
       URL: https://arxiv.org/abs/2211.08028
       (cit. on pp. 117, 118, 133–139, 141, 142, 212).

[163] G. Stark, *optimization*, https://github.com/kratsg/optimization,
       Accessed: 2022-05-24, 2020 (cit. on p. 119).

[164] ATLAS Collaboration,
       Search for supersymmetry in final states with missing transverse momentum and multiple
       b-jets in proton–proton collisions at $\sqrt{s} = 13$ TeV with the ATLAS detector,
       JHEP **06** (2018) 107, arXiv: 1711.01901 [hep-ex] (cit. on pp. 131, 140, 146).

[165] P. Z. Skands, *Tuning Monte Carlo Generators: The Perugia Tunes*,
       Phys. Rev. D **82** (2010) 074018, arXiv: 1005.3457 [hep-ph] (cit. on p. 131).

[166] P. Kant et al., *HatHor for single top-quark production: Updated predictions and*
       uncertainty estimates for single top-quark production in hadronic collisions,
       Comput. Phys. Commun. **191** (2015) 74, arXiv: 1406.4403 [hep-ph] (cit. on p. 131).

[167] A. L. Read, *Presentation of search results: the CL_s technique*, J. Phys. G **28** (2002) 2693
       (cit. on p. 138).

[168] D. R. Tovey, *Measuring the SUSY mass scale at the LHC*,
       Physics Letters B **498** (2001) 1 (cit. on p. 145).

[169] D. R. Tovey, *Inclusive SUSY searches and measurements at ATLAS*,
       EPJ direct **4** (2002) 1 (cit. on p. 146).

[170] O Helene, *Upper limit of peak area*,
       Nuclear Instruments and Methods in Physics Research **212** (1983) 319 (cit. on p. 174).

[171] J. Wess and B. Zumino, *Supergauge transformations in four dimensions*,
       Nuclear Physics B **70** (1974) 39 (cit. on p. 196).

Appendices

Appendix A

Theory

A.1   Supersymmetry Lagrangians

The Lagrangian for chiral supermultiplets in the Wess-Zumino Model [171] for a free fermion is given by

$$
\begin{aligned}
\mathcal{L}_{\text{chiral}} = \mathcal{L}_{\text{free}} + \mathcal{L}_{\text{int.}} &= -\partial^\mu \phi^{\star i} \partial_\mu \phi_i + i\psi^{\dagger i} \bar{\sigma}^\mu \partial_\mu \psi_i + F^{\star i} F_i + \mathcal{L}_{\text{int.}} \\
&= \underbrace{-\partial^\mu \phi^{\star i} \partial_\mu \phi_i}_{\mathcal{L}_{\text{scalar}}} + \underbrace{i\psi^{\dagger i} \bar{\sigma}^\mu \partial_\mu \psi_i}_{\mathcal{L}_{\text{fermion}}} \underbrace{-\frac{1}{2}(W^{ij}\psi_i\psi_j + W^{\star}_{ij}\psi^{\dagger i}\psi^{\dagger j}) - W^i W^{\star}_i}_{\mathcal{L}_{\text{auxiliary}}},
\end{aligned}
\tag{A.1}
$$

where σ are the Pauli matrices and W is the superpotential, given by

$$
W = \frac{1}{2}M^{ij}\phi_i\phi_j + \frac{1}{6}y^{ijk}\phi_i\phi_j\phi_k,
\tag{A.2}
$$

for the fermion field mass M^{ij} and Yukawa coupling y^{ijk}.

The Lagrangian for the gauge supermultiplets with a massless gaugino field A, Weyl fermion gaugino λ ($a = 1, \ldots, N$ for $N^2 - 1$ generators of SU(3), SU(2)and U(1)groups), gauge coupling g, structure constant f^{abc1}, gauge group represent hermitian matrices T and the bosonic auxiliary field D [24] is given by

$$
\mathcal{L}_{\text{gauge}} = -\frac{1}{4}F^a_{\mu\nu}F^{\mu\nu a} + i\lambda^{\dagger a}\bar{\sigma}^\mu \nabla_\mu \lambda^a + \frac{1}{2}D^a D^a,
\tag{A.3}
$$

where

$$
F^a_{\mu\nu} = \partial_\mu A^a_\nu - \partial_\nu A^a_\mu + gf^{abc}A^b_\mu A^c_\nu \text{ and } \nabla_\mu \lambda^a = \partial_\mu \lambda^a + gf^{abc}A^b_\mu \lambda^c.
\tag{A.4}
$$

---

[1] $f^{abc} = 0$ for Abelian gauge theories [24].

The resulting general SUSY Lagrangian is a combination of chiral and gauge supermultiplet interactions,

$$
\begin{aligned}
\mathcal{L}_{\text{SUSY}} =& \mathcal{L}_{\text{chiral}} + \mathcal{L}_{\text{gauge}} \\
& - \sqrt{2} g (\phi^\star T^a \psi) \lambda^a - \sqrt{2} g \lambda^{\dagger a} (\psi^\dagger T^a \phi) + g (\phi^\star T^a \phi) D^a,
\end{aligned}
\tag{A.5}
$$

where the F-terms are fixed by Yukawa couplings and fermion mass terms and the D-terms are fixed by the gauge interactions [24].

A.2 Parameters and Numerical Constraints of the pMSSM

A summary of the free parameters and numerical constraints of the pMSSM.

Parameter	Min. value	Max. value	Note
$m_{\tilde{L}_1}(= m_{\tilde{L}_2})$	90 GeV	4 TeV	LH slepton (first two gens.) mass
$m_{\tilde{e}_1}(= m_{\tilde{e}_2})$	90 GeV	4 TeV	RH slepton (first two gens.) mass
$m_{\tilde{L}_3}$	90 GeV	4 TeV	LH stau doublet mass
$m_{\tilde{e}_3}$	90 GeV	4 TeV	RH stau mass
$m_{\tilde{Q}_1}(= m_{\tilde{Q}_2})$	200 GeV	4 TeV	LH squark (first two gens.) mass
$m_{\tilde{u}_1}(= m_{\tilde{u}_2})$	200 GeV	4 TeV	RH up-type squark(first two gens.) mass
$m_{\tilde{d}_1}(= m_{\tilde{d}_2})$	200 GeV	4 TeV	RH down-type squark(first two gens.) mass
$m_{\tilde{Q}_3}$	100 GeV	4 TeV	LH squark (third gen.) mass
$m_{\tilde{u}_3}$	100 GeV	4 TeV	RH top squark mass
$m_{\tilde{d}_3}$	100 GeV	4 TeV	RH bottom squark mass
$|M_1|$	0 GeV	4 TeV	Bino mass parameter
$|M_2|$	70 GeV	4 TeV	Wino mass parameter
$|\mu|$	80 GeV	4 TeV	Bilinear Higgs mass parameter
M_3	200 GeV	4 TeV	Gluino mass parameter
$|A_t|$	0 GeV	4 TeV	Trilinear top coupling
$|A_b|$	0 GeV	4 TeV	Trilinear bottom coupling
$|A_\tau|$	0 GeV	4 TeV	Trilinear τ lepton coupling
$|M_A|$	100 GeV	4 TeV	Pseudoscalar Higgs boson mass
$\tan\beta$	1	60	Ratio of the Higgs vacuum expectation values

Table A.1: The 19 parameters of the pMSSM. Taken from Ref [27].

Parameter	Min. value	Max. Value
$\Delta\rho$	-0.0005	0.0017
$\Delta(g-2)_\mu$	-17.7×10^{-10}	43.8×10^{-10}
$\mathrm{BR}(b \to s\gamma)$	2.69×10^{-4}	3.87×10^{-4}
$\mathrm{BR}(B_s \to \mu^+\mu^-)$	1.6×10^{-9}	4.2×10^{-9}
$\mathrm{BR}(B^+ \to \tau^+\nu_\tau)$	66×10^{-6}	161×10^{-6}
$\Omega_{\tilde{\chi}_1^0}h^2$	-	0.1208
$\Gamma_{invis(SUSY)}(Z)$	-	2 MeV
Masses of charged sparticles	100 GeV	-
$m(\tilde{\chi}_1^\pm)$	103 GeV	-
$m(\tilde{u}_{1,2}, \tilde{d}_{1,2}, \tilde{c}_{1,2}, \tilde{s}_{1,2})$	200 GeV	-
$m(h)$	124 GeV	128 GeV

Table A.2: Experimental numerical constraints imposed on the pMSSM. Taken from Ref [27].

Appendix B

b-tagging Calibration

B.1   *b*-tagging Algorithms

Hyperparameters for the MV2 and DL1R multivariate algorithms can be seen in Tables B.1 and B.2 respectively. Table B.3 shows the inputs to each of the high-level multivariate *b*-tagging algorithms.

Hyperparameter	Value
Number of trees	1000
Depth	30
Minimum node size	0.05%
Cuts	200
Boosting type	Gradient boost
Shrinkage	0.1
Bagged sample fraction	0.5

Table B.1: List of optimised hyperparameters used in the MV2 tagging algorithm. Taken from Ref [92].

Hyperparameter	Value
Number of input variables	28
Number of hidden layers	8
Number of nodes [per layer]	[78, 66, 57, 48, 36, 24, 12, 6]
Number of Maxout layers [position]	3[1, 2, 6]
Number of parallel layers per Maxout layer	25
Number of training epochs	240
Learning rate	0.0005
Training minibatch size	500

Table B.2: List of optimised hyperparameters used in the DL1R tagging algorithm. Taken from Ref [92].

Input	Variable	Description
Kinematics	p_T	Jet p_T
	η	Jet $|\eta|$
IP2D/ IP3D	$\log(p_b/p_l)$	Likelihood ratio between the *b*-jet and light-jet hypotheses
	$\log(p_b/p_c)$	Likelihood ratio between the *b*-jet and *c*-jet hypotheses
	$\log(p_c/p_l)$	Likelihood ratio between the *c*-jet and light-jet hypotheses
SV1	$m(\mathrm{SV})$	Invariant mass of tracks at the secondary vertex assuming pion mas
	$f_E(\mathrm{SV})$	Energy fraction of the tracks associated with the secondary vertex
	$N_\mathrm{TrkAtVtx}(\mathrm{SV})$	Number of tracks used in the secondary vertex
	$N_\mathrm{2TrkVtx}(\mathrm{SV})$	Number of two-track vertex candidates
	$L_{xy}(\mathrm{SV})$	Transverse distance between the primary and secondary vertex
	$L_{xyz}(\mathrm{SV})$	Distance between the primary and the secondary vertex
	$S_{xyz}(\mathrm{SV})$	Distance between the primary and the secondary vertex divided by its uncertainty
	$\Delta R(\vec{p}_\mathrm{jet}, \vec{p}_\mathrm{vtx})(\mathrm{SV})$	ΔR between the jet axis and the direction of the secondary vertex relativeto the primary vertex
JETFITTER	$m(\mathrm{JF})$	Invariant mass of tracks from displaced vertices
	$f_E(\mathrm{JF})$	Energy fraction of the tracks associated with the displaced vertices
	$\Delta R(\vec{p}_\mathrm{jet}, \vec{p}_\mathrm{vtx})(\mathrm{JF})$	ΔR between the jet axis and the vectorial sum of momenta of all tracksattached to displaced vertices
	$S_{xyz}(\mathrm{JF})$	Significance of the average distance between PV and displaced vertices
	$N_\mathrm{TrkAtVtx}(\mathrm{JF})$	Number of tracks from multi-prong displaced vertices
	$N_\mathrm{2TrkVtx}(\mathrm{JF})$	Number of two-track vertex candidates (before decay chain fit)
	$N_{1-\mathrm{trk\ vertices}}(\mathrm{JF})$	Number of single-prong displaced vertices
	$N_{\geq 2-\mathrm{trk\ vertices}}(\mathrm{JF})$	Number of multi-prong displaced vertices
JETFITTER	$L_{xyz}(\mathrm{2nd/3rd\ vtx})(\mathrm{JFc})$	Distance of 2nd or 3rd vertex from PV
(*c*-tagging)	$L_{xy}(\mathrm{2nd/3rd\ vtx})(\mathrm{JFc})$	Transverse displacement of the 2nd or 3rd vertex
	$m_\mathrm{Trk}(\mathrm{2nd/3rd\ vtx})$	Invariant mass of tracks associated with 2nd or 3rd vertex
	$E_\mathrm{Trk}(\mathrm{2nd/3rd\ vtx})$	Energy fraction of the tracks associated with 2nd or 3rd vertex
	$f_E(\mathrm{2nd/3rd\ vtx})(\mathrm{JFc})$	Fraction of charged jet energy in 2nd or 3rd vertex
	$N_\mathrm{TrkAtVtx}(\mathrm{2nd/3rd\ vtx})(\mathrm{JFc})$	Number of tracks associated with 2nd or 3rd vertex
	$Y_\mathrm{trk}^\mathrm{min}, Y_\mathrm{trk}^\mathrm{max}, Y_\mathrm{trk}^\mathrm{avg}$	Min., max. and avg. track rapidity of tracks at 2nd or 3rd vertex
RNN	d_0	Transverse Impact Parameter of each track inside a jet
	z_0	Longtidunal Impact Parameter of each track inside a jet
	$\Delta R(\vec{p}_\mathrm{jet}, \vec{p}_\mathrm{trk})$	Angular distance between the track and the jet-axis
	Track grade	Category of hit pattern for a given track

Table B.3: Input variables used by the MV2 and the DL1R algorithms. The JETFITTER *c*-tagging (JETFITTER *c*-tagging plus RNN) variables are used only by the DL1R algorithm. Table taken and adjusted from Ref. [92].

B.2   Calibration Results

This appendix will present all calibration results for all single-cut as well as pseudo-continuous operating points for the DL1r tagger.

Remaining Operating Point B-Efficiency and Scale Factors

(a) 85%

(b) 77%

(c) 70%

(d) 60%
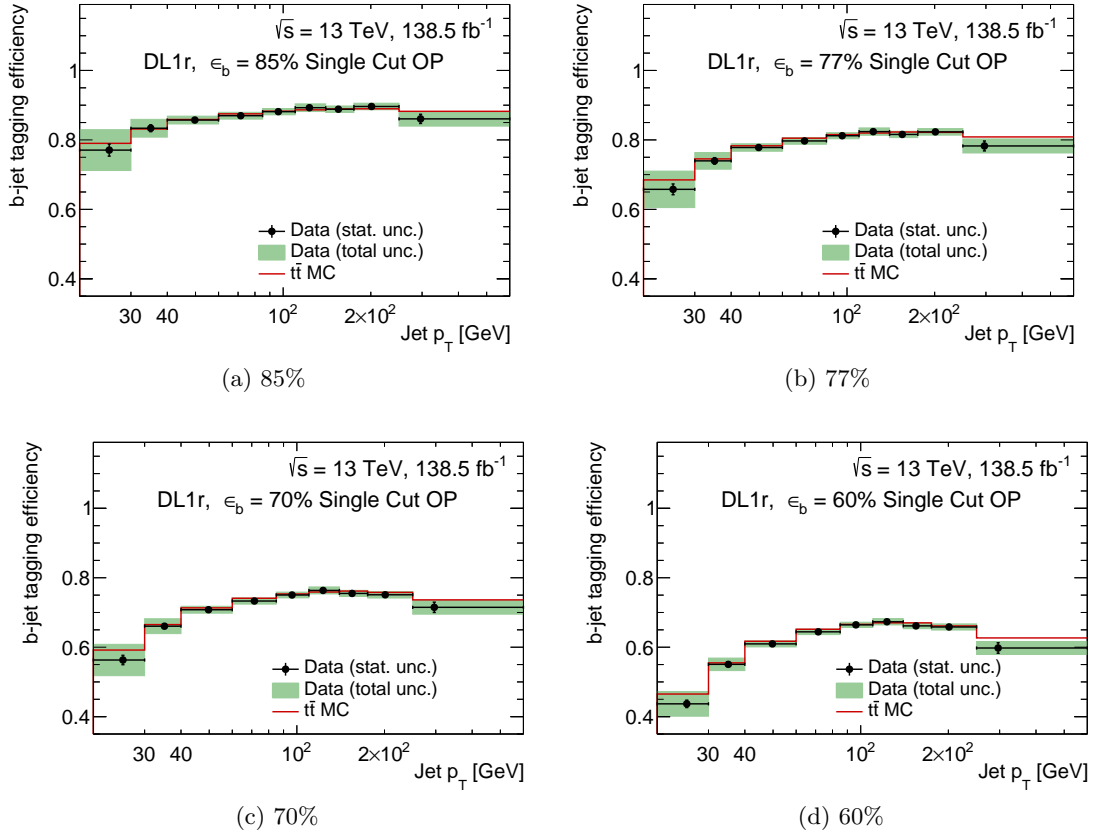
Figure B.1: Measured *b*-efficiency in Monte-Carlo for the DL1r tagger and various fixed cut operating points.

Remaining Single-Cut Operating Point Uncertainty Tables

Tables B.4 to B.7 present the systematic impact on each transverse momentum bin of the respective operating point scale factor. All uncertainty tables are for the DL1r tagger.

(a) 85%

(b) 77%

(c) 70%

(d) 60%
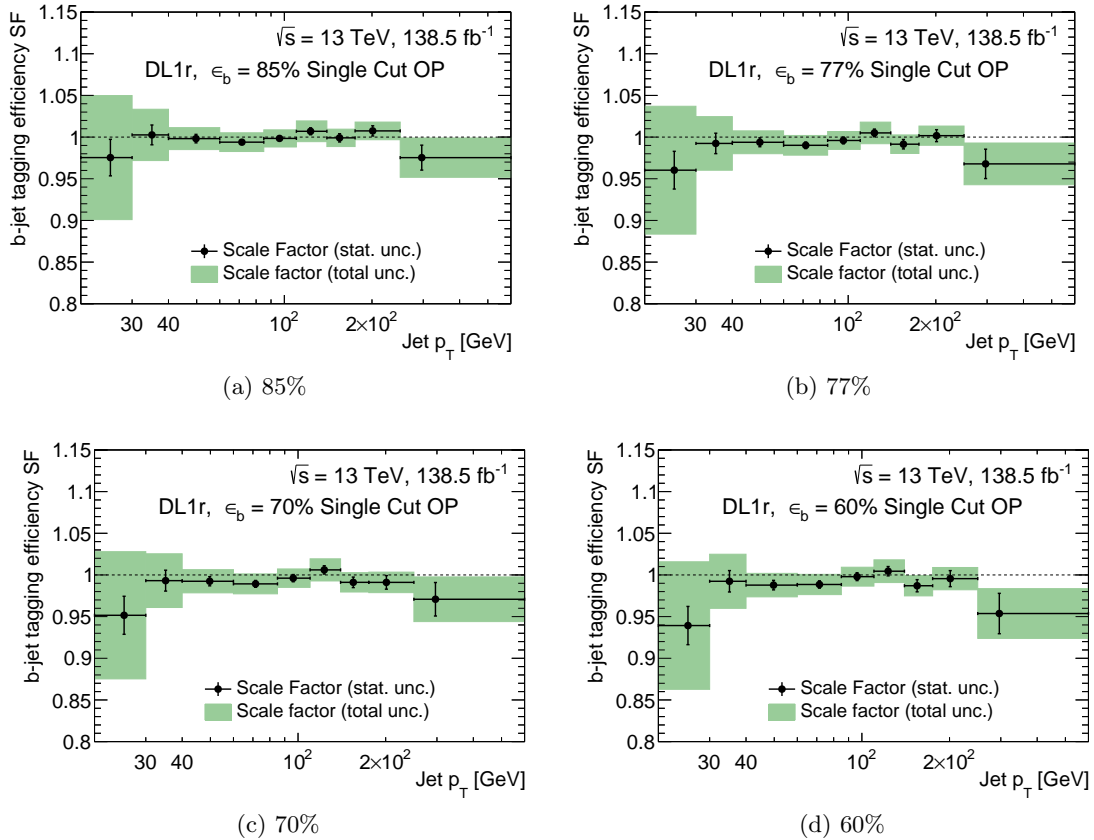
Figure B.2: Measured *b*-efficiency data-to-MC scale factors, i.e. the *b*-efficiency measurements divided by the *b*-efficiency in the nominal $t\bar{t}$ simulation, for the DL1r tagger and various fixed cut operating points.

Grouped Uncertainty / p_T [GeV]	20-30	30-40	40-60	60-85	85-110	110-140	140-175	175-250	250-600
Jet Energy Resolution	5.45	0.85	0.50	0.53	0.38	0.17	0.19	0.28	0.35
Jet Energy Scale	4.99	2.16	0.29	0.18	0.27	0.12	0.17	0.26	0.22
$t\bar{t}$ PS+Hadronisation+PDF	2.49	1.00	0.73	0.51	0.72	0.95	0.73	0.67	0.61
Z+jets Cross section+PDF	2.44	0.76	0.04	0.25	0.04	0.12	0.01	0.05	0.22
Flavour Tagging	2.28	0.86	0.28	0.10	0.09	0.12	0.04	0.11	0.23
$t\bar{t}$ ISR+FSR	1.85	1.04	0.47	0.41	0.31	0.60	0.34	0.28	0.44
Single-top ISR+FSR+Interference	1.76	0.73	0.56	0.75	0.54	0.47	0.54	0.45	1.55
Single-top PS+Hadronisation+PDF	1.72	0.64	0.53	0.29	0.14	0.05	0.03	0.03	0.07
Pileup Reweighting	1.43	0.14	0.10	0.03	0.05	0.04	0.03	0.04	0.00
Lepton Reconstruction	0.89	0.28	0.13	0.07	0.06	0.06	0.03	0.03	0.07
Fake leptons modelling	0.77	0.47	0.45	0.05	0.06	0.10	0.06	0.05	0.06
VV Cross section+PDF	0.14	0.41	0.21	0.08	0.06	0.07	0.02	0.04	0.11
Remaining	0.02	0.01	0.01	0.00	0.01	0.02	0.01	0.00	0.01
Total Systematic Uncertainty	9.21	3.20	1.43	1.22	1.08	1.26	1.01	0.95	1.80

Table B.4: Tabular breakdown of the percentage uncertainties joined into physically-motivated groups for the DL1r tagger for a 60% operating point.

(a) 85%

(b) 77%

(c) 70%

(d) 60%

Figure B.3: Total uncertainties for the measured *b*-efficiency data-to-MC scale factors for the DL1r tagger and various fixed cut operating points.

Grouped Uncertainty / p_T [GeV]	20-30	30-40	40-60	60-85	85-110	110-140	140-175	175-250	250-600
Jet Energy Resolution	5.34	0.87	0.49	0.53	0.37	0.15	0.14	0.28	0.28
Jet Energy Scale	4.94	2.16	0.29	0.18	0.27	0.11	0.17	0.26	0.25
$t\bar{t}$ PS+Hadronisation+PDF	2.47	0.99	0.71	0.50	0.71	0.94	0.73	0.67	0.61
Z+jets Cross section+PDF	2.34	0.75	0.04	0.25	0.04	0.11	0.01	0.05	0.22
Flavour Tagging	2.26	0.86	0.28	0.10	0.09	0.12	0.05	0.10	0.23
$t\bar{t}$ ISR+FSR	1.80	1.02	0.46	0.40	0.30	0.60	0.33	0.28	0.46
Single-top PS+Hadronisation+PDF	1.74	0.63	0.53	0.29	0.13	0.05	0.04	0.04	0.05
Single-top ISR+FSR+Interference	1.74	0.71	0.56	0.74	0.54	0.46	0.54	0.45	1.56
Pileup Reweighting	1.41	0.13	0.11	0.03	0.05	0.04	0.03	0.05	0.01
Lepton Reconstruction	0.88	0.27	0.13	0.07	0.06	0.06	0.03	0.03	0.07
Fake leptons modelling	0.75	0.47	0.45	0.05	0.06	0.10	0.06	0.04	0.06
VV Cross section+PDF	0.14	0.41	0.21	0.08	0.06	0.07	0.02	0.03	0.10
Remaining	0.02	0.01	0.01	0.00	0.01	0.02	0.01	0.00	0.01
Total Systematic Uncertainty	9.07	3.18	1.41	1.20	1.07	1.24	1.00	0.95	1.81

Table B.5: Tabular breakdown of the percentage uncertainties joined into physically-motivated groups for the DL1r tagger for a 70% operating point.

Grouped Uncertainty / p_T [GeV]	20-30	30-40	40-60	60-85	85-110	110-140	140-175	175-250	250-600
Jet Energy Resolution	5.45	0.95	0.49	0.54	0.30	0.13	0.13	0.27	0.30
Jet Energy Scale	4.84	2.20	0.28	0.18	0.27	0.12	0.17	0.25	0.23
$t\bar{t}$ PS+Hadronisation+PDF	2.44	0.98	0.70	0.49	0.70	0.92	0.71	0.66	0.64
Z+jets Cross section+PDF	2.36	0.76	0.06	0.25	0.04	0.12	0.01	0.05	0.22
Flavour Tagging	2.23	0.85	0.28	0.10	0.08	0.12	0.05	0.09	0.20
Single-top PS+Hadronisation+PDF	1.78	0.62	0.52	0.30	0.14	0.05	0.04	0.04	0.04
$t\bar{t}$ ISR+FSR	1.75	0.98	0.45	0.39	0.29	0.58	0.32	0.28	0.47
Single-top ISR+FSR+Interference	1.73	0.71	0.56	0.74	0.53	0.46	0.53	0.42	1.56
Pileup Reweighting	1.35	0.13	0.11	0.03	0.05	0.04	0.03	0.04	0.01
Lepton Reconstruction	0.87	0.27	0.13	0.07	0.07	0.06	0.03	0.03	0.07
Fake leptons modelling	0.78	0.47	0.45	0.04	0.06	0.11	0.07	0.04	0.06
VV Cross section+PDF	0.14	0.41	0.20	0.08	0.06	0.07	0.02	0.03	0.09
Remaining	0.02	0.01	0.01	0.00	0.01	0.02	0.01	0.00	0.01
Total Systematic Uncertainty	9.06	3.21	1.39	1.19	1.03	1.22	0.98	0.92	1.82

Table B.6: Tabular breakdown of the percentage uncertainties joined into physically-motivated groups for the DL1r tagger for a 77% operating point.
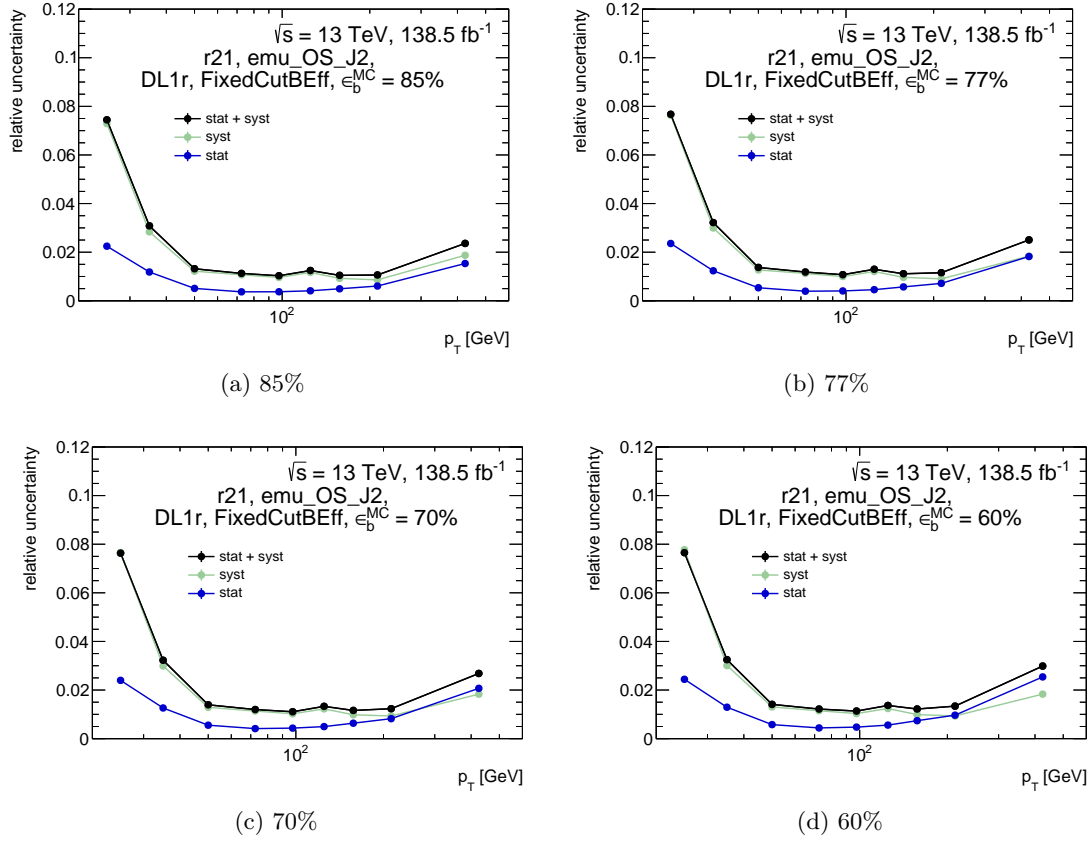
Grouped Uncertainty / p_T [GeV]	20-30	30-40	40-60	60-85	85-110	110-140	140-175	175-250	250-600
Jet Energy Resolution	4.90	0.88	0.49	0.48	0.30	0.13	0.12	0.29	0.23
Jet Energy Scale	4.78	2.07	0.28	0.17	0.26	0.12	0.17	0.24	0.26
Z+jets Cross section+PDF	2.37	0.69	0.05	0.25	0.04	0.11	0.01	0.05	0.20
$t\bar{t}$ PS+Hadronisation+PDF	2.34	0.93	0.67	0.46	0.67	0.89	0.68	0.61	0.61
Flavour Tagging	2.09	0.83	0.27	0.10	0.08	0.13	0.04	0.08	0.18
Single-top PS+Hadronisation+PDF	1.77	0.63	0.50	0.27	0.13	0.05	0.04	0.03	0.06
Single-top ISR+FSR+Interference	1.71	0.68	0.53	0.71	0.52	0.44	0.52	0.41	1.62
$t\bar{t}$ ISR+FSR	1.63	0.92	0.41	0.36	0.27	0.56	0.31	0.28	0.46
Pileup Reweighting	1.29	0.14	0.10	0.03	0.06	0.04	0.03	0.04	0.02
Lepton Reconstruction	0.83	0.26	0.12	0.07	0.06	0.06	0.03	0.03	0.06
Fake leptons modelling	0.70	0.47	0.42	0.14	0.06	0.11	0.08	0.04	0.06
VV Cross section+PDF	0.14	0.40	0.20	0.07	0.06	0.07	0.02	0.03	0.08
Remaining	0.02	0.01	0.01	0.00	0.01	0.02	0.01	0.00	0.01
Total Systematic Uncertainty	8.60	3.04	1.34	1.14	0.99	1.18	0.94	0.88	1.85

Table B.7: Tabular breakdown of the percentage uncertainties joined into physically-motivated groups for the DL1r tagger for a 85% operating point.

Pseudo-continous B-Tagging Scale Factors

(a) 20-30 GeV (b) 30-40 GeV (c) 40-60 GeV

(d) 60-85 GeV (e) 85-110 GeV (f) 110-140 GeV

(g) 140-175 GeV (h) 175-250 GeV (i) 250-600 GeV
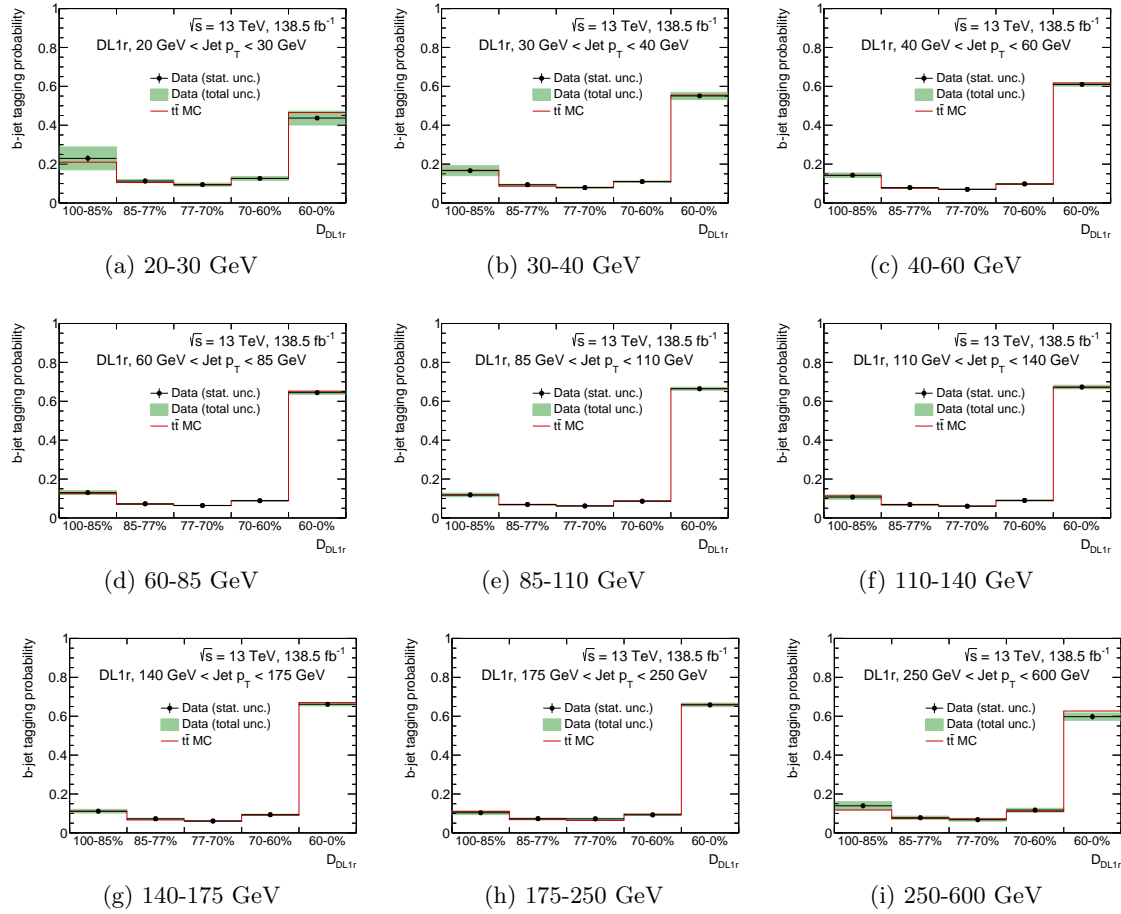
Figure B.4: Measured *b*-efficiency for the DL1r tagger with fixed cut operating points. For the pseudo continues calibration drawn as a function of the operating points and split into different p_T-bins.

Remaining Pseudo-Continous Operating Point Uncertainty Tables

Tables B.8 to B.16 present the systematic impact on each transverse momentum bin of the respective operating point scale factor. All uncertainty tables are for the DL1r tagger.
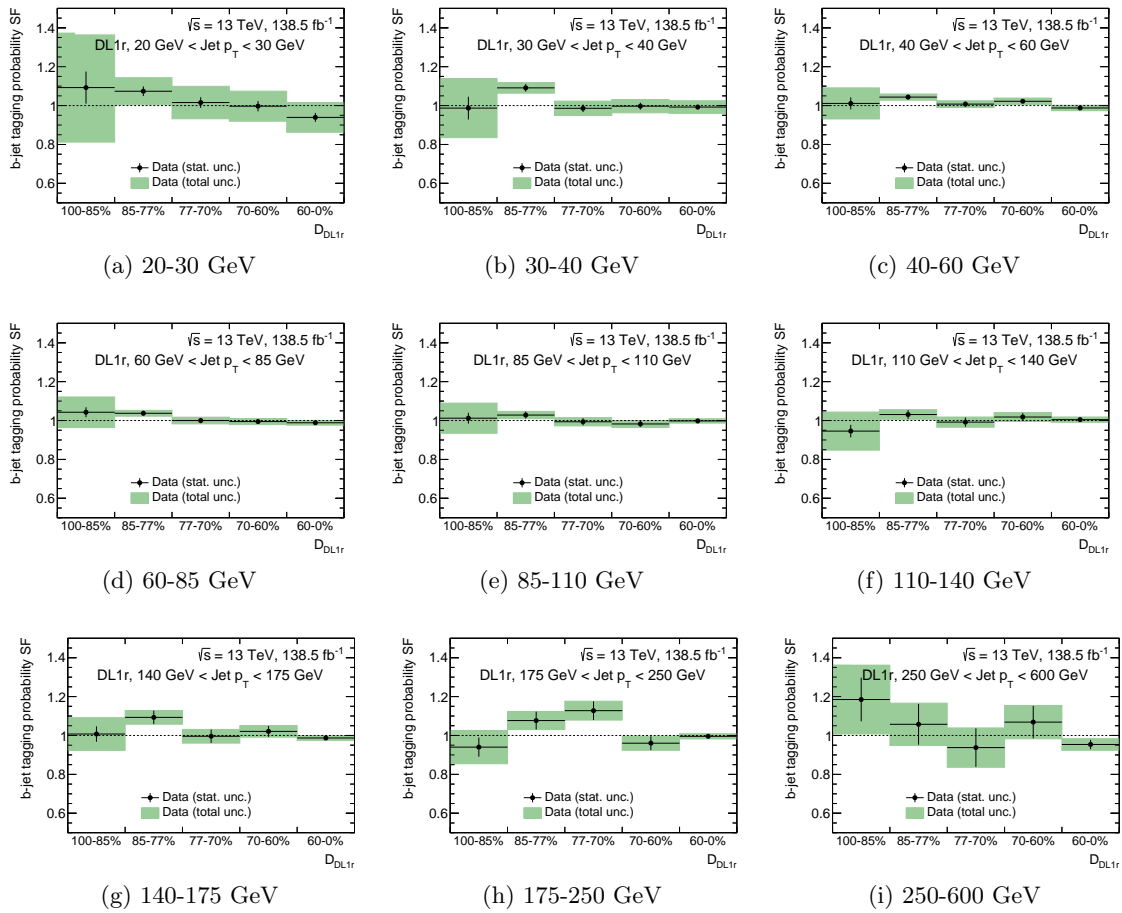
Figure B.5: Measured *b*-efficiency data-to-MC scale factors, i.e. the *b*-efficiency measurements divided by the *b*-efficiency in the nominal $t\bar{t}$ simulation, for the DL1r tagger with fixed cut operating points. For the pseudo continues calibration drawn as a function of the operating points and split into different p_T-bins.

Grouped Uncertainty / w_1, w_2	100-85%	85-77%	77-70%	70-60%	60-0%
Jet Energy Resolution	16.48	2.77	6.15	4.98	5.45
Jet Energy Scale	16.06	4.46	4.55	4.76	4.99
Z+jets Cross section+PDF	7.96	2.43	2.48	2.01	2.44
$t\bar{t}$ PS+Hadronisation+PDF	7.85	2.38	2.29	2.43	2.49
Flavour Tagging	7.01	1.27	2.06	2.18	2.28
Single-top PS+Hadronisation+PDF	5.95	1.75	1.99	1.82	1.72
Single-top ISR+FSR+Interference	5.73	1.56	1.71	1.65	1.76
$t\bar{t}$ ISR+FSR	5.63	0.96	1.49	1.61	1.85
Pileup Reweighting	4.34	0.97	0.99	1.34	1.43
Lepton Reconstruction	2.78	0.62	0.80	0.85	0.89
Fake leptons modelling	2.36	0.27	0.94	0.68	0.77
VV Cross section+PDF	0.47	0.13	0.14	0.14	0.14
Remaining	0.06	0.03	0.03	0.02	0.02
Total Systematic Uncertainty	28.91	6.97	9.26	8.59	9.21

Table B.8: Tabular breakdown of the percentage uncertainties joined into physically-motivated groups for the DL1r tagger for the p_T range 20-30 GeV.

Grouped Uncertainty / w_1, w_2	100-85%	85-77%	77-70%	70-60%	60-0%
Jet Energy Scale	10.35	1.15	2.50	2.16	2.16
$t\bar{t}$ PS+Hadronisation+PDF	4.68	0.65	0.86	0.94	1.00
$t\bar{t}$ ISR+FSR	4.63	0.46	0.74	0.91	1.04
Jet Energy Resolution	4.40	0.61	1.77	0.99	0.85
Flavour Tagging	4.14	0.67	0.74	0.86	0.86
Z+jets Cross section+PDF	3.44	0.25	0.77	0.74	0.76
Single-top ISR+FSR+Interference	3.41	0.46	0.71	0.61	0.73
Single-top PS+Hadronisation+PDF	3.21	0.67	0.59	0.56	0.64
Fake leptons modelling	2.37	0.50	0.49	0.45	0.47
VV Cross section+PDF	1.98	0.31	0.39	0.40	0.41
Lepton Reconstruction	1.32	0.20	0.25	0.27	0.28
Pileup Reweighting	0.71	0.21	0.15	0.11	0.14
Remaining	0.04	0.02	0.01	0.01	0.01
Total Systematic Uncertainty	15.25	1.99	3.62	3.13	3.20

Table B.9: Tabular breakdown of the percentage uncertainties joined into physically-motivated groups for the DL1r tagger for the p_T range 30-40 GeV.

Grouped Uncertainty / w_1, w_2	100-85%	85-77%	77-70%	70-60%	60-0%
$t\bar{t}$ PS+Hadronisation+PDF	4.02	0.37	0.59	0.64	0.73
Single-top ISR+FSR+Interference	3.20	0.31	0.48	0.55	0.56
Single-top PS+Hadronisation+PDF	2.96	0.32	0.43	0.50	0.53
Jet Energy Resolution	2.92	0.57	0.48	0.43	0.50
Fake leptons modelling	2.55	0.17	0.48	0.43	0.45
$t\bar{t}$ ISR+FSR	2.45	0.18	0.35	0.40	0.47
Jet Energy Scale	1.66	0.61	0.28	0.27	0.29
Flavour Tagging	1.64	0.19	0.28	0.27	0.28
VV Cross section+PDF	1.21	0.16	0.20	0.20	0.21
Lepton Reconstruction	0.75	0.07	0.12	0.12	0.13
Pileup Reweighting	0.60	0.05	0.11	0.12	0.10
Z+jets Cross section+PDF	0.30	0.05	0.30	0.05	0.04
Remaining	0.06	0.01	0.01	0.01	0.01
Total Systematic Uncertainty	8.01	1.08	1.29	1.31	1.43

Table B.10: Tabular breakdown of the percentage uncertainties joined into physically-motivated groups for the DL1r tagger for the p_T range 40-60 GeV.

Grouped Uncertainty / w_1, w_2	100-85%	85-77%	77-70%	70-60%	60-0%
Single-top ISR+FSR+Interference	4.75	0.42	0.68	0.72	0.75
Jet Energy Resolution	3.20	0.20	0.64	0.47	0.53
$t\bar{t}$ PS+Hadronisation+PDF	3.06	0.18	0.36	0.43	0.51
$t\bar{t}$ ISR+FSR	2.44	0.13	0.24	0.35	0.41
Single-top PS+Hadronisation+PDF	1.83	0.05	0.36	0.26	0.29
Z+jets Cross section+PDF	1.64	0.22	0.21	0.26	0.25
Jet Energy Scale	1.14	0.39	0.15	0.21	0.18
Fake leptons modelling	0.92	1.18	0.02	0.05	0.05
Flavour Tagging	0.66	0.08	0.08	0.11	0.10
VV Cross section+PDF	0.50	0.06	0.07	0.07	0.08
Lepton Reconstruction	0.44	0.06	0.08	0.07	0.07
Pileup Reweighting	0.21	0.04	0.04	0.03	0.03
Remaining	0.01	0.01	0.00	0.00	0.00
Total Systematic Uncertainty	7.56	1.37	1.13	1.11	1.22

Table B.11: Tabular breakdown of the percentage uncertainties joined into physically-motivated groups for the DL1r tagger for the p_T range 60-85 GeV.

Grouped Uncertainty / w_1, w_2	100-85%	85-77%	77-70%	70-60%	60-0%
$t\bar{t}$ PS+Hadronisation+PDF	5.02	0.35	0.60	0.67	0.72
Single-top ISR+FSR+Interference	3.83	0.32	0.49	0.50	0.54
Jet Energy Resolution	2.24	0.39	0.98	0.36	0.38
$t\bar{t}$ ISR+FSR	2.01	0.14	0.19	0.23	0.31
Jet Energy Scale	1.92	0.25	0.24	0.26	0.27
Single-top PS+Hadronisation+PDF	0.95	0.04	0.15	0.08	0.14
Flavour Tagging	0.59	0.04	0.06	0.08	0.09
Lepton Reconstruction	0.48	0.05	0.10	0.06	0.06
Fake leptons modelling	0.44	0.08	0.07	0.04	0.06
Pileup Reweighting	0.43	0.11	0.07	0.05	0.05
VV Cross section+PDF	0.42	0.04	0.06	0.05	0.06
Z+jets Cross section+PDF	0.31	0.05	0.04	0.03	0.04
Remaining	0.06	0.01	0.01	0.01	0.01
Total Systematic Uncertainty	7.40	0.70	1.31	0.98	1.08

Table B.12: Tabular breakdown of the percentage uncertainties joined into physically-motivated groups for the DL1r tagger for the p_T range 85-110 GeV.

Grouped Uncertainty / w_1, w_2	100-85%	85-77%	77-70%	70-60%	60-0%
$t\bar{t}$ PS+Hadronisation+PDF	7.48	0.52	0.75	0.85	0.95
$t\bar{t}$ ISR+FSR	4.71	0.44	0.39	0.58	0.60
Single-top ISR+FSR+Interference	3.70	0.23	0.47	0.36	0.47
Jet Energy Resolution	1.08	0.18	0.44	0.11	0.17
Flavour Tagging	1.06	0.20	0.09	0.12	0.12
Jet Energy Scale	1.00	0.23	0.32	0.21	0.12
Z+jets Cross section+PDF	0.90	0.05	0.15	0.11	0.12
Fake leptons modelling	0.89	0.08	0.21	0.10	0.10
VV Cross section+PDF	0.61	0.07	0.06	0.08	0.07
Lepton Reconstruction	0.51	0.06	0.06	0.06	0.06
Single-top PS+Hadronisation+PDF	0.43	0.12	0.03	0.09	0.05
Pileup Reweighting	0.34	0.09	0.02	0.04	0.04
Remaining	0.13	0.01	0.01	0.02	0.02
Total Systematic Uncertainty	9.88	0.83	1.15	1.15	1.26

Table B.13: Tabular breakdown of the percentage uncertainties joined into physically-motivated groups for the DL1r tagger for the p_T range 110-140 GeV.

Grouped Uncertainty / w_1, w_2	100-85%	85-77%	77-70%	70-60%	60-0%
$t\bar{t}$ PS+Hadronisation+PDF	5.42	0.26	0.50	0.75	0.73
Single-top ISR+FSR+Interference	4.12	0.32	0.49	0.51	0.54
$t\bar{t}$ ISR+FSR	2.51	0.24	0.28	0.30	0.34
Jet Energy Scale	1.34	0.19	0.22	0.21	0.17
Jet Energy Resolution	0.96	0.14	0.16	0.31	0.19
Fake leptons modelling	0.67	0.26	0.18	0.05	0.06
Flavour Tagging	0.32	0.04	0.06	0.07	0.04
Single-top PS+Hadronisation+PDF	0.31	0.02	0.09	0.11	0.03
Lepton Reconstruction	0.24	0.03	0.03	0.04	0.03
Pileup Reweighting	0.21	0.04	0.05	0.02	0.03
VV Cross section+PDF	0.16	0.01	0.02	0.02	0.02
Z+jets Cross section+PDF	0.09	0.02	0.02	0.01	0.01
Remaining	0.05	0.00	0.01	0.01	0.01
Total Systematic Uncertainty	7.49	0.60	0.83	1.04	1.01

Table B.14: Tabular breakdown of the percentage uncertainties joined into physically-motivated groups for the DL1r tagger for the p_T range 140-175 GeV.

Grouped Uncertainty / w_1, w_2	100-85%	85-77%	77-70%	70-60%	60-0%
$t\bar{t}$ PS+Hadronisation+PDF	5.28	0.07	0.56	0.68	0.67
Single-top ISR+FSR+Interference	3.55	0.32	0.12	0.42	0.45
Jet Energy Resolution	2.49	0.58	0.18	0.27	0.28
$t\bar{t}$ ISR+FSR	2.45	0.35	0.32	0.26	0.28
Jet Energy Scale	2.11	0.29	0.31	0.27	0.26
Flavour Tagging	0.72	0.06	0.06	0.09	0.11
Z+jets Cross section+PDF	0.40	0.02	0.07	0.06	0.05
Pileup Reweighting	0.36	0.05	0.02	0.08	0.04
Fake leptons modelling	0.32	0.02	0.02	0.04	0.05
Single-top PS+Hadronisation+PDF	0.29	0.02	0.10	0.11	0.03
VV Cross section+PDF	0.24	0.04	0.02	0.05	0.04
Lepton Reconstruction	0.22	0.09	0.05	0.08	0.03
Remaining	0.02	0.02	0.01	0.03	0.00
Total Systematic Uncertainty	7.63	0.82	0.77	0.95	0.95

Table B.15: Tabular breakdown of the percentage uncertainties joined into physically-motivated groups for the DL1r tagger for the p_T range 175-250 GeV.

Grouped Uncertainty / w_1, w_2	100-85%	85-77%	77-70%	70-60%	60-0%
Single-top ISR+FSR+Interference	9.98	2.17	1.60	1.62	1.55
$t\bar{t}$ PS+Hadronisation+PDF	3.82	0.30	0.92	0.60	0.61
$t\bar{t}$ ISR+FSR	2.88	0.95	1.08	0.55	0.44
Jet Energy Scale	1.58	0.80	0.31	0.43	0.22
Jet Energy Resolution	1.44	0.75	0.61	0.20	0.35
Z+jets Cross section+PDF	1.25	0.08	0.17	0.21	0.22
Flavour Tagging	1.09	0.09	0.12	0.24	0.23
VV Cross section+PDF	0.51	0.06	0.02	0.09	0.11
Lepton Reconstruction	0.38	0.09	0.07	0.08	0.07
Single-top PS+Hadronisation+PDF	0.37	0.40	0.33	0.35	0.07
Fake leptons modelling	0.36	0.04	0.03	0.09	0.06
Pileup Reweighting	0.12	0.12	0.13	0.04	0.00
Remaining	0.05	0.03	0.02	0.02	0.01
Total Systematic Uncertainty	11.43	2.67	2.28	1.94	1.80

Table B.16: Tabular breakdown of the percentage uncertainties joined into physically-motivated groups for the DL1r tagger for the p_T range 250-600 GeV.

Appendix C

Gluino Pair Production With Multiple *b*-jets
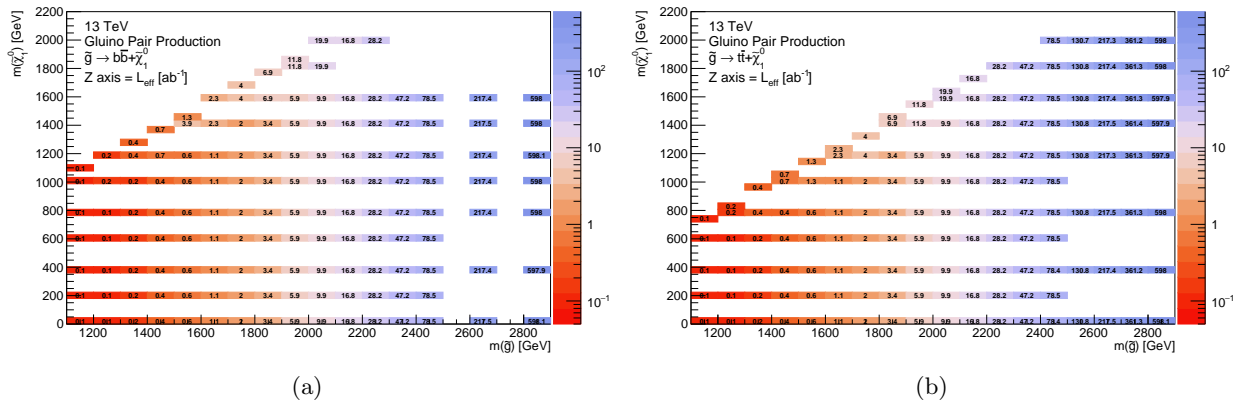
C.1 Effective Luminosity of the Signal Processes

Figure C.1: The effective luminosity ($L_{\mathrm{eff}}[\mathrm{ab}^{-1}]$) calculated for each (a) Gbb and (b) Gtt signal process using the cross section for the model and the number of Monte Carlo generated events.

C.2 Exclusion Limits - Best Expected Signal Regions
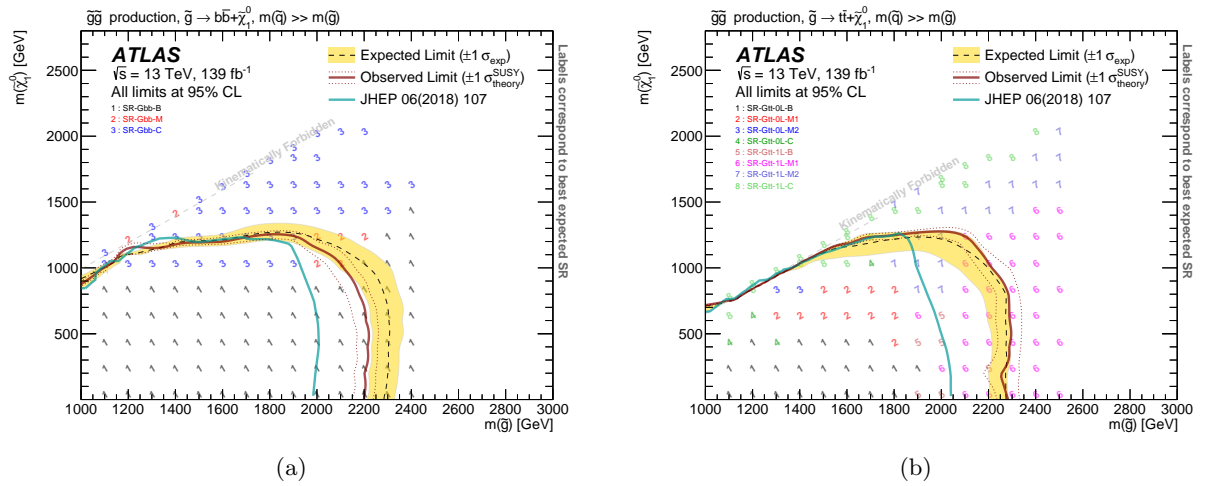
Figure C.2: Result of exclusion fit for the analysis regions for the (a) Gbb and (b) Gtt model-space. The dashed line shows the 95% CL expected limit. The shaded bands around the expected limits show the impact of the experimental and background-modelling systematic uncertainties. The labels correspond to the signal region which generates the best expected CL_s value for the given signal model. Taken from Ref. [162].

Appendix D

Multi-bin Shape Fit

D.1 Effective Mass Observable for Very Compressed Gbb
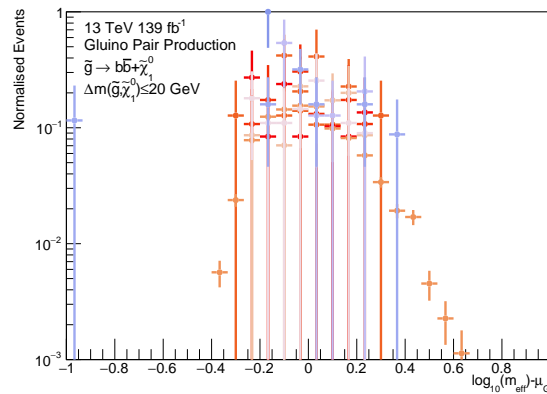
(a)

Figure D.1: The $\log 10(\mathrm{m_{eff}})$ distribution normalised to unity and centred by the fitted Gaussian mean. The signals included are all $\Delta m = 20$ GeV Gbb signal processes from Section 8.1.

D.2 Control Region Mismodelling Plots

As mentioned in Section 9.3, mismodelling is observed in the CR histogram in the $\log 10(\mathrm{m_{eff}})$ bin [3.05, 3.1] GeV and plots of some of the key analysis variables showing significant mismodelling can be seen in Figures D.2.

It is clear from Figure D.2(a) that the majority of the mismodelling originates were 6- and 7-jets are present in the event. Figure D.2(c) also shows that it could originate from events with $60 \lesssim \mathrm{m_{T,min}^{b-jets}} \lesssim 100$ GeV. By restricting the selection further to only 6- and 7-jet events, plots for the leading jet, leading lepton and key discriminating variables can be seen in Figures D.3, D.4 and D.5 respectively. Here it is evident, as mentioned in Section 9.3, there is a range of
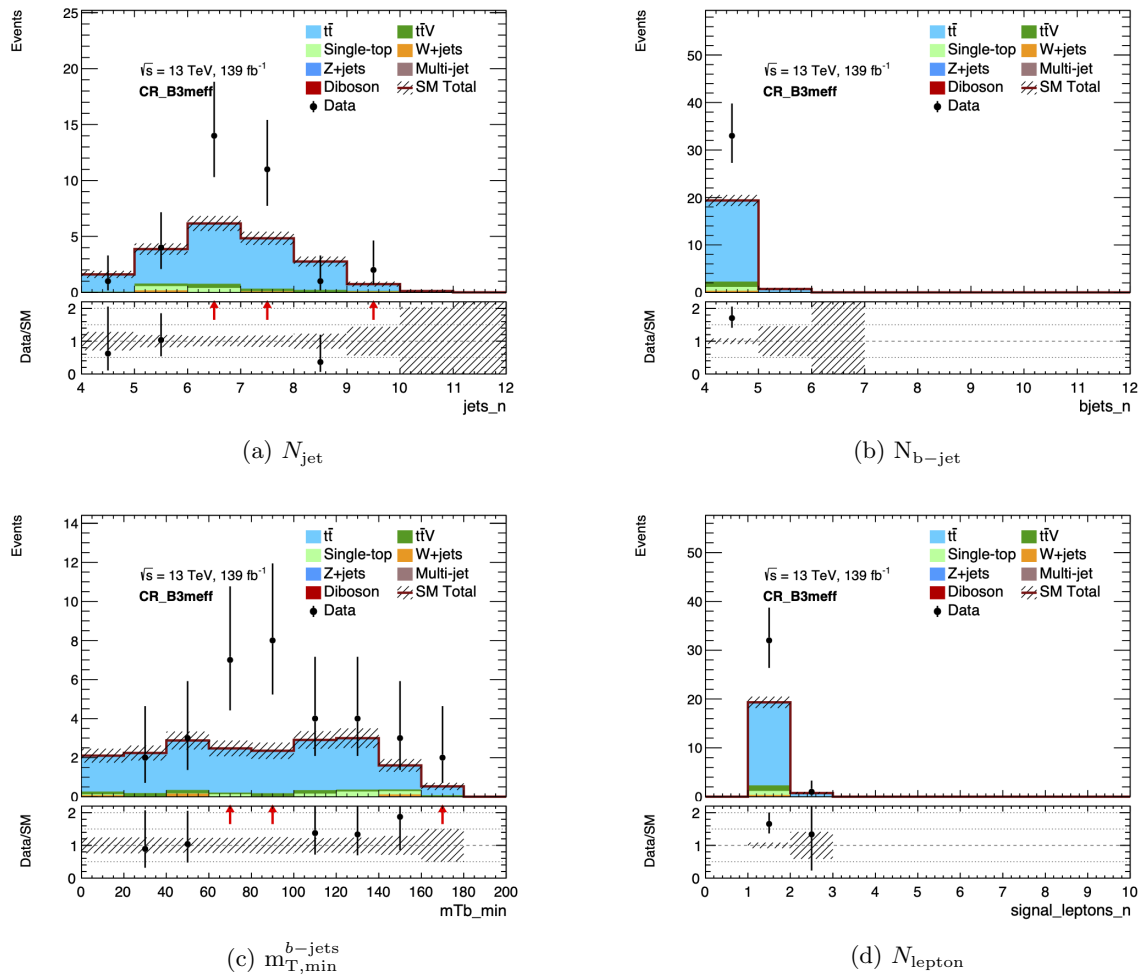
(a) N_{jet}

(b) $N_{\text{b−jet}}$

(c) $m_{\text{T,min}}^{b-\text{jets}}$

(d) N_{lepton}

Figure D.2: Key analysis distributions were the data is significantly mismodelled by the MC in the $\log 10(m_{\text{eff}})$ bin [3.05, 3.1] GeV of the CR histogram.

mismodelling in leading jet and leptons as well as the data in $E_{\mathrm{T}}^{\mathrm{miss}}$ distribution being generally underpredicted by the MC.
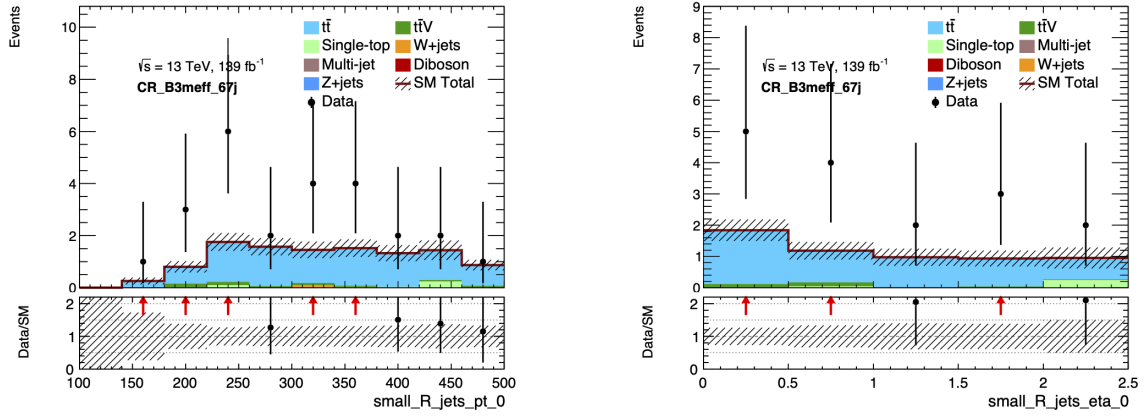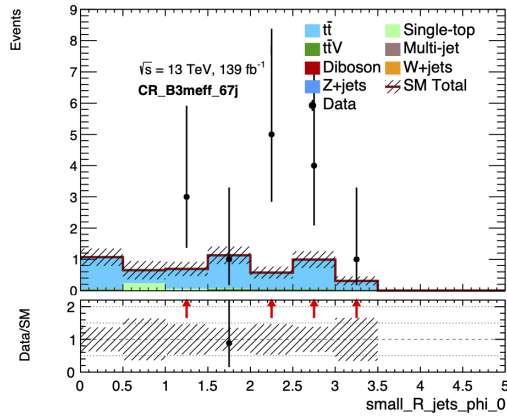

(a) Leading jet p_{T}

(b) Leading jet η

(c) Leading jet ϕ

Figure D.3: The leading jet for the CR histogram in the [3.05,3.1] GeV $\log 10(\mathrm{m_{eff}})$ bin and restricting the events further to only those with 6- or 7-jet events present.

(a) Leading lepton p_{T}
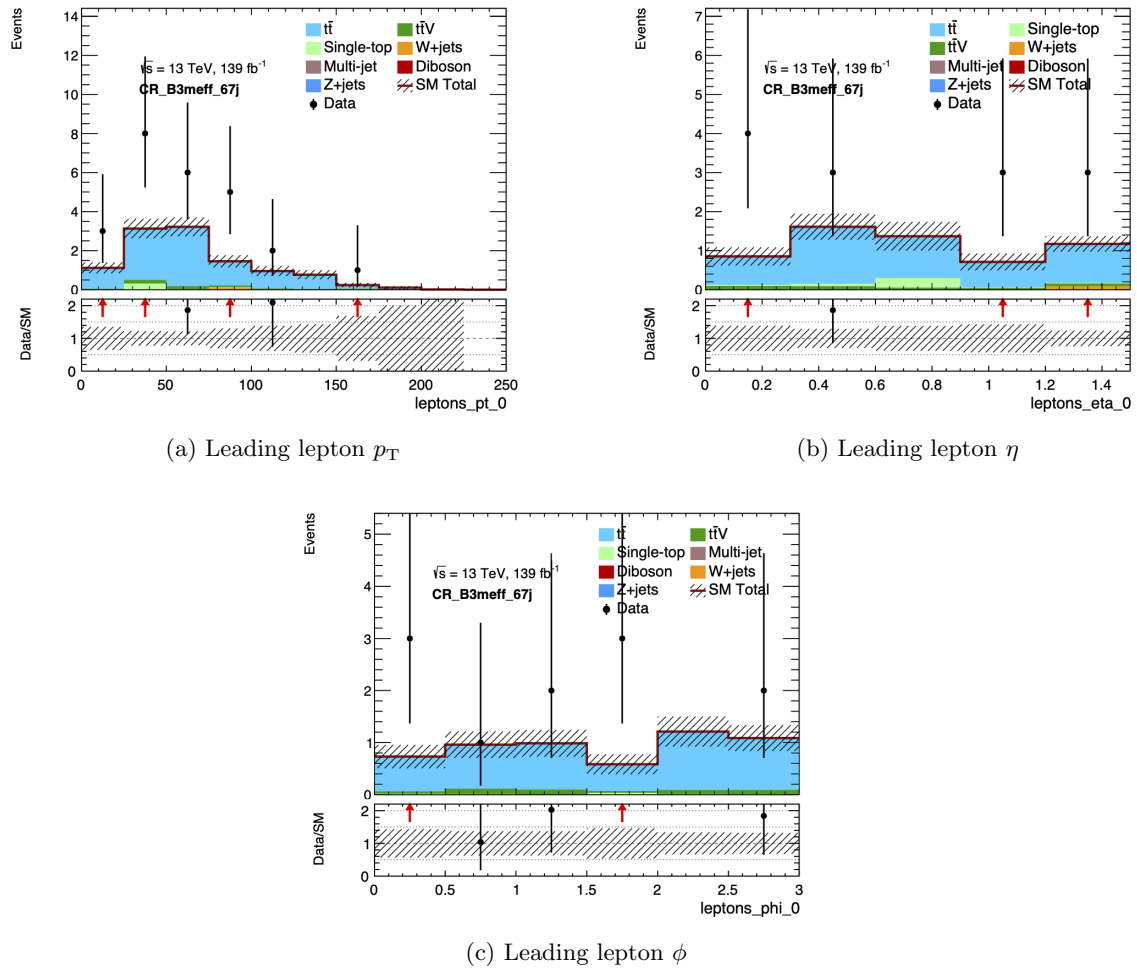

(b) Leading lepton η

(c) Leading lepton ϕ

Figure D.4: The leading lepton for the CR histogram in the [3.05,3.1] GeV $\log 10(\mathrm{m_{eff}})$ bin and restricting the events further to only those with 6- or 7-jet events present.

(a) $E_{\mathrm{T}}^{\mathrm{miss}}$

(b) $\mathrm{m_{eff}}$

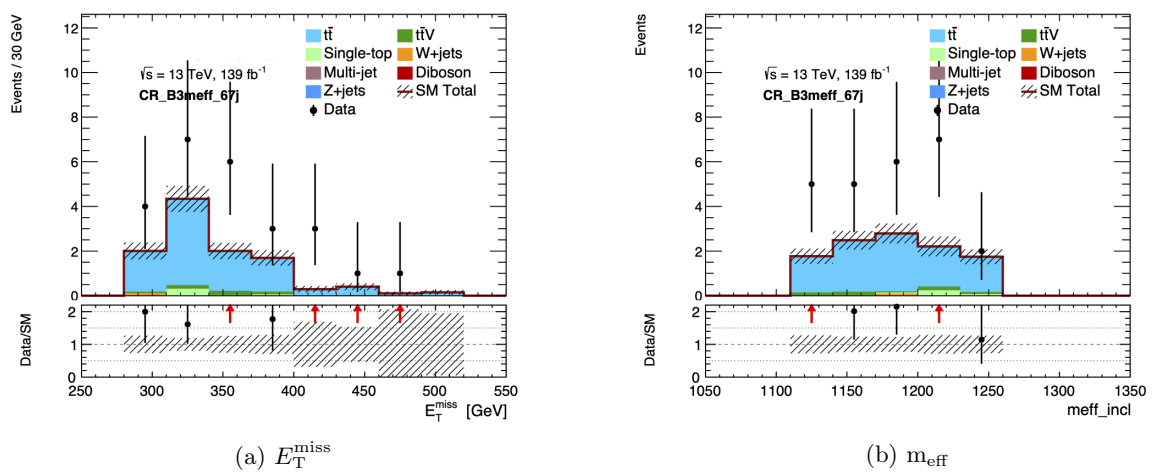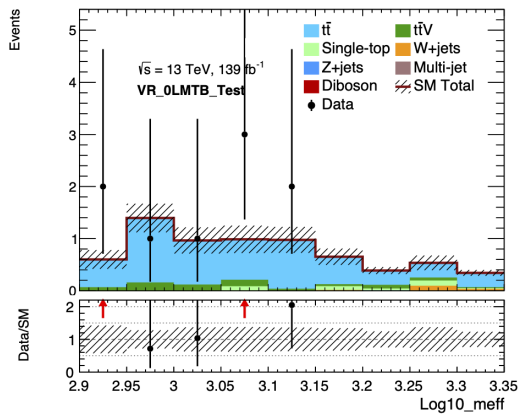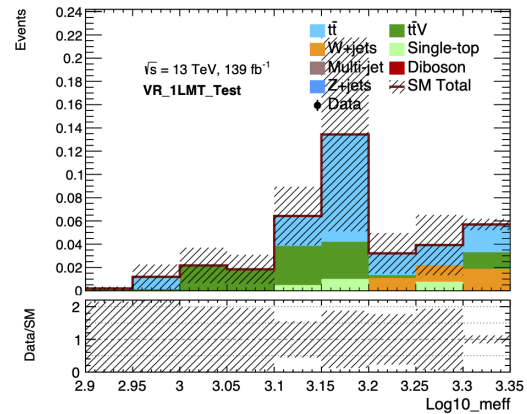Figure D.5: Key discriminating analysis variables for the CR histogram in the [3.05,3.1] GeV $\log 10(\mathrm{m_{eff}})$ bin and restricting the events further to only those with 6- or 7-jet events present.
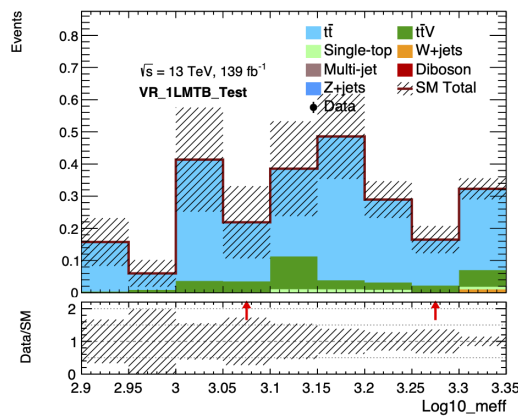
D.3 VR Histograms with SR Jet Multiplicity Requirement

(a) VR-0L-MTB Histogram

(b) VR-1L-MT Histogram

(c) VR-1L-MTB Histogram

Figure D.6: Each validation region with it's jet multiplicity requirement equivalent to the SR requirement ($N_{\text{jet}} \geq 10$).

## D.4 Technical Details for Performing the Fits

This appendix will denote all the technical information of the analysis strategy performed in Chapter 9 to allow the reader to replicate what was performed in this thesis.

The implementation of the fit strategy was based upon the 36fb^{-1} *strong multi-b* search[1] [1], which used a two-dimensional multi-bin approach based upon the observables; the number of jets and the effective mass. This is depicted in, for the one-lepton channel, in Figure D.7.

Since the strategy in Chapter 9 is not a two-dimensional approach but instead one dimensional in the $\log 10(\text{m}_{\text{eff}})$ observable, where the binning is defined in Table 9.3 and the selections for

---

[1]

The Git repository link for the 36fb^{-1} analysis is `https://gitlab.cern.ch/MultiBJets/MBJ_HistFitter/-/tree/ATLAS-CONF-2018-041`.
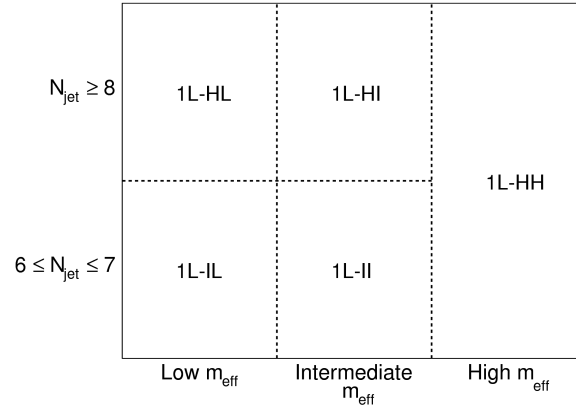
(a)

Figure D.7: Schematic presenting the multiple signal region bins in the one-lepton channel for the analysis strategy of Ref. [1].

each region are in Table 9.2[2].

Another significant aspect of establishing the workflow is how to include the arbitrary Gaussian signal into the likelihood fits. There are several ways to implement this and the simplest method was to create ROOT NTuples. The code used to create these (ROOT) NTuples can be found in the git repository in the path;

$MBJ_HF_ROOT/NTupleSignalCreator/GausSigNTuple.py,

where the only argument is `--NEvts`, which decides the number of events distributed according to a Gaussian function for each mean in m_{eff}-space (GeV). The range of means for which a Gaussian is created is hardcoded and thus, will be required to change for each unique search. A ROOT NTuple was created per signal and validation region because the Gaussian events are designed to be 100% efficient in surviving each region selection criteria and hence, the easiest solution compatible with HistFitter (HF) [102] is to produce a NTuple per region. Since the code to produce the NTuple only produces Gaussian-distributed events, the method used so that they have 100% acceptance in the region was by setting an ROOT alias for each observable in the region definition. The value of each alias is set so that it surpasses the selection threshold. The logic for this was based on a method that is used in the strong multi-b analysis, where a weight equal to one is added to events for the scenario where the weight applies only to signal or background processes, for example. That code can be found in the following path related to any *strong multi-b* analysis HistFitter Git repository:

$MBJ_HF_ROOT/metadata/utilities/output_to_hf/addKinRWSignal.py.

This is the basis of the workflow. In terms of performing likelihood fits in HF, different arguments are required depending on the physics goal. In terms of running the discovery fits performed in Section 9.5.1, each result is based upon the `-z` option that enables the discovery hypothesis test statistic to be performed. For each unblinded discovery plot (Figures 9.12-9.13), each result in

---

[2]The Git link for the analysis presented in this chapter can be found here `https://gitlab.cern.ch/MultiBJets/MBJ_HistFitter/-/tree/feature/MIshapeFit`.

the plot is a fit performed with each Gaussian signal model set as the signal sample argument in HF.

The slightly more complicated approach is the discovery sensitivity in Section 9.6.2, which involves adding the signal to the blinded[3] data. Here, for all Gtt and Gbb signals in the parameter-space, a scan across each Gaussian model is performed and hence, the total number of fits is greatly increased and therefore, this is only recommended to be run on a local computer system if the time taken to perform each LH fit is (relatively) quick (< 30 seconds) otherwise the use HTcondor system is recommended. Injecting signal in the data is primarily performed by the HF method `buildHisto` (lines 253 of `$MBJ_HF_ROOT/python/3b.py`), because it needs to be manually created because of the other histograms in HF being directly created from the ROOT NTuples. An example command for obtaining a discovery sensitivity LH fit for the Gtt model $m(\tilde{g}, \tilde{\chi}_1^0) = 2100, 1000$ GeV with a single Gaussian function ($\mu_G = 2300$ GeV) is,

```
HistFitter.py −wz −f −F excl python/3b.py ++config
config/mbj_139000.json config/mbj_patchShapefit.json
++regions B0meff B1meff B2meff B3meff B4meff B5meff
B6meff B7meff B8meff ++regionOutput shapefit
++signalSample Gauss_2300 ++unblind True ++FakeData
++InjectSignal Gtt_2100_5000_1000.
```

By simply removing `++FakeData ++InjectSignal Gtt_2100_5000_1000` from that line would result in a LH fit for the unblinded SR for the Gaussian function $\mu_G = 2300$ GeV.

To set limits the code is analogous to when performing an unblinded discovery fit scan, that is, without the signal injection process. The HF argument `-z` is replaced with `-l` to perform the hypothesis test inversion instead of using the discovery hypothesis test statistic. An example of an unblinded signal strength limit for the same Gaussian function can be obtained using:

```
HistFitter.py −wl −f −F excl python/3b.py ++config
config/mbj_139000.json config/mbj_patchShapefit.json
++regions B0meff B1meff B2meff B3meff B4meff B5meff
B6meff B7meff B8meff ++regionOutput shapefit
++signalSample Gauss_2300 ++unblind True.
```

Both fits are run with the HF exclusion fit type (`-F excl`). It was found that `-z` discovery hypothesis test, although unconventionally used, results in the same p-value for the HF fit types `excl` and `disc` and thus, is appropriate for use.

In terms of creating the final figures presented in Section 9.5, the creation of the one-dimensional discovery fit plot can be created by the code;

```
python $MBJ_HF_ROOT/AnalysisPYs/p0ScanPlot.py −−InputPath <Path>
−−Signal <Keyword>.
```

---

[3]Blinded data in HF by default uses the pre-fit background estimate but this code replaces it with the post-fit background estimate.

Where the `Signal` argument can be used to select the signal injected or more generally as a keyword for example selecting a specific analysis region that would be used in the filenames of the HF output files in the path, `<Path>`. Similarly, one can produce the one-dimensional signal strength limit plot, albeit without the keyword argument.

python $MBJ_HF_ROOT/AnalysisPYs/XSecLimPlot.py ——InputPath <Path>.

The two-dimensional plots are all based on the HF code that is used to plot exclusion contours in the mass plane of the two model parameters;

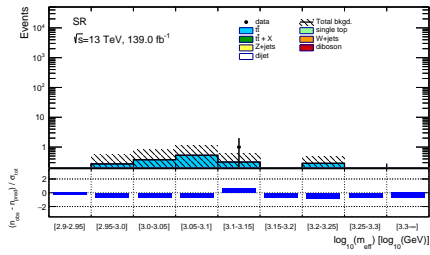$MBJ_HF_ROOT/HistFitter/scripts/harvestToContours.py.

This code requires a `json` or `txt` file as input so this aspect was again manually created, where the information that is plotted is extracted from the respective fit results. An example of the general workflow that was performed in this analysis can be seen in the bash script; `$MBJ_HF_ROOT/MakeJSONs.sh`, which individually produces `json` files for each set of information required for plotting and then combines for a final `json` file from which is used for plotting. Examples of the code used to create the whole set of two-dimensional plots can be found in the bash script `$MBJ_HF_ROOT/2DGridPlots.sh`.
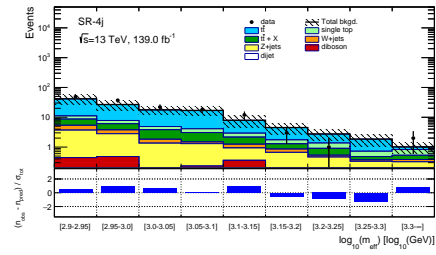
D.5   Supporting Fit Results

Table D.1 presents the breakdown of the full systematic configuration for an example discovery fit using the $10^\mu = 2675$ GeV Gaussian signal when Gtt $m(\tilde{g}, \tilde{\chi}_1^0) = 2000, 1200$ GeV is included in the blinded data for the SR histogram.

Uncertainty of channel	SR_B0meff	SR_B1meff	SR_B2meff	SR_B3meff	SR_B4meff	SR_B5meff	SR_B6meff	SR_B7meff	SR_B8meff
Total background expectation	0.11	0.28	0.37	0.59	0.35	0.23	0.39	0.31	1.33
Total statistical ($\sqrt{N_{exp}}$)	±0.33	±0.53	±0.61	±0.77	±0.60	±0.48	±0.63	±0.56	±1.15
Total background systematic	±0.21 [195.15%]	±0.23 [81.62%]	±0.32 [84.69%]	±0.45 [76.97%]	±0.23 [65.76%]	±0.16 [69.86%]	±0.19 [49.61%]	±0.17 [53.95%]	±1.22 [91.46%]
alpha_JER2	±0.12 [110.7%]	±0.11 [38.3%]	±0.11 [28.3%]	±0.17 [29.3%]	±0.09 [24.3%]	±0.16 [67.8%]	±0.03 [6.9%]	±0.06 [19.1%]	±0.02 [1.4%]
alpha_JER1	±0.12 [108.6%]	±0.12 [42.8%]	±0.01 [2.1%]	±0.23 [39.5%]	±0.05 [15.3%]	±0.07 [29.1%]	±0.03 [7.2%]	±0.04 [11.8%]	±0.01 [1.1%]
alpha_JER0	±0.12 [108.2%]	±0.09 [33.8%]	±0.09 [23.9%]	±0.22 [37.5%]	±0.09 [25.5%]	±0.03 [14.6%]	±0.03 [8.4%]	±0.06 [19.6%]	±0.03 [2.1%]
alpha_JER6	±0.11 [107.3%]	±0.06 [21.4%]	±0.08 [20.5%]	±0.11 [18.5%]	±0.11 [30.0%]	±0.02 [4.2%]		±0.05 [15.9%]	±0.02 [1.3%]
alpha_JER4	±0.11 [106.9%]	±0.03 [11.0%]	±0.00 [0.79%]	±0.01 [1.0%]	±0.00 [0.09%]	±0.07 [31.1%]	±0.03 [8.3%]	±0.04 [12.1%]	±0.02 [1.4%]
alpha_JER3	±0.11 [105.5%]	±0.07 [23.7%]	±0.21 [55.6%]	±0.12 [20.1%]	±0.00 [0.04%]	±0.05 [23.2%]	±0.00 [0.69%]	±0.04 [13.9%]	±0.02 [1.6%]
gamma_stat_SR_B0meff_cuts_bin_0	±0.09 [79.7%]	±0.00 [0.00%]	±0.00 [0.00%]	±0.00 [0.00%]	±0.00 [0.00%]	±0.00 [0.00%]	±0.00 [0.00%]	±0.00 [0.00%]	±0.00 [0.00%]
alpha_JER5	±0.06 [59.9%]	±0.03 [10.3%]	±0.05 [12.2%]	±0.02 [2.9%]	±0.01 [1.9%]	±0.05 [22.0%]	±0.02 [5.1%]	±0.04 [11.9%]	±0.02 [1.3%]
alpha_JES6	±0.05 [49.2%]	±0.04 [13.2%]	±0.09 [23.3%]	±0.07 [11.2%]	±0.02 [5.8%]	±0.00 [1.8%]	±0.06 [15.8%]	±0.01 [2.3%]	±0.01 [0.57%]
alpha_JES1	±0.04 [41.9%]	±0.04 [15.0%]	±0.09 [23.6%]	±0.23 [39.3%]	±0.02 [4.8%]	±0.02 [10.6%]	±0.05 [12.1%]	±0.03 [10.9%]	±0.01 [0.70%]
alpha_JES0	±0.04 [41.0%]	±0.05 [18.7%]	±0.14 [37.6%]	±0.21 [36.1%]	±0.02 [5.2%]	±0.01 [2.4%]	±0.05 [13.3%]	±0.02 [6.3%]	±0.01 [0.47%]
alpha_ttbar_theory_syst_SR_B0meff	±0.03 [29.6%]	±0.00 [0.00%]	±0.00 [0.00%]	±0.00 [0.00%]	±0.00 [0.00%]	±0.00 [0.00%]	±0.00 [0.00%]	±0.00 [0.00%]	±0.00 [0.00%]
alpha_JES2	±0.03 [26.2%]	±0.00 [0.82%]	±0.01 [2.7%]	±0.00 [0.16%]	±0.01 [4.2%]	±0.01 [3.3%]	±0.01 [3.2%]	±0.01 [2.0%]	±0.00 [0.13%]
mu_ttbar_B0meff	±0.02 [14.6%]	±0.00 [0.00%]	±0.00 [0.00%]	±0.00 [0.00%]	±0.00 [0.00%]	±0.00 [0.00%]	±0.00 [0.00%]	±0.00 [0.00%]	±0.00 [0.00%]
alpha_JMS_JET_Rtrk_Tracking3_frozen_mass	±0.01 [13.6%]	±0.02 [8.7%]	±0.02 [5.8%]	±0.04 [6.4%]	±0.03 [7.9%]	±0.01 [4.2%]	±0.03 [7.4%]	±0.01 [4.2%]	±0.00 [0.28%]
alpha_JMS_JET_Rtrk_Tracking2_frozen_mass	±0.01 [13.6%]	±0.02 [8.7%]	±0.02 [5.8%]	±0.04 [6.4%]	±0.03 [7.9%]	±0.01 [4.2%]	±0.03 [7.4%]	±0.01 [4.2%]	±0.00 [0.28%]
alpha_JMS_JET_Rtrk_TotalStat_frozen_mass	±0.01 [13.6%]	±0.02 [8.7%]	±0.02 [5.8%]	±0.04 [6.4%]	±0.03 [7.9%]	±0.01 [4.2%]	±0.03 [7.4%]	±0.01 [4.2%]	±0.00 [0.28%]
alpha_JMS_JET_Rtrk_Tracking1_frozen_mass	±0.01 [13.6%]	±0.02 [8.7%]	±0.02 [5.8%]	±0.04 [6.4%]	±0.03 [7.9%]	±0.01 [4.2%]	±0.03 [7.4%]	±0.01 [4.2%]	±0.00 [0.28%]
alpha_JMS_JET_Rtrk_Baseline_frozen_mass	±0.01 [13.6%]	±0.00 [0.47%]	±0.02 [5.8%]	±0.04 [6.4%]	±0.03 [7.9%]	±0.01 [4.2%]	±0.03 [7.4%]	±0.01 [4.2%]	±0.00 [0.27%]
alpha_JMS_JET_Rtrk_Modelling_frozen_mass	±0.01 [13.6%]	±0.00 [0.45%]	±0.00 [0.26%]	±0.04 [6.4%]	±0.03 [7.9%]	±0.01 [4.2%]	±0.03 [7.4%]	±0.01 [4.2%]	±0.00 [0.27%]
alpha_bTag_L	±0.01 [10.3%]	±0.02 [8.2%]	±0.02 [6.4%]	±0.02 [3.8%]	±0.02 [4.9%]	±0.01 [3.2%]	±0.02 [5.1%]	±0.01 [1.6%]	±0.01 [0.43%]
alpha_rw-oneside	±0.00 [2.8%]	±0.00 [1.2%]	±0.00 [0.11%]	±0.01 [1.2%]	±0.01 [2.2%]	±0.00 [1.9%]	±0.01 [3.4%]	±0.01 [3.7%]	±0.00 [0.28%]
alpha_bTag_C	±0.00 [2.2%]	±0.00 [0.82%]	±0.00 [0.21%]	±0.02 [2.6%]	±0.00 [0.35%]	±0.01 [2.2%]	±0.00 [0.08%]	±0.01 [1.7%]	±0.00 [0.16%]
alpha_JVT	±0.00 [2.0%]	±0.01 [2.3%]	±0.01 [1.7%]	±0.01 [1.6%]	±0.00 [1.1%]	±0.00 [1.1%]	±0.00 [0.83%]	±0.00 [0.43%]	±0.00 [0.06%]
alpha_JER7	±0.00 [1.9%]	±0.07 [25.7%]	±0.00 [0.22%]	±0.14 [23.1%]	±0.14 [38.8%]	±0.01 [2.3%]	±0.01 [2.7%]	±0.01 [3.6%]	±0.00 [0.37%]
alpha_ttbb_syst	±0.00 [1.6%]	±0.01 [2.2%]	±0.00 [0.90%]	±0.03 [4.6%]	±0.01 [3.0%]	±0.00 [0.34%]	±0.00 [0.95%]	±0.01 [2.6%]	±0.00 [0.04%]
alpha_ttcc_syst	±0.00 [0.93%]	±0.02 [8.4%]	±0.00 [0.22%]	±0.02 [3.7%]	±0.01 [3.7%]	±0.00 [0.73%]	±0.00 [0.72%]	±0.01 [2.3%]	±0.00 [0.03%]
alpha_bTag_extrapol_charm	±0.00 [0.22%]	±0.01 [3.2%]	±0.00 [0.34%]	±0.00 [0.05%]	±0.00 [1.4%]	±0.00 [0.10%]	±0.00 [0.65%]	±0.00 [0.86%]	±0.00 [0.04%]
alpha_kin_RW	±0.00 [0.21%]	±0.00 [1.0%]	±0.00 [1.1%]	±0.01 [1.2%]	±0.01 [2.0%]	±0.00 [2.1%]	±0.01 [3.3%]	±0.01 [2.9%]	±0.00 [0.22%]
mu_SIG	±0.00 [0.12%]	±0.00 [0.10%]	±0.00 [0.40%]	±0.00 [0.77%]	±0.01 [3.5%]	±0.03 [13.7%]	±0.06 [15.5%]	±0.11 [34.7%]	±1.22 [91.6%]
alpha_JES4	±0.00 [0.11%]	±0.00 [0.00%]	±0.00 [0.11%]	±0.00 [0.34%]	±0.00 [0.25%]	±0.00 [0.63%]	±0.00 [0.10%]	±0.00 [0.00%]	±0.00 [0.00%]
alpha_JES5	±0.00 [0.02%]	±0.04 [15.7%]	±0.00 [0.21%]	±0.00 [0.17%]	±0.00 [0.05%]	±0.00 [0.06%]	±0.00 [0.12%]	±0.00 [0.15%]	±0.00 [0.00%]
alpha_bTag_B	±0.00 [0.01%]	±0.00 [1.1%]	±0.00 [1.0%]	±0.01 [2.5%]	±0.01 [2.2%]	±0.00 [0.96%]	±0.00 [0.55%]	±0.00 [0.88%]	±0.00 [0.01%]
Lumi	±0.00 [0.00%]	±0.00 [0.25%]	±0.00 [0.80%]	±0.00 [0.15%]	±0.00 [0.46%]	±0.00 [1.6%]	±0.00 [1.2%]	±0.00 [1.4%]	±0.04 [2.8%]
alpha_bTag_extrapol_highPt	±0.00 [0.00%]	±0.00 [0.05%]	±0.00 [0.11%]	±0.00 [0.64%]	±0.00 [1.2%]	±0.00 [1.2%]	±0.01 [1.6%]	±0.01 [4.6%]	±0.00 [0.17%]
gamma_stat_SR_B1meff_cuts_bin_0	±0.00 [0.00%]	±0.13 [46.3%]	±0.00 [0.00%]	±0.00 [0.00%]	±0.00 [0.00%]	±0.00 [0.00%]	±0.00 [0.00%]	±0.00 [0.00%]	±0.00 [0.00%]
alpha_ttbar_theory_syst_SR_B5meff	±0.00 [0.00%]	±0.00 [0.00%]	±0.00 [0.00%]	±0.00 [0.00%]	±0.00 [0.00%]	±0.03 [13.0%]	±0.00 [0.00%]	±0.00 [0.00%]	±0.00 [0.00%]
alpha_Z_jets_syst_SR_B6meff	±0.00 [0.00%]	±0.00 [0.00%]	±0.00 [0.00%]	±0.00 [0.00%]	±0.00 [0.00%]	±0.00 [0.00%]	±0.00 [0.26%]	±0.00 [0.00%]	±0.00 [0.00%]
alpha_Z_jets_syst_SR_B2meff	±0.00 [0.00%]	±0.00 [0.00%]	±0.01 [3.2%]	±0.00 [0.00%]	±0.00 [0.00%]	±0.00 [0.00%]	±0.00 [0.00%]	±0.00 [0.00%]	±0.00 [0.00%]
alpha_ttbar_theory_syst_SR_B7meff	±0.00 [0.00%]	±0.00 [0.00%]	±0.00 [0.00%]	±0.00 [0.00%]	±0.00 [0.00%]	±0.00 [0.00%]	±0.00 [0.00%]	±0.05 [15.4%]	±0.00 [0.00%]
mu_ttbar_B3meff	±0.00 [0.00%]	±0.00 [0.00%]	±0.00 [0.00%]	±0.11 [18.9%]	±0.00 [0.00%]	±0.00 [0.00%]	±0.00 [0.00%]	±0.00 [0.00%]	±0.00 [0.00%]
alpha_ttbar_theory_syst_SR_B2meff	±0.00 [0.00%]	±0.00 [0.00%]	±0.08 [21.3%]	±0.00 [0.00%]	±0.00 [0.00%]	±0.00 [0.00%]	±0.00 [0.00%]	±0.00 [0.00%]	±0.00 [0.00%]
alpha_ttbar_theory_syst_SR_B4meff	±0.00 [0.00%]	±0.00 [0.00%]	±0.00 [0.00%]	±0.00 [0.00%]	±0.09 [24.7%]	±0.00 [0.00%]	±0.00 [0.00%]	±0.00 [0.00%]	±0.00 [0.00%]
alpha_Z_jets_syst_SR_B7meff	±0.00 [0.00%]	±0.00 [0.00%]	±0.00 [0.00%]	±0.00 [0.00%]	±0.00 [0.00%]	±0.00 [0.00%]	±0.00 [0.00%]	±0.00 [1.1%]	±0.00 [0.00%]
alpha_WZ_muR_muF_syst	±0.00 [0.00%]	±0.00 [0.00%]	±0.00 [0.00%]	±0.00 [0.71%]	±0.00 [0.00%]	±0.00 [0.62%]	±0.00 [0.09%]	±0.00 [0.17%]	±0.00 [0.04%]
alpha_JES3	±0.00 [0.00%]	±0.00 [0.00%]	±0.00 [0.00%]	±0.00 [0.18%]	±0.00 [0.00%]	±0.00 [0.00%]	±0.00 [0.00%]	±0.00 [0.00%]	±0.00 [0.00%]
alpha_topEW_syst_SR_B5meff	±0.00 [0.00%]	±0.00 [0.00%]	±0.00 [0.00%]	±0.00 [0.00%]	±0.00 [0.00%]	±0.01 [6.2%]	±0.00 [0.00%]	±0.00 [0.00%]	±0.00 [0.00%]
alpha_st_theory_syst_SR_B2meff	±0.00 [0.00%]	±0.00 [0.00%]	±0.00 [0.25%]	±0.00 [0.00%]	±0.00 [0.00%]	±0.00 [0.00%]	±0.00 [0.00%]	±0.00 [0.00%]	±0.00 [0.00%]
mu_ttbar_B5meff	±0.00 [0.00%]	±0.00 [0.00%]	±0.00 [0.00%]	±0.00 [0.00%]	±0.00 [0.00%]	±0.04 [15.7%]	±0.00 [0.00%]	±0.00 [0.00%]	±0.00 [0.00%]
alpha_WZ_ckkw_syst	±0.00 [0.00%]	±0.00 [0.00%]	±0.00 [1.0%]	±0.00 [0.00%]	±0.00 [0.00%]	±0.01 [4.5%]	±0.00 [0.00%]	±0.00 [0.00%]	±0.00 [0.02%]
alpha_st_theory_syst_SR_B7meff	±0.00 [0.00%]	±0.00 [0.00%]	±0.00 [0.00%]	±0.00 [0.00%]	±0.00 [0.00%]	±0.00 [0.00%]	±0.00 [0.00%]	±0.00 [0.45%]	±0.00 [0.00%]
alpha_topEW_syst_SR_B2meff	±0.00 [0.00%]	±0.00 [0.00%]	±0.02 [6.2%]	±0.00 [0.00%]	±0.00 [0.00%]	±0.00 [0.00%]	±0.00 [0.00%]	±0.00 [0.00%]	±0.00 [0.00%]
alpha_ttbar_theory_syst_SR_B1meff	±0.00 [0.00%]	±0.07 [26.9%]	±0.00 [0.00%]	±0.00 [0.00%]	±0.00 [0.00%]	±0.00 [0.00%]	±0.00 [0.00%]	±0.00 [0.00%]	±0.00 [0.00%]
mu_ttbar_B6meff	±0.00 [0.00%]	±0.00 [0.00%]	±0.00 [0.00%]	±0.00 [0.00%]	±0.00 [0.00%]	±0.00 [0.00%]	±0.13 [33.1%]	±0.00 [0.00%]	±0.00 [0.00%]
mu_ttbar_B4meff	±0.00 [0.00%]	±0.00 [0.00%]	±0.00 [0.00%]	±0.00 [0.00%]	±0.09 [24.1%]	±0.00 [0.00%]	±0.00 [0.00%]	±0.00 [0.00%]	±0.00 [0.00%]

Table D.1: Tabular breakdown of the full systematic configuration for an example discovery fit using th GeV is included in the blinded data for the SR histogram.
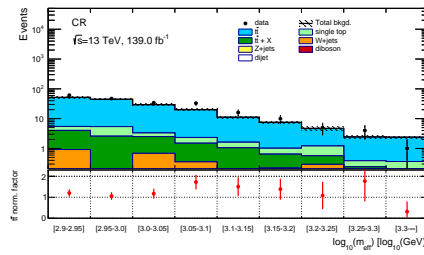
## D.6 Background-only Fit Results

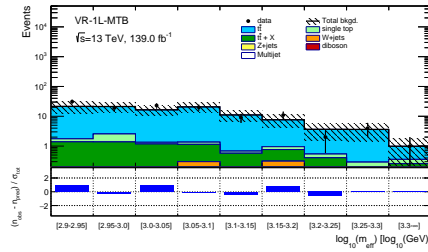(a) SR

(b) SR-4j

(c) CR pre-fit

Figure D.8: (a)-(b) ((c)) Post-fit (pre-fit) event yield in signal (control) regions. The upper panel presents the observed number of events and the predicted background yield after (before) the fit. The background category $t\bar{t} + X$ includes $t\bar{t}W/Z$, $t\bar{t}H$ and $t\bar{t}t\bar{t}$ events. All uncertainties described in Section 9.4 are included in the uncertainty band. The bottom panel of the CR plot displays the $t\bar{t}$ normalisation obtained from the fit.
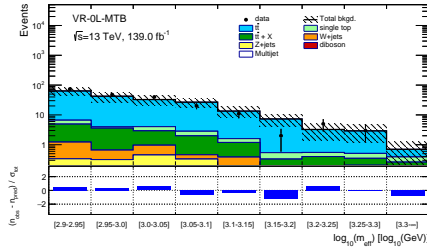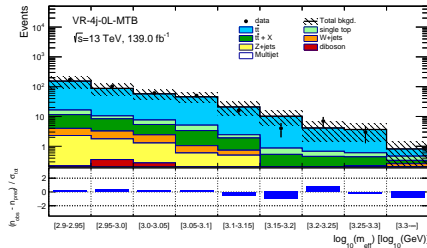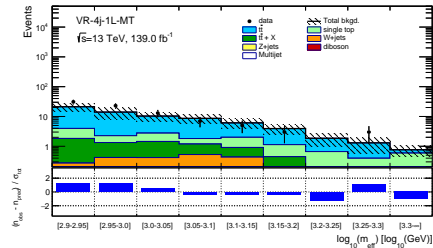
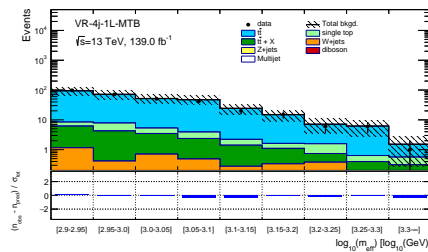(a) VR-0L-MTB
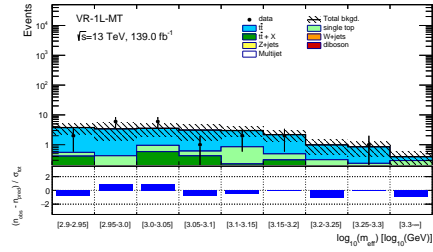
(b) VR-1L-MT

(c) VR-1L-MTB

Figure D.9: Post-fit event yield in high N_{jet} validation regions. The upper panel presents the observed number of events and the predicted background yield after the fit. The background category $t\bar{t} + X$ includes $t\bar{t}W/Z$, $t\bar{t}H$ and $t\bar{t}t\bar{t}$ events. All uncertainties described in Section 9.4 are included in the uncertainty band.

(a) VR-4j-0L-MTB

(b) VR-4j-1L-MT

(c) VR-4j-1L-MTB

Figure D.10: Post-fit event yield in low N_{jet} validation regions. The upper panel presents the observed number of events and the predicted background yield after the fit. The background category $t\bar{t} + X$ includes $t\bar{t}W/Z$, $t\bar{t}H$ and $t\bar{t}t\bar{t}$ events. All uncertainties described in Section 9.4 are included in the uncertainty band.